

**AERODYNAMIC EXCITATION OF THE DIAMETRAL
MODES OF AN INTERNAL AXISYMMETRIC CAVITY**

By

KAREEM AWNY ALY, B.SC, M.SC

A Thesis

Submitted to the school of graduate studies

in partial fulfillment of the requirements

for the degree

Doctor of Philosophy

McMaster University

© Copyright by Kareem Aly, December 2008

**AERODYNAMIC EXCITATION OF THE DIAMETRAL
MODES OF AN INTERNAL AXISYMMETRIC CAVITY**

**Doctor of Philosophy (2008)
(Mechanical Engineering)**

**McMaster University
Hamilton, Ontario, Canada**

**TITLE: Aerodynamic excitation of the diametral modes of an internal
axisymmetric cavity**

AUTHOR: Kareem Mohamed Awany Aly, B.Sc., M.Sc. (Cairo University)

SUPERVISOR: Dr. Samir Ziada

NUMBER OF PAGES: 231 (XXIV, 207)

ABSTRACT

The aerodynamic excitation of the diametral acoustic modes of an axisymmetric cavity-duct system is investigated experimentally. The change experienced by the acoustic diametral modes with the increase of the mean flow Mach number is investigated numerically. The first objective of this research is to examine the ability of the axisymmetric free shear layer forming along the cavity mouth to excite the asymmetric diametral modes which do not have preferred azimuthal orientations. The dependency of the system aeroacoustic response on both the cavity length and its depth is investigated to determine the limitations imposed by the relative dimensions of the cavity on the excitation process. The azimuthal behaviour of the self-excited diametral modes is also characterized.

An experimental set-up is designed to ensure the coincidence of the frequencies of the shear layer oscillation with the acoustic resonance frequencies. The selection of the test section dimensions is based on finite element simulation of the acoustic diametral modes for several geometries. To simulate the diametral modes at different flow Mach numbers, a finite difference code is developed based on a two-step computational aeroacoustic approach. This approach allows the simulation of the acoustic field, taking into account the convection effect of the mean flow.

The experimental results show that the diametral modes are very liable to be self-excited when the mean flow Mach number is higher than 0.1. The level of acoustic pressure during the diametral mode resonance increases rapidly with the increase of the ratio of the cavity depth, d , to the pipe diameter, D . However, the maximum acoustic pressure during each resonance decreases with the increase of the ratio of the cavity length, L , to the pipe diameter, D . The self-excitation of the diametral modes is sustainable with d/D as small as $1/12$. Further reduction in this ratio may result in complete suppression of the resonance. For deep cavities, $d/D > 3/12$, the first and second diametral modes are more liable to excitation than the higher order modes. This is attributed to

the fact that the low order modes have relatively higher radial acoustic particle velocity amplitude at the cavity mouth compared to the higher order ones. For $d/D=1/12$, the higher order modes have relatively higher radial acoustic particle velocity amplitude and consequently their tendency to be self-excited increases. For long cavities, $L/D>2/3$, the duct longitudinal acoustic modes start to be excited and become more dominant as the cavity length is further increased. The excitation mechanism of these longitudinal modes has not been investigated in this work since sufficient details already exist in the literature.

The azimuthal behaviour of the diametral modes is characterized for all the tested cases. For short cavities, the diametral modes are classified as spinning modes; while for long cavities, $L/D>1/2$, the orientation of the mode changes randomly over time. Small imperfections in the axisymmetric geometry result in what is described as partially spinning modes. An analytical model is developed to describe quantitatively the spinning behaviour of the diametral modes. The free shear layer and the diametral modes are found to be fully coupled in the azimuthal direction. The random behaviour of the diametral modes in the case of long cavities is attributed to the increase of randomness in the turbulent shear layer.

The numerical simulations show that the diametral modes experience considerable changes with the increase of the mean flow Mach number. At the cavity mouth, both the amplitude and phase distributions of the acoustic particle velocity are altered with the increase of the Mach number. This demonstrates the importance of considering the effect of the mean flow on the acoustic power production process. Moreover, the resonance frequency of the diametral modes decreases with the increase of the Mach number.

To my Parents

ACKNOWLEDGMENTS

First of all praise to God the greatest, the most merciful, the all beneficent, the omniscient, who guided the man to know which he did not know.

The work on this thesis has been an inspiring, often exciting, sometimes challenging, but always interesting. This thesis has been possible by the help of many people, who made it an enjoyable experience. I wish to express my sincere gratitude to my supervisor Dr. Samir Ziada, who guided this work and helped whenever I was in need with their encouragement, continuous support, and many fruitful discussions. To him I owe a great debt for the many values I learned in my academic career. I would also like to express my sincere thanks to my Ph.D supervisory committee members Dr. David Weaver and Dr. Chan Ching for their valuable suggestions and remarks that assessed me a lot through all the tasks of this study.

I am also indebted to the technicians of Mechanical Engineering Department at McMaster University, especially Mr. Dave Schick, Mr. Ron Lodewyks, and Mr. Joe Verhaeghe for their help in building the experimental test facility.

Last but not least, I would like to thank my parents, brother and sister for their unconditional love and support, which helped me to overcome all the difficulties and to progress in my work.

NOMENCLATURE

Roman letters

A	Acoustic pressure amplitude (maximum pressure) [Pa]
a	Coefficient in the spatial derivative formula \square
a_{ij}	Coefficient in Runge-Kutta stage i \square
aa	time shift [s]
b	Coefficient in the spatial derivative scheme \square
b_i	Coefficient in Runge-Kutta stage i \square
bb_i	Coefficient in the spatial derivative scheme \square
c	Speed of sound [m/s]
[C]	The damping matrix [N s/m]
c_a	Acoustic propagation speed in the axial direction [m/s]
c_p	Acoustic phase velocity [m/s]
c_t	Acoustic propagation speed in the transverse direction [m/s]
ct	Coefficient in the time marching scheme \square
D	Main pipe diameter [m]
D_i	Central difference operator [1/m]
D_i^B	Backward difference operator [1/m]
D_i^F	Forward difference operator [1/m]
d	Cavity depth [m]
e	Coefficient in the spatial derivative formula \square
e_i	Coefficient in Runge-Kutta stage i \square
ee_i	Coefficient in the spatial derivative scheme \square
F_b	Frequency correspond to the most amplified perturbation in the free shear layer [Hz]
F_f	Frequency of the external forcing excitation [Hz]
f	Frequency [Hz]
f_e	Broad band excitation maximum frequency [Hz]
g	Coefficient in the spatial derivative scheme \square
h	The height of 2-D duct [m]
J_m	Bessel function of the first kind \square
k	Acoustic wave number [1/m]

kk	Exponential decay rate of the trapped mode pressure [1/m]
$[K]$	The stiffness matrix [N/m]
L	Cavity length [m]
L_{min}	Minimum length for cavity to exhibit convection instability [m]
ℓ	Impinging length scale [m]
M	Mach number []
m	diametral mode number []
$[M]$	The mass matrix [Kg]
N	circular mode number []
n	Free shear layer mode number []
\mathcal{P}	Acoustic power production [W]
p_a	Acoustic pressure [Pa]
p_{mN}	Acoustic pressure of the combined acoustic mode of m diametral and N circular mode order [Pa]
p_0	Mean pressure [Pa]
p'	Perturbation pressure [Pa]
R	circular duct radius [m]
R_a	Gas constant [J/kg.K]
r	radial distance from the centerline of the duct [m]
Re_{d0}	Reynolds number based on the initial boundary layer thickness []
St	Strouhal number []
s_i	Coefficient in the spatial derivative scheme []
T	Temperature [K]
t	time [s]
U	Mean flow velocity [m/s]
U_a	Acoustic particle velocity [m/s]
u_a	Axial acoustic particle velocity [m/s]
u_0	Axial mean flow velocity [m/s]
u_p	Shear layer characteristic phase velocity [m/s]
u_τ	Friction velocity [m/s]
u'	Axial perturbation velocity [m/s]
\vec{U}	Mean flow velocity vector [m/s]
\vec{U}_a	Acoustic particle velocity vector [m/s]
v_a	Radial acoustic particle velocity [m/s]

v_e	Broad band excitation velocity [m/s]
v_0	Radial mean flow velocity [m/s]
v'	Radial perturbation velocity [m/s]
\vec{V}'	Perturbation velocity vector [m/s]
w_a	Azimuthal acoustic particle velocity [m/s]
w_0	Azimuthal mean flow velocity [m/s]
w'	Azimuthal perturbation velocity [m/s]
x	Axial distance [m]
y	Radial distance from the pipe wall [m]

Greek letters and symbols

α	Coefficient in the spatial derivative scheme []
β	Coefficient in the spatial derivative scheme []
γ	Specific heat ratio []
δ_0	Boundary layer thickness [m]
δ^*	Boundary layer displacement thickness [m]
ε_i	Coefficient in the time marching scheme []
ϵ_i	Coefficient in the time marching scheme []
θ	Azimuthal angle [rad]
θ_0	Boundary layer momentum thickness [m]
μ	Eigenvalue of the mass stiffness matrix [rad/s]
ν	Kinematic viscosity [m ² /s]
ξ	Empirical value of the acoustic production delay []
ϖ	Vorticity [1/s]
ρ	Total density [kg/m ³]
ρ_0	Mean density [kg/m ³]
ρ'	perturbation density fluctuation [kg/m ³]
$\tilde{\phi}$	Mode shape of the potential function
Φ_v	Acoustic particle velocity potential function
$\{\phi\}$	Eigenvector of the mass stiffness matrix [1/m]
ψ	Phase angle [rad]
ω	Angular frequency [rad/s]

ω_k	Duct cut off frequency [rad/s]
\mathcal{F}	Arbitrary variable []
ϕ_i	Runge-Kutta correction of stage i []
\mathfrak{R}	Empirical value of the ratio of the vortex convection velocity to the mean flow velocity []
\mathcal{V}	Volume [m ³]

CONTENTS

ABSTRACT	iii
ACKNOWLEDGMENTS	vi
Nomenclature	vii
List of tables	xv
List of Figures	xvi
CHAPTER 1 Introduction.....	1
1.1. Scope of the work.....	2
1.2. Thesis outline	4
CHAPTER 2 Literature review	5
2.1. Free shear layer instability.....	6
2.1.1. Forced perturbation of free shear layers:	9
2.1.2. Impinging free shear layers:	10
2.2. Classification of cavity oscillation	13
2.2.1. Flow field inside the cavity	14
2.2.2. Feedback Mechanisms	18
2.3. Cavity oscillation frequencies	20
2.4. Cavity resonance oscillation	24
2.4.1. Deep cavity resonance	24
2.4.2. Confined shallow cavity.....	26
2.5. Acoustic resonance of straight ducts.....	29
2.6. Computational Aeroacoustics.....	32
2.6.1. Linearized Euler approach	33
2.6.2. Spatial discretization	35
2.6.3. Time marching techniques	37
2.7. Summary and proposed research.....	39

CHAPTER 3	Experimental test Facility and Instrumentation.....	41
3.1.	Test facility.....	41
3.2.	Test section.....	43
3.2.1.	Introduction of orientation preference.....	47
3.3.	Simulation of acoustic modes.....	49
3.3.1.	Results and design criteria	50
3.4.	Instrumentations	51
3.4.1.	Pitot tube.....	52
3.4.2.	Pressure Transducer.....	53
3.4.3.	Hotwire	53
3.5.	Experimental procedures	54
CHAPTER 4	excitation of diametral modes	56
4.1.	Boundary layer measurements	57
4.1.1.	Displacement and momentum thicknesses	58
4.2.	Overview of the acoustic response	61
4.3.	Effect of cavity length	69
4.3.1.	Effect of cavity length on the Strouhal number	77
4.3.2.	Effect of cavity length on the pressure amplitude.....	79
4.3.3.	Effect of the cavity length on the acoustic field.....	81
4.4.	Effect of cavity depth.....	85
4.4.1.	Strouhal number of cavity resonance	94
4.4.2.	Effect of cavity depth on the pressure amplitude.....	95
4.4.3.	Effect of cavity depth on the mode shape	97
4.4.4.	Mode selectivity	100
4.5.	Effect of the shear layer hydrodynamic instability.....	103
4.6.	Summary.....	104

CHAPTER 5	Diametral modes azimuthal behaviour	106
5.1.	Analysis of the time average phase data	107
5.1.1.	Results of the first test section design	108
5.1.2.	Results of the second test section design	109
5.2.	Analysis of the time signal	110
5.2.1.	Visual representation	111
5.3.	Two orthogonal modes model	116
5.3.1.	Mathematical formulation	116
5.3.2.	Parametric study	117
5.3.3.	Characteristics of partially spinning modes	120
5.3.4.	Analysis of the experimental data	122
5.4.	Free shear layer azimuthal behaviour	123
5.4.1.	Cavity with splitter plate	124
5.4.2.	Hot wire measurements	127
5.5.	Summary	133
CHAPTER 6	Numerical Approach and code development	136
6.1.	Unsteady acoustic calculations	137
6.1.1.	System of governing equations	137
6.1.2.	Calculation of the spatial derivatives	139
6.1.3.	Time marching scheme	141
6.1.4.	Numerical filter	144
6.1.5.	Treatment of the boundary conditions	145
6.1.6.	Program algorithm	146
6.2.	Mean flow calculations	148
CHAPTER 7	Results of the Numerical Simulation	150
7.1.	Determination of the resonance frequency	151

7.2. The effect of mean flow field on acoustic resonance	154
7.2.1. Mean flow simulation.....	155
7.2.2. Effect of mean flow on the resonance frequency.....	156
7.2.3. Effect of mean flow on the mode shape	157
7.2.4. Analytical consideration and comparison with numerical simulation ...	167
7.3. Axisymmetric cavity-duct system	170
7.3.1. Numerical mesh	171
7.3.2. Effect of mean flow on the resonance frequency.....	173
7.3.3. Effect of mean flow on the mode shape	173
7.4. Summary.....	176
CHAPTER 8 Summary and Conclusions	179
8.1. Research contributions.....	182
8.2. Recommendations for future work	183
APPENDIX A Additional Experimental results	193
APPENDIX B Uncertainty analysis	205

LIST OF TABLES

Table 3-1 Dimensions of tested cavities	45
Table 4-1 List of displacement thickness, momentum thickness and shape factor at different flow velocities.....	60
Table 5-1 Phase difference and pressure amplitude ratios for different experimental cases of the first test section design ($d/D=2/12$)	109
Table 5-2 Phase difference and pressure amplitude ratios for different experimental cases of the second test section design ($d/D=2/12$)	110
Table 6-1 coefficients of the Optimized prefactored scheme	142
Table 6-2 Coefficients of the five stages step of LDDRG	143
Table 6-3 Coefficients of the six stages step of LDDRG.....	143
Table 7-1 The phase speed at different Mach numbers	169

LIST OF FIGURES

Figure 2-1 Flow visualization of a plane mixing layer, (Chevray, 1984).	7
Figure 2-2 Jet large scale structure growth rate for different perturbation Strouhal number, O, Axisymmetric nozzle; x, plane nozzle. (Freymuth, 1966)	8
Figure 2-3 evolution of wave amplitude with downstream distance for different forcing levels, θ_0 is the momentum thickness at the separation edge. ○ 70dB; ● 80 dB; ◻ 90 dB; x 100 dB (Freymuth, 1966)	11
Figure 2-4 General features of the self-sustained oscillation of impinging free shear layer (Rockwell, 1983)	12
Figure 2-5 Strouhal number of the impinging free shear layer Oscillation as a function of the dimensionless impinging length (Ziada and Rockwell, 1982)	13
Figure 2-6 Different types of flow field for shallow cavity (Tracy and Plentovich, 1993)	15
Figure 2-7 Illustration of the interaction between the free shear layer vortices (primary) and the spanwise cells (Rockwell and Knisely, 1980)	16
Figure 2-8 Instantaneous vorticity contours of a) mixing-layer and b) wake oscillation types at three different instants in time during one oscillation cycle (Rowley et al., 2002)	18
Figure 2-9 Matrix categorization of fluid-dynamic, fluid-resonant, and fluid-elastic types of cavity oscillations (Rockwell & Naudascher, 1978)	19
Figure 2-10 the Strouhal number of cavity oscillation over a range of Mach number. The data were collected from different sources. (Tam and Block, 1978) .	21
Figure 2-11 Variation of cavity mode Strouhal numbers with cavity length to depth ratio (data from Ethembaoglu (1978) – dark points represent predominant modes, solid lines represent theory from Rockwell (1977)) (Rockwell and Naudascher, 1978)	22
Figure 2-12 upward and downward frequency (f) jumps associated with self-excited oscillations at constant cavity length – dark points represent predominant modes. (Schachenmann and Rockwell, 1980)	28
Figure 2-13 Diametral and circular acoustic modes of cylindrical duct. Areas with same color are in-phase and areas with different color are out of phase	30
Figure 3-1 Schematic of the test facility	42

Figure 3-2 Schematic of the diffuser design.....	44
Figure 3-3 Schematic drawing of the test section showing the inlet bell-mouth and the axisymmetric cavity-duct system	46
Figure 3-4 Schematic drawing of the first cavity design. Cavity depth is 25 mm and cavity length is 100 mm.	46
Figure 3-5 Schematic drawing of the second cavity design. Cavity depth is 25 mm and cavity length is 100 mm.	47
Figure 3-6 position of the acrylic plates inside the cavity. a) one acrylic plate inserted inside the cavity, b) 4 acrylic plates inserted inside the cavity.....	48
Figure 3-7 Variation of the first diametral mode frequency with the main pipe length ($L/d=1$, $d/D=2/12$)	51
Figure 3-8 The mode shapes of the first, second and third acoustic resonance modes. $L/d=1$, $d/D=2/12$	52
Figure 3-9 Locations of the pressure transducers. a) first design, b) second design..	55
Figure 4-1 Radial profile of mean velocity profile at the cavity upstream edge for reference velocity of 31 m/s at the end of the bell mouth	57
Figure 4-2 Radial distribution of the dimensionless RMS amplitude of fluctuation velocity at the cavity upstream edge for reference velocity of 31 m/s at the end of the bell mouth (the continuous line is a moving average of the measurement data)	59
Figure 4-3 Representation of using the average velocity in the calculation of the boundary layer parameters	60
Figure 4-4 Acoustic pressure spectrum for cavity with $L/d=1$, $d/D=2/12$ at 64m/s ...	61
Figure 4-5 Waterfall plot and 2-D pressure contours for $L/d=1$, $d/D=2/12$. m is the diametral mode number, n is the free shear layer mode number.....	63
Figure 4-6 Mode shape of first diametral mode combined with a longitudinal mode, $f=1600\text{Hz}$ ($L/d=1$, $d/D=2/12$).....	64
Figure 4-7 Frequencies and amplitudes of the dominant acoustic modes as function of flow velocity ($L/d=1$, $d/D=2/12$). m is the diametral mode number, n is the free shear layer mode number.....	66
Figure 4-8 Dimensionless pressure amplitude and Strouhal number of the excited acoustic modes at different flow velocities ($L/d=1$, $d/D=2/12$). n is the shear layer mode number.....	67

Figure 4-9 Dimensionless acoustic pressure as function of the Strouhal number ($L/d=1$, $d/D=2/12$)	68
Figure 4-10 Waterfall plot and 2D pressure contours for $L/d=2$, $d/D=2/12$. m is the diametral mode number, n is the free shear layer mode number	70
Figure 4-11 Waterfall plot and 2D pressure contours for $L/d=3$, $d/D=2/12$. m is the diametral mode number, n is the free shear layer mode number	71
Figure 4-12 Waterfall plot and 2D pressure contours for $L/d=4$, $d/D=2/12$. m is the diametral mode number, n is the free shear layer mode number	72
Figure 4-13 Waterfall plot and 2D pressure contours for $L/d=5$, $d/D=2/12$. m is the diametral mode number, n is the free shear layer mode number	73
Figure 4-14 Waterfall plot and 2D pressure contours for $L/d=6$, $d/D=2/12$. m is the diametral mode number, n is the free shear layer mode number	74
Figure 4-15 Dimensionless pressure with the Strouhal number for $L/d=3$, $d/D=2/12$	77
Figure 4-16 Strouhal number as function of cavity length to depth ratio (L/d) the data is for cavities with $d/D=2/12$	78
Figure 4-17 Effect of cavity length on the maximum dimensionless pressure for the different free shear layer modes (m : the acoustic mode number, n : the free shear layer mode number, The lines are for visual aid only)	79
Figure 4-18 Effect of Mach number on the maximum dimensionless pressure for the different free shear layer modes (m : the acoustic mode number, n : the free shear layer mode number)	81
Figure 4-19 Vector plots of the acoustic particle velocity amplitude of the first diametral mode ($d/D=2/12$, $L/d=1$)	83
Figure 4-20 Radial component of the acoustic particle velocity along the cavity mouth corresponding to acoustic pressure of one Pascal at the center of the cavity floor ($d/D=2/12$)	84
Figure 4-21 Waterfall plot and 2D pressure contours for $L/d=2$, $d/D=1/12$. m is the diametral mode number, n is the free shear layer mode number	87
Figure 4-22 Waterfall plot and 2D pressure contours for $L/d=6$, $d/D=1/12$. m is the diametral mode number, n is the free shear layer mode number	88
Figure 4-23 Waterfall plot and 2D pressure contours for $L/d=0.5$, $d/D=4/12$. m is the diametral mode number, n is the free shear layer mode number	89

Figure 4-24 Waterfall plot and 2D pressure contours for $L/d=3/2$, $d/D=4/12$. m is the diametral mode number, n is the free shear layer mode number.....	90
Figure 4-25 Dimensionless pressure as a function of the Strouhal number for $L/d=2$, $d/D=1/12$	91
Figure 4-26 Dimensionless pressure as a function of the Strouhal number for $L/d=1/2$, $d/D=4/12$	93
Figure 4-27 Strouhal numbers of cavity free shear layer modes for all tested cases.	94
Figure 4-28 Maximum dimensionless acoustic pressure of the first diametral mode for different cavity depths to pipe diameter ratio, (a) excitation by cavity first free shear layer mode ($n=1$); (b) excitation by cavity second free shear layer mode ($n=2$).	96
Figure 4-29 Maximum radial acoustic particle velocity for different d/D ratios. The data corresponds to acoustic pressure of one Pascal at the center of the cavity floor ($L/D=2/12$).....	97
Figure 4-30 Contour plots of the radial particle velocity ($d/D=2/12$, $L/d=1$).....	99
Figure 4-31 Axial distribution of acoustic pressure decay for various cavity dimensions. m is the acoustic mode order. x is measured from the cavity center.	100
Figure 4-32 Frequency of the dominant diametral acoustic modes a) $d/D=1/12$, $L/D=2/12$; b) $d/D=2/12$, $L/D=2/12$; c) $d/D=4/12$, $L/D=2/12$. (m : the acoustic mode order, n : the free shear layer mode number)	102
Figure 4-33 Dimensionless acoustic pressure with the strouhal number based on the separation momentum thickness. The data are for cavities with $d/D=2/12$, $L/d=1$ to 6. All the data points correspond to the first reonance mode..	103
Figure 5-1 Typical time signals of different pressure transducers during the resonance of the first diametral acoustic mode. First test section set-up.	112
Figure 5-2 The time change of the phase difference between pressure transducers. For $L/d = 1$, $d/D=2/12$ & $U= 64$ m/s	113
Figure 5-3 Schematic illustration of the parameters of the visual representation technique	114
Figure 5-4 Snap shots of the instantaneous pressure distribution at the cavity floor. The snap shots are equally spaced over half a cycle. The red and blue contours are out of phase ($L/d=1$, $d/D=2/12$ & $U=64$ m/s)	115

Figure 5-5 Pressure amplitude contour plots of the resultant modes of the superposition of two orthogonal modes with zero temporal phase difference	118
Figure 5-6 Snap shots of the pressure contour of spinning mode. The snap shots are equally spaced over half a cycle. The mode is the result of the superposition of two orthogonal modes with 90° temporal phase shift, and amplitude ratio of 1.	119
Figure 5-7 Snap shots of the pressure contour of a partially spinning mode. The snap shots are equally spaced over half a cycle. The mode is the result of the superposition of two orthogonal modes with 90° temporal phase shift, and amplitude ratio of 0.4.	120
Figure 5-8 Pressure amplitude over the outer perimeter for a partially spinning mode with amplitude ratio of 0.4.....	121
Figure 5-9 Pressure phase over the outer perimeter for a partially spinning mode with amplitude ratio of 0.4	122
Figure 5-10 The time dependent change of the principal orientation of the first acoustic mode ($L/d = 2$, $d/D = 2/12$ & $U = 123$ m/s), first test section design.	124
Figure 5-11 The time change of the amplitude ratio of the first acoustic mode ($L/d = 2$, $d/D = 2/12$ & $U = 123$ m/s) , first test section design.	125
Figure 5-12 Configuration of cavity with one splitter plate and the diametral modes associated with it ($L/d = 1$, $d/D = 2/12$) , first test section design.....	126
Figure 5-13 Time signal of pressure transducer (PT1) for cavity with single splitter plate. ($U = 64$ m/s) , first test section design.	127
Figure 5-14 Close-up details of the sound pressure RMS amplitude spectra for cavity with single splitter plate, first test section design.	128
Figure 5-15 Schematic of the locations of the pressure transducers and the hot wire probes used in measuring the azimuthal phase of the velocity fluctuation, , second test section design.	129
Figure 5-16 Radial distribution of the amplitude of the velocity fluctuation during the resonance of the first diametral mode excited by the first shear layer mode; $m = 1$, $n = 1$, $U = 67$ m/s, $x/L = 0.5$	130

Figure 5-17 Radial distribution of the phase of the velocity fluctuation during the resonance of the first diametral mode excited by the first shear layer mode; $m=1$, $n=1$, $U=67$ m/s, $x/L=0.5$	131
Figure 5-18 Radial distribution of the amplitude of the velocity fluctuation during the resonance of the first diametral mode excited by the first shear layer mode; $m=1$, $n=2$, $U=33$ m/s, $x/L=0.5$	132
Figure 5-19 The time dependent change of the azimuthal phase difference of the velocity fluctuation and the acoustic pressure for the first acoustic mode excited by the first free shear layer modes, test conditions correspond to those of fig. 5-16.	133
Figure 5-20 The time dependent change of the azimuthal phase difference of the velocity fluctuation and the acoustic pressure for the first acoustic mode excited by the first free shear layer modes, test conditions correspond to those of fig. 5-18.	134
Figure 6-1 The axial velocity fluctuation contours at different times.....	137
Figure 6-2 Dispersive characteristics of the fourth order optimized scheme (Ashcroft & Zhang, 2003).....	140
Figure 6-3 schematic of a computational grid used to avoid a grid point at the centerline	145
Figure 6-4 The algorithm of the FORTRAN code developed to solve the acoustic perturbation equations.....	147
Figure 7-1 Time signal of the cavity floor forced oscillation	152
Figure 7-2 Amplitude spectra of the cavity floor forced oscillation	152
Figure 7-3 Spectrum of the pressure fluctuation resulting from the broad band excitation of the numerical domain.....	153
Figure 7-4 Schematic of the 2-D computational domain. Cavity length is 25 mm and cavity depth is 25 mm.....	154
Figure 7-5 Dimensionless velocity profile of the mean flow at the middle of the 2-D computational domain for $M=0.1$. The dotted lines mark the cavity mouth	155
Figure 7-6 Dimensionless frequency of the first transverse mode as a function of the mean flow Mach number.....	156

Figure 7-7 Contours of the pressure amplitude of the first transverse acoustic mode of planar cavity-duct system. $M=0$, $L=25\text{mm}$, $d=25\text{mm}$ and the duct height = 150mm	158
Figure 7-8 Pressure amplitude along the duct wall as a ratio to the amplitude of the pressure at the cavity floor. $L=25\text{mm}$, $d=25\text{mm}$ and the duct height = 150mm	159
Figure 7-9 Snap shots of the contours of the acoustic pressure over half a cycle. The contours legend is just to demonstrate the relative amplitude of the contours. $M=0$, $L=25\text{mm}$, $d=25\text{mm}$ and the duct height = 150mm	161
Figure 7-10 Variation of the pressure phase in the axial direction along the duct wall. $L=25\text{mm}$, $d=25\text{mm}$ and the duct height = 150mm	162
Figure 7-11 Axial Phase speed of the pressure for $M=0.2$. $L=25\text{mm}$, $d=25\text{mm}$ and the duct height = 150mm	163
Figure 7-12 Contour plot of the amplitude of the vertical particle velocity at zero flow. $L=25\text{mm}$, $d=25\text{mm}$ and the duct height = 150mm	164
Figure 7-13 Contour plots of the amplitude of the vertical particle velocity. The contours legend is just to demonstrate the relative amplitude of the contours. $L=25\text{mm}$, $d=25\text{mm}$ and the duct height = 150mm	165
Figure 7-14 Snap shots of the vertical particle velocity contours for $M=0.2$. The contours legend is just to demonstrate the relative amplitude of the contours.	166
Figure 7-15 Phase of the vertical particle velocity along the cavity mouth. $L=25\text{mm}$, $d=25\text{mm}$ and the duct height = 150mm	167
Figure 7-16 Dimensionless frequency of the first transverse mode as a function of the mean flow Mach number. Experimental data is for $L/d=2$, $d/D=1/12$	171
Figure 7-17 longitudinal and circular cross section of the mesh used in the simulation of the axisymmetric geometry. $L/d=1$ and $d/D=2/12$	172
Figure 7-18 Dimensionless frequency of the first diametral mode as a function of the mean flow Mach number. $L/d=1$ and $d/D=2/12$	174
Figure 7-19 Mode shape of the first diametral mode in terms of the contours of the pressure amplitudes. The contours legend is just to demonstrate the relative amplitude of the contours. $M=0.0$, $L/d=1$ and $d/D=2/12$	175

Figure 7-20 Variation of the first diametral mode pressure phase in the axial direction along the duct wall. $L/d=1$ and $d/D=2/12$	176
Figure 7-21 Contour plots of the amplitude of the radial particle velocity of the first diametral mode. The contours legend is just to demonstrate the relative amplitude of the contours. $L/d=1$ and $d/D=2/12$	177
Figure 7-22 Phase of the first diametral mode radial particle velocity along the cavity mouth. $L/d=1$ and $d/D=2/12$	178
Figure A-1 Radial mean velocity profile at the cavity upstream edge for reference velocity of 40 m/s at the end of the bell mouth	193
Figure A-2 Radial mean velocity profile at the cavity upstream edge for reference velocity of 55 m/s at the end of the bell mouth	194
Figure A-3 Radial mean velocity profile at the cavity upstream edge for reference velocity of 80 m/s at the end of the bell mouth	194
Figure A-4 Radial distribution of the dimensionless RMS amplitude of fluctuation velocity at the cavity upstream edge for reference velocity of 40 m/s at the end of the bell mouth (the continuous line is a moving average of the measurement data)	195
Figure A-5 Radial distribution of the dimensionless RMS amplitude of fluctuation velocity at the cavity upstream edge for reference velocity of 55m/s at the end of the bell mouth (the continuous line is a moving average of the measurement data)	195
Figure A-6 Radial distribution of the dimensionless RMS amplitude of fluctuation velocity at the cavity upstream edge for reference velocity of 80 m/s at the end of the bell mouth (the continuous line is a moving average of the measurement data)	196
Figure A-7 Waterfall plot and 2D pressure contours for $L/d=4$, $d/D=1/12$. m is the diametral mode number, n is the free shear layer mode number	197
Figure A-8 Waterfall plot and 2D pressure contours for $L/d=8$, $d/D=1/12$. m is the diametral mode number, n is the free shear layer mode number	198
Figure A-9 Waterfall plot and 2D pressure contours for $L/d=10$, $d/D=1/12$. m is the diametral mode number, n is the free shear layer mode number	199
Figure A-10 Waterfall plot and 2D pressure contours for $L/d=12$, $d/D=1/12$. m is the diametral mode number, n is the free shear layer mode number	200

Figure A-11 Waterfall plot and 2D pressure contours for $L/d=1$, $d/D=4/12$. m is the diametral mode number, n is the free shear layer mode number201

Figure A-12 Waterfall plot and 2D pressure contours for $L/d=2$, $d/D=4/12$. m is the diametral mode number, n is the free shear layer mode number202

Figure A-13 Waterfall plot and 2D pressure contours for $L/d=5/2$, $d/D=4/12$. m is the diametral mode number, n is the free shear layer mode number....203

Figure A-14 Waterfall plot and 2D pressure contours for $L/d=3$, $d/D=4/12$. m is the diametral mode number, n is the free shear layer mode number204

CHAPTER 1

INTRODUCTION

The need to suppress large-amplitude pressure oscillations arising from the flow over cavities has motivated the investigation of such flow since the 1950s (Krishnamurty 1955). Flow over cavities is well known to be a potential source of acoustic resonance excitation in numerous engineering applications including jet engines, rockets, piping system, control valves, airplane wheel wells and other fuselage openings for sensors and optical devices. Flow-excited acoustic resonances can cause acute noise levels, significant alteration of the operating conditions and, in some cases, can result in catastrophic failure due to acoustic fatigue of the cavity structure.

Flow over a cavity-backed aperture represents a complicated dynamic flow despite the simple geometry. The separated flow at the upstream cavity edge forms a free shear layer over the cavity mouth, which is hydrodynamically unstable. The hydrodynamic instability of the shear layer amplifies the vortical disturbances at the upstream edge as they are convected downstream to form distinct vortices. The interaction between these vortices and the cavity downstream edge generates pressure perturbations (acoustic waves). These acoustic waves are then propagated upstream through the adjacent domain to trigger new vortical disturbances at the upstream edge and thereby close the feedback cycle.

Whenever the cavity is attached to a confined domain, the pressure perturbations can excite the acoustic natural modes of the domain if the shear layer oscillation frequency coincides with the frequency of one of the acoustic modes. In such situations, the vortical disturbance at the upstream edge is triggered by the velocity oscillation associated with the acoustic resonance (acoustic particle velocity) and the acoustic energy at the downstream edge is generated due to the interaction between the vortices and the acoustic particle velocity. Therefore, the feedback process is strongly dependant on the acoustic field and its interaction with the shear layer.

The excitation of the acoustic diametral modes of an axisymmetric cavity-duct system has not been investigated thoroughly before, despite the relevance of this flow geometry to many engineering applications such as piping systems, jet engines, turbomachinery, control valves, rocket engines and many others. The interaction mechanism between the diametral modes and the axisymmetric cavity shear layer is currently not well understood. Moreover, the excitation of the diametral acoustic modes, which are *asymmetric* modes, by the cavity *axisymmetric* free shear layer produces a peculiar condition in which the diametral mode has no preferred orientation. Another phenomenon that has not been investigated before is the effect of the mean flow on the acoustic modes and the associated particle velocity fields. Characterizing this effect is crucial for better understanding of the aeroacoustics excitation mechanism and the generation of acoustic power which sustains the acoustic resonance.

1.1. Scope of the work

This work investigates the aerodynamic excitation of acoustic diametral modes of axisymmetric cavity-duct system and the effect of the mean flow on the acoustic mode. The investigation can be categorized into three tasks. First, experiments are performed to determine whether the diametral modes can be excited and when the excitation of the diametral modes is a major issue. This task also includes characterizing the effect of the flow velocity and cavity geometry on the excitation process. The second task focuses on the azimuthal behaviour of the diametral mode and the associated shear layer oscillation.

Finally, the effect of the mean flow on the acoustic mode shape is investigated in the third task by means of numerical simulations.

To accomplish the first task, a series of experiments is performed to study the excitation process for different cavity dimensions over a velocity range up to 145m/s, while the main duct dimensions are kept constant. All the studied geometries are for shallow cavities (cavity length to depth ratio ≥ 1), except one case that has a length to depth ratio of 0.5. The pressure response is measured at the cavity floor with the use of pressure transducers. Finite element analysis is performed to provide the acoustic mode shape for the different cavity-duct geometries at zero flow. The results of this analysis are used to explain some of the experimental observations. Hotwire measurements are performed to characterize the upstream boundary layer

For the second task, the test section is instrumented with multiple pressure transducers to measure simultaneously the pressure oscillation at different orientations at the cavity floor. The measurements are performed for all the geometries, which are tested in the first task. Based on the characteristics of the mode shape and the analysis of the time signal of the pressure transducers, a new analytical model is proposed to describe the different azimuthal behaviours observed in the experiments. The effect of orientation preference due to geometrical deviation from axisymmetry on the azimuthal behaviour is studied by inserting acrylic plates inside the cavity at specific orientations. The interaction between the shear layer and the acoustic mode is investigated using the pressure transducers in conjunction with a set of two hot-wire probes inserted in the free shear layer. This setup allows determination of the relation between the azimuthal behaviours of the shear layer and that of the acoustic mode.

The third task requires the development of a numerical code which is based on a two-step computational aeroacoustics approach. In this approach, the acoustic effect on the mean flow and the aeroacoustics sources are not considered. Two-dimensional planar and three-dimensional axisymmetric versions of the code are developed. The simulation determines the effect of the mean flow on different aspects of the acoustic mode characteristics, which

include the acoustic resonance frequency, distribution of the pressure amplitude and phase and the distribution of the acoustic particle velocity amplitude and phase.

1.2. Thesis outline

This thesis consists of eight chapters. In Chapter 2, the literature review on free shear layer instability, oscillation of grazing flow over cavities, mean flow effect on sound propagation inside ducts and computational aeroacoustics is summarized. In Chapter 3, the experimental setup and the measurement techniques used in this research are described. The experimental results relating to the excitation of the diametral modes and the effect of cavity length and depth on the excitation process are presented and analysed in Chapter 4. In Chapter 5, the azimuthal behaviour of the diametral modes is studied and an analytical model is developed to describe and quantify the observed behaviour. The numerical approach and the development of the FORTRAN code used in predicting the effect of the mean flow on the acoustic mode is presented in Chapter 6. In Chapter 7, the simulation of the effect of the mean flow on the acoustic mode is presented. The summary and the conclusions of this work as well as some recommendations for future work are provided in Chapter 8.

CHAPTER 2

LITERATURE REVIEW

The early attention the grazing flow over cavity-backed aperture received was because of the appearance of this flow geometry as a source of oscillation and noise generation in naval and aeronautical industries (Krishnamurty, 1955). More recently, flow over cavities has been extensively investigated because of its wide range of applications such as piping system (Lafon, et al., 2003), control valves (Ziada and Bühlmann, 1989), combustion chambers and rocket engines (Flandro, 1986) and Aero-optical applications (Ahuja and Chambers, 1987).

Cavity oscillations are self-sustained by a feedback excitation mechanism. The two main components of this mechanism are the inherent instability of the cavity shear layer and a feedback phenomenon, the latter of which depends on the nature of system oscillation. The shear layer instability causes small vorticity perturbations at the cavity leading edge to grow rapidly as they travel downstream with the flow. As these amplified vorticity perturbations reach the cavity downstream corner, the feedback phenomenon completes the excitation mechanism cycle by generating new perturbations at the cavity upstream corner. Cavity oscillations are classified according to the nature of the feedback phenomenon that triggers the self-sustained oscillation. Rockwell and

Naudascher (1978) classified this excitation mechanism into three categories: 1) fluid-dynamic, 2) fluid-resonant, and 3) fluid-elastic oscillation.

In this chapter, the relevant physical phenomena which include the free shear layer instability and the different feedback mechanisms are reviewed. Critical review of the literature on the cavity fluid-resonance oscillation is then presented. The characteristics of the diametral acoustic modes are discussed based on the available literature, followed by a review of the numerical techniques to predict the effect of mean flow on acoustic wave propagation.

2.1. Free shear layer instability

In this section, the general behaviour and characteristics of the free shear layer are presented. This includes detailing the behaviour of the shear layer under forced excitation and the behaviour of impinging free shear layer which is similar to the fluid dynamic mechanism of cavity oscillations.

Free shear layers are formed when two parallel streams with different velocities are merged together. Examples of this flow are mixing layers, jets, wakes, and flow over backward facing step and cavities. Free shear layers, in general, are characterized as inherently unstable flows. The instability of a flow is simply the ability of small perturbations in the flow to grow to form larger vortical structures. Figure 2-1 (Chevray, 1984) shows three snap shots of flow visualization of plane mixing layer. In the snap shots, which are sequenced in time, it can be seen how a perturbation grows and evolve as it is convected downstream. The inviscid stability theory developed by Lord Rayleigh (1880) accurately predicts the range of frequencies over which free shear layers are unstable. Also, the growth rate of small perturbations is predictable with the inviscid stability theory.

The application of the inviscid stability theory to analyse the hyperbolic-tangent velocity profile had been conducted by Michalke (1964, 1965). He determined numerically the stability characteristics of both temporal and spatial waves for the hyperbolic-tangent velocity profile with velocity ratio equal one (i.e. the velocity of one stream is zero). For both temporal and spatial analysis,

the results show that the free shear layer is unstable for a finite band of frequencies. The selectivity in the growth rate acts as a 'frequency gate' to weak perturbations.

The experiments of Freymuth (1966) on laminar axisymmetric jet show a good agreement between the experimental and the theoretical results of the spatial stability theory. Freymuth used an externally controlled perturbation to excite the free shear at different frequencies. Figure 2-2 (Freymuth, 1966) shows the experimental and theoretical growth rates of small perturbations for different Strouhal number. The experimental data are for laminar axisymmetric and plane jets. The Strouhal number, st , is based on the perturbation frequency, f , the momentum thickness of the boundary layer at the nozzle edge, θ_0 , and the jet velocity, U , ($St = f\theta_0/U$). As can be seen, there is a good agreement between the spatial theory and experiment for $St < 0.012$. For higher Strouhal numbers, the agreement with the curve of temporal growing disturbances is better. The maximum growth rate corresponds to a Strouhal number of 0.0167.

Since the linear stability theory is based on small perturbation assumption, it is not capable to predict the behaviour of the perturbation after the Kelvin-Helmholtz instability waves (the low amplitude oscillation near the

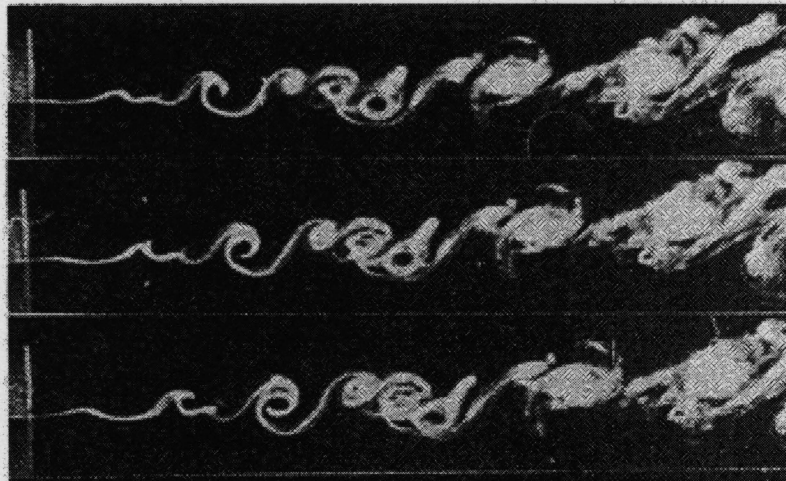


Figure 2-1 Flow visualization of a plane mixing layer, (Chevray, 1984).

nozzle in fig. 2-1) reach its maximum growth level. At this level, the Kelvin-Helmholtz waves evolve into a periodic array of compact spanwise vortices moving at, approximately, the average velocity of the mixing layer with a wavelength corresponding to that of the fundamental frequency ($St.=0.0167$) in the case of unforced free shear layer.

Miksad (1972) studied the nonlinear evolution of a mixing layer. He found that the nonlinear effects become important when the amplitude of the fundamental component reaches 3.5% of the mean velocity. Also, he documented the generation of the harmonic, subharmonic and 3/2-harmonic modes. The harmonic modes are not unstable waves of the basic flow. Their amplitudes are about one order of magnitude lower than the fundamental frequency amplitude, and they are damped quickly after reaching the maximum value. When the fundamental component reaches its maximum amplitude, the subharmonic component becomes the most unstable mode. This is reflected in a sharp increase in the subharmonic growth rate which has been observed by Ho & Hunang (1982). The growth of the subharmonic mode results in the pairing phenomenon in which neighbouring vortices wrap around each other to form a

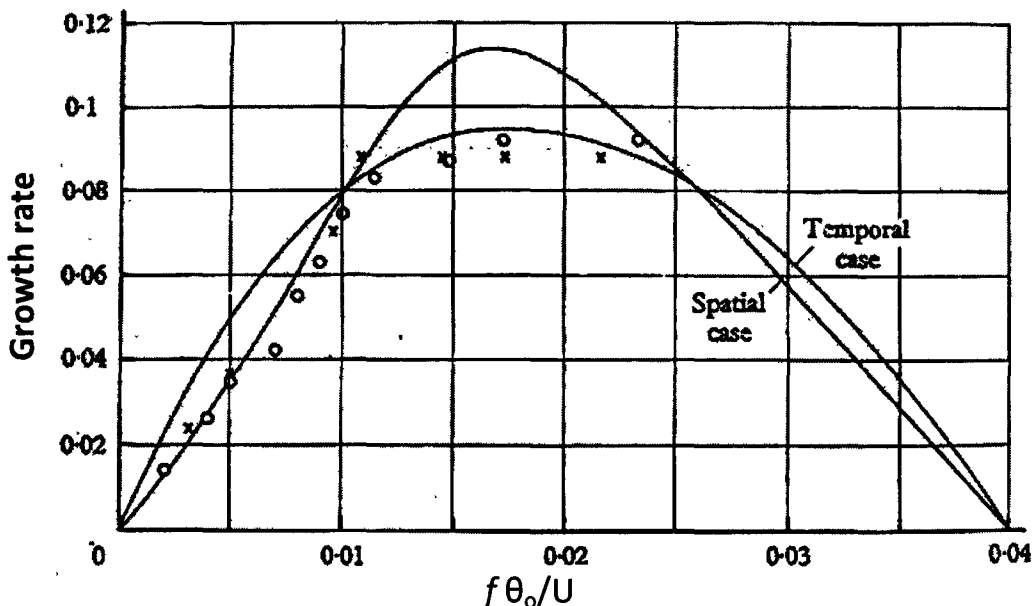


Figure 2-2 Jet large scale structure growth rate for different perturbation Strouhal number: o, Axisymmetric nozzle; x, plane nozzle. (Freymuth, 1966)

larger vortex. The rapid growth of the subharmonic disturbance is caused by a secondary subharmonic instability mechanism that arises when the fundamental mode fluctuations have reached its maximum value.

The boundary layer characteristics of the flow at the separation edge have a great effect on the transition of the free shear layer. One of the most important effects is the influence of the boundary layer momentum thickness on the most amplified frequency of the free shear layer. As mentioned earlier, the Strouhal number of this frequency, based on the boundary layer momentum thickness and the average velocity of the two streams, equals to 0.032 for the case of laminar boundary layer. This value changes to 0.044-0.048 as the boundary layer becomes turbulent (Hussain & Zaman, 1981). Generally, the literature shows discrepancy in the measured fundamental frequency in the case of turbulent boundary layer. Scott and John (2003) suggested that the initial instability in the case of turbulent boundary layer is dependent on the boundary layer inner scales (the friction velocity, u_τ and ν/u_τ) rather than on the outer scales (free stream velocity and the momentum thickness). They based this conclusion on their experimental data which show that only the near-wall vorticity participates in the initial instability.

2.1.1. Forced perturbation of free shear layers:

The study of the effect of external excitation on the free shear layer development was used to understand the effect of upstream feedback on the generation of self-sustaining oscillations. External excitation can be applied in two ways; the first is mechanically with a ribbon or an oscillating flap, the second is acoustically by means of loudspeakers (Ho & Huerre, 1984). For the low Mach number flow, the acoustic waves add energy into the fluctuation field mainly at the trailing edge. For higher flow velocities, comparable to the sound speed, the shear layer can directly be excited acoustically without the mediation of a splitter plate (Tam, 1978). The studying of externally excited free shear layers gives a good insight into the effect of some flow parameters. The nonlinear interaction between two frequencies had been studied by Sato (1970) who excited the free shear layer at two different frequencies. He showed that both frequencies amplify independently when their amplitudes are small, but

when they exceed a certain level, a mutual interaction takes place, and the growth of each component is suppressed by the presence of the other. Also, the nonlinear interaction of the two frequencies leads to the generation of new frequencies equal to the sum and the difference of the two frequencies. Higher harmonics of these new frequencies also are produced. It has also been noticed that the excitation of the shear layer at a single frequency suppresses the broadband turbulence and leads to a very organized train of vortical structures. In addition, the appearance of the sub-harmonic component is delayed for the case of single forcing frequency (Ho & Huerre, 1984).

The value of the forcing frequency relative to the most amplified one, F_b , was found to be a crucial parameter in determining the way the perturbation will grow. For forcing frequency, F_f , higher than half F_b , it is found that the first generated vortical structures have the same frequency as the external perturbation. When the forcing frequency decreases until it lies in the range bounded by $1/3F_b$ and the $1/2F_b$, the vortical structures are formed at the forcing frequency first harmonic ($2F_f$). Neighbouring vortices are laterally displaced and subsequently wrap around each other to form a single structure at the external perturbation frequency. Regarding the effects of forcing level on the free shear layer evolution, Freymuth (1966), fig. 2-3, showed that when the excitation level (perturbation amplitude/the free stream velocity) is of the order of 10^{-4} , the location at which the perturbation amplitude reaches its maximum moves upstream, and that the perturbation amplitude saturates to a constant level despite the increase in the forcing level.

The information presented in this section will help understanding some of the cavity oscillation behaviour which will be mentioned next. In this case, the excitation of the free shear layer is provided by a feedback signal generated by the flow dynamics in the downstream region of the cavity.

2.1.2. Impinging free shear layers:

The impinging free shear layer is characterized by its ability to sustain a moderate level of organized oscillations. A lot of work had been done to determine the dependency of these kinds of flows on the geometrical and

hydrodynamic parameters. In this part of the chapter, the general characteristics of impinging shear flows are briefly reviewed.

The self-sustained oscillation of impinging free shear layers involves a number of events as shown in fig. 2-4 (Rockwell, 1983). If we start from the impingement of the free shear layer vortex structure upon a downstream surface, the events of the oscillation will proceed as follow. First, the flow impingement generates a pressure pulse that travels upstream. The pressure pulse perturbs the free shear layer at the separation edge causing it to oscillate. The fraction of the incident wave energy which transforms to vortical perturbation depends on the receptivity of the free shear layer. As the free shear layer progresses downstream, the initial perturbation grows and forms a new vortex. These events constitute the self-excitation mechanism which generates and sustains the shear layer oscillations.

The frequency of the self-sustained oscillation is controlled by the length and velocity scales of the impinging free shear layer. Usually, the length scale is

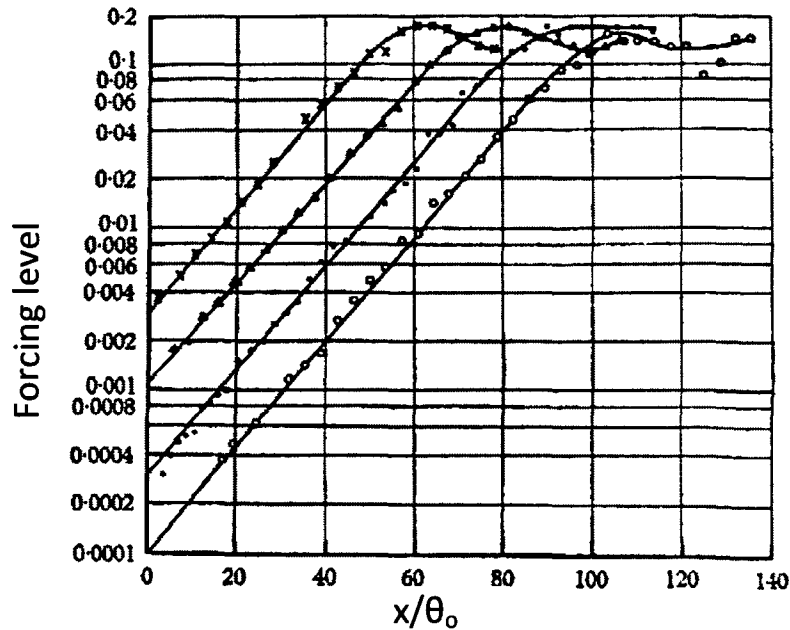


Figure 2-3 evolution of wave amplitude with downstream distance for different forcing levels, θ_0 is the momentum thickness at the separation edge. ○70dB; ● 80 dB; □ 90 dB; x 100 dB (Freymuth, 1966)

taken to be the distance between the separation and impingement edges. The hydrodynamic wave phase velocity is considered as the velocity scale. For flows with velocities comparable to the sound speed, a delay time due to the travel of the pressure wave upstream is also taken into account. Tam (1974) suggested the following criteria to estimate the oscillation frequency:

$$\frac{\ell}{u_p} + \frac{\ell}{c} = \frac{n}{f} \quad 2-1$$

Where, ℓ , is the aforementioned length scale and u_p is the phase velocity. c is the speed of sound associated with the traveling pressure wave. f is the oscillation frequency, and $n= 1,2,\dots$ represents the number of wavelengths existing between the separation and impinging edges.

Ziada and Rockwell (1982) examined the number of wavelengths (n) which exist between the separation and impinging edges. They studied mixing layer impinging upon an edge while changing the distance between the separation and the impinging edges. They found that the oscillation adjusts its frequency to match two criteria. The first is to keep the phase difference

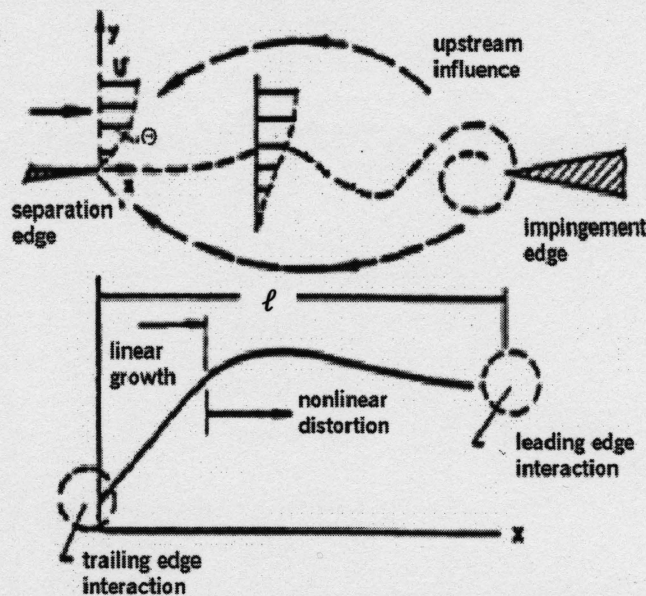


Figure 2-4 General features of the self-sustained oscillation of impinging free shear layer (Rockwell, 1983)

between the velocity fluctuations at separation and impingement satisfying the relation $2n\pi$, where in this context, n still has the same aforementioned definition. The second criterion is to maintain the frequency inside a certain range around the naturally most amplified free shear layer frequency. Sato (1984) suggested that this range is about 20 to 30 percent of the frequency of the maximum growth rate. To satisfy these conditions, the frequency of the oscillation changes in a stepwise fashion as shown in fig. 2-5 (Ziada and Rockwell, 1982).

The preceding sections cover the general phenomena associated with the cavity free shear layer instability. The next section reviews specifically various types of cavity driven flow oscillations.

2.2. Classification of cavity oscillation

This section provides an overview of the flow inside cavities undergoing self-excited oscillations. The different types of cavity self-sustained oscillation are highlighted with emphasis on the physical mechanism involved in each type. In subsection 2.2.1, the general characteristics of the driven flow inside the cavity are presented. This includes the description of the steady state flow, the three-dimensional effects and the nature of hydrodynamic instability of the

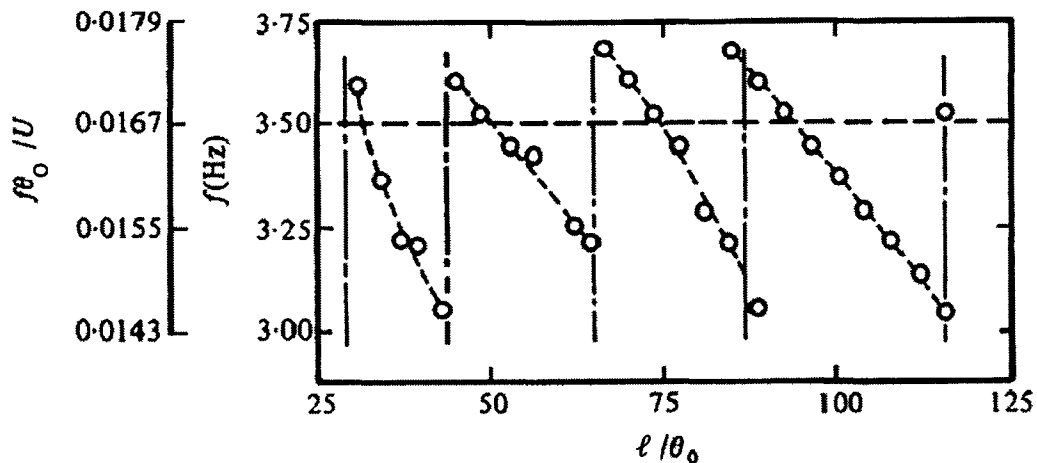


Figure 2-5 Strouhal number of the impinging free shear layer Oscillation as a function of the dimensionless impinging length (Ziada and Rockwell, 1982)

shear layer. In subsection 2.2.2, the classification of the different feedback mechanisms are reviewed.

2.2.1. Flow field inside the cavity

Whatever the nature of the involved feedback, the driven flow inside the cavity has always a strong effect on the oscillation behaviour. Researchers showed that the type of shallow cavity flow and oscillation depends essentially on the geometrical aspect ratio of the cavity and the ratio of the incoming flow boundary layer momentum thickness to the cavity geometrical dimensions.

a) Steady flow field

Regarding the steady flow field inside the cavity, Tracy and Plentovich (1993) followed Wilcox (1990) in classifying the cavity flow field, based on its length to depth ratio, into four categories (open, closed, transitional-closed and transitional-open) as shown in fig. 2-6. For open cavity flow, the flow overpasses the cavity and creates a free shear layer over it. This type of flow inherently exhibits high-level of oscillation. For shallower cavity, the flow separates at the upstream corner and reattaches to the cavity floor. The flow separates from the floor again to pass over the downstream cavity corner. This flow is called closed cavity and has two separate circulation zone near both corners. The closed cavity flow, in general, does not produce any strong oscillation. The transitional-open and the transitional-closed flows occur for length to depth ratio that fall between those for closed and open cavity flows. The type of the flow can be identified from the distribution of the steady pressure distribution over the cavity floor.

The range of the length to depth ratio over which each type of cavity flow occurs is strongly dependent on the flow speed. At low flow velocity, Shen and Floryan (1985) showed that closed flow type is established at length to depth ratio of four. On the other hand, at supersonic speeds, closed flow type starts to occur at length to depth ratio of thirteen (Wilcox, 1990). Regardless of the speed of the flow, the establishment of the closed flow type can be considered as an upper limit after which cavity flow does not exhibit strong oscillation.

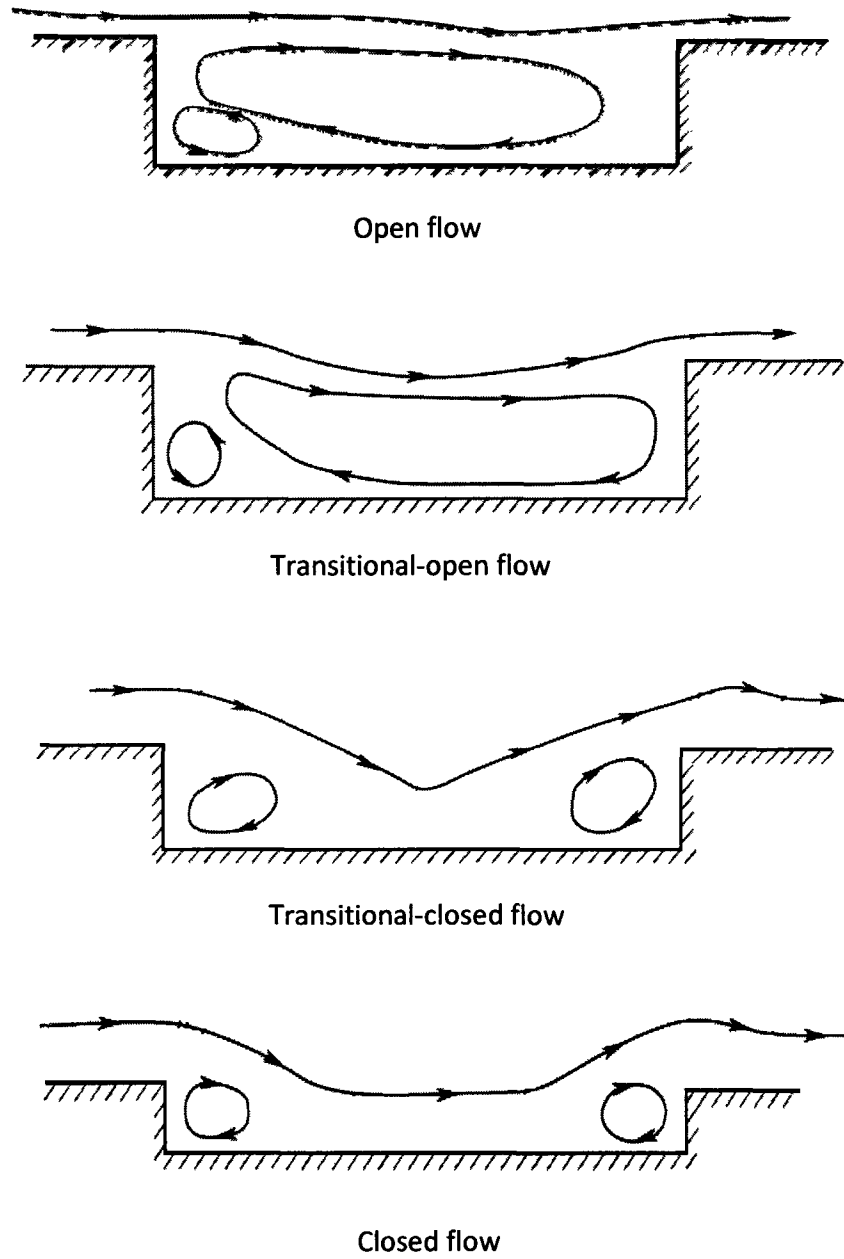


Figure 2-6 Different types of flow field for shallow cavity (Tracy and Plentovich,1993)

b) Three dimensionality of the cavity flow

Maul & East (1963) studied the three-dimensional characteristics of the flow inside a cavity for low-speed water flows. They studied different cavity depth to length ratios using pressure tapes distributed over the cavity span and by means of wall visualizations technique based on viscous coating. They observed stationary periodical circulation cells in the spanwise direction whose number and size vary with the depth to length ratio of the cavity. The visualization showed also that the cells are not always uniformly distributed. The width of the cavity also influenced the three-dimensional behaviour. Tracy & Plentovich (1993) reported a slight change in the amplitude and the frequency of the cavity oscillation with the cavity width. Rockwell & Knisely (1980) demonstrated the existence of spanwise modulations in the mixing layer using hydrogen bubbles visualization technique. Figure 2-7 (Rockwell and Knisely, 1980) shows schematically the interaction between the free shear layer oscillation and the spanwise cells. Recently, Larcheveque et al (2007) simulated 3-D cavity flow using Large-eddy simulation. The results show large span wise modulation in the streamwise velocity associated with the spanwise cell. This modulation explains the wavy front of the shear layer shown in fig. 2-7.

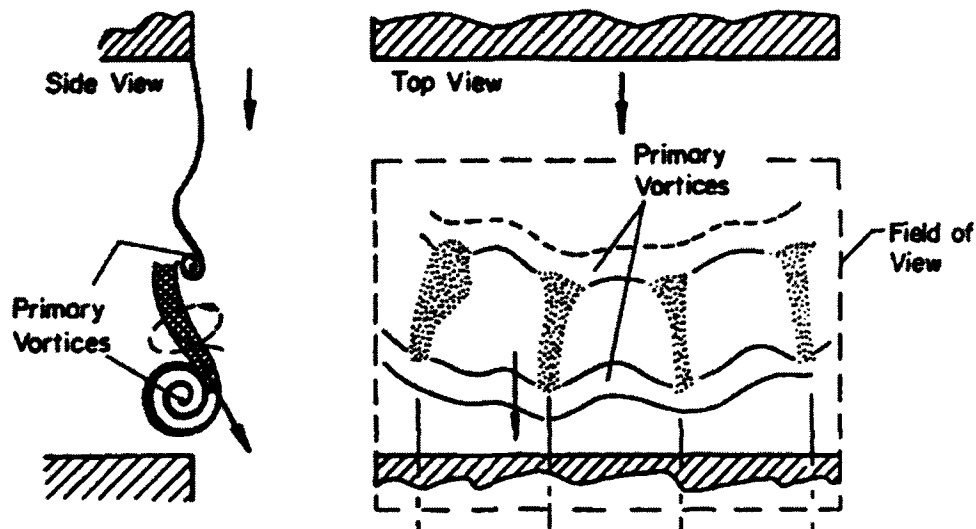


Figure 2-7 Illustration of the interaction between the free shear layer vortices (primary) and the spanwise cells (Rockwell and Knisely, 1980)

c) Nature of hydrodynamic instability of the cavity flow

The cavity free shear layer exhibits two types of hydrodynamic instability. The first one is convection instability which follows the description given in section 2.1. The second type is global instability (wake like instability). The first type is the more dominant and most reported.

Sarohia (1977) characterized a minimum length for the cavity to exhibit convection instability oscillations. Sarohia provided experimental values of the dimensionless minimum length as a function of d/δ_0 . This dimensionless length is given by:

$$L_{\min} \sqrt{Re_{\delta_0}} / \delta_0 \quad 2-2$$

where L_{\min} is the cavity minimum length required to initiate free shear layer oscillation, δ_0 is the incoming flow boundary layer thickness, and Re_{δ_0} is the Reynolds number based on the boundary layer thickness. For the case of Sarohia's experiments, which were conducted on axisymmetric external cavity with laminar boundary layer at its upstream corner, the value of the suggested dimensionless formula was around 0.3 for cavity depths larger by one order of magnitude than the incoming boundary layer thickness. When the depth is of the same order as the boundary layer thickness, it was found that the depth has a significant effect on L_m .

Regarding the wake type oscillation, Gharib & Roshko (1987) observed experimentally that the cavity free-shear layer starts to oscillate as a wake behind a bluff body instead of mixing layer type of oscillation, if the ratio of the cavity length to the incoming boundary layer momentum thickness exceeds a certain value. Rowley et al. (2002) were able to predict this phenomenon numerically using two-dimensional direct numerical simulation. Figure 2-8 (Rowley et al., 2002) shows the instantaneous vorticity contours of mixing-layer oscillation type and wake oscillation type at three different time instants during the oscillation cycle. Wake type oscillation is different from the mixing-layer type oscillation in two ways: 1) wake type is accompanied by a large increase in drag; 2) the oscillation frequency of the wake type oscillations is dependent on

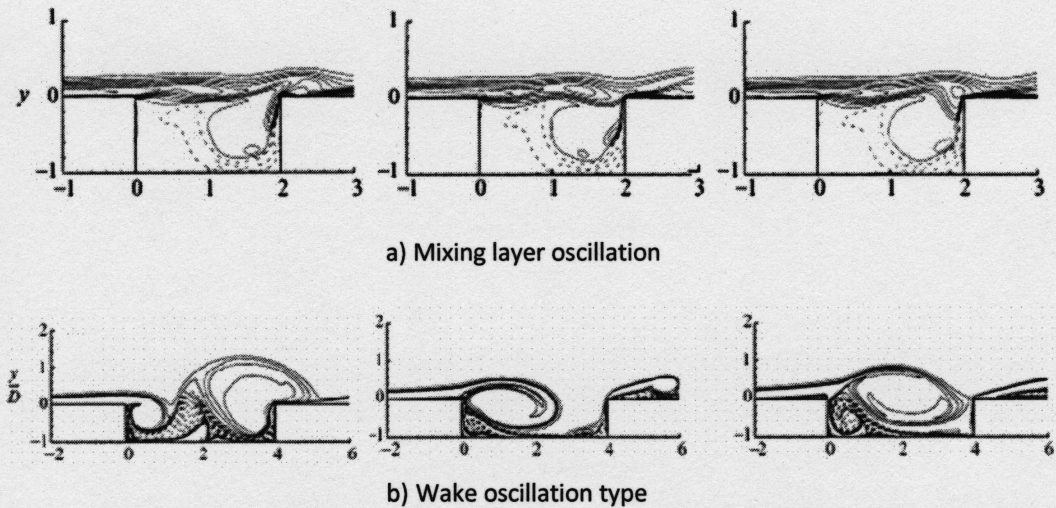


Figure 2-8 Instantaneous vorticity contours of a) mixing-layer and b) wake oscillation types at three different instants in time during one oscillation cycle (Rowley et al., 2002)

the cavity depth. Regarding the value of cavity length at which this switch occurs, Rowley et al. (2002) reported, after they compared their results with those of Gharib & Roshko (1987), that the ratio of the cavity length to the incoming boundary layer momentum thickness at which the switch occurs is dependent on the Reynolds number and the nature of the boundary layer. Recently, Suponitsky et al. (2005) simulated 3-D cavity flow and showed that transition from the wake type to the convection type oscillation can be achieved by introducing three-dimensionality. However, this supposition needs more studies it can be confirmed.

2.2.2. Feedback Mechanisms

Cavity oscillations can be classified according to the nature of the coupling mechanism that triggers the self-sustained oscillation. Rockwell & Naudascher (1978) classified the excitation mechanism into three categories: 1) fluid-dynamic, 2) fluid-resonant, and 3) fluid-elastic Oscillation. Figure 2-9 shows some examples of the three categories.

For the fluid-dynamic oscillation (Sarohia, 1977; Tam & Block, 1978, Ahuja & Mendoza, 1995 and Chatellier, et al., 2004), the upstream feedback

perturbation is generated from the interaction between the free-shear layer oscillation and the downstream cavity edge. For this case, the feedback mechanism behaves like impinging free shear layer which was described earlier. However, when the displacement of one or more walls of the cavity is large enough to control the free-shear layer oscillation; the excitation mechanism is defined as fluid-elastic. This mechanism may occur only if the resonance frequency of the cavity structure is within the region of the most amplified frequency of the free-shear layer.

The fluid-resonant oscillation is produced by the coupling between the free-shear layer oscillation and a resonant acoustic field. In this kind of flows, part of the mean flow energy is transferred to acoustic energy to sustain the acoustic resonance, which in turn generates a strong vorticity fluctuation at the separation region of the shear layer. This mutual interaction produces a relatively high level of initial perturbation in the free-shear layer. This leads to a strong and highly coherent oscillation (Nomoto and Culick, 1982; Rockwell,

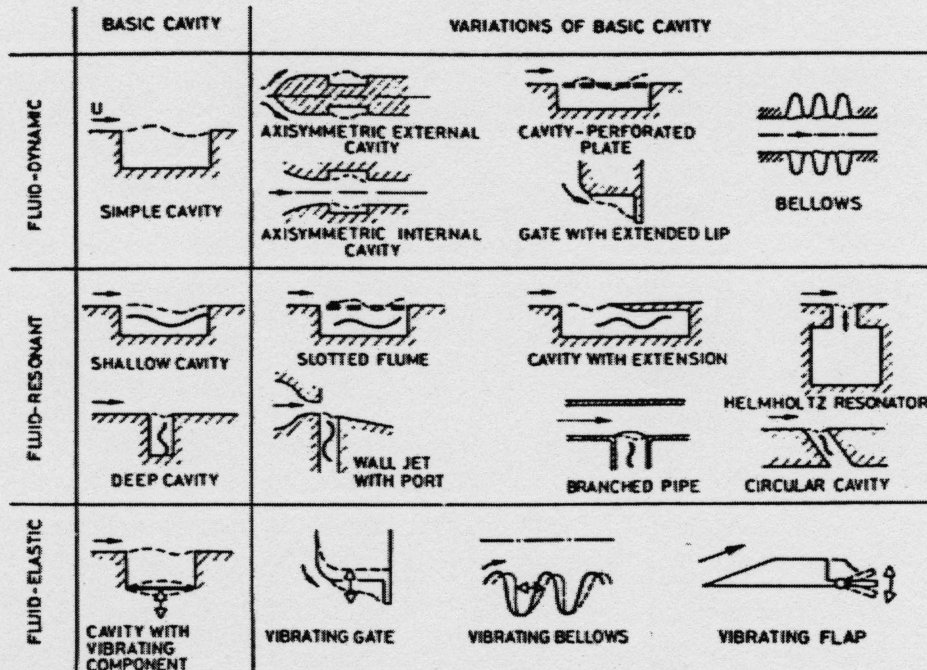


Figure 2-9 Matrix categorization of fluid-dynamic, fluid-resonant, and fluid-elastic types of cavity oscillations (Rockwell & Naudascher, 1978)

1983), which is not achieved in the case of the fluid-dynamic oscillation.

Acoustic resonance of the cavity volume “alone” can be excited for deep cavities (East, 1966; Ziada, 1994; Ziada & Shine, 1999). It is also often observed for shallow cavities subjected to high subsonic or supersonic mean flow. At low Mach number, however, shallow cavities can excite the acoustic modes of a confined domain attached to it. Stubos et al. (1999), Huang & Weaver (1994), Davies (1981), Rockwell & Schachenmann (1982, 1983) and Geveci et al. (2003) investigated the coupling between a circular cavity and the longitudinal resonance modes of the attached pipes. Keller & Escudier (1983) and Ziada et al. (2003) studied experimentally the coupling between the cavity shear layer and the transverse modes of a duct housing a cavity.

One of the important parameters for different coupling mechanisms is the oscillation frequency. The oscillation frequency has to satisfy different criteria for the coupling to occur at this frequency. The next section presents some of the suggested formulas and models that predict the cavity oscillation frequencies.

2.3. Cavity oscillation frequencies

The selective nature of the free-shear layer instability that was discussed before forces the cavity oscillation to occur over a limited frequency range. Also, the phase shift that should be maintained to satisfy the feedback mechanism between the perturbations at the trailing and the leading edges of the cavity imposes another condition on the oscillation frequency to be self-sustained. All experimental data, that are available, show clear evidence of this selective characteristic. As shown in fig. 2-10, Tam and Block (1978) collected experimental data from different sources and plotted them in the form of Strouhal number against the Mach number. The Strouhal number is based on the cavity length and the mean flow outside the cavity. The data cluster into three groups with a jump in the Strouhal number between one group and the following one. Each group is called cavity mode or cavity free shear layer mode. The mode number represents how many oscillation wave-lengths exist along the cavity free shear layer. Figure 2-10 shows also that the Strouhal number of each

mode tends to decrease with the increase of the Mach number. The dispersal of the data in each group is the result of the change of other parameters beside the Mach number.

Ethembaoglu's (1978) experimental data, shown in fig. 2-11, demonstrates a decline in the Strouhal number of all the observed modes as the length to depth ratio is decreased. Block (1976) suggested that the reflection of the sound wave by the cavity bottom wall could be the cause of that change in the Strouhal number as the cavity length to depth ratio decreases. The change of the aspect ratio (Length/depth) alters the flow inside the cavity and consequently changes the convection speed of the hydrodynamic oscillation over the cavity, which contributes to the change of the Strouhal number. The ratio of the boundary layer thickness to the cavity length was also found to be an important parameter in determining the Strouhal numbers of the cavity modes (Tam and Block, 1978).

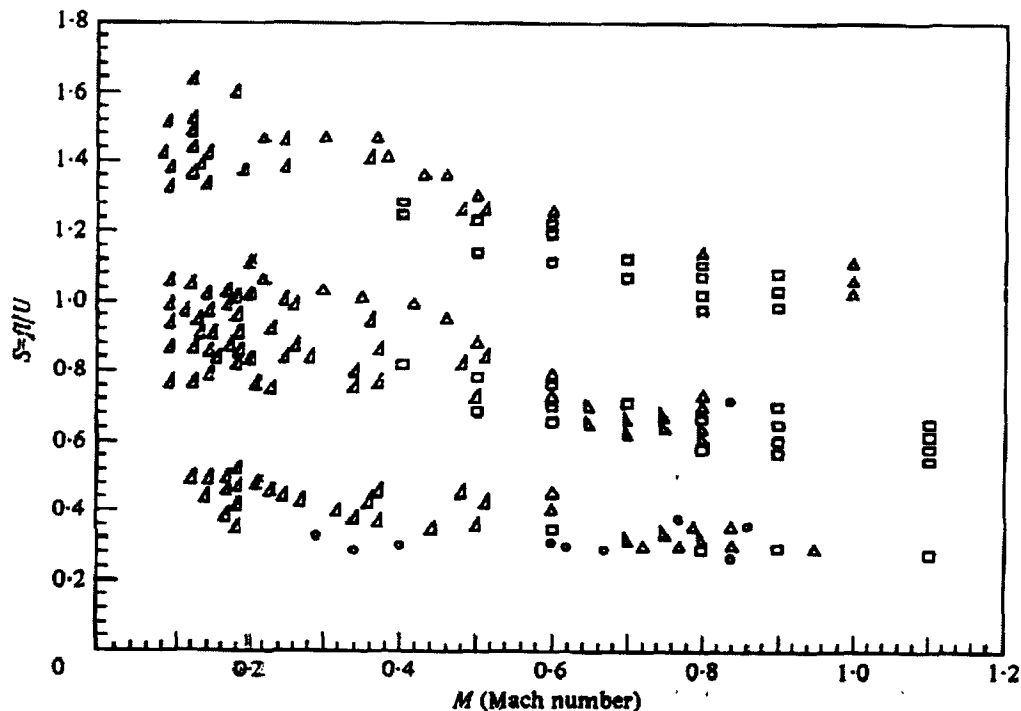


Figure 2-10 the Strouhal number of cavity oscillation over a range of Mach number. The data were collected from different sources. (Tam and Block, 1978)

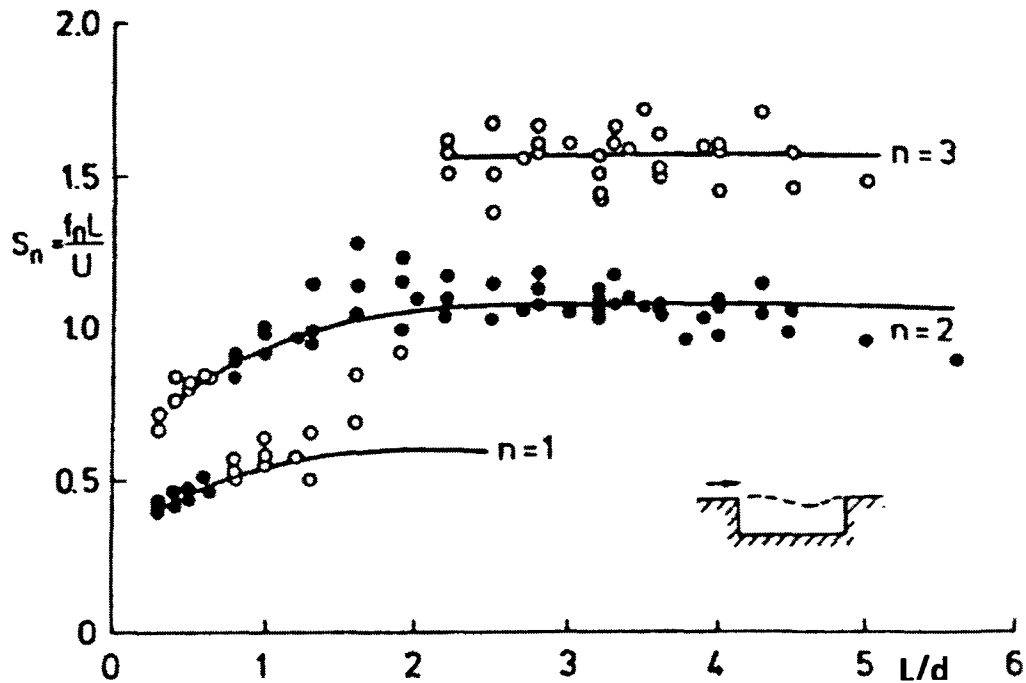


Figure 2-11 Variation of cavity mode Strouhal numbers with cavity length to depth ratio (data from Ethembaoglu (1978) – dark points represent predominant modes, solid lines represent theory from Rockwell (1977)) (Rockwell and Naudascher, 1978)

A semi-empirical formulation for the prediction of the oscillation frequencies has been suggested first by Rossiter (1964). This describes the time interval of the feedback cycle by taking into account the traveling speed of the free-shear layer oscillation and the time taken by the sound wave to reach the cavity leading edge. The semi-empirical formula has two empirical constants and it takes the following form:

$$St = \frac{f L}{U} = \frac{n - \xi}{M + \frac{1}{\mathcal{R}}} \quad 2-3$$

St is the Strouhal number of the n mode based on the cavity length L , f the oscillation frequency of the free-shear layer, and U is the free stream flow velocity. The velocity is usually taken to be the mean flow velocity prior the

separation edge. M is the Mach number of the free-stream velocity which represent the delay time that the sound wave takes to reach the cavity upstream edge. ξ and \mathfrak{R} are two empirical constants. The first one accounts for the time lag between the vortex reaching the end of the cavity and the emission of the sound wave due to the impingement of the vortex on the cavity trailing edge. The latter constant is the ratio of the oscillation phase (convection) speed to the free stream flow velocity. The empirical constants are used to fit the experiment data. Rossiter's formula well predicts the oscillation frequency for the range of Mach number higher than 0.4. However, Chatellier et al. (2004) showed that Rossiter's formula can be tweaked to fit the data at low Mach number, but the resulting values of the empirical constants are found meaningless and could neither predict the correct time lag nor the free-shear layer convection speed. At very low Mach number, the controversial issue of weak upstream pressure sound signal that can't trigger the oscillation rises. In this case, it is argued that the cavity oscillation is controlled by the natural instability of the free-shear layer (Disimilea and Toy, 2004).

Following Rossiter's formula, a group of researchers worked on improving the oscillation frequency prediction by including more aspects of the phenomena in the prediction method. One example of this work is the comprehensive mathematical model developed by Tam and Block (1978). This model takes into consideration the finite shear layer thickness effects and acoustic reflection from the bottom and upstream end walls of the cavity. The model agreed well with the experimental data over a range of Mach number from 0.2 to 1.2. At Mach number smaller than 0.2, the cavity depth acoustic resonance modes were found to be responsible of triggering the oscillation.

The previous discussion summarizes the main approaches used to predict the cavity oscillation frequencies. Most of this work is directed toward the fluid-dynamic oscillation. For fluid-resonance, the oscillation frequency corresponds to the acoustic resonance. However, the same approaches are used to determine the range of Strouhal number fluid-resonance can be self-sustained. In the next section, the fluid-resonant coupling mechanism main features are reviewed as it represents the main focus of this thesis.

2.4. Cavity resonance oscillation

As mentioned earlier, coupling between the cavity shear layer and the acoustic modes of adjacent volumes can produce a large amplitude acoustic pressure. Different studies have been conducted to determine if the mechanism of the acoustic power generation in fluid-resonance oscillation is the same as that of the fluid-dynamic oscillation. Some of these works that describe special characteristics of the cavity resonance mechanism are reviewed in the following.

In this section, attention will be focussed on the cavity resonance mechanism at subsonic speeds. This limits the resonance to occur in only two scenarios. The First is the excitation of acoustic resonance inside the cavity itself, e.g. as in deep or Helmholtz resonator cavity. The second scenario is the excitation of acoustic resonance inside the duct that the cavity is attached to.

2.4.1. Deep cavity resonance

For quite a long time, attention has been directed to the deep cavity resonance like that rises in transport pipe-line systems with closed side branch. Elder (1978) conducted experimental and theoretical studies of wall-mounted cavity subjected to turbulent flow. The suggested analytical model considered the acoustic source to be the fluctuation of volume flow in and out from the cavity.

Nelson et al. (1981&1983) used a detailed momentum and energy analysis of the flow field to determine the source of the sound power generated by a grazing flow over a Helmholtz resonator. Their study has shown that the fluctuating Coriolis force produced from the interaction of the potential and vortical flows is the only term in the linearized flow momentum equation that is not in balance with the fluctuating pressure gradient. Based on this, they proposed that the main mechanism of energy exchange between the flow field and the acoustic field is associated with this unbalanced Coriolis force.

The studies of Nelson et al. have shown also a direct relation between the acoustic pressure level and the concentration of vorticity in the unsteady developed vortex sheet in a manner that the vortical structure cancels the

unsteady potential flow at the upstream edge such that the Kutta condition is satisfied. This interaction at the separation edge extracts energy from the acoustic field. On the other hand, the Coriolis acceleration acts to decrease the vorticity concentration at the downstream edge. These events extract energy from the flow field and add it to the acoustic field. The unbalance between the rate of energy extracted and added to the acoustic field represents the acoustic energy generated by the free shear layer.

Information on the behaviour of the deep cavity resonance with changes in the flow parameters can be found in many experimental works (Pollack, 1980 and Bruggeman, et al. 1989). Ziada (1994) sheds light on the vortical structures movement over the cavity opening by using flow visualization techniques. In this experiment, the acoustic depth mode resonance was excited by the shear layer first and second oscillation modes. The Strouhal number of the first free shear layer mode, at which the strongest acoustic resonance occurs, tended to decrease as the system acoustic damping decreased. The decrease of the acoustic damping causes the cavity to be able to sustain higher sound pressure level. The cause of this decrease in the Strouhal number was suggested to be the nonlinear response of the shear layer to large-amplitude acoustic pulsations. High amplitude acoustic resonance was found to have an influence also on the position and the phase speed of the shear layer vortical structures.

Another feature, that distinguishes the fluid-resonance coupling from the fluid-dynamic one, is its dependency on the acoustic resonance mode shape. This feature causes the coupling phenomena to behave differently for some changes in the flow geometry. An example of this is the increase in the acoustic resonance pressure level when replacing sharp edges by rounded edges in the case of two consecutive deep cavities (Bruggman et al., 1991). This finding seems to contradict the commonly accepted idea that rounding-off sharp edges should reduce the pulsation amplitude of non-resonant impinging shear flows.

The mechanism of excitation in the case of duct resonances by shallow cavity is considered to be similar to the mechanism of exciting resonance in deep cavity. The main difference between the two cases is the acoustic resonance

mode shape. The next section demonstrates the differences between the shallow and deep cavity resonances.

2.4.2. Confined shallow cavity

The acoustic resonance mode shape and the mean flow inside the cavity are the main two differences between deep and confined shallow cavities. These differences can change the response of the resonating pipe to various flow conditions and also to different methods of oscillation suppression.

In the late seventies, inconsistency had been noticed between the predicted and measured combustion-stability characteristics of Titan Segmented rocket engine. Brown et al. (1981) tested a full-scale model of rocket motor and showed that vortex shedding from the ring baffles inside the rocket engine can couple with the acoustic modes of the rocket engine chamber causing acoustic resonance inside the cavity. Flandro (1986) used linear stability theory with consideration of feed-back to model the coupling between the cavity free shear layer oscillation and the rocket chamber acoustics. A dipole kind source generated by the impingement of the vortices on the downstream corner was considered to be the main sound source. The system was found to be sensitive to the position of the downstream corner relative to the vortical structures. The model showed that acoustic resonance can be avoided if the shear layer momentum thickness at the separation point satisfies the inequality:

$$\theta_o > U / (4\pi f) \quad 2-4$$

where f is the frequency of the mode of interest and U is the flow velocity at the separation edge.

Hourigan et al. (1990) studied experimentally and numerically the excitation of longitudinal resonance modes by flow in a duct containing two sets of baffles. The unsteady flow field between the two baffles was computed using discrete-vortex model. The interaction between the flow field and the acoustic resonance, which was obtained by finite element method, was computed using Howe's theory of aerodynamic sound (Howe, 1975). The phase between the

acoustic mode and the vortex traveling past the downstream baffle was found to be the controlling parameter for having sound power generation from the free shear layer or not. Recalling Howe's theory, the flow vorticity contribution to the acoustic power generation, due to its convection in the sound field, can be calculated using the following equation:

$$\mathcal{P} = \int (\rho \int \overline{\omega} \cdot (\overline{U} \times \overline{U}_a) dV) dt \quad 2-5$$

where, \mathcal{P} , is the power generated, or absorbed, by the vortical structure, $\overline{\omega}$ is the vorticity vector, \overline{U} is the mean flow vector and \overline{U}_a is the acoustic particle velocity vector. The vorticity vector, $\overline{\omega}$, can be decomposed into steady state vorticity and fluctuating vorticity vectors. Assuming that the mean velocity vector, \overline{U} , is relatively constant, it can be deduced that the time average contribution of the steady state vorticity to the acoustic power production is zero. On the other hand, the contribution of the fluctuating vorticity depends on its phase relative to the acoustic particle velocity. Therefore, the acoustic resonance can be sustained when the acoustic power production is higher than the acoustic losses. Moreover, the amplitude of the acoustic pressure over the lock-on range will depend on the phase in the region of power production.

Characteristics of cavity coupling with longitudinal duct resonance modes had been demonstrated by Schachenmann and Rockwell (1980). Their experiments were carried out on an axisymmetric cavity located at the outlet end of a circular duct. The cavity was subjected to low Mach number turbulent flow. The oscillation was found to be self-adjusted in a way that the frequencies of oscillation lay within or near the range of the most unstable frequencies of turbulent shear layer. Figure 2-12 shows this kind of behaviour that looks rather similar to that of the impinging free shear layer. As the length of the cavity changes, the frequency jumps up or down to stay close to the most unstable frequency range and at the same time locks-on to one of the duct modes. At the initial phase of the frequency jump, the new mode starts to appear in the pressure spectra and the old frequency appears in the spectra also for a short range. When the difference in the frequency of two consecutive modes is large so that the shear layer change in frequency from one mode to the other would not

help to keep the oscillation close to the most unstable range, dead zones without resonance appear before the frequency jumps.

The excitation of diametral and transverse modes (also called cross-modes) has not drawn much attention as in the case of longitudinal modes. However, if excited, it can generate a relatively high sound pressure level as it exhibits low radiation losses through the duct. This is because the frequencies of these cross-modes are lower than the cut-off frequency of the duct. Ziada et al (2003) reported transverse mode resonance of a 2-D duct by a single shallow cavity mounted on one of the duct walls. The first three modes of the free shear layer were able to excite the transverse acoustic mode. The sound pressure level was higher when the resonance was excited by a lower free-shear layer mode. Keller & Escudier (1983) observed resonance of the diametral mode of an axisymmetric cavity exposed to a very high transonic flow speed. The main observation was that the diametral mode had a stationary orientation for each experimental run. If the physical model was dismantled and then re-assembled, the mode orientation changed. The suggested reason for this observation is that

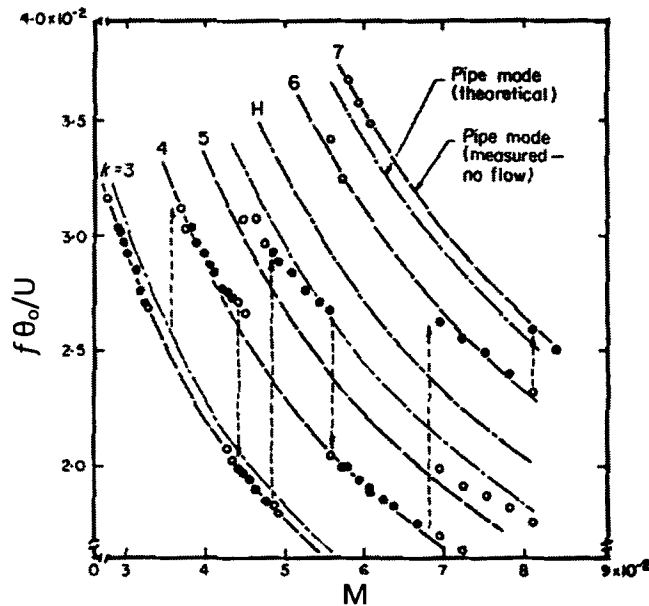


Figure 2-12 upward and downward frequency (f) jumps associated with self-excited oscillations at constant cavity length – dark points represent predominant modes. (Schachenmann and Rockwell, 1980)

the model had a small deviation from the pure axisymmetric geometry. No detailed data had been given for the flow condition or the Strouhal number over which the diametral mode was excited.

The previous sections complete the review of the main features and the state of knowledge of the excitation of acoustic resonance by flow over shallow cavities. The next section addresses the characteristics of the acoustic resonance modes of straight ducts independently from the excitation source.

2.5. Acoustic resonance of straight ducts

The purpose of this section is to introduce the fundamental characteristics of the acoustic resonances associated with the cavity-duct system. The section starts with a general discussion of the resonance phenomenon, followed by reviewing the effect of mean flow on this phenomenon. At the end, the specific characteristics of the diametral modes are discussed.

Typically, the acoustic resonances of enclosed domains result from pressure waves that travel in the domain and reflect off the boundaries. At the resonance frequency, the superposition of the incident and reflected waves forms a standing wave with amplitude depending on the spatial position (Kinsler et al., 2000). Blevins (1979) provides formulas for the resonance frequencies and mode shape (waveform) of different geometries. All the formulas are derived for the condition of zero flow, solid wall and zero radiation from the domain openings. Consideration of the wall response and acoustic radiation will alter the frequency and the mode shape of the resonance. For cylindrical ducts, the mode shapes can be classified as longitudinal, diametral and circular. Figure 2-13 shows schematics of the first and second diametral and circular modes. Frequently, the excited mode is a combination of two or all three types.

The effect of the mean flow on the acoustic resonance of ducts was studied as a part of the investigations of sound propagation and radiation in ducts. The duct-modes characterise, to a certain extent, the propagation and the

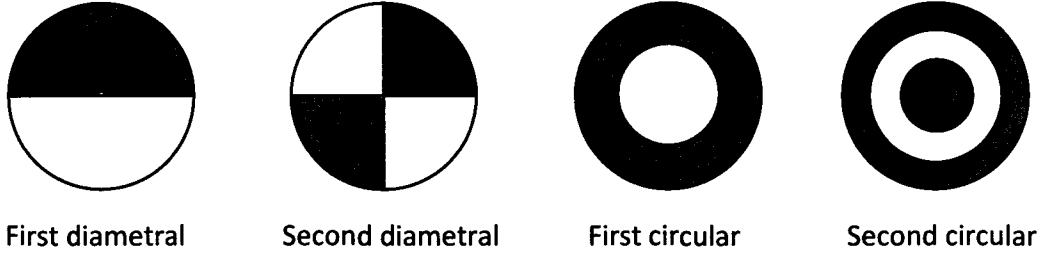


Figure 2-13 Diametral and circular acoustic modes of cylindrical duct. Areas with same color are in-phase and areas with different color are out of phase

radiation of the sound. The motivation behind the majority of the work in the literature was to investigate the noise radiating from jet engine fans. Eversman (1971), Nayfeh et al. (1975) and Rice (1976) are among numerous others who studied the effect of mean flow on the sound propagation in ducts. Eversman (1991) provides a comprehensive review on this subject.

Eversman (1991) reported an analytical model describing the sound propagation in a solid-wall cylindrical duct with outer radius R , reference speed of sound of c , mean flow Mach number M and excitation frequency ω . According to this model, the sound pressure can be described as follow:

$$p_{mN}(x, r, \theta, t) = p_{mN} J_m(k_{mN}r) \exp [i(\frac{\omega R}{c}t \pm m\theta \pm k_{xmN}x)] \quad 2-6$$

where, $J_m(k_{mN}r)$, is Bessel function of the first kind. The propagating wave can be expressed in term of combining different forms of the equation 2-6 based on the integer values m and N , which are the diametral and circular mode order, respectively. The longitudinal traveling wave at constant azimuthal angle takes the form

$$p_{mN} \propto \exp [i(\frac{\omega R}{c} \pm k_{xmN}x)] \quad 2-7$$

The parameter k_{xmN} is the wave number in the axial direction. This parameter can be real or complex depending on the Mach number, k_{mN} and $\frac{\omega R}{c}$. When $(1 - M^2)(k_{mN} \frac{\omega R}{c})^2 > 1$, the value of k_{xmN} becomes complex:

$$Re(k_{xmN}) = -\frac{\omega R M}{c(1-M^2)} \quad 2-8$$

$$Im(k_{xmN}) = \frac{\omega R}{c(1-M^2)} \sqrt{(1-M^2) \left(k_{mN} \frac{\omega R}{c}\right)^2 - 1} \quad 2-9$$

The development of the computational techniques has allowed the simulation and analysis of more complicated geometries and flow field. Also, it allows the simulation of the coupling between the acoustic source and the propagating sound field. The finite element method was first adopted to perform the numerical simulation by Astley & Eversman (1981). Later on, the finite difference and finite volume were adopted in what is widely now known as computational aeroacoustics (CAA). For example, Li et al. (2004) studied the propagation of diametral modes in non-uniform axisymmetric duct. The linearized Euler equations were used to simulate sound propagation in the housing of a turbo fan. The results show that the mean flow has a noticeable effect on of the resonance mode location within the duct.

The diametral modes of the axisymmetric cavity-duct system are different in nature from the modes of straight ducts. They are classified as acoustic resonance trapped modes. The trapped modes are known to occur in unbounded fluids and wave guides where the perturbation energy is localized in regions in which there are some changes in the domain geometry or the fluid properties. As an example, Cooper & Peake (2000) showed that trapped acoustic modes exists in aeroengine intakes because of the change of the duct cross section upstream of the fan and the swirling flow downstream the fan. This causes the acoustic power to be trapped between the inlet and the fan. For the case under investigation, the presence of the axisymmetric cavity lowers the local transverse cut-off frequency to be below the cut-off frequency of the main duct. This reduction in the frequency prevents the local acoustic energy generated at the cavity from propagating along the duct and thereby a new resonance frequency is introduced to the system.

The effect of the mean flow velocity on the diametral mode of cavity-duct system has not been investigated before. However, it is evident from the

available work in the literature that the mean flow can have a noticeable effect on the resonance modes. Also, the previous studies do not focus on clarifying the effect of mean flow on the field of the acoustic particle velocity, which has an important role on the production of acoustic power as explained in the previous section. For this reason, the investigation of the effect of mean flow on the diametral mode is performed as a part of this thesis work. A computation aeroacoustic code was especially developed for this purpose. In the next section, a review of some of the numerical techniques used in CAA is presented.

2.6. Computational Aeroacoustics

The progress in computational aeroacoustics is driven largely by the demand of aviation noise reduction and improving the design of jet engines. The generation of sound from aerodynamic source involves nonlinear, unsteady turbulent flow (Coloniuc & Lele, 2004). The radiated noise from such flow has usually much smaller amplitude compared to the other hydrodynamic parameters. Therefore, the propagating sound is usually treated as a linear problem.

According to Coloniuc & Lele (2004), the sound propagation in a uniform media in the presence of reflecting surfaces and sound scattering in a non-uniform medium are all considered linear problems. This includes sound propagation in ducts with non-uniform flows including the interaction with geometrical changes and mean-flow variations. Therefore, the study of the effect of the mean flow on the acoustic resonance of the cavity-duct system can be treated as a linear problem.

The acoustic wave linear propagation is physically characterized by very low dissipation. The dissipation is generally due to viscous, thermal conduction and molecular thermal relaxation effect (Kinsler, et al. 2000). This makes the artificial numerical dissipation, which is usually tolerated for the hydrodynamic oscillation, unacceptable when the sound propagation is considered. The acoustic wave propagation in air is also non-dispersive for most conditions. This imposes limitation on the minimum points needed to resolve certain wave length.

In this section, the linearized Euler approach is outlined as it is the adequate computational aeroacoustics approach for the current research as explained in the previous couple of paragraphs. This is followed by the discussion of the spatial and temporal discretization schemes available in the literature. Details of the different issues arising from the discretization process are also presented.

2.6.1. Linearized Euler approach

The linearized Euler approach is classified as a hybrid two step approach. In the first step, the hydrodynamic flow field is calculated to provide the mean flow data and the acoustic source terms if it is required. In the second step, a linearized form of the compressible unsteady governing equations is used to simulate the propagation of the acoustic waves within the hydrodynamic field and in the far field. Since the length scales of the hydrodynamic and acoustic oscillation are different especially at low Mach number, the acoustic field can be computed using relatively coarser computational mesh compared to the mesh required for the hydrodynamic domain (Tam, 1995).

The general Linearized Euler Equations (LEE) for small perturbations are derived from Navier-Stokes Equations by ignoring the diffusion term and linearizing the equations around the mean flow values. Doing this, the LEEs in the cylindrical coordinates take the following form:

$$\frac{\partial \rho'}{\partial t} + \nabla \cdot (\rho' \bar{\mathbf{U}} + \rho_0 \bar{\mathbf{V}}') = 0 \quad 2-10$$

$$\frac{\partial u'}{\partial t} + \bar{\mathbf{U}} \cdot \nabla u' + \bar{\mathbf{V}}' \cdot \nabla u_0 + \frac{\partial p'}{\rho_0 \partial x} = 0 \quad 2-11$$

$$\frac{\partial v'}{\partial t} + \bar{\mathbf{U}} \cdot \nabla v' + \bar{\mathbf{V}}' \cdot \nabla v_0 + \frac{\partial p'}{\rho_0 \partial r} = 0 \quad 2-12$$

$$\frac{\partial w'}{\partial t} + \bar{\mathbf{U}} \cdot \nabla w' + \bar{\mathbf{V}}' \cdot \nabla w_0 + \frac{\partial p'}{\rho_0 r \partial \theta} = 0 \quad 2-13$$

$$\frac{\partial p'}{\partial t} + \bar{U} \cdot \nabla p' + \bar{V}' \cdot \nabla p_0 + \gamma(p' \nabla \cdot \bar{U} + p_0 \nabla \cdot \bar{V}') = 0 \quad 2-14$$

where, ρ' , is the density perturbation, \bar{V}' , is the vector of the velocity perturbation, and p' , is the pressure perturbation. ρ_0, \bar{U}, p_0 are the counterpart mean flow quantities. u is the axial velocity; v the radial velocity; w the azimuthal velocity.

The system of linearized Euler equations in the form given here, has three different eigenmodes that support vortical, entropy and acoustic components of the flow (Ewert & Schröder, 2003). This fact causes the generation of non-trivial instability oscillations (vorticity wave) when a domain containing free shear layer flows is simulated with LEE with zero source terms. The instability wave grows as it is convected with the flow and interacts with the acoustic field. The interaction leads to the contamination of the acoustic field and unphysical growth in the amplitude of the acoustic parameters.

Bogey et al. (2002) proposed a solution for this problem by modifying the LEE to suppress the linear terms that support the Rayleigh's instability. They reported that this approximation is good for high frequency sound propagation and does not affect significantly the propagation of low frequency sound. In a different approach, Ewert & Schröder (2003) were able to develop a system of equations that can reasonably describe the propagation of the acoustic wave without suffering from the excitation of the hydrodynamic instability. The different eigenmodes of the linearized Euler equations were separated in the frequency wave number domain. The eigenmodes govern the vorticity and entropy waves were then removed and the system of equations was transferred back to the spatial-time domain. The latter approach is used to develop the numerical code used in the present study as it is considered more suitable than the first one. Also, in chapter 6, a demonstration of the growth of vorticity wave within the free shear layer region is presented.

In the next section, the issues arising from the spatial discretization of the governing equations are addressed. This includes an outline of the dispersion and dissipation of the acoustic wave due to the discretization scheme.

The generation of spurious waves due to the finite size of the numerical mesh is also discussed.

2.6.2. Spatial discretization

There are different methods to perform the spatial discretization of the governing equations. Recently, the finite difference method has been the most used method in computational aeroacoustics studies. The reason behind this is that the finite difference method proved to be overall better when considering the trade-off between the computation efficiency, ease of implementation, memory requirement, and efficiency of parallelization (Coloniuc & Lele, 2004). Other spatial discretization methods include spectral, finite elements and finite volume methods. A limitation of the finite difference method is that it is only conservative when the computational grid lines are parallel to the coordinate axis. This limitation drives the use of curvilinear system of coordinates when irregular geometries are simulated. For the cavity-duct system under investigation, the regular Cartesian and cylindrical coordinates are proper for the simulation of the 2-D and axisymmetric cases, respectively.

An advantage of the finite difference method is that it is easy to formulate high order accuracy schemes adopting this method. The increase of the order of accuracy reduces the required grid resolution, but at the same time, it increases the number of operations per node. This implies that there is a limit on the most efficient scheme. The different schemes can be classified as explicit or implicit (compact). To understand the difference between the two categories, a general approximation to the first central difference spatial derivative, \mathcal{F}' , of the variable, \mathcal{F} , may be written as follow (Lele, 1992):

$$\beta \mathcal{F}'_{i-2} + \alpha \mathcal{F}'_{i-1} + \mathcal{F}'_i + \alpha \mathcal{F}'_{i+1} + \beta \mathcal{F}'_{i+2} = e \frac{\mathcal{F}_{i+3} - \mathcal{F}_{i-3}}{6 \Delta x} + b \frac{\mathcal{F}_{i+2} - \mathcal{F}_{i-2}}{4 \Delta x} + a \frac{\mathcal{F}_{i+1} - \mathcal{F}_{i-1}}{2 \Delta x} \quad 2-15$$

where β , α , a , b and e are constants with their values determined based on the required order of accuracy and any other special optimization. For explicit schemes, β and α are equal to zero and the derivative is calculated explicitly

from the values of the main variable at different nodes. For the implicit scheme, β and α are not zeros and, to determine the derivative, a system of equations of f is needed to be solved. The main advantage of the implicit (compact) schemes is that for the same order of accuracy they require less numbers of terms on the right hand side of equation 2-15, compared to the explicit schemes. The higher order-schemes with large stencil size (number of points on the right hand side of equation 2-15) require special formula to implement the physical boundary conditions. Hixon (2000) split the central difference compact scheme into backward and forward schemes, with their summation resulting in the original central difference scheme. This trick reduces the stencil size of the sixth order scheme from 5 points to 3, which requires only one boundary stencil.

As mentioned earlier, the linear propagation of acoustic wave experiences very small physical dissipation. Therefore the numerical schemes have to be non-dissipative. Pulliam (1986) showed that the upwind schemes, which are widely used in solving hydrodynamic problems, have an equivalent central difference scheme with added dissipation. On the other hand, the central difference schemes are not dissipative. Therefore, they are widely used in simulation of acoustics problems.

Another issue that arises from the discretization process is the unphysical dispersion behaviour. In spatial domain, dispersion means that the phase speed depends on the wavelength of the oscillation. This problem is routed in the differentiation scheme used for the discretization. Fourier analysis of the numerical approximation can determine the dispersion characteristics. The analysis reveals that the wavenumber estimated by the differentiation scheme (modified wavenumber) for a certain wave differs from the real wavenumber if the number of grid nodes along the real wavelength is below certain limits. The difference between the two wavenumbers causes the wave to travel at different phase speeds. Very short waves can even have a negative phase speed and form what is known as spurious wave. A good review on this work is found in Vichnevetsky (1987). Different researchers optimized this coefficient to lower the dissipation and dispersion characteristics of the solution and to lower the number of points needed per wavelength to resolve certain

oscillation. An example of this is the work done by Ashcroft & Zhang (2003). They based their scheme on Hixon's prefactored schemes (Hixon, 2000). The scheme of Ashcroft & Zhang is used in the present work to calculate the spatial derivatives. This scheme was chosen because it needs a relatively small number of points per wavelength and does not need special treatment at the boundary. The details of the scheme are provided in chapter 6.

Spurious waves are waves that have a wave length shorter than what the numerical grid can resolve. These waves may be produced due to several reasons (Coloniuc & Lele, 2004). The initial conditions usually contain some discontinuities which produce spurious waves. Also, boundary conditions and geometrical singularity may produce spurious waves. As mentioned earlier, the central difference schemes that are mostly used in computational aeroacoustics do not experience any dissipation. Accordingly, to eliminate the spurious waves from the computational domain artificial dissipation is needed. This is usually achieved by adding artificial viscosity to the governing equations or by filtering them from the solution. The artificial dissipation should not affect the well resolved waves while damping the spurious ones. Tam et al. (1993) outlined some of the available artificial viscosity schemes, while, Alpert (1981) demonstrated the use of implicit and explicit filters.

The next section discusses the temporal discretization of the partial differential equations. This includes a brief discussion of the classification of the different schemes followed by a description of Runge-Kutta methods.

2.6.3. Time marching techniques

Any aeroacoustics problem involves both spatial and temporal variation. Therefore, the numerical solution of the problem requires spatial and temporal discretization. When the *semi-discrete* approach is considered, the spatial and temporal discretizations are performed separately. The spatial derivatives are calculated following the discussion presented in the previous section. After the calculations of the spatial derivatives, the system of partial differential equations is reduced to a system of nonlinear ordinary equations. The ordinary differential equations are solved by implementing the temporal discretization (Time

marching scheme). The effect of the time marching scheme on the final solution is as important as the spatial discretization. The time marching scheme has its separate order of accuracy, dissipation and dispersion characteristics.

The time marching schemes can be classified as explicit or implicit schemes. The explicit schemes require the calculation of the spatial derivatives and other source terms based on the values of the previous time step. The implicit schemes require the calculation of the spatial derivatives and other source terms based on the values of the new and the previous time steps. The time step for implicit schemes is relatively longer than the explicit schemes time steps. This gives the implicit scheme an advantage when high frequency components are not desired or when the goal is reaching a steady state solution.

For explicit schemes, the Runge-Kutta method has received the most attention. The Runge-Kutta is a predictor corrector method where the calculation involves multiple stages over which the solution improves. For ordinary differential equation of the form

$$\frac{d\mathcal{F}}{dt} = \mathcal{F}(t, \mathcal{F}) \quad 2-16$$

The general s-stages Runge-Kutta method takes the form

$$\mathcal{F}^n = \mathcal{F}^{n-1} + \Delta t \sum_{i=1}^s b_i \varphi_i \quad 2-17$$

$$\varphi_i = \mathcal{F}(t^{n-1} + \Delta t e_i, \mathcal{F}^{n-1} + h \sum_{j=1}^{i-1} a_{ij} \varphi_j) \quad 2-18$$

where, Δt is the time step, \mathcal{F}^n is the numerical approximation for $\mathcal{F}(nh)$. The coefficients b_i, e_i and a_{ij} are determined by satisfying a series of conditions.

The scheme coefficients may be optimized to minimize the numerical dissipation and dispersion of the temporal discretization. Hu et al. (1996) optimized the 4, 5 and 6 stage schemes as well as two steps schemes. This optimization increases the time step limit that is based on the level of numerical dissipation. Moreover, the use of two steps scheme allows the optimization

without significant reduction in the order of accuracy. Stanescu & Habashi (1998) developed 2N-storage implementation of these schemes. In this scheme, N is the number of degrees of freedom of the system which are the number of grid points time the number of variables.

2.7. Summary and proposed research

The oscillation of grazing flows over cavities has been extensively studied over the last fifty years. The focus was first directed toward the fluid-dynamic oscillation at subsonic and supersonic flows. By the seventies, the fluid-resonance oscillation started to attract some attention. The resonance of cavity depth modes, shallow cavities at supersonic flow and cavity-duct longitudinal modes were all investigated in some detail. However, it is surprising that the excitation of the trapped modes of the cavity-duct system is poorly addressed in the literature. The trapped modes are highly localized which reduces the radiation losses. This results in a relatively high acoustic pressure amplitude as reported in the few studies that addressed trapped modes. All the work on the excitation of longitudinal modes of cavity-duct systems do not mentioned the appearance of trapped modes. Accordingly, it is important to determine when the excitation of the trapped modes occurs. This includes investigating the effect of the flow velocity and cavity geometry on the excitation process.

The trapped modes of *axisymmetric* cavity are the diametral ones. The diametral modes are asymmetric. The interaction between this *asymmetric* modes and the *axisymmetric* shear layer of the cavity was never addressed in the literature. The effect of the geometrical preference and the three-dimensionality of the problem on the excitation process need to be investigated. The current research investigates the excitation of the diametral modes of axisymmetric cavity-duct system to improve the fundamental understanding of the excitation of the trapped modes in general and of the interaction of the asymmetric mode with axisymmetric acoustic source (the free shear layer) in particular.

The acoustic power generation during the fluid-resonance depends on the mode shape of the acoustic resonance. Most of, if not all of, the predictions of the power generation are based on the mode shape at zero flow velocity despite

the fact that resonance starts to occur at moderate subsonic flows. The literature on sound propagation in duct shows that the mean flow has an effect on the mode shapes. The effect of the mean flow velocity of the diametral mode of cavity-duct system has not been investigated before. For this reason, the investigation of the effect mean flow on the diametral mode is performed. This includes investigating the effect of the mean flow on the acoustic particle velocity.

It is believed that the finding of the current research will improve the state of knowledge of the excitation of the trapped modes of cavity-duct system. This will help in the development of better techniques for acoustic resonance control and suppression.

CHAPTER 3

EXPERIMENTAL TEST FACILITY AND INSTRUMENTATION

This chapter details the experimental setup used in this study. This includes the description of the test facility, the test section design and the measurement instrumentations. The test section is optimized to study the excitation of the diametral modes of the cavity-duct system. The optimization of the test section is based on the characteristics of the diametral modes obtained from numerical simulations which were performed to calculate the diametral mode shapes. The results of these simulations are also presented.

3.1. Test facility

The tests are conducted using an open loop wind tunnel. A schematic diagram of the wind tunnel is shown in fig. 3-1. The tunnel is equipped with a centrifugal blower powered by 50 hp motor. The flow rate through the wind tunnel is changed by varying the blower speed using a variable driving speed control unit. This setup is capable of producing a flow velocity in the test section

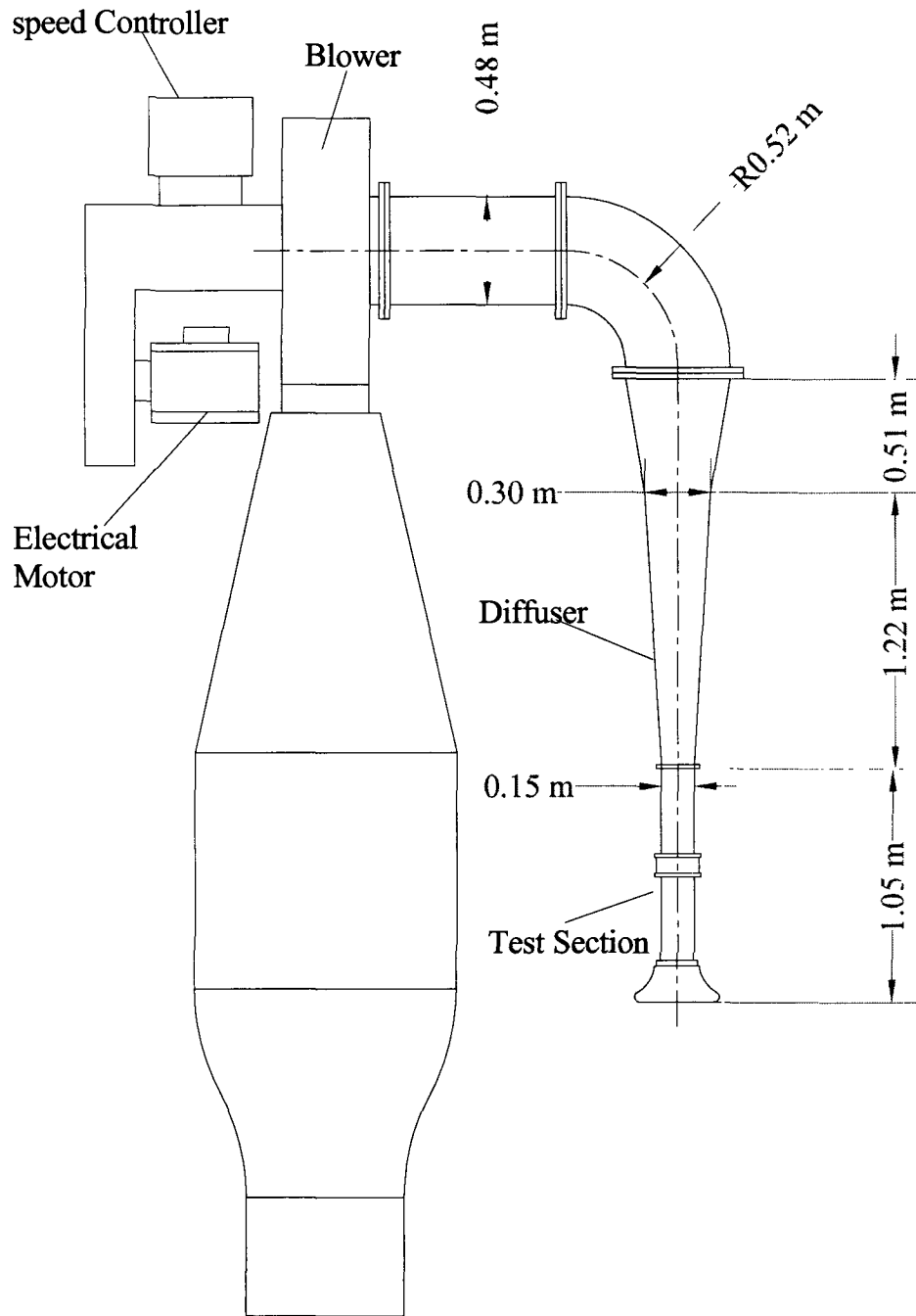


Figure 3-1 Schematic of the test facility

up to 150 m/s at the blower maximum rotational speed. It is noteworthy that the maximum velocity in the test section is found to depend slightly on the cavity dimension and the pressure amplitude of the acoustic resonance.

The test section is connected to the suction side of the blower by means of an axisymmetric diffuser. The ratio of the cross section area of the test section to the blower inlet area is 1/10. This relatively large area ratio imposed some difficulties in the design of the diffuser. A comprehensive numerical simulation, using a commercial CFD package, was conducted to determine the most suitable design. The final diffuser design is shown fig. 3-2. The diffuser consists of two sections that are made out of 1.5 mm steel sheet. The upstream section is a four feet long diffuser with included angle of 7 degrees. The inlet and outlet diameters of this section are 150 mm and 300 mm, respectively. The downstream part is two feet long with 300 mm inlet diameter and 475 mm outlet diameter. Two conical guide vanes are mounted inside this section with a perforated plate covering the outlet of the two central guide vanes, see fig. 3-2. The perforated plate has a loss coefficient of 7. This configuration prevents the flow from separating from the outer wall. On the inlet side of the test section, a parabolic shaped wooden contraction is used to insure uniform inlet velocity profile and to minimize both the turbulence level and the pressure drop.

3.2. Test section

The test section is an axisymmetric physical model that was built to study the excitation of diametral modes of an axisymmetric cavity in a duct. The design of the test section facilitates the investigation of the effect of the change of both the length and the depth of the cavity on the excitation mechanism. Figure 3-3 shows a schematic of the test section geometry. The test section consists of two 150 mm in diameter clear acrylic pipes. Each pipe is 450 mm long, with 6.25 mm wall thickness. The criteria of choosing the different dimensions of the pipe will be discussed in section 3.3. The connection between the two pipes has a bigger diameter to form an axisymmetric internal cavity. Two small flanges, glued to the two pipes, are used to attach the two pipes to the cavity.

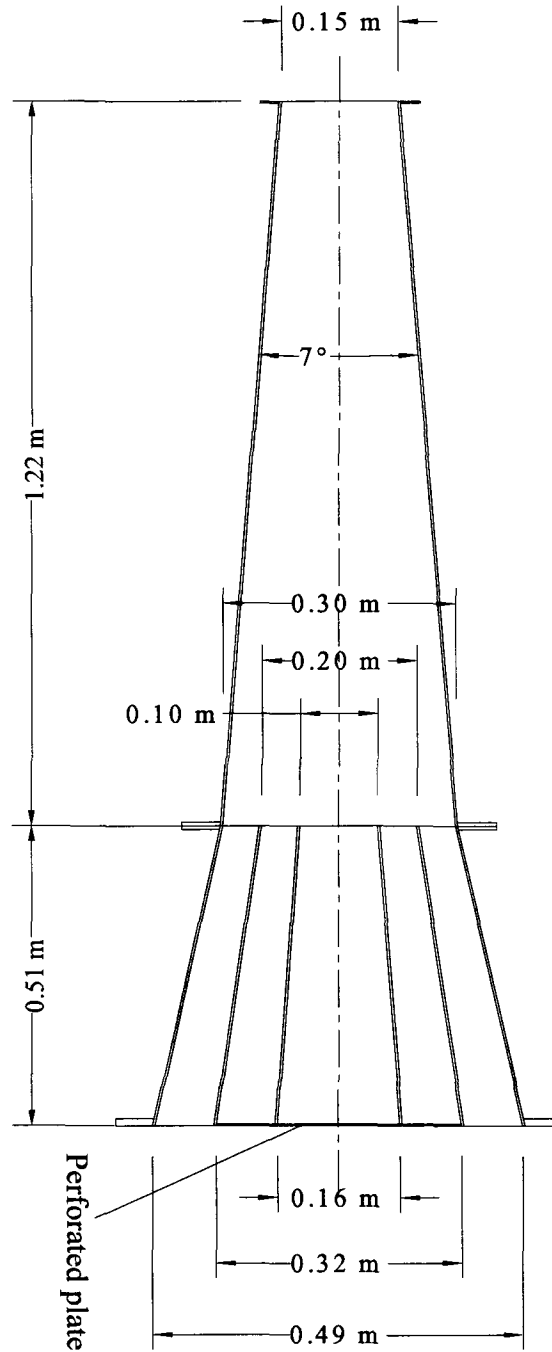


Figure 3-2 Schematic of the diffuser design

Two designs of the cavity are considered in the study. Figure 3-4 shows a schematic drawing of the first design. In this design, the cavity is made out of 200 mm clear acrylic pipes to form 25 mm deep cavity. To change the length of the cavity, different pieces with different lengths varying from 25 mm to 150 mm with a step of 25 mm were used. Two end disks bolted to the pipe flanges form the cavity upstream and downstream side walls. All parts fastened together using threaded rods. In the second design, shown in fig. 3-5, acrylic flanges are used to form the cavity. The acrylic flanges are machined on CNC machine to ensure dimensions accuracy. The flanges have wall thickness of 25 mm to provide higher stiffness compared with the first design. Increasing the cavity wall stiffness reduces the acoustic losses due to the vibrations of the cavity wall; also a stiffer wall prevents geometrical deformations during the assembly. Three sets of flanges with 175 mm, 200 mm and 250 mm in inner diameter are made to test cavity depths of 12.5 mm, 25 mm and 50 mm, respectively. These depths are equivalent to depth to pipe diameters ratios of 1/12, 2/12 and 4/12, respectively. Each set consists of 9 pieces; two end disks, five flanges 25 mm in thickness and two flanges 12.5 mm in thickness. With this setup, the cavity length can be changed from 25 mm to 150 mm with a step of 25 mm for the three cavity depths. This arrangement allowed that the pressure transducers are always positioned at the middle of the cavity length. The cavity length to depth ratios studied vary from 0.5 to 12 as listed in table 3-1. Threaded rods are used to fasten all the parts together. O-rings are used to seal all the interfaces between the different parts of the test section, as shown in fig. 3-5. This prevents air leakage from or to the test section and minimize the acoustic losses due to the fluctuation of the air leakage with the acoustic pressure.

Table 3-1 Dimensions of tested cavities

d (mm)	Ratio d/D	Tested ratios of L/d
12.5	1/12	2, 4, 6, 8, 10, 12
25	2/12	1, 2, 3, 4, 5, 6
50	4/12	0.5, 1, 1.5, 2, 2.5, 3

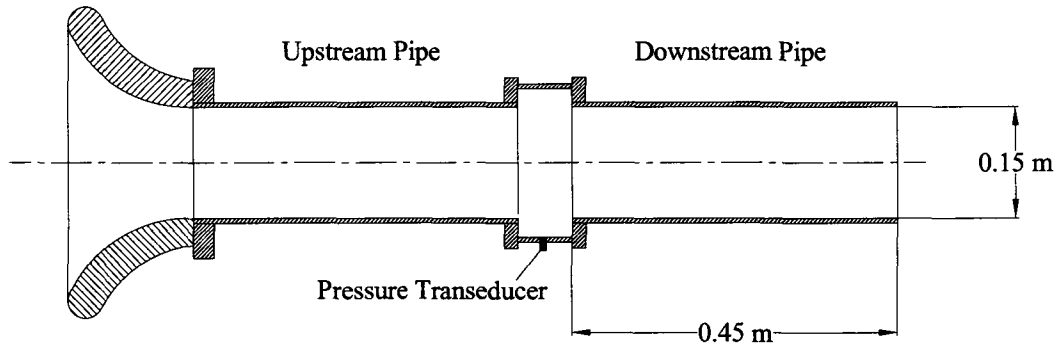


Figure 3-3 Schematic drawing of the test section showing the inlet bell-mouth and the axisymmetric cavity-duct system

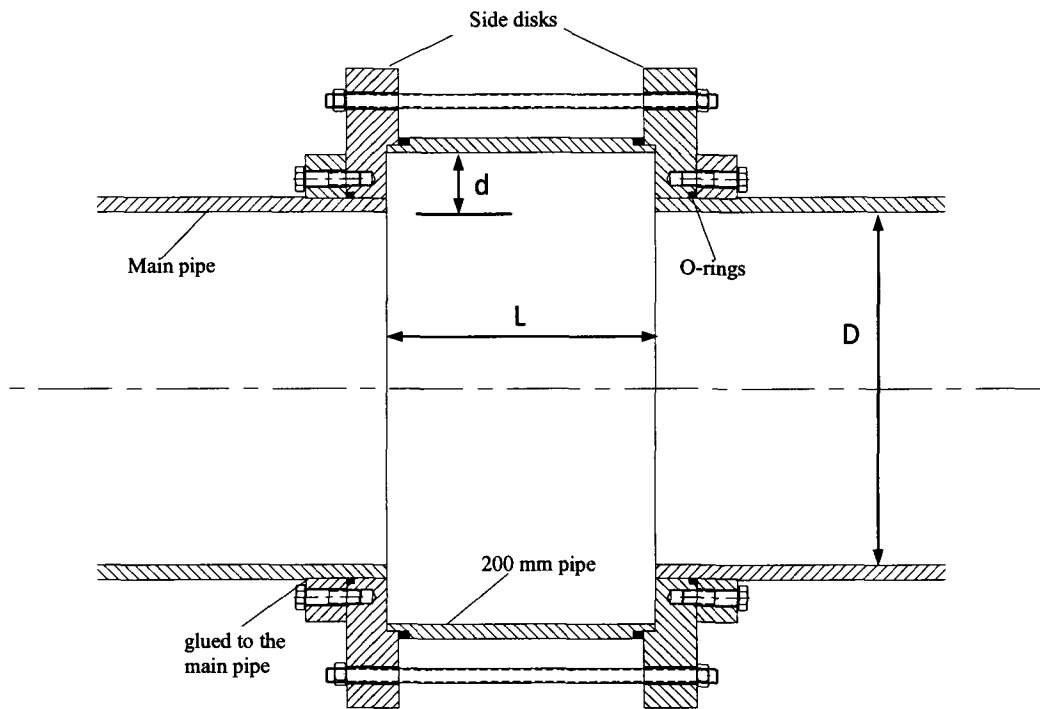


Figure 3-4 Schematic drawing of the first cavity design. Cavity depth is 25 mm and cavity length is 100 mm.

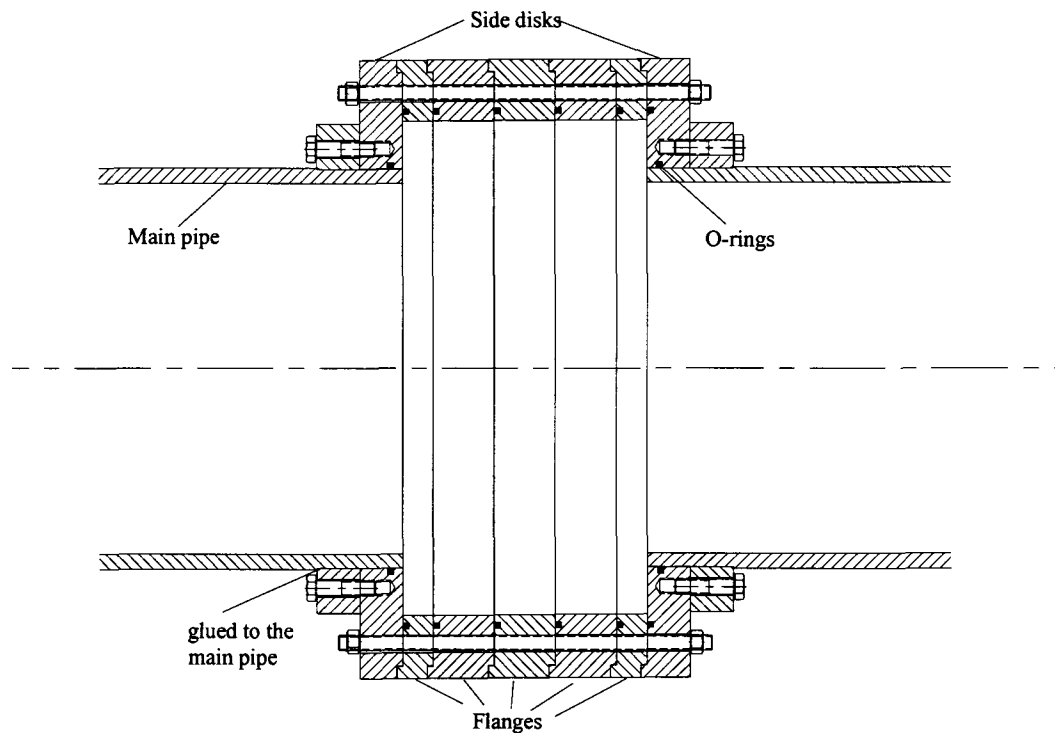


Figure 3-5 Schematic drawing of the second cavity design. Cavity depth is 25 mm and cavity length is 100 mm.

3.2.1. Introduction of orientation preference

Part of this investigation is to study the effect of introducing orientation preference by altering the axisymmetric domain. Acrylic pieces, 5 mm thick, are inserted inside the cavity to provide orientation preferences. Two cases are studied. For the first case, one acrylic piece is inserted inside the cavity as shown in fig. 3-6(a). The acrylic piece is arrangement with respect to the pressure transducers such that they are positioned 90° , 135° and 180° from the acrylic piece. For the second case, four pieces are inserted with 90° angle separating consecutive pieces as shown in fig. 3-6(b). For both cases, the depth and length of the cavity were 25mm. The acrylic pieces are bolted to the downstream side wall of the cavity to prevent them from moving. It is important to mention that the first design of the cavity is used to perform these tests.

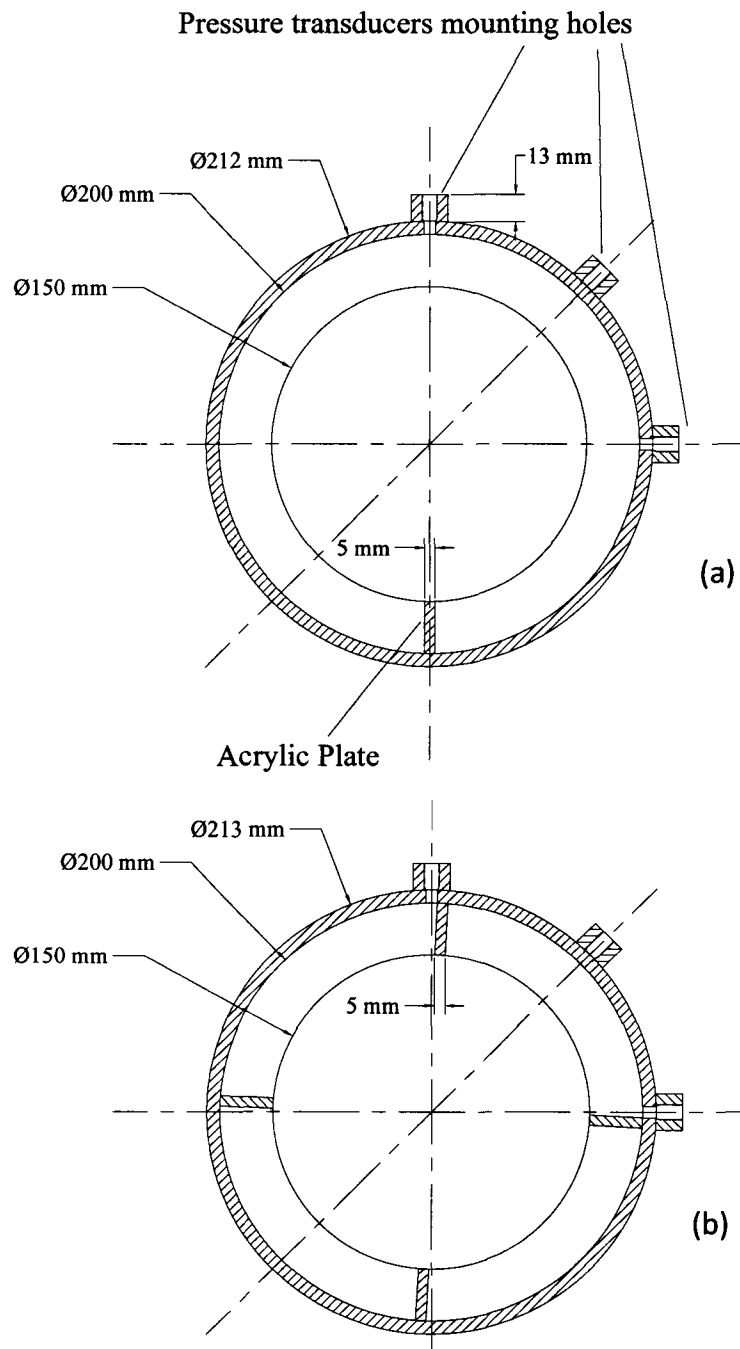


Figure 3-6 position of the acrylic plates inside the cavity. a) one acrylic plate inserted inside the cavity, b) 4 acrylic plates inserted inside the cavity

3.3. Simulation of acoustic modes

It is very important to base the design of the test section on a firm understanding of the characteristics of the acoustic resonance diametral modes. Numerical simulations of the cavity-duct system domain, with no flow, are conducted to determine the mode shapes of the acoustic resonance. The focus is on determining the frequencies and the mode shapes of the diametral modes and on studying the effect of changing the geometry on these modes.

A finite element commercial package (ABAQUS) is used to perform the simulations. ABAQUS has a special numerical module to extract the natural modes of both vibrations and acoustic problems. The eigenvalue problem for natural modes of a small amplitude fluctuation of a finite element model is:

$$(\mu^2[M] + \mu[C] + [K])\{\phi\} = 0 \quad 3-1$$

where $[M]$ is the mass matrix, $[C]$ is the damping matrix, $[K]$ is the stiffness matrix, μ is the eigenvalue; and $\{\phi\}$ is the eigenvector of the resonance mode. This equation is available directly from a linear perturbation of the equilibrium equation of the system. For the current simulations, damping is set to zero during eigenvalue extraction. In this case, μ becomes an imaginary eigenvalue, $\mu = i\omega$, where ω is the angular frequency, and the eigenvalue problem can be written as:

$$(-\omega^2[M] + [K])\{\phi\} = 0 \quad 3-2$$

Air at room temperature is chosen as the working fluid. The density is set to 1.2 kg/m^3 and the bulk modulus, k , is calculated as the speed of sound square time the density. The speed of sound is calculated from the ideal gas relation, $c = \sqrt{\gamma R_a T}$, where, γ is the specific heat ratio, R_a is the gas constant and T is the temperature in degree Kelvin. For the simulation γ is set to 1.4, R is set to $0.287 \text{ kJ}/(\text{kg} \cdot \text{K})$ and T is taken to be 293 K. A 4-node tetrahedral mesh is used to construct numerical models. The boundary conditions at each end of the duct are set to zero acoustic pressure (free end) to simulate the open ends with no radiation. Walls are modeled as solid boundaries with zero pressure-gradient.

3.3.1. Results and design criteria

Different geometries were simulated to examine the effects of the cavity dimensions on the diametral modes frequencies. The results of the simulations show that the frequencies of diametral modes decrease with the increase of cavity dimensions. Based on the simulation results and the available maximum flow velocity, a minimum length of the cavity is chosen to ensure the excitation of the first 4 diametral modes by the first shear layer mode of oscillation. The selected length, L , is 25 mm for cavity depth, d , of 25 mm; resulting in a length to depth ratio, L/d , of one which is the lower limit for shallow cavities.

In addition to the aforementioned set of simulations, another set of simulations were conducted to determine the main pipe length. The test section length was designed to be sufficiently long such that its length has no effects on the shape or the frequency of the diametral modes. Figure 3-7 shows the change of the first diametral mode frequency as a function of the length of the upstream and downstream pipe sections. It is seen that the mode frequency is practically uninfluenced by these pipes as long as their length to diameter ratio exceeds a value of 2. This means that no significant acoustic energy propagates to any added mass beyond this length. For this reason, the pipes used in the experiment were made three diameters long to ensure low acoustic radiation from the test section ends. The above simulations were made for a cavity with $L/d=1$, $d/D=2/12$, which is the shortest cavity considered in this study. Additional simulations were performed for the other cavities. The results showed larger cavity depth and length require shorter pipe length to ensure no effect on the diametral modes compared to smaller depth or length. Thus, the selected pipe length to be used during the tests does affect neither the acoustic mode shapes nor their frequencies for all tested cavities.

Figure 3-8 shows the mode shapes of the first three diametral acoustic modes for a cavity with $L/d = 1$ attached to 450 mm long pipes at both ends. The diametral modes are shown in the form of normalized acoustic pressure contours. It is clear from Fig. 3-8 that the diametral modes are locked to the cavity. Moreover, the higher modes are more concentrated near the cavity than the lower ones. The simulation also provided the main characteristics of the

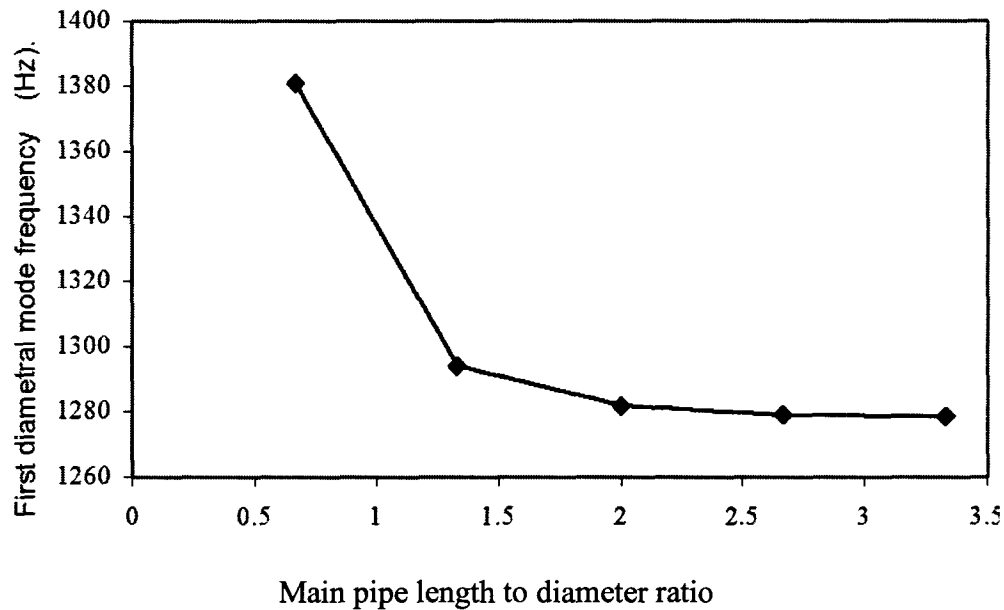


Figure 3-7 Variation of the first diametral mode frequency with the main pipe length ($L/d=1$, $d/D=2/12$)

acoustic modes. First, the maximum acoustic pressure occurs at the cavity floor and midway along its length. Therefore, the pressure transducers were installed at these locations. Secondly, the acoustic pressure varies in the form of sine function over the cavity circumference and the number of the complete sine cycles made by the acoustic pressure over the circumference is equal to the mode number. This information was used in choosing the relative position of the pressure transducers and in the analysis of the measurement data.

3.4. Instrumentations

The course of the testing includes measurements of the mean flow velocity, the boundary layer velocity profile, cavity free shear layer fluctuation and the acoustic pressure. The mean flow velocity is measured by means of a static pitot tube; while the boundary layer velocity profile and the velocity fluctuation in the cavity free shear layer are obtained using hot-wire anemometers. For measuring the acoustic pressure, up to four pressure transducers are used simultaneously. In the next subsections the different instruments are discussed.

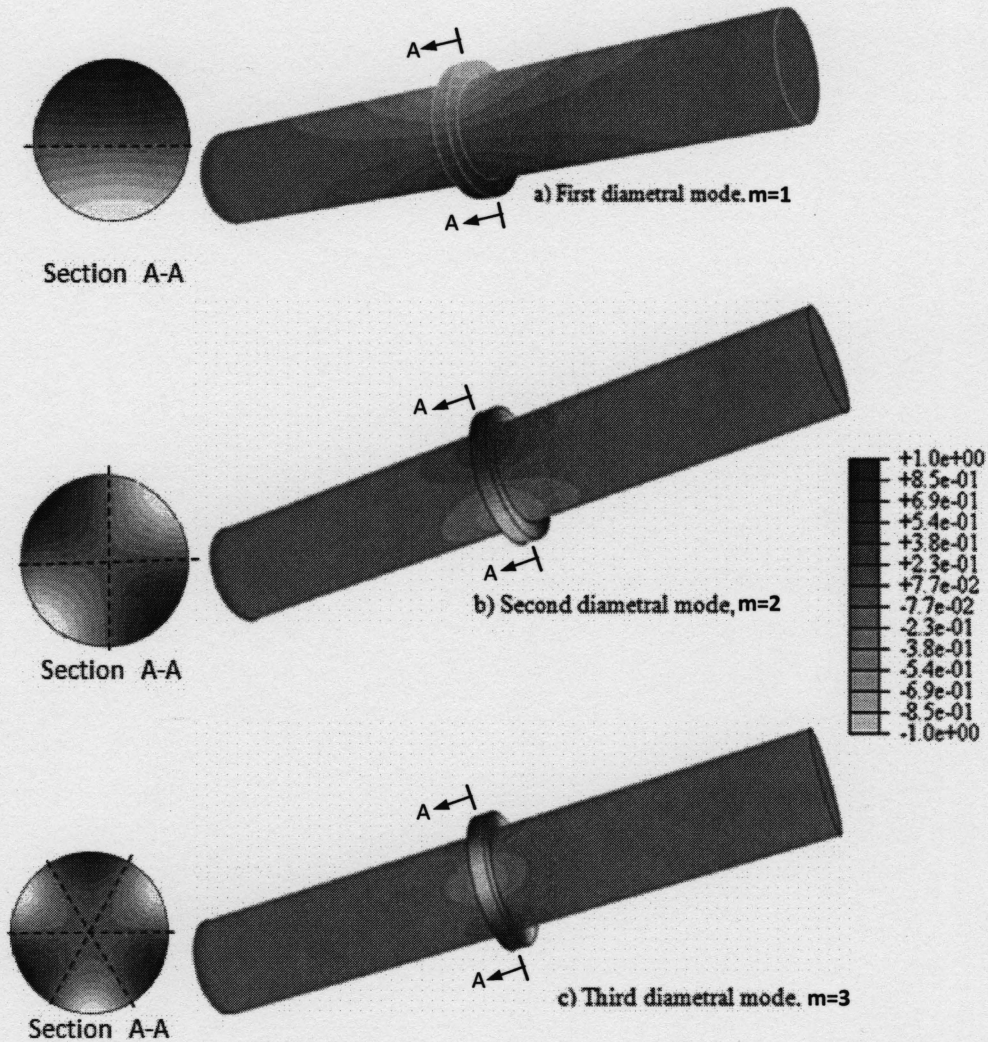


Figure 3-8 The mode shapes of the first, second and third acoustic resonance modes. $L/d=1$, $d/D=2/12$

3.4.1. Pitot tube

A pitot-tube located directly downstream the bell mouth contraction was used to measure the dynamic head at the center line of the test section. At this section, the flow velocity was found uniform within 0.5% as was verified with several measurements over the cross section. The Pitot tube was connected to a

Validyne diaphragm type differential pressure transducer model no. DP45-14. The electrical bridge of the pressure transducer was adjusted using a pressure pump and an accurately calibrated pressure transducer. This secondary calibration procedure was repeated several times to estimate the uncertainty. The standard deviation in the calibration procedure was found to be 0.5% of the full scale.

3.4.2. Pressure Transducer

Up to four pressure transducers were used simultaneously to obtain the instantaneous acoustic pressure at different physical angles around the circumference of the cavity floor. The relative positions of the pressure transducers were chosen to capture the azimuthal distribution of the pressure amplitude. Figure 3.9 shows the relative positions of the pressure transducers for both the first and second design of the cavity. The pressure transducers are flush mounted to the inside surface of the cavity floor. The pressure transducers used in the present experiments are piezoelectric type sensors. They are structured with a diaphragm that is supported by a rigid column of quartz. An acceleration-compensation sensing element is added to the pressure transducer to minimize vibration sensitivity. The transducer has a sensitivity of 7.3mV/kPa and a resonance frequency of 250 kHz.

3.4.3. Hotwire

A Constant temperature hot-wire anemometer (CTA) is used to measure the mean velocity distribution in the boundary layer at the cavity upstream separation edge. The velocity fluctuation is also measured over the boundary layer. During these measurements, the cavity was filled to prevent acoustic resonance. A DANTEC hot-wire probe type 55P11, mounted on an L-shaped hot-wire holder and connected to DISA bridge type 56C16 CTA, is used. The hot-wire holder is mounted on a traverse mechanism, to serve moving hot-wire across the boundary layer. The traverse mechanism has a displacement resolution of 20 μ m.

Two hot-wire anemometers are used simultaneously to measure the amplitude of the stream wise velocity fluctuation in the cavity free shear layer at

the middle of the cavity length. The calculation of the phase difference between the two velocity fluctuation signals are the main goal of this measurement. The two hot-wire probes, mounted on straight hot-wire holders, are positioned at 90° with each other along the circumference of the cavity, e.g. at positions 180° & 270° indicated in fig. 3-9(b). The sensing element of the probe was oriented normal to the flow and cavity centerline. To compare the phase change of the velocity fluctuation to the phase change of the acoustic pressure, two pressure transducer are used, which are located 180° from the hot-wire probes, i.e. at 0° & 90° in fig. 3-9(b). It is worth mentioning that the hot-wires are calibrated in the test section using a pitot tube located very closely to the hot-wire element. The cavity is covered during the calibration to minimize the level of the velocity fluctuations. King's law is used to relate the output voltage to the velocity calculated from the pitot tube measurement.

3.5. Experimental procedures

Other than during the hot-wire measurements, the experimental procedure was set-up to measure the acoustic pressure on the cavity floor, for the different geometries of the cavity, over a range of mean flow velocity. The mean flow velocity is measured first for the different blower rotational speed. The Pitot tube is then removed for the rest of the measurement to ensure the uniformity of the flow approaching the cavity. The blower rotational speed is then gradually decreased in steps. The step is chosen to be 3.33% of the blower maximum speed, which results in a change of flow velocity of approximately 3.33% of the maximum flow velocity.

For each flow velocity, the amplitude spectrum of each pressure transducer signal, the phase difference and the coherence spectra between the pressure transducers are calculated. Fifty averages of one second length are used to obtain each spectrum. The sampling rate is set to 32768 Hz. Also, a time signal is recorder for further analysis as will be mentioned in the next chapter. The data acquisition is performed using a 16-bit 4-channel National Instrument card model PCI-4452. The data acquisition card is equipped with anti-aliasing filter. Labview program is used for acquiring and analysing the signals.

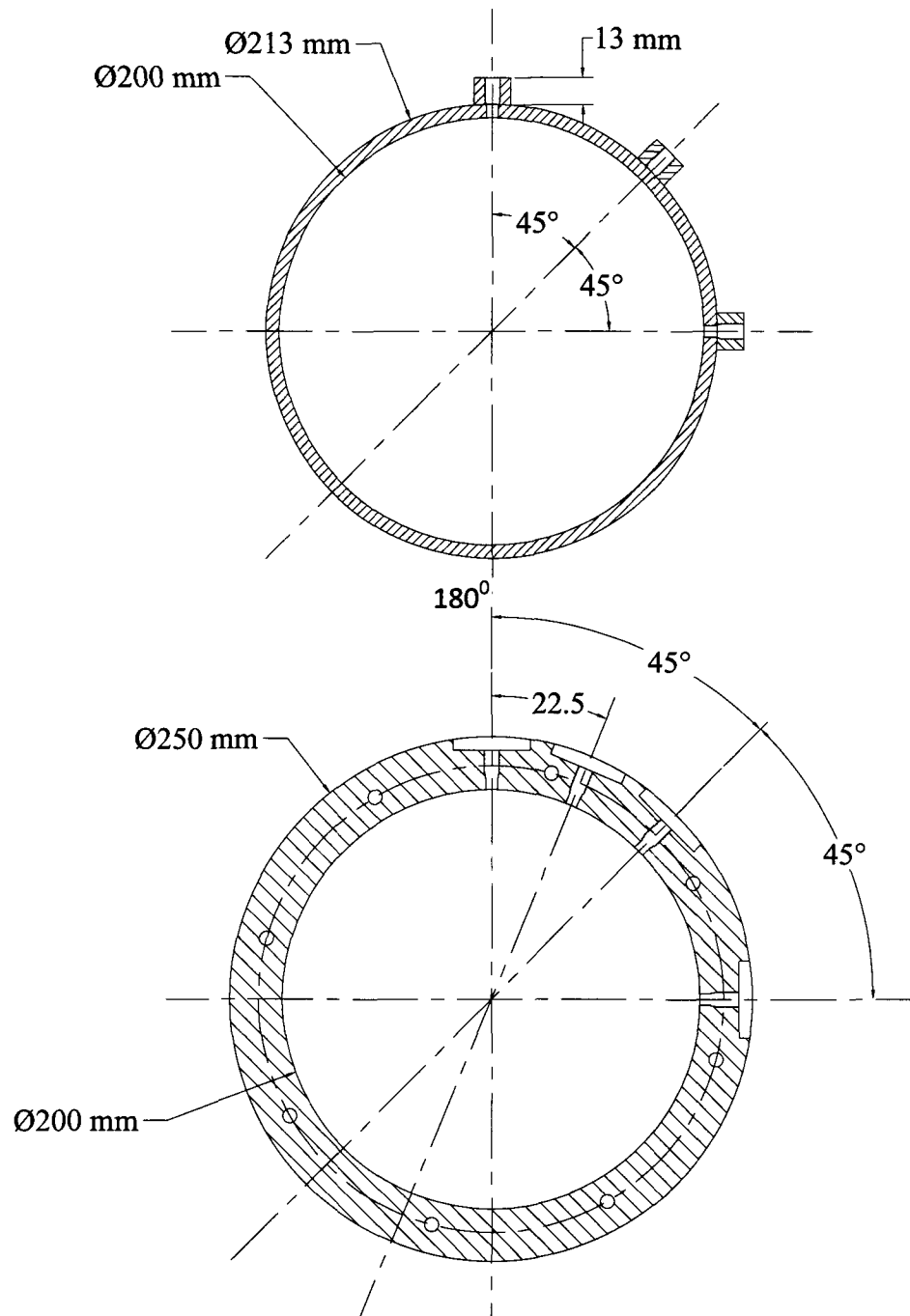


Figure 3-9 Locations of the pressure transducers. a) first design, b) second design

CHAPTER 4

EXCITATION OF DIAMETRAL MODES

This chapter presents the characteristics of the aerodynamic excitation of the cavity-duct system diametral modes. The discussion is based on the experimental measurements performed on the test facility which is described in previous chapter. The measurements were performed for different cavity dimensions. The effect of cavity length (L) and depth (d) on the excitation process is investigated thoroughly. The cavity length to depth ratio (L/d) is the dimensionless form used to represent the cavity length. However, the cavity length to pipe diameter ratio (L/D) is used in some context. The cavity depth to pipe diameter ratio (d/D) is used to represent the cavity depth.

The operating conditions and the boundary layer data at the upstream edge of the cavity are presented in section 4.1. Section 4.2 gives an overview of the typical aeroacoustic response of the cavity-duct system for Mach number up to 0.4. In sections 4.3 & 4.4, the effects of the cavity length and depth on various aspects of the excitation phenomenon are discussed, respectively. This includes the effects on the general aeroacoustic response, Strouhal number, acoustic pressure level and diametral mode shape.

4.1. Boundary layer measurements

In this section, the results of the boundary layer measurements are presented to establish the characteristics of the boundary layer at the cavity upstream separation edge. The measurements are conducted by means of a hotwire at several mean velocities with the cavity covered as mentioned in the previous chapter. A Pitot tube located at the end of the bell mouth was used to measure the reference mean velocity in each case. The mean velocity profile, distribution of the streamwise velocity fluctuation, the displacement thickness and the momentum thickness are determined from these measurements.

Figure 4.1 shows the radial profile of mean velocity for 31 m/s reference mean velocity. Additional profiles for mean velocities of 40.2, 56.5 and 79 m/s are given in Appendix A. The boundary layer at the cavity upstream separation edge is relatively thin compared to the tube diameter, which is a result of the short length of the upstream pipe. To capture accurately the variation in the mean velocity in the radial direction, a traverse mechanism with $20\mu\text{m}$

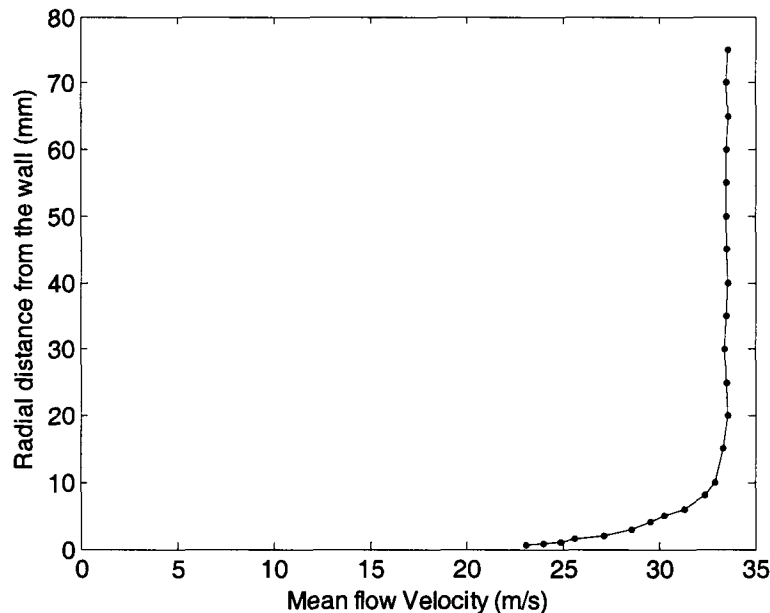


Figure 4-1 Radial profile of mean velocity profile at the cavity upstream edge for reference velocity of 31 m/s at the end of the bell mouth

resolution was used to position the hotwire. Near the pipe wall, the traversing step was 0.25mm. The mean velocity is virtually constant over most of the cross section. The boundary layer thickness is about 20 mm for the 31 m/s case. For the other measured cases, the data showed a decrease in the boundary layer thickness as the velocity increases. At 79 m/s, the boundary layer thickness is reduced to about 12 mm. Outside of the boundary layer, the standard deviation of the mean velocity is 0.35%.

The radial profile of the turbulence intensity, for mean velocity of 31m/s, is shown in fig. 4-2. The turbulent intensity is normalized by the mean velocity outside the boundary layer in the denominator. The velocity RMS amplitude outside the boundary layer represents fluctuations in the mean flow rather than turbulence fluctuation. This supposition was verified by comparing simultaneous time signals of the velocity at two different points located outside the boundary layer. The level of the RMS amplitude of the mean flow fluctuations is about 2% of the local mean velocity and it appears to be constant at all measured flow rates as it can be seen in Appendix A. Inside the boundary layer, the velocity RMS amplitude increases as the turbulent intensity increases until it reaches a maximum near 2 mm from the wall. This Maximum amplitude decreases monotonically with the increase of the flow rate; it drops from 8.5% at 31m/s mean velocity to 6.5% at 79m/s mean velocity.

4.1.1. Displacement and momentum thicknesses

The displacement and momentum thicknesses were calculated considering cylindrical coordinates system that has its origin at the pipe centerline. Assuming that the displacement and momentum thicknesses are small compared to the pipe radius, the following expressions can be derived:

$$\delta^* = \int_0^R \left(1 - \frac{u_o(y)}{U}\right) \left(1 - \frac{y}{R}\right) dy \quad 4-1$$

$$\theta_o = \int_0^R \frac{u_o(y)}{U} \left(1 - \frac{u_o(y)}{U}\right) \left(1 - \frac{y}{R}\right) dy \quad 4-2$$

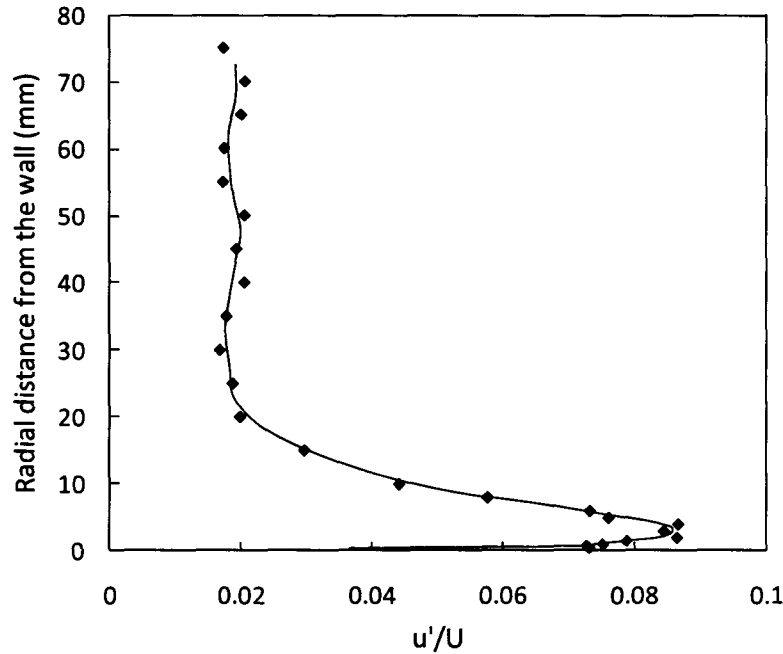


Figure 4-2 Radial distribution of the dimensionless RMS amplitude of fluctuation velocity at the cavity upstream edge for reference velocity of 31 m/s at the end of the bell mouth (the continuous line is a moving average of the measurement data)

where, δ^* is the displacement thickness, y is the distance from the wall, R is the pipe radius, U_0 is the mean velocity and θ is the momentum thickness. Due to the relatively small velocity deficit in the boundary layer, the values of the displacement and momentum thicknesses change significantly with small variation of the velocity in the region outside the boundary layer. To eliminate this undesirable effect, the average value of the velocity outside the boundary layer is calculated and used as the velocity in this region as shown in fig.4-3.

Table 4-1 lists the values of the displacement thickness, momentum thickness and the shape factor for various flow velocities in the test section. It was difficult to perform additional measurements at higher than 80 m/s. This is due to the decrease in the rate of the change of the displacement and momentum thicknesses as the velocity increases, which increases the discrepancy in the measurements. The tabulated data shows that the displacement and momentum thicknesses decrease with the increase of the velocity which agrees well with the

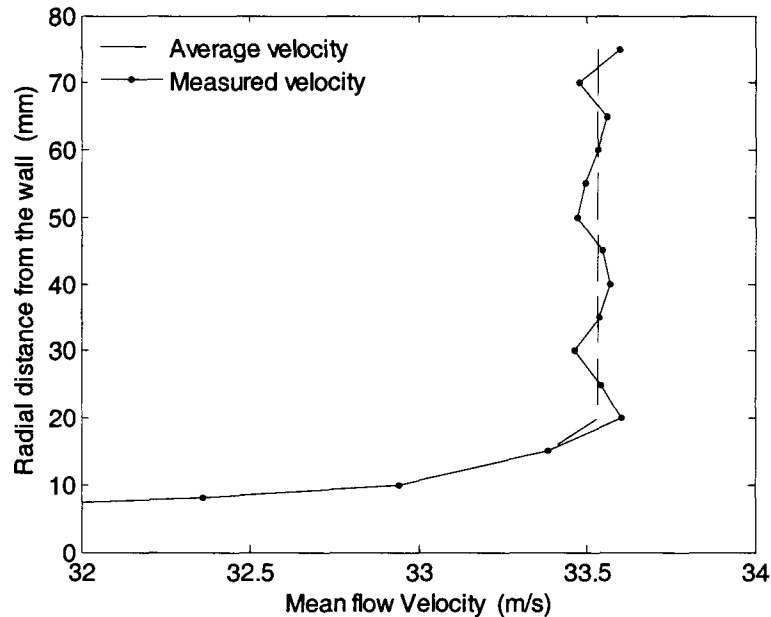


Figure 4-3 Representation of using the average velocity in the calculation of the boundary layer parameters

literature. Moreover, the shape factor is reasonably constant and approximates the shape factor for the turbulent boundary layer over a flat plate. It is also important to point out that both displacement and momentum thicknesses are small compare to the cavity depth under investigation, which ranges between 12.5 and 50 mm. This ensures that the ratios of these thicknesses to the cavity depth is not limiting or restricting the oscillation process.

Table 4-1 List of displacement thickness, momentum thickness and shape factor at different flow velocities

Average velocity (m/s)	Displacement Thickness (mm)	Momentum Thickness (mm)	Shape Factor
31	1.28	0.92	1.39
40	1.21	0.873	1.38
56.5	1.09	0.834	1.31
79	1.05	0.79	1.33

4.2. Overview of the acoustic response

The objective of this section is to illustrate the main characteristics of the excitation mechanism of the diametral modes. For this purpose, the test results of one cavity of 25mm in depth and length ($L/d=1$, $d/D=2/12$) are presented in some detail. This geometry is studied using the first and second test section designs. The two cases yield similar results except that the pressure amplitude level for the case of the second design is higher as the system damping is lower. Therefore, only the results of the second design are presented. It is noteworthy that the discussion, in this section, is based on the analysis of the power spectra of the pressure time traces, similar to the one shown in fig.4-4. The mode orientation or spinning behaviour of the excited acoustics modes is discussed later in Chapter 5.

Generally, for each of the tested cavities, a number of acoustic pressure spectra were recorded for different flow velocities up to the highest capacity of the blower. Each spectrum is the average of 40 data samples, each of which is

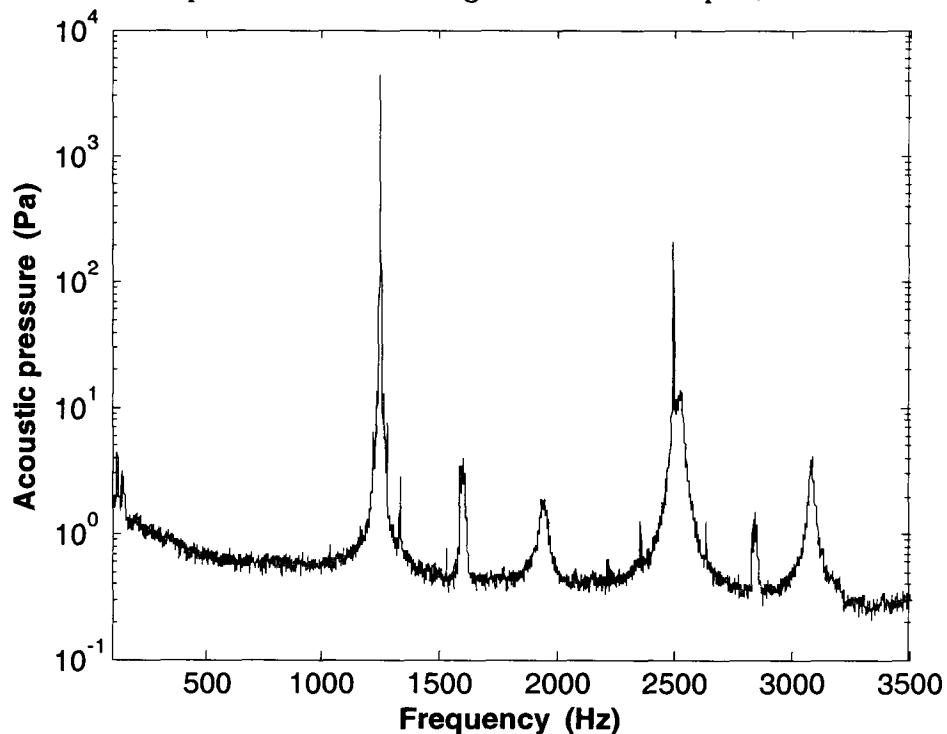


Figure 4-4 Acoustic pressure spectrum for cavity with $L/d=1$, $d/D=2/12$ at 64m/s

one second long yielding a frequency resolution of one Hertz. The time signals were sampled at a frequency of 32 kHz. Figure 4-4 shows a typical example of pressure spectrum for cavity with $L/d=1$, $d/D=2/12$ at 64m/s mean velocity. To gain overall perspective of the system behaviour, the acoustic pressure spectra are presented together in the form of a three dimensional waterfall plots. These are simply isometric views of pressure spectra including gray scale contours for the root mean square (RMS) acoustic pressure. The spectral peaks, therefore, appear darker than the rest of the spectra. The acoustic pressure scale has a maximum of 170 dB and a minimum of 60 dB. The logarithmic scale is used to help illustrate the relatively low amplitude peaks beside the dominant ones on the same graph. Two-dimensional top views of the pressure contours, in the velocity versus frequency plane, are also provided below each isometric view. These views illustrate the velocities at which different acoustic resonance modes are excited. This representation will be used for all tested cases to illustrate the aeroacoustic response of the cavity-duct system.

According to the aforementioned presentation scheme, fig. 4-5 depicts the waterfall plot and the 2-D pressure contours of the RMS acoustic pressure for the cavity with $L/d=1$ and $d/D=2/12$. The spectra correspond to a velocity range from 15 to ≈ 140 m/s. As can be seen in these plots, the first four acoustic diametral resonance modes ($m= 1$ to 4) are strongly excited. The maximum sound pressure level measured during these tests reached about 172.5 dB. It is noteworthy that the frequencies of these resonance modes agree well with the values obtained from the numerical simulation. For example, the measured first mode frequency at a mean flow velocity of 30 m/s is 1269 Hz; while the calculated one is 1280 Hz. It is noticeable that the acoustic resonance frequencies of the different modes decrease slightly with the flow velocity. This phenomenon was investigated using numerical simulation and the results are presented in chapter 7. It is clear that for the current setup, the excitation of the diametral modes excitation dominates the system response. However, the plots show a weak excitation of some longitudinal modes and some diametral-longitudinal combined modes. As an example of such combined modes, fig. 4-6 shows the contour plot of the resonance mode shape at 1600 Hz, which is weakly excited between 60 and 80m/s as shown in fig. 4-5. This mode shape is

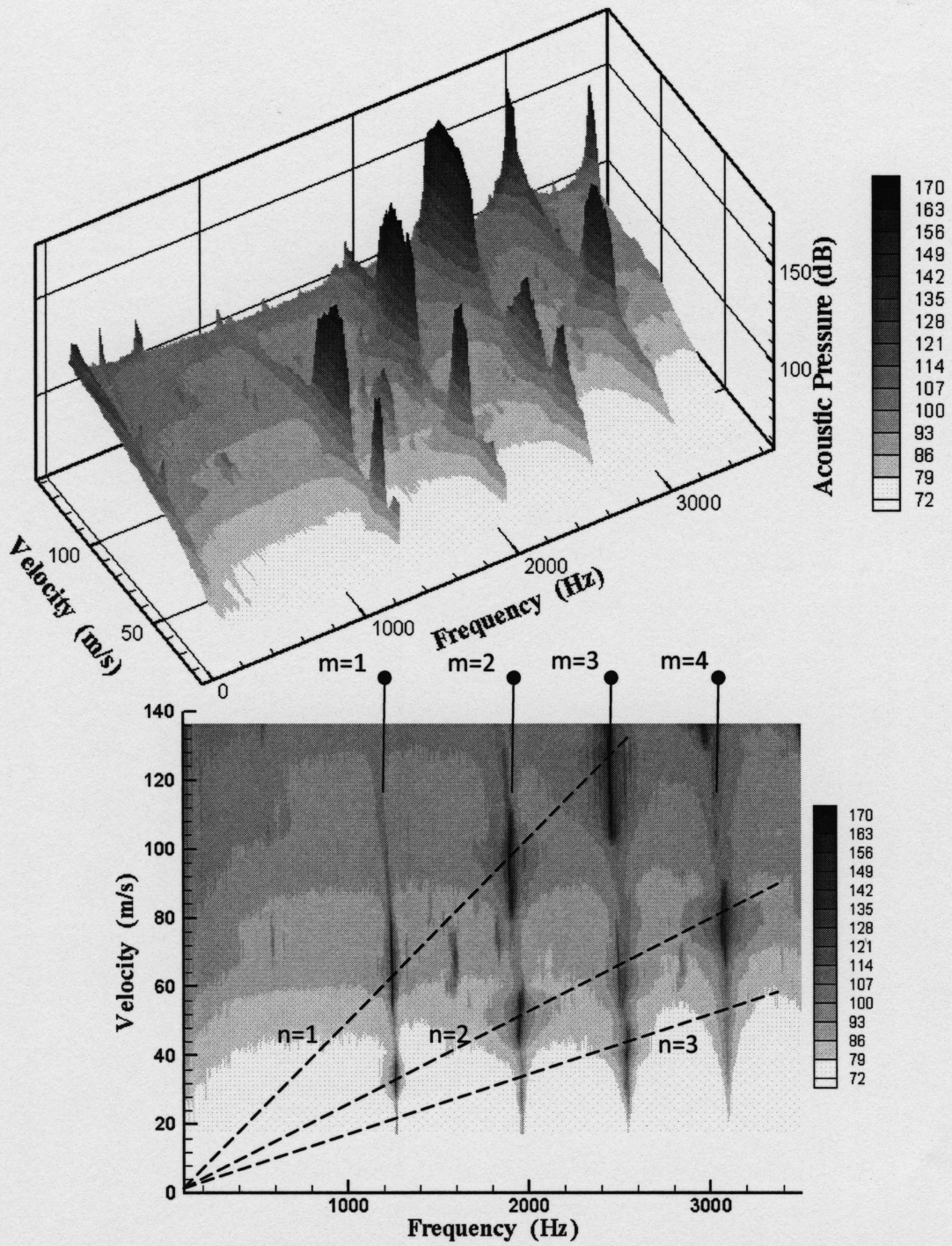


Figure 4-5 Waterfall plot and 2-D pressure contours for $L/d=1$, $d/D=2/12$. m is the diametral mode number, n is the free shear layer mode number

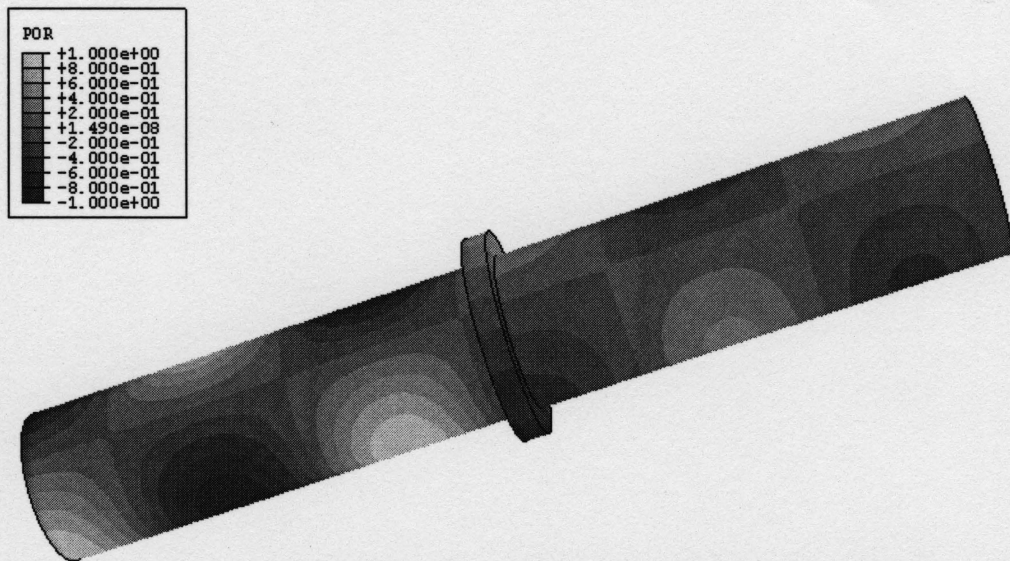


Figure 4-6 Mode shape of first diametral mode combined with a longitudinal mode, $f=1600\text{Hz}$ ($L/d=1$, $d/D=2/12$)

obtained by means of finite element analysis of the cavity-duct system. However, it should be noted that the location of the pressure antinodes of the combined modes may not be at the middle of the cavity where the pressure transducers are mounted. The measured amplitude therefore may be lower than the actual maximum amplitude of these modes.

Referring again to fig. 4-5, each acoustic mode ($m=1-4$) is seen to be excited over multiple ranges of flow velocity. These ranges correspond to specific Strouhal numbers associated with three different instability modes of the cavity shear layer oscillations ($n = 1-3$). However, the pressure spectra show no sign of organized shear layer oscillations other than those resulting from acoustic resonance. Sarohia (1977) reported an empirical model that sets a lower limit below which the fluid-dynamic oscillation cannot be self-sustained. The model depends on the length of the cavity, the boundary layer thickness and the Reynolds' number based on the boundary layer thickness. Plugging the values for the current tests into the model shows that the fluid-dynamic oscillation can be self-sustainable at any flow velocity higher than 40m/s . This indicates that the absence of the fluid-dynamic oscillation can be attributed to the strong acoustic resonance feedback due to the cavity confinement.

Figure 4-7a shows the frequencies of the dominant acoustic modes as a function of the flow velocity. The data show upward and downward frequency jumps, from one acoustic mode to another, with increase of the velocity. This behaviour exemplifies the general trend of cavity-excited acoustic resonance as reported by, for example, Schachenmann & Rockwell (1980). In general, the first and second free shear layer modes ($n=1,2$) excite the first four diametral modes ($m=1-4$), alternatively. However, the third free shear layer mode ($n=3$) excites the second and third diametral modes over very narrow velocity ranges. These results suggest that the higher order acoustic modes are not excited if another lower order mode is excited by a lower order cavity shear layer mode. For example, between 60-70m/s, the third diametral acoustic mode is not excited by the second free shear layer mode because the first acoustic mode ($m=1$) is excited strongly by the first shear layer mode ($n=1$). Figure 4-7b shows the acoustic pressure amplitude of the dominant modes as a function of the flow velocity. Pronounced acoustic resonances start to appear in the pressure spectra above a mean flow velocity of $U \approx 30$ m/s, which corresponds to a Mach number of approximately 0.09. At higher flow velocities, the amplitude goes up and down over each lock-in region with the mean amplitude rising as the velocity increases.

Figures 4-8a & b show the dimensionless pressure amplitude of the excited modes and the Strouhal number of each mode while it is excited as functions of the flow velocity, respectively. The dimensionless pressure amplitude is the RMS acoustic pressure normalized by the dynamic head of the mean flow ($1/2\rho U^2$). The Strouhal number, $f_r L/U$, is based on the cavity length, L , the resonance mode frequency, f_r , and the mean flow velocity, U . Generally, at least one mode is excited at any flow velocity above 30 m/s, which indicates that the cavity-duct system is very liable to flow-excited acoustic resonance. Simultaneous excitation of two acoustic modes is observed during the experiment. However in most cases, the different modes were excited alternatively in time. Scrutiny of fig. 4-8 shows that the first free shear layer mode generates the strongest acoustic resonances, reaching a dimensionless amplitude of 1.8, whereas the highest dimensionless amplitude excited by the second shear layer mode is about 0.9. For the excitation by a certain free shear

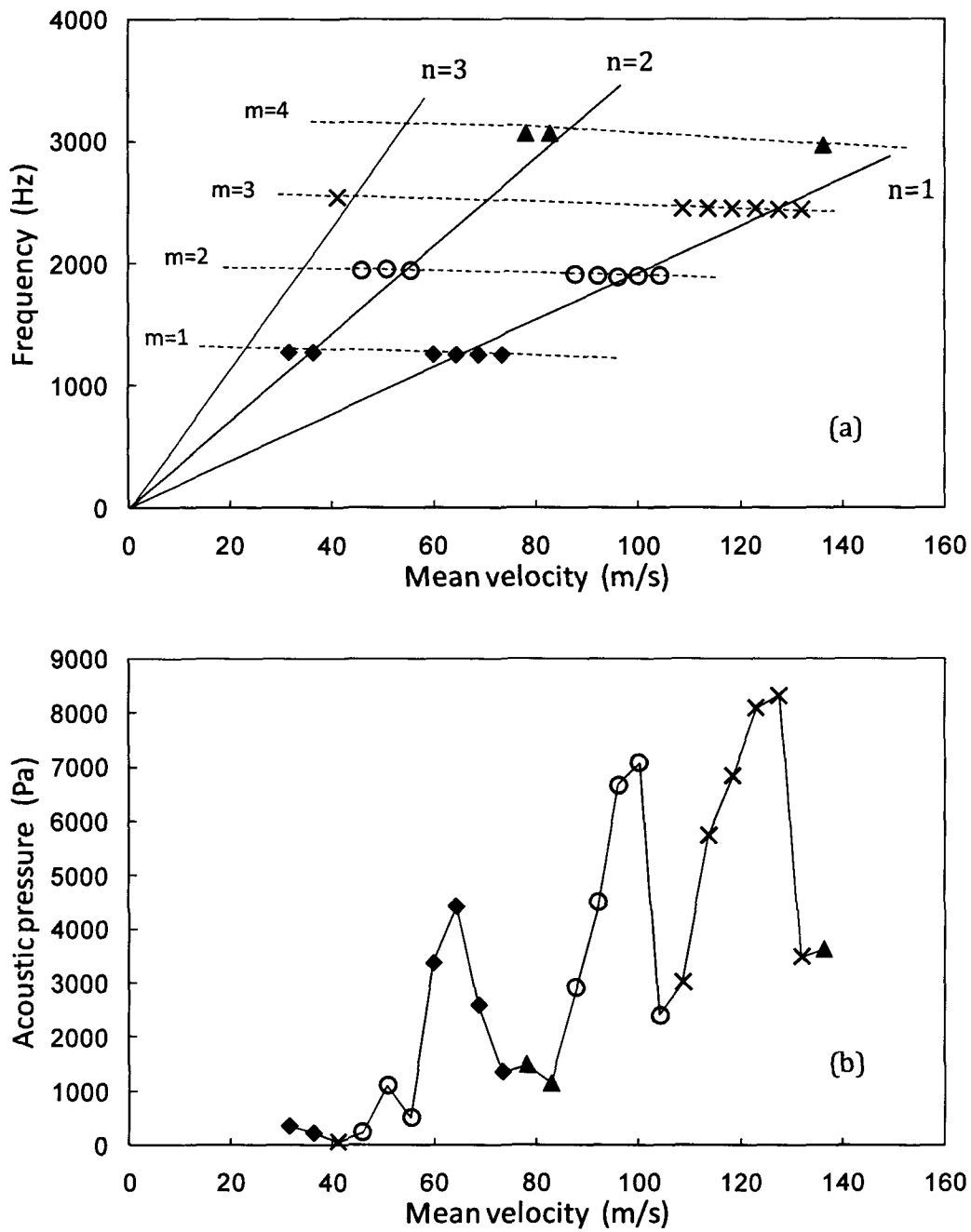


Figure 4-7 Frequencies and amplitudes of the dominant acoustic modes as function of flow velocity ($L/d=1, d/D=2/12$). m is the diametral mode number, n is the free shear layer mode number

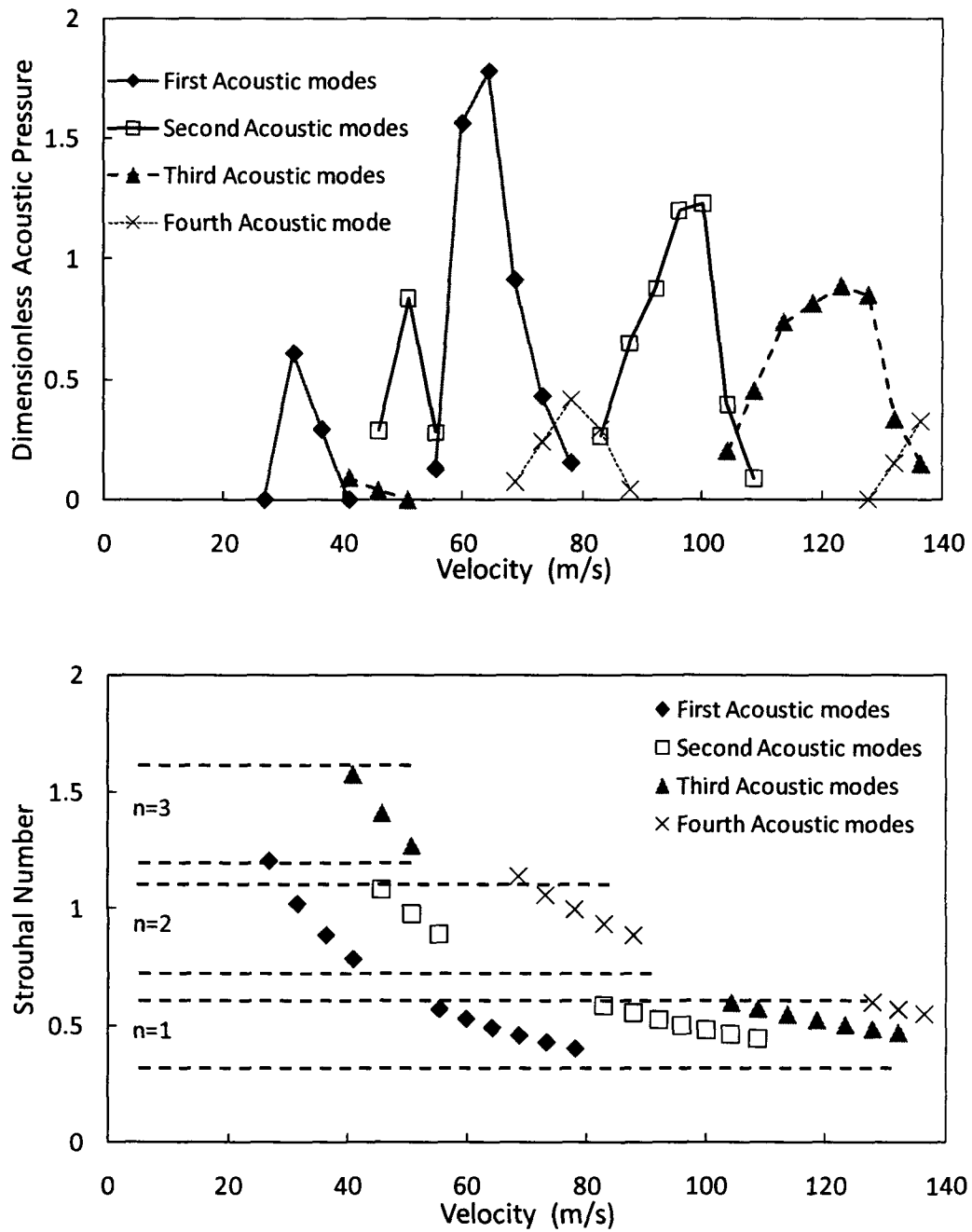


Figure 4-8 Dimensionless pressure amplitude and Strouhal number of the excited acoustic modes at different flow velocities ($L/d=1$, $d/D=2/12$). n is the shear layer mode number

layer mode, the dimensionless amplitude at resonance decreases with the flow velocity and consequently as the order of the diametral mode increases.

The two parts of fig. 4-8 can be merged in one graph depicting the dimensionless amplitude against the Strouhal number as shown in fig. 4-9. From this graph, we can easily determine the Strouhal numbers of different shear layer modes. It is noticeable that these Strouhal numbers remain virtually constant for different acoustic resonance modes. The first cavity free shear layer mode, $n = 1$, excites the acoustic modes over a Strouhal number range from 0.4 to 0.6. The maximum acoustic pressure over this range occurs at a Strouhal number close to 0.5. Following a similar trend, the second cavity free shear layer mode, $n = 2$, generates resonance over a Strouhal number range from 0.8 to 1.15, and the maximum amplitude occurs at a Strouhal number near 1. The third cavity free shear layer mode, $n = 3$, is observed to excite the third diametral mode to a dimensionless amplitude near 0.1 over a narrow velocity range near 41 m/s, which corresponds to a Strouhal number of 1.55.

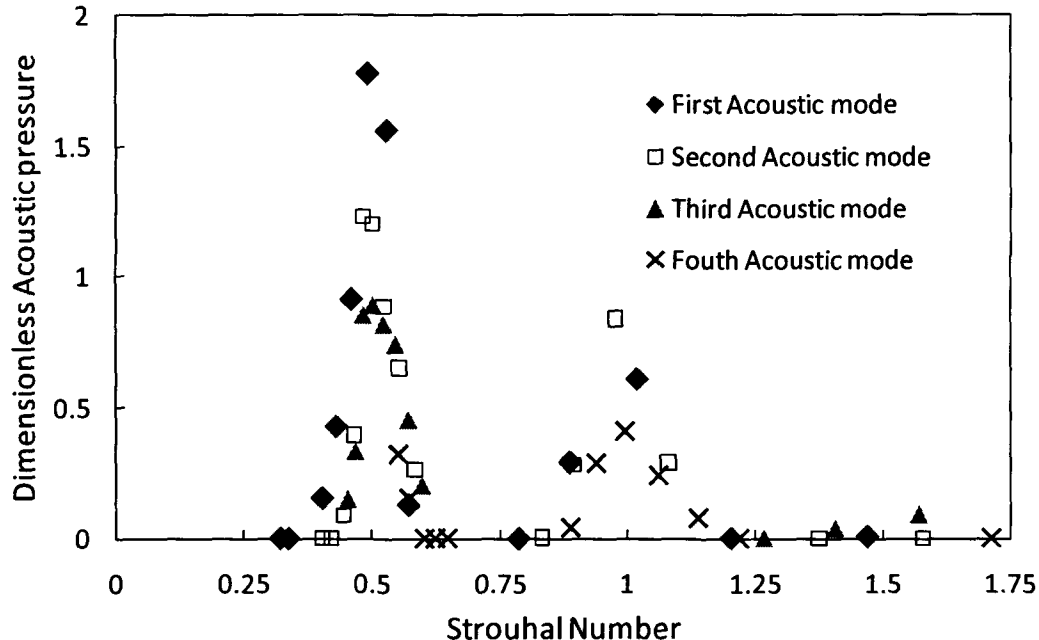


Figure 4-9 Dimensionless acoustic pressure as function of the Strouhal number ($L/d=1$, $d/D=2/12$)

To conclude, the flow over the axisymmetric cavity can excite strongly the acoustic diametral modes, although these acoustic modes do not have a preferred orientation. In addition, for the present confined axisymmetric cavity, acoustic resonances are excited at much lower Mach numbers ($M > 0.09$) than those corresponding to unconfined shallow cavity oscillations. The Strouhal numbers of the first and second shear layer modes appear to have constant values, which are independent of the acoustic mode order or the Mach number. This differs from the Strouhal number of the fluid-dynamic oscillation that decreases with the increase of the Mach number (Tam & Block, 1978). The next section presents the effect of changing the cavity length on the system behaviour.

4.3. Effect of cavity length

This section discusses the effect of changing the cavity length on the acoustic response of the cavity-duct system. The cavity depth was kept constant at 25mm ($d/D=2/12$). The effect of cavity length on the Strouhal number, the acoustic pressure amplitude and the acoustic resonance mode shape is discussed in this section. First, the general trends of the aeroacoustic response are discussed based on the waterfall plots and the 2-D pressure contours. In subsection 4.3.1, the effect of the cavity length on the Strouhal number is detailed. In subsection 4.3.2, analysis is performed to understand the physics behind the change of the pressure amplitude with the cavity length. The finite element analysis of the effect of the cavity length on the acoustic particle velocity is presented in subsection 4.3.3.

Figures 4-10 to 4-14 show the waterfall plots and the 2-D contours of the RMS acoustic pressure for $L/d=2$ to 6. Straight lines are drawn on each 2-D plot to mark the different shear layer modes. The different diametral modes are also marked for visual aid. The unmarked peaks are corresponding to either higher harmonics of excited diametral modes or longitudinal and combined modes. As a general observation not related to the acoustic resonance mechanism, the increase of the cavity length seems to increase the cavity-duct system flow resistance. This is clear from the decrease of the maximum tested flow velocity with the increase of the cavity length, as shown in figs. 4-10-4-14.

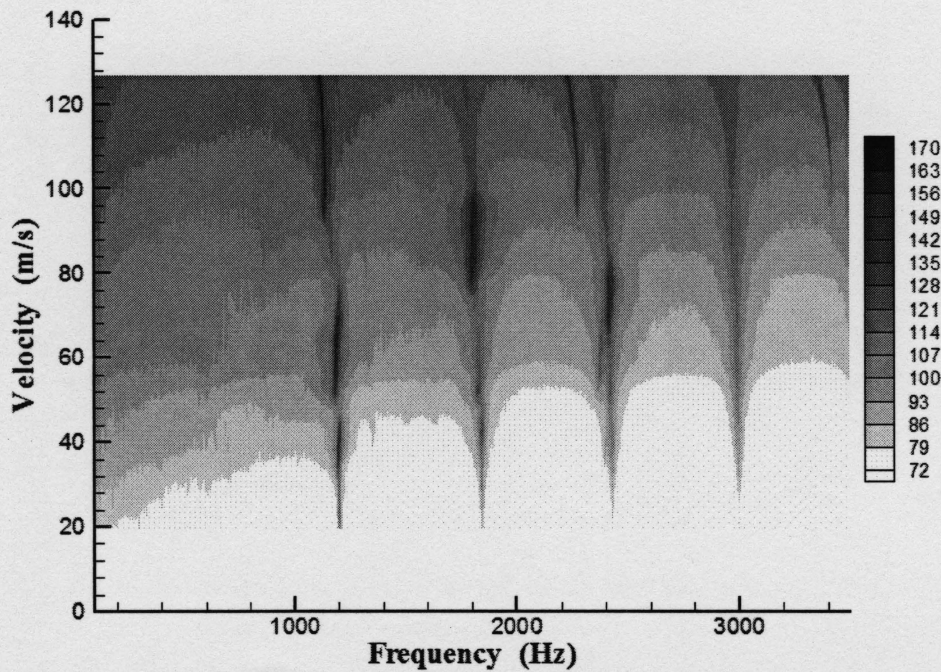
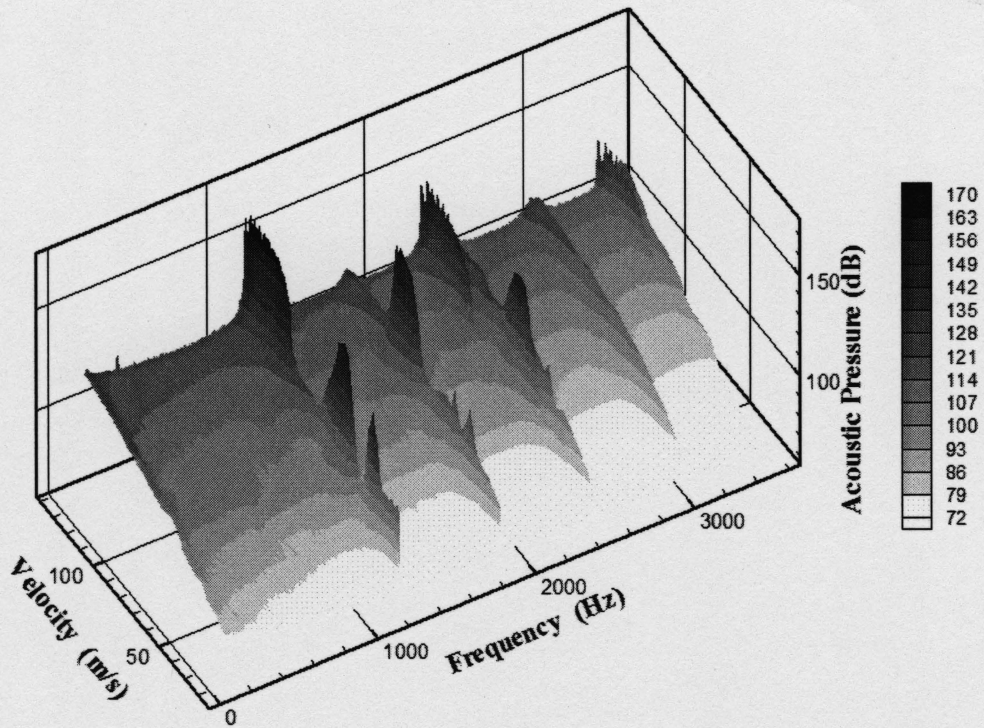


Figure 4-10 Waterfall plot and 2D pressure contours for $L/d=2$, $d/D=2/12$. m is the diametral mode number, n is the free shear layer mode number

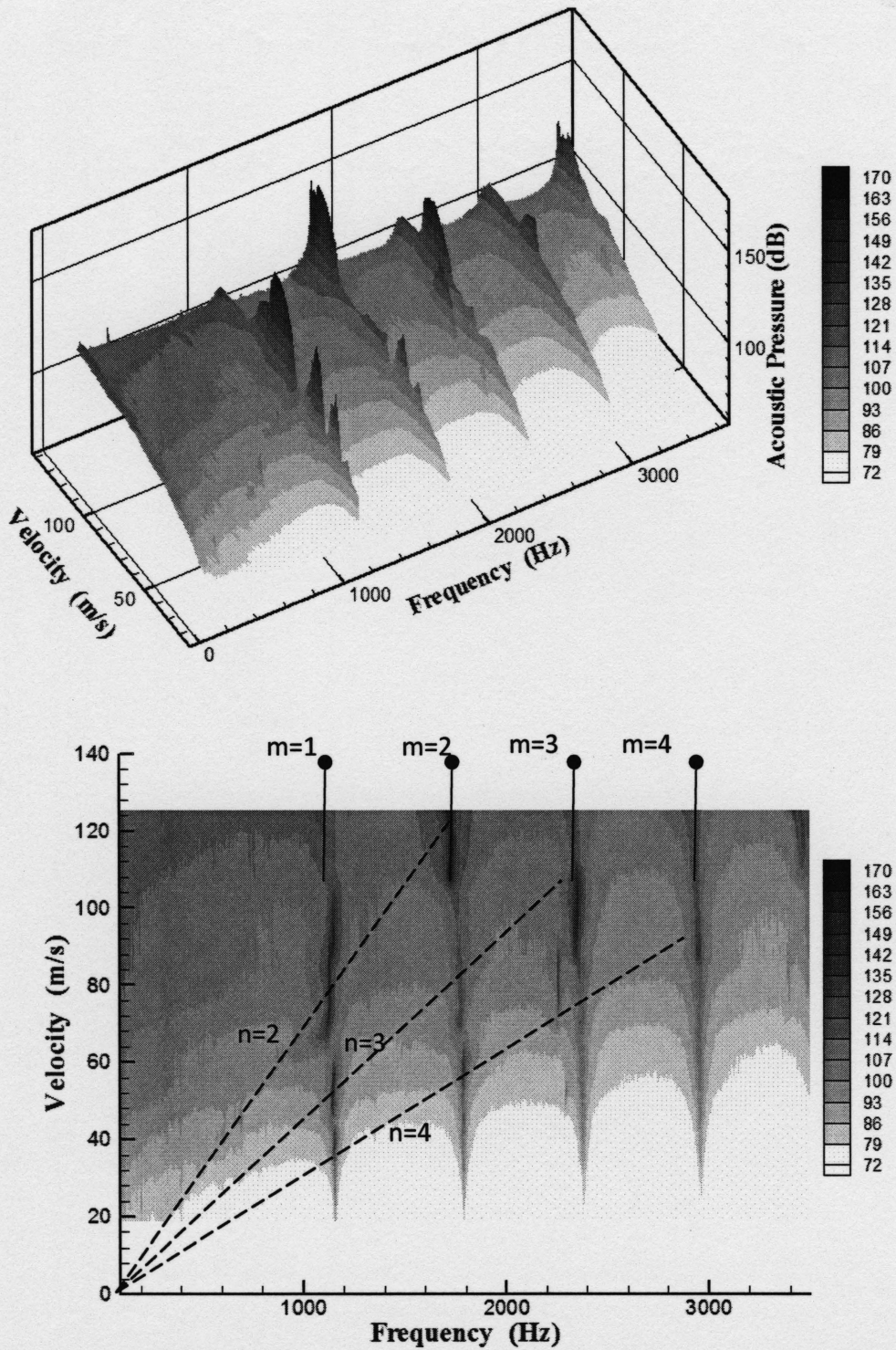


Figure 4-11 Waterfall plot and 2D pressure contours for $L/d=3$, $d/D=2/12$. m is the diametral mode number, n is the free shear layer mode number

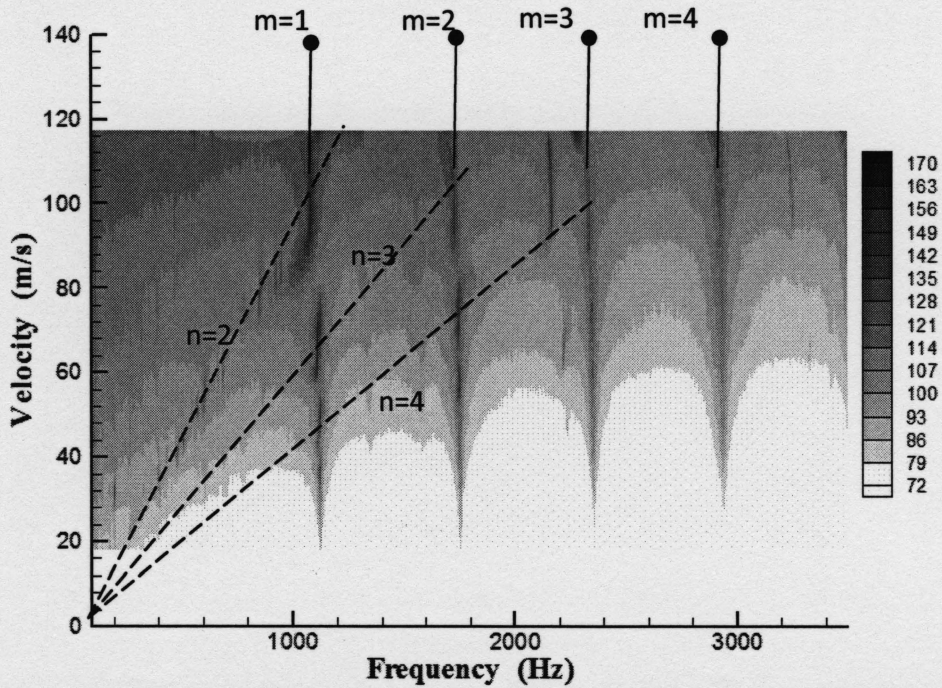
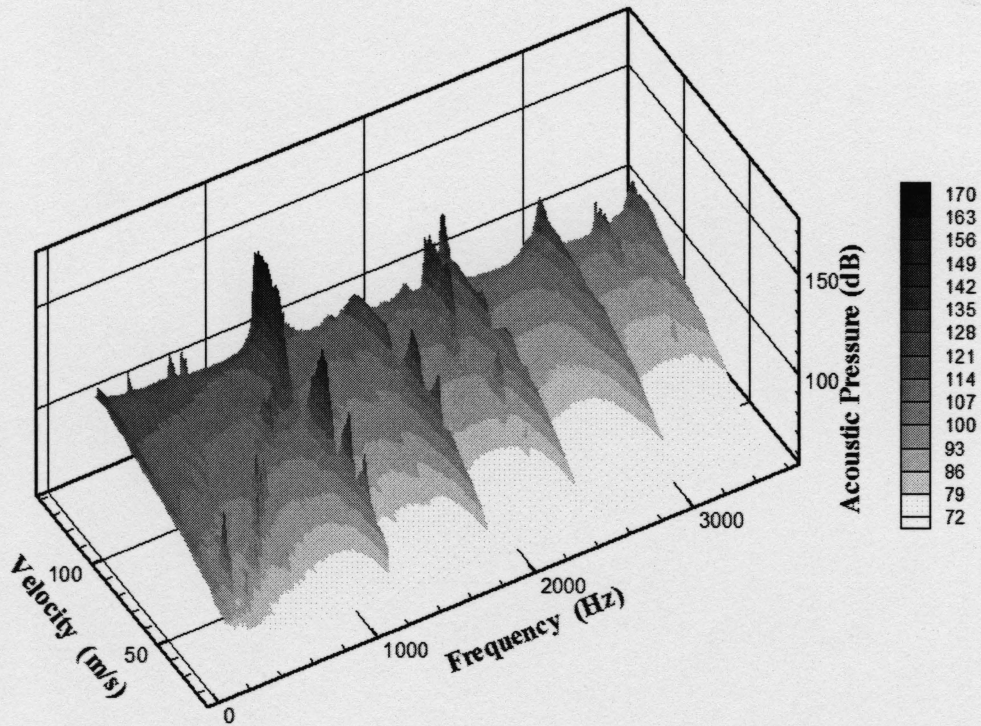


Figure 4-12 Waterfall plot and 2D pressure contours for $L/d=4$, $d/D=2/12$. m is the diametral mode number, n is the free shear layer mode number

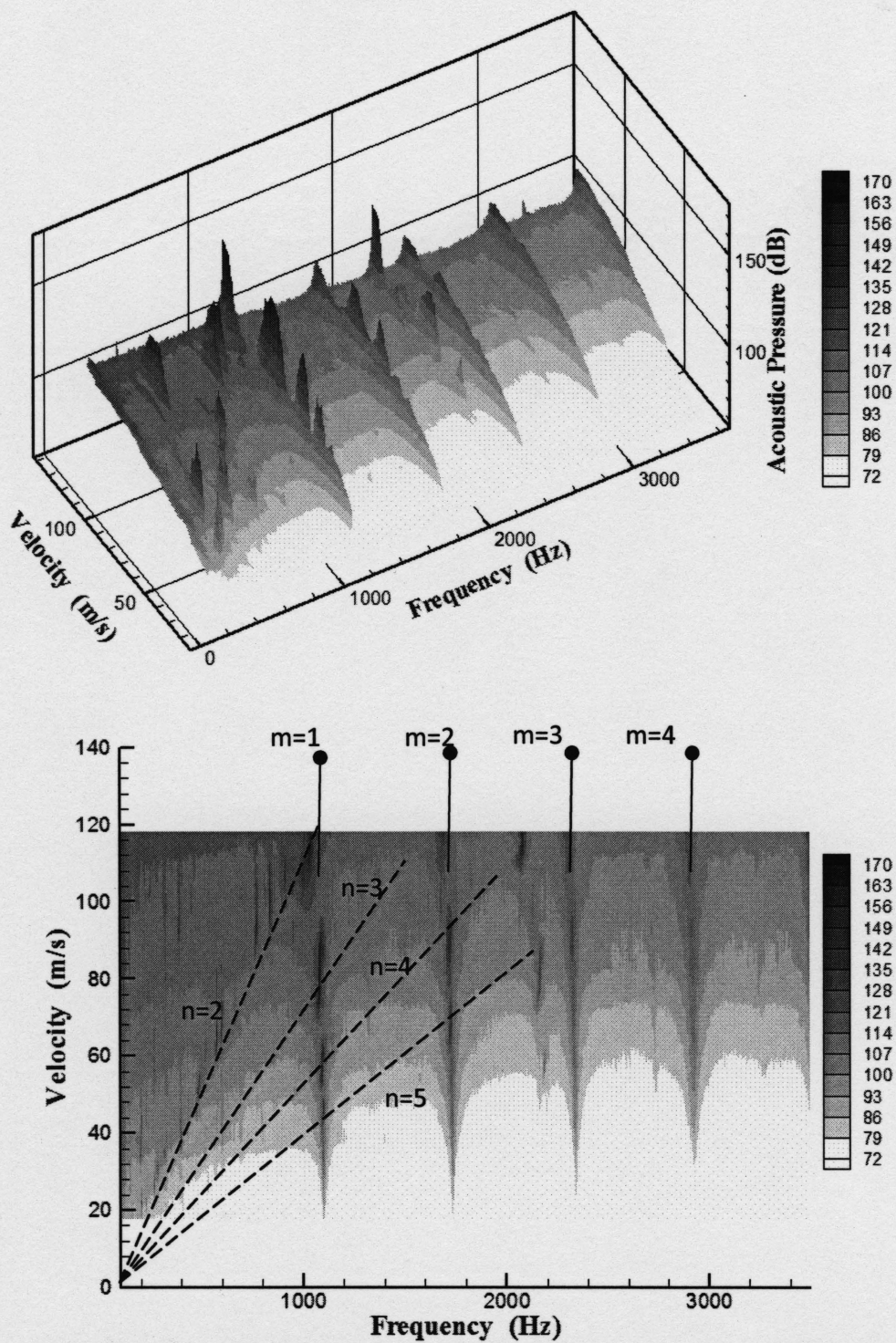


Figure 4-13 Waterfall plot and 2D pressure contours for $L/d=5$, $d/D=2/12$. m is the diametral mode number, n is the free shear layer mode number

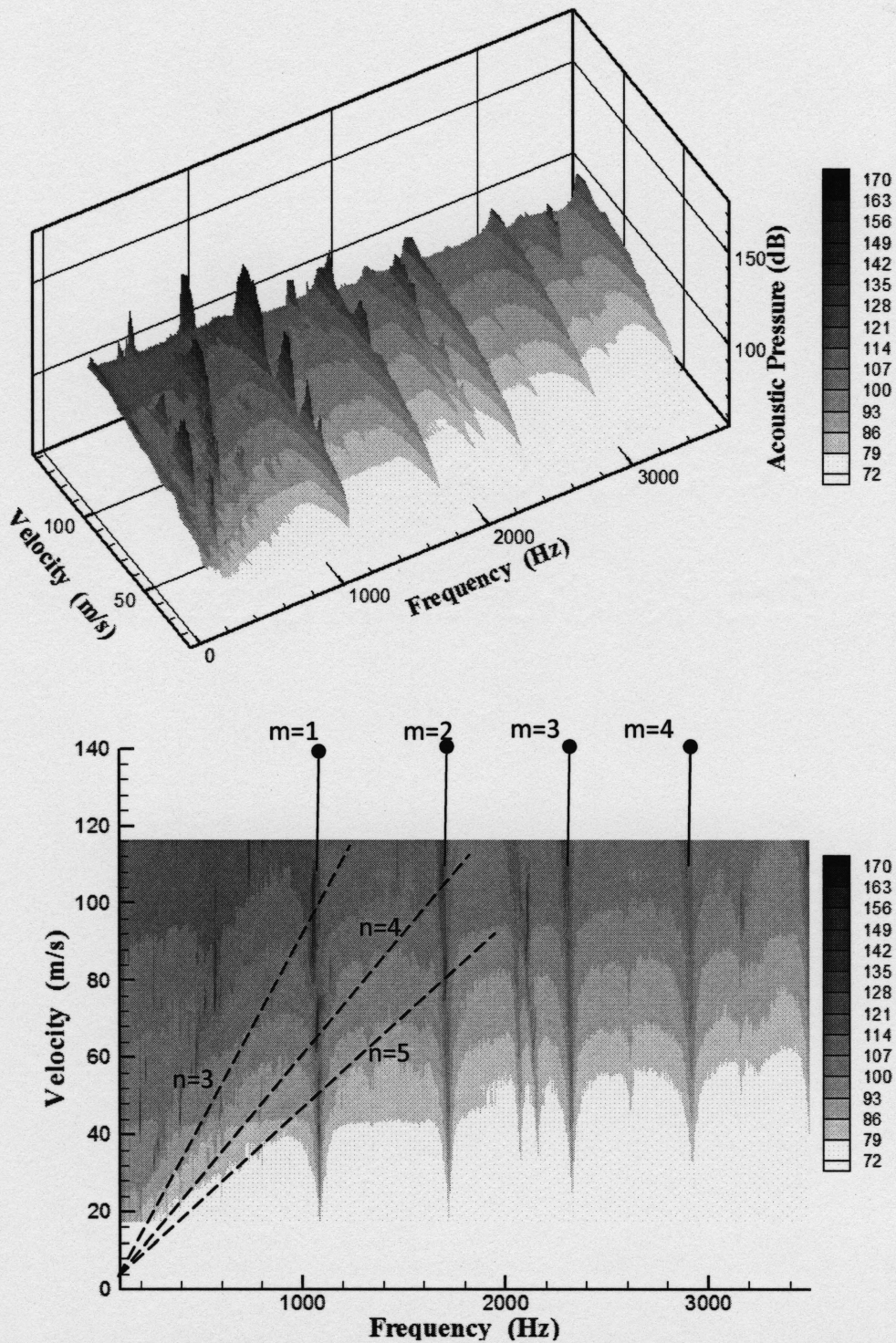


Figure 4-14 Waterfall plot and 2D pressure contours for $L/d=6$, $d/D=2/12$. m is the diametral mode number, n is the free shear layer mode number

Starting with the data of the cavity with $L/d=2$, shown in fig. 4-10, the behaviour of this case is very similar to the cavity with $L/d=1$, which is discussed in previous section. The change of cavity length alters the velocity ranges over which the acoustic modes are excited. It is noteworthy that, in these two cases, the longitudinal acoustic modes of the pipe have not been excited during the tests. At low flow velocity, the increase of the cavity length from $L=25\text{mm}$ ($L/d=1$, $d/D=2/12$) to $L=50\text{mm}$ ($L/d=2$, $d/D=2/12$) results in a drop in the diametral mode frequencies by about 5% from the case of $L/d=1$. In both cases, the resonance frequencies decrease with the increase of the mean flow velocity. This observation is more pronounced for the lower diametral modes. Though, when the first diametral mode is excited by the second free shear layer mode, the frequency appears to be rather constant or experience a very slight increase.

The results of the cavity with $L/d=3$ are shown in fig. 4-11. This geometry is able to excite the diametral modes strongly with second, third and fourth shear layer modes. However, the level of pressure amplitude is lower than the amplitude level in the previous two cases ($L/d=1, 2$). In this case, longitudinal modes are also excited, but with extremely small amplitude. At 95m/s , the second free shear layer mode shifts from exciting the first diametral mode to excite a longitudinal mode that has a frequency just about 10Hz higher than the diametral mode frequency. According to the finite element simulation, this longitudinal mode has a pressure anti-node at the middle of the cavity length, which explains its relative strong appearance in the waterfall plot. However, the longitudinal mode has relatively lower amplitude than the diametral modes which is expected due to its high level of radiation losses.

Longer cavities ($L/d=4-6$), shown in figs. 4-12-14, are also capable of exciting the diametral modes, even with the fourth shear layer mode. But, the pressure amplitude decreases consistently with the length. The velocity range over which certain shear layer mode can excite certain diametral mode depends on the cavity length and the pipe diameter. The cavity length determines the shear layer oscillation frequency for a given flow velocity and the pipe diameter determines the frequencies of the diametral modes. Thus, in general, the ratio of cavity length over the pipe diameter (L/D) dictates the aeroacoustic response of

the cavity-duct system. However, the aspect ratio of the cavity (L/d) slightly affects the Strouhal number, and the cavity size alters the frequencies of the diametral modes.

Re-examining the aeroacoustic response of different cavities shows that the essential feature which distinguishes long cavities ($L/d=3-6$) from short ones ($L/d=1-2$) is the appearance of small spectral peaks indicating that the pipe longitudinal modes can also be excited for long cavities. The spectral peaks of the longitudinal modes follow constant Strouhal number lines. This is more noticeable at frequencies lower than the first diametral mode frequency. In this context, it should be re-emphasised that it is not appropriate to compare the amplitudes of the longitudinal modes with those of the diametral modes. However, it is clear that the level of the pressure amplitude of the longitudinal modes and the number of the longitudinal modes being excited show consistent increase with the increase of the cavity length. They start as very few and faint traces in the waterfall plot for $L/d=3$ in fig. 4-11, and continue to gain strength as the cavity length increases until they are continually excited over most of the velocity range for the cavity with $L/d=6$, as shown in fig. 4-14. However, the longitudinal modes seem to subside as soon as one of the diametral modes is excited. This can be seen in fig. 4-12 for a cavity length of $L/d=4$ at 68m/s, where the first diametral mode is excited, and also in fig. 4-13 for a cavity length of $L/d=5$ at 80m/s, where the first diametral mode is excited by the third shear layer mode. Moreover, the diametral and the longitudinal modes are not excited simultaneously, but rather alternately.

For cavity length to depth ratio equal to 3 and higher, the excitation of the numerous longitudinal modes shows basically that one free shear layer mode dominates the hydrodynamic instability of the flow. For all cases, the acoustic resonance of the longitudinal modes is found to initially follow a constant Strouhal number relationship that corresponds to the second shear layer mode. With increasing velocity, the Strouhal number of the shear layer mode seems to decrease. The average Strouhal number of the dominant free shear layer mode, which excites the longitudinal modes, is found to vary between 1.15 and 1.2 for different cavities.

In the following subsection, the effect of cavity length on the Strouhal number of the fluid-resonance oscillation is discussed. The Strouhal number of the fluid-resonance mechanism can be different from the Strouhal number of the fluid-dynamic oscillation.

4.3.1. Effect of cavity length on the Strouhal number

To examine the effect of the cavity length on the Strouhal number and the pressure amplitude, a series of plots similar to fig. 4-9 depicting dimensionless amplitude against the Strouhal number of the acoustic resonance were constructed for all tested cases. As another example, the results for $L/d=3$ is shown in fig. 4-15. For all excited modes, the dimensionless pressure amplitude experiences a rapid increase and decrease over different ranges of Strouhal number that correspond to different cavity free shear layer modes. The Strouhal number of a certain amplitude peak is considered to be the fluid resonance Strouhal number of the corresponding free shear layer mode.

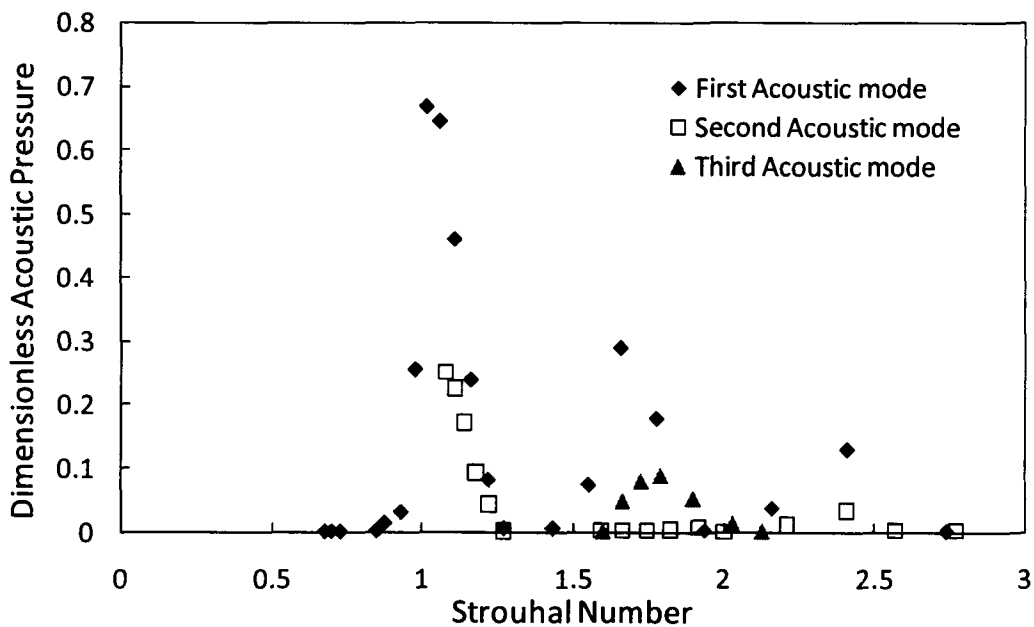


Figure 4-15 Dimensionless pressure with the Strouhal number for $L/d=3$, $d/D=2/12$.

Figure 4-16 shows the Strouhal number as a function of the cavity length to depth ratio. Comparing the current data with those reported by Rockwell & Naudascher (1978), shows that the current values are within the scatter of the reported data. For the current data, the average Strouhal numbers of the first four shear layer modes are 0.48, 1.01, 1.63 and 2.41, respectively. Scrutiny of the average Strouhal number values reveals that the Strouhal number increases with larger steps as the mode number increases such that the limit that the Strouhal number of the fourth mode is closer to 2.5 than 2. Similar trend can be observed in the study of the excitation of duct transverse modes by a 2-D shallow cavity reported by Ziada et al. (2003). However, the data for the fluid-dynamic oscillation reported by Rockwell & Naudascher (1978) and Tam & Block (1978) shows that the step between the Strouhal numbers of two consecutive shear layer modes is independent of the mode order. This difference between the fluid-dynamic and fluid-resonance oscillations can be attributed to the difference in the feedback mechanisms of the two types of oscillations. This proposition needs further investigation to develop a model for the fluid-

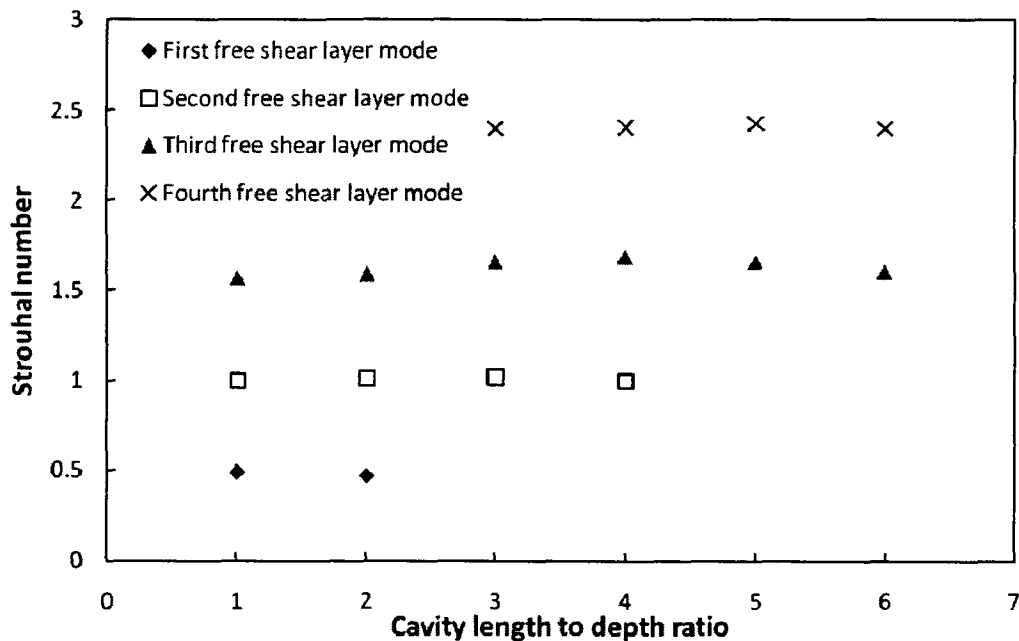


Figure 4-16 Strouhal number as function of cavity length to depth ratio (L/d) the data is for cavities with $d/D=2/12$

resonance Strouhal number.

In the next subsection, the effect of cavity length on the pressure amplitude is studied. As mentioned earlier, the contour plots for cavities with lengths $L/d=2-6$, shown in figs 4-10 to 4-14, demonstrate definite decrease in the pressure amplitude as the cavity length is increased. Next subsection highlights some of the physics behind this trend.

4.3.2. Effect of cavity length on the pressure amplitude

Figure 4-17 shows the maximum dimensionless amplitudes occurring at different free shear layer modes for all cavity lengths. In the figure, “ n ” is the cavity free shear layer mode number and “ m ” is the diametral mode order. These data points are extracted from the graphs of the dimensionless pressure versus the Strouhal number, which were discussed in section 4.3.1. All data points correspond to the first diametral mode. Generally; fig. 4-17 shows a decrease in the dimensionless acoustic pressure amplitude as the cavity gets longer. Due to

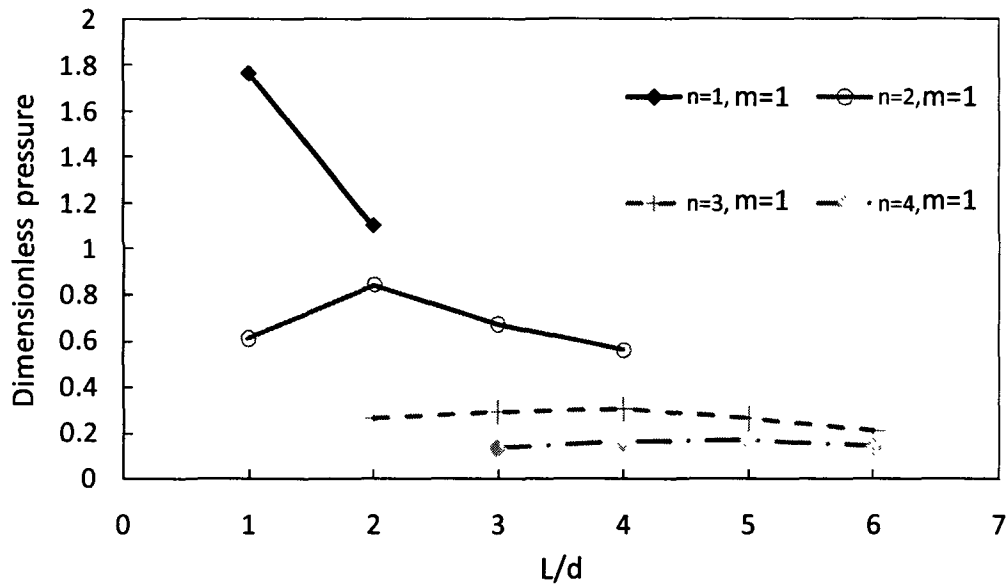


Figure 4-17 Effect of cavity length on the maximum dimensionless pressure for the different free shear layer modes (m : the acoustic mode number, n : the free shear layer mode number, The lines are for visual aid only)

the limited capacity of the wind tunnel, the low order shear layer modes ($n=1,2$) did not excite the first acoustic mode for the cases of long cavities. This limits the number of data points available for $n=1, 2$.

It is clear that the pressure amplitude decreases with the increase of the order of the free shear layer mode. This decrease may be attributed to the reduction of both the size and the fluctuation velocity of the shear layer vortical structures. In the next chapter, it will be shown that, for constant cavity length, the size and the fluctuation velocity amplitude of the shear layer vortices decrease with the increase in the order of the shear layer mode. Also, the relative increase in the broadband turbulence fluctuation, compared to the shear layer fluctuation velocity, reduces both the concentration of vorticity and the level of azimuthal coherence of the shear layer.

Figure 4-17 shows that the resonance amplitude caused by the second, third and fourth shear layer modes increases with the cavity length at the beginning then starts decreasing after a certain length. This length varies from one shear layer mode to another. It is noteworthy that the mean flow velocity is not the same for all cases. To examine the effect of the mean flow velocity, the same data are plotted against the mean flow Mach number in fig. 4-18. Data corresponding to the excitation of the second and third diametral modes is added to broaden the comparison. The dimensionless pressure amplitude increases with the mean Mach number until a Mach number between 0.15 and 0.2. Thereafter, the amplitude decreases with further increases in the Mach number. All free shear layer modes seem to follow the same trend. Plotting the dimensionless pressure amplitude against the Mach number shows more clearly the drop of the maximum resonance amplitude as the order of the free shear layer increases.

In fig. 4-18, the data corresponding to the different diametral modes ($m=1, 2$ & 3) aligns together depending on the shear layer mode. This improves the confidence in the generality of the current normalization parameters. However, it appears that the dimensionless pressure amplitude also decreases with the increase of the order of the diametral modes, especially in the case of the second free shear layer mode ($n=2$).

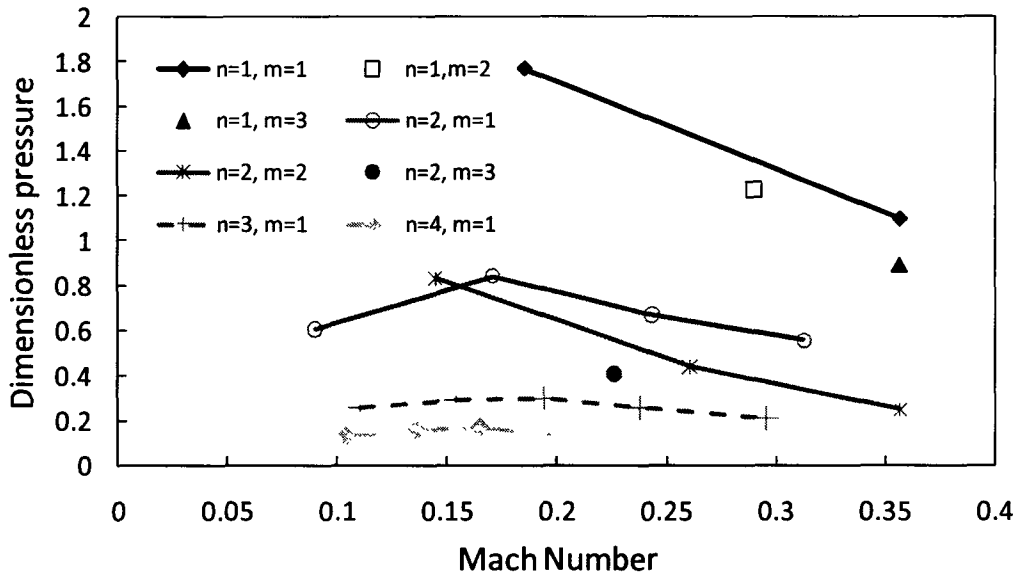


Figure 4-18 Effect of Mach number on the maximum dimensionless pressure for the different free shear layer modes (m : the acoustic mode number, n : the free shear layer mode number)

In the next subsection, a finite element analysis of the diametral modes for different cavity lengths is presented. The analysis focuses on the acoustic particle velocity associated with the acoustic resonance modes.

4.3.3. Effect of the cavity length on the acoustic field

As mentioned earlier, the excitation mechanism is influenced by any change in the acoustic particle velocity distribution which is generated by the resonant sound field. This section focuses on the effect of the cavity length on the particle velocity distribution, and consequently on the excitation mechanism. The difference in the susceptibility of the first three diametral modes to the aerodynamic excitation is also investigated. It should be recalled here that the vorticity-based contribution to the acoustic power is linearly proportional to the acoustic particle velocity. To be more precise, it is proportional to the particle velocity component perpendicular to both the flow and the vorticity of the free shear layer. Thus, changes in the acoustic particle velocity distribution and/or amplitude affect directly the acoustic power production.

To determine the distribution of the acoustic particle velocity amplitude, U_a , associated with the acoustic resonance modes, the amplitude of the pressure domain, P , is calculated first using finite element commercial package “ABAQUS”, as described in the previous chapter. From the pressure domain, the acoustic particle velocity is calculated using Euler’s equation:

$$\rho_o \frac{\partial U_a(t)}{\partial t} = -\nabla p_a(t) \quad 4-3$$

Considering sinusoidal fluctuation of the pressure results in:

$$U_a = \frac{\nabla p_a}{2\pi f} \quad 4-4$$

where, ρ_o is the average air density and f is the acoustic resonance frequency. In the current calculation, the density of air is considered 1.2 kg/m³. The pressure gradient is calculated using a MATLAB program. The accuracy of the MATLAB program was tested by estimating the particle velocity for simple acoustic mode shapes which have closed form solutions.

Figure 4-19 shows vector plots of the acoustic particle velocity over two different cross-sections for the first diametral mode of a cavity with a length and depth of 25mm ($d/D=2/12$, $L/d=1$). The pressure nodal plane is perpendicular to the plane of cross-section A-A. The two figures show the cross-sections with the maximum particle velocity. For this case, the perpendicular component of the particle velocity to both the mean flow and the free shear layer vorticity is the radial component. In cross-section B-B, the thin inner circle represents the main pipe circumference which is the edge of the cavity. Along the cavity edge, the *radial* particle velocity is maximum at the plane of cross-section A-A and decreases continuously in either orientation until it reaches zero at a plane 90° from section A-A.

Figure 4-20 shows the maximum *radial* component of the acoustic particle velocity amplitude over the cavity mouth for $L/d=1$, 3 and 6. These particle velocity distributions correspond to cross-section A-A of the first diametral mode with a maximum acoustic pressure of one Pascal at the centre of

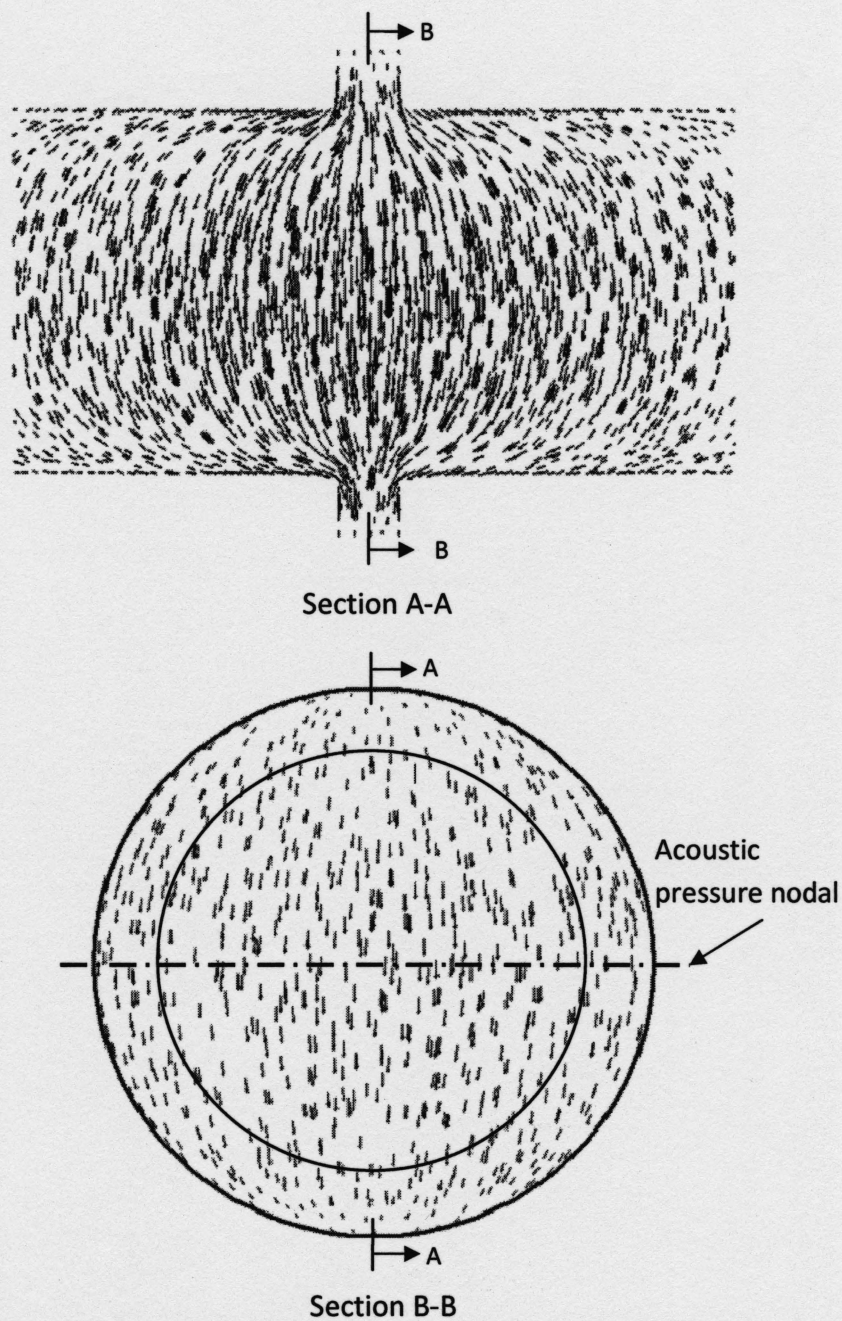


Figure 4-19 Vector plots of the acoustic particle velocity amplitude of the first diametral mode ($d/D=2/12$, $L/d=1$)

the cavity floor. Additional cavities with $L/d=2, 4$ and 5 were also simulated, but only three cases are presented here to show the trend of the change in the particle velocity distribution with the cavity length. The average amplitudes of the *radial* acoustic particle velocity along the cavity length are $1.09, 1.06$ and 1.00 mm/s for $L/d=1, 3$ and 6 , respectively. This indicates that the length of the cavity has no major effect on the amplitude of the acoustic particle velocity and consequently not on the acoustic power production either. The second and third diametral modes were also simulated for a cavity similar to that analysed for the first mode ($d/D=2/12$ and $L/d=1$). The average values of the particle velocity radial components are 1.24 and 1.22 mm/s for the second and third diametral modes, respectively. Since these values are higher than those of the first mode, the drop in the acoustic resonance amplitude for the case of the higher order diametral modes must be the result of three-dimensional effects and the increase in the system losses. *In the rest of the chapter, the average amplitude along the cavity length of the radial particle velocity is used without presenting the complete distribution over the cavity mouth.*

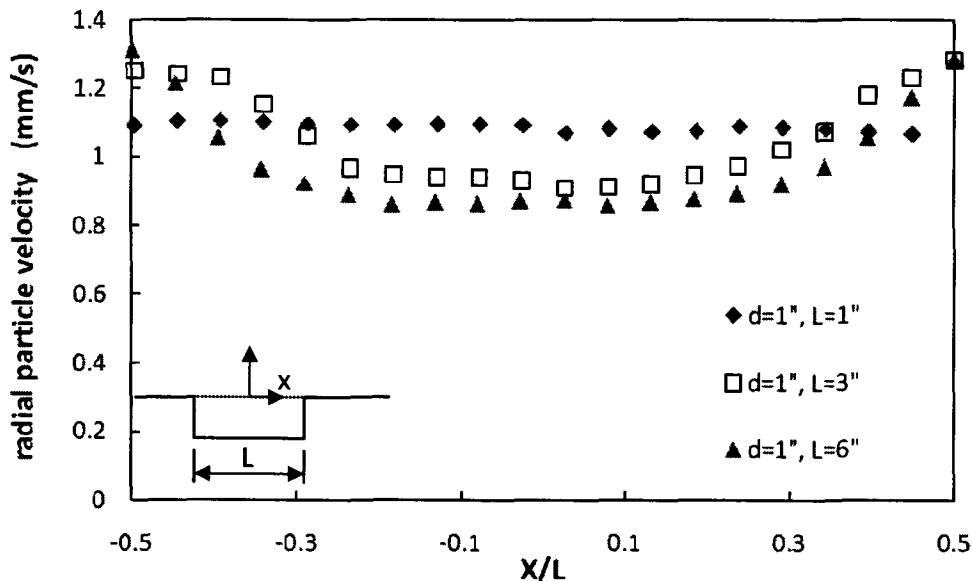


Figure 4-20 Radial component of the acoustic particle velocity along the cavity mouth corresponding to acoustic pressure of one Pascal at the center of the cavity floor ($d/D=2/12$)

To summarize the discussion on the effect of the cavity length on the aeroacoustic response of the cavity-duct system, it is shown that all the studied lengths are capable of exciting the diametral modes. The excitation of acoustic resonance is self-sustainable for Mach numbers higher than 0.09. The general aeroacoustic response depends on the ratio of the cavity length to pipe diameter (L/D). The Strouhal number of the fluid-resonance phenomenon is independent of the cavity length over the tested range ($L/d=1-6$). Regarding the excitation level, the dimensionless pressure amplitude decreases with the cavity length. This decrease seems to be better correlated with the Mach number of the flow. Regarding the acoustic mode shape, the change of the diametral mode shape with the cavity length does not seem to have a significant effect on the radial component of the acoustic particle velocity and consequently not on the acoustic power production either.

4.4. Effect of cavity depth

This section discusses the effect of changing the cavity depth, with respect to the pipe diameter (D), on the acoustic response of the cavity-duct system. As in the previous section, the general behaviour is first described. This is followed by a discussion of the effect of the cavity depth on the Strouhal number, the pressure amplitude, the acoustic mode shape and the mode selectivity.

Two cavity depths were investigated in addition to the one studied in the previous section. For each depth, the cavity length was changed from 25 mm to 150 mm with a step of 25mm. The two new depths are 12.5 mm and 50 mm. Thus, the three tested cavity depths, d , relative to the pipe diameter, D , are $d/D= 1/12, 2/12$ & $4/12$. For the first depth ($d/D=1/12$), the maximum cavity length to depth ratio is $L/d=12$. This L/d ratio is classified as a closed cavity, for which the free shear layer reattaches to the cavity floor. On the other hand, for $d/D=4/12$, the minimum L/d is 0.5, which is classified as a deep cavity. Those two extremes demonstrate the wide range of cavity dimensions investigated in this section. Figures 4-21 to 4-24 show the waterfall plots and the 2-D pressure contours of the RMS acoustic pressure for cavities with $L/d=2, d/D=1/12$;

$L/d=6$, $d/D=1/12$; $L/d=1/2$, $d/D=4/12$ and $L/d=3/2$, $d/D=4/12$, respectively. The plots for the rest of the cases are in Appendix A.

The contour plot for the cavity with $L/d=2$ and $d/D=1/12$ shows that the first four diametral modes are excited. Each mode is excited over different velocity ranges by the first and second shear layer modes. The excitation of the diametral modes by the third shear layer mode is rather weak. This behaviour is similar to that of the cavity with $L/d=1$, $d/D=2/12$ (fig. 4-5). In both cases, the flow velocities for frequency coincidence between the diametral modes and the free shear layer modes are similar. This is because the range of flow velocity, or more accurately the range of the Mach number, over which the frequencies coincide depends on the ratio of the cavity length to the pipe diameter (L/D), which is similar in both cases.

The sound pressure level for cavities with $d/D=1/12$ is generally lower than the sound pressure level for cavities with $d/D=2/12$, as can be seen from comparing fig. 4-21 and fig. 4-5. Figure 4-25 shows the dimensionless amplitude of the diametral modes versus the Strouhal number for a cavity with $L/d=2$, $d/D=1/12$. The Strouhal numbers of the first and second free shear layer modes are about 0.44 and 0.88, respectively. This indicates a drop in the convection speed of the free shear layer vortex in comparison to the cavities with $d/D=2/12$. Regarding the pressure amplitude, the maximum dimensionless pressure of the first diametral mode is about 0.1 when it is excited by the first free shear layer mode. This is about twenty times lower than the maximum amplitude for the cavity with $L/d=1$, $d/D=2/12$ (fig.4-9). For the second diametral mode, the dimensionless amplitude decreases by a factor of 4 with the decrease of the cavity depth. Moreover, the decrease in the amplitudes of the third and fourth diametral modes is of the same order as the second diametral mode or less. This indicates that the effect of changing the cavity depth depends on the mode order. This phenomenon is further investigated in sections 4.4.2 and 4.4.3.

The frequencies of diametral modes of the cavity with $d/D=1/12$ are higher than those for the cavity with $d/D=2/12$. For example, the first diametral mode frequencies for the cavities with $L/d=2$, $d/D=1/12$ (fig. 4-21) and $L/d=1$,

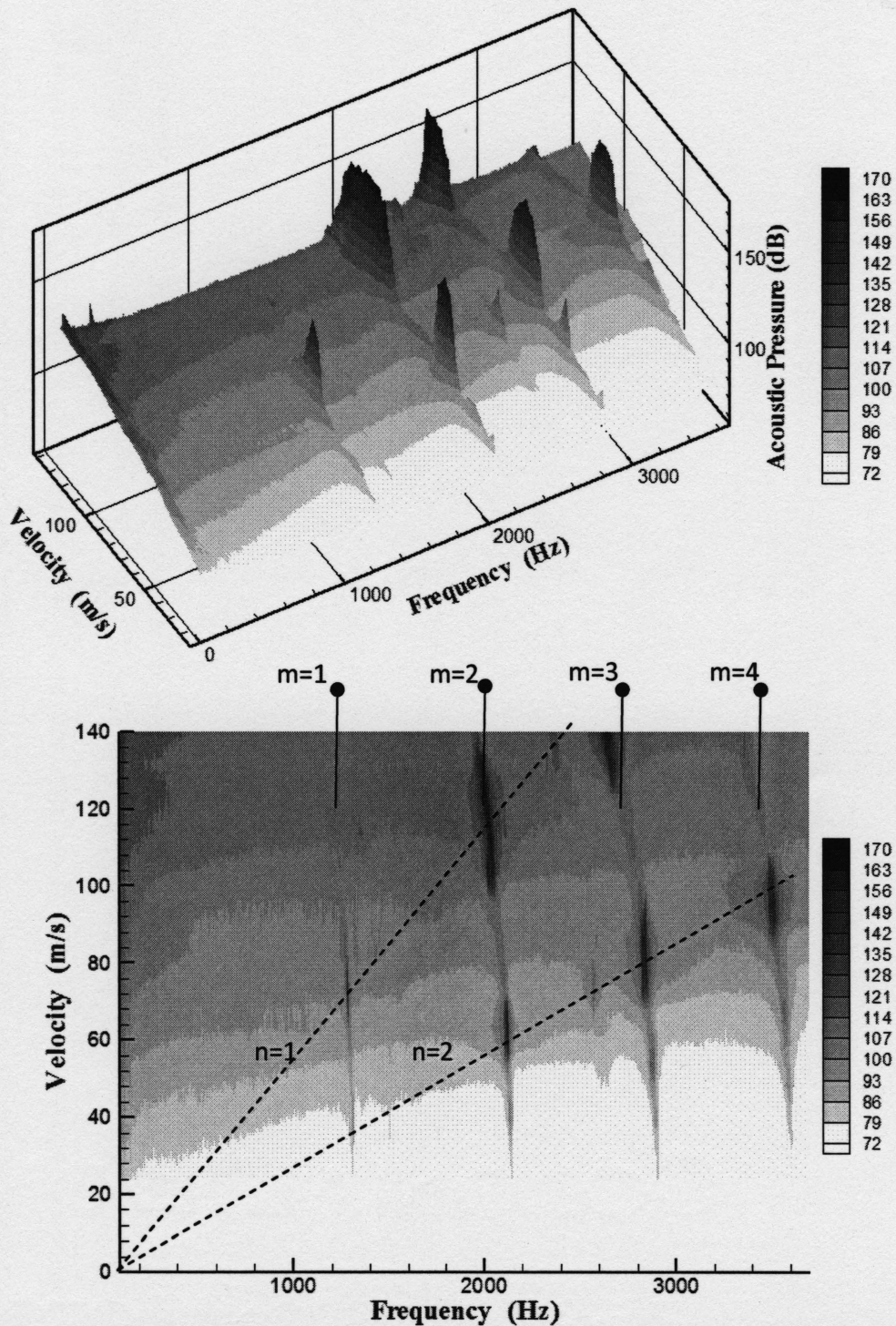


Figure 4-21 Waterfall plot and 2D pressure contours for $L/d=2$, $d/D=1/12$. m is the diametral mode number, n is the free shear layer mode number

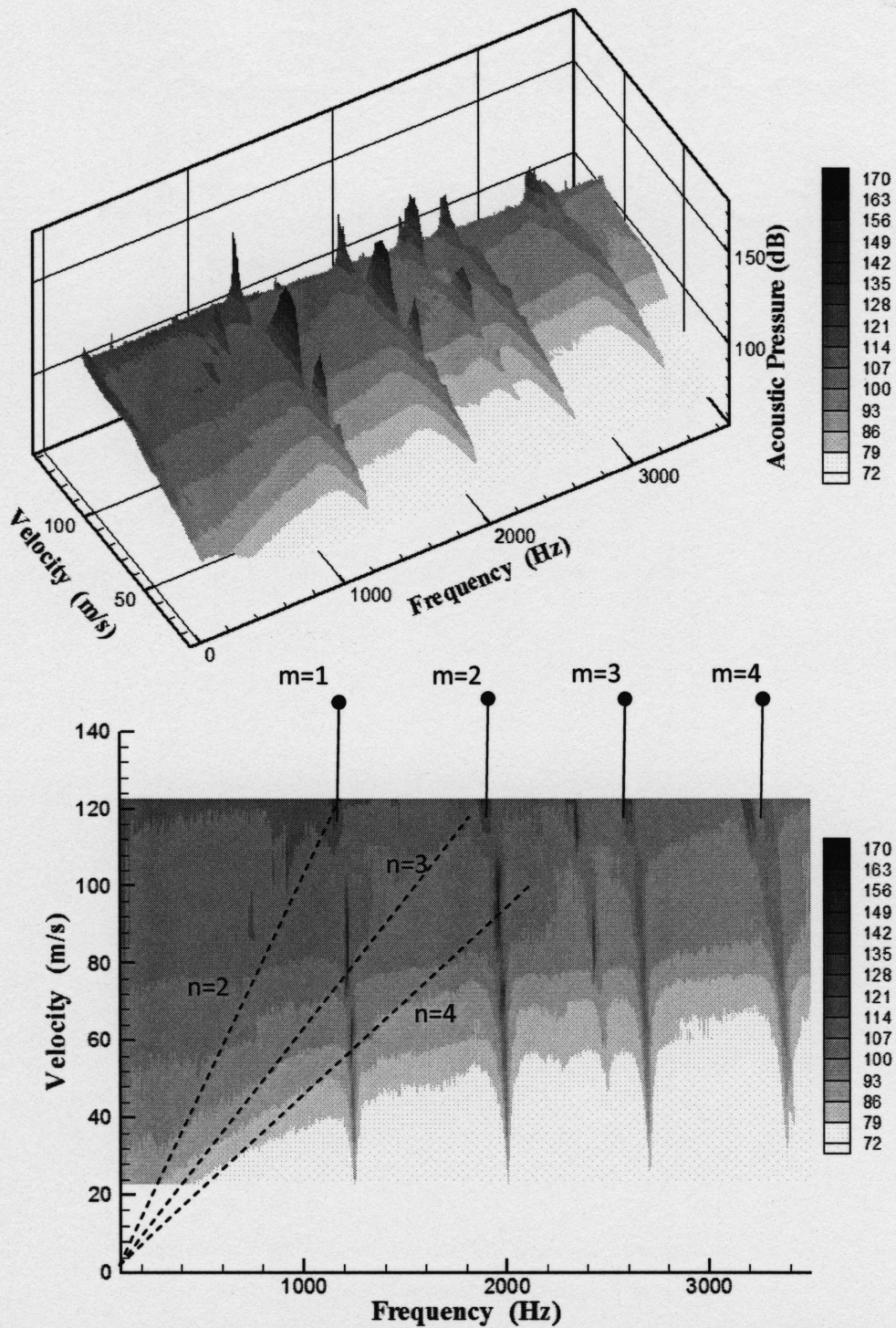


Figure 4-22 Waterfall plot and 2D pressure contours for $L/d=6$, $d/D=1/12$. m is the diametral mode number, n is the free shear layer mode number

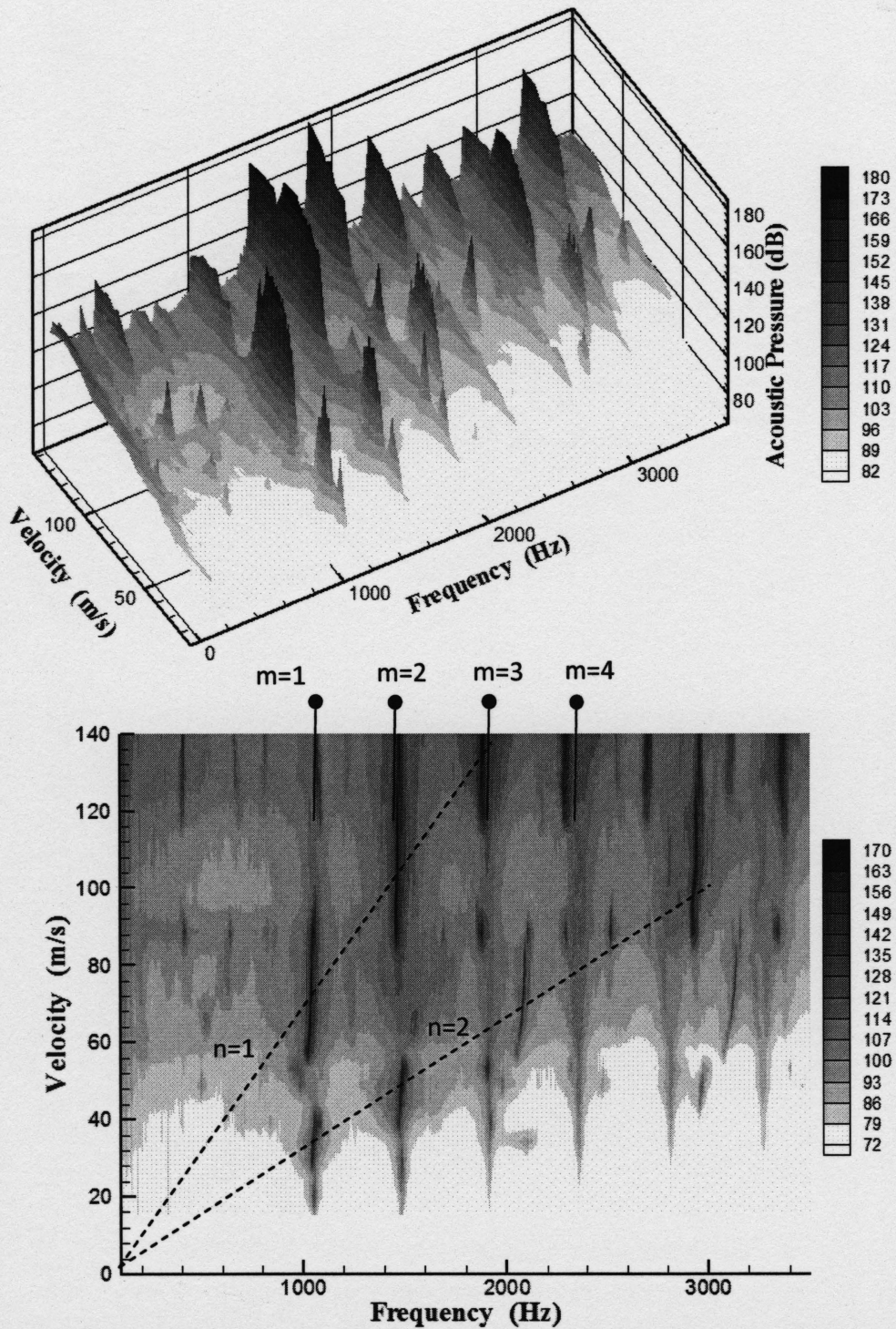


Figure 4-23 Waterfall plot and 2D pressure contours for $L/d=0.5$, $d/D=4/12$. m is the diametral mode number, n is the free shear layer mode number

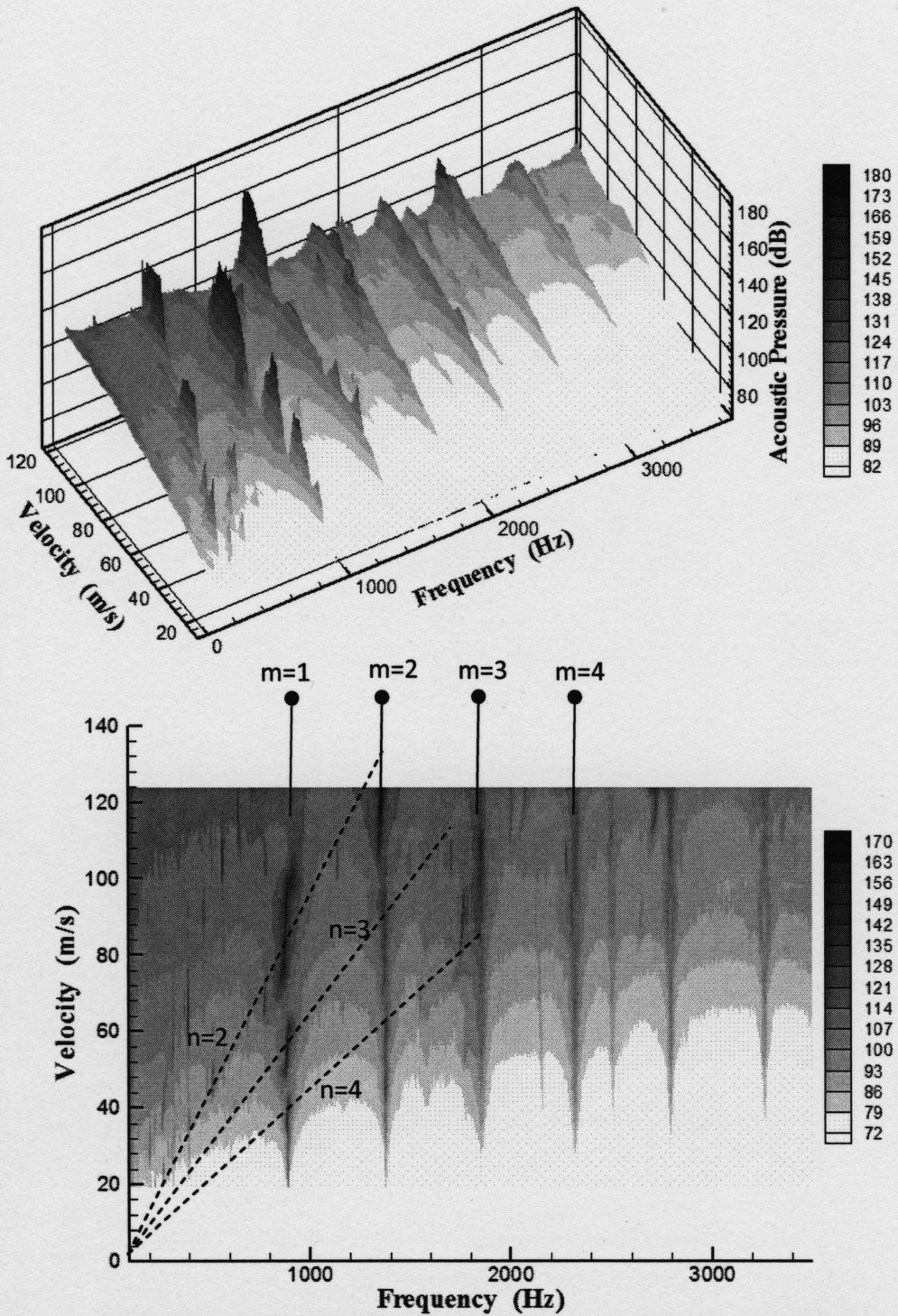


Figure 4-24 Waterfall plot and 2D pressure contours for $L/d=3/2$, $d/D=4/12$. m is the diametral mode number, n is the free shear layer mode number

$d/D=2/12$ (fig. 4-5) at 30m/s are 1312Hz and 1267Hz, respectively. This decrease in the resonance frequency is due to the larger diameter of the cavity floor. When the cavity depth increases, the average pipe diameter increases which causes a decrease in the diametral mode frequency and vice versa.

All the diametral mode frequencies of cases $L/D=2/12$, $d/D=2/12$ (fig. 4-5) and $L/D=2/12$, $d/D=1/12$ (fig. 4-21) decrease with the flow velocity. However, the rate of drop in the second case ($d/D=1/12$) is higher. For example, the drop in the frequency of the second diametral mode at a Mach number of 0.4, from its low flow velocity value, is approximately 4.5% for $L/D=2/12$, $d/D=1/12$, and 8% for $L/D=2/12$, $d/D=2/12$. Moreover, in both cases, the rate of frequency drop appears to increase with the Mach number. In Chapter 6, these effects will be shown to be caused by the mean flow.

Regarding the excitation of longitudinal modes, very weak excitation is noticed for a cavity length of $L/d=6$ (fig.4-22), which is the same length at which the longitudinal modes start to be excited for the case of $d/D=2/12$. The

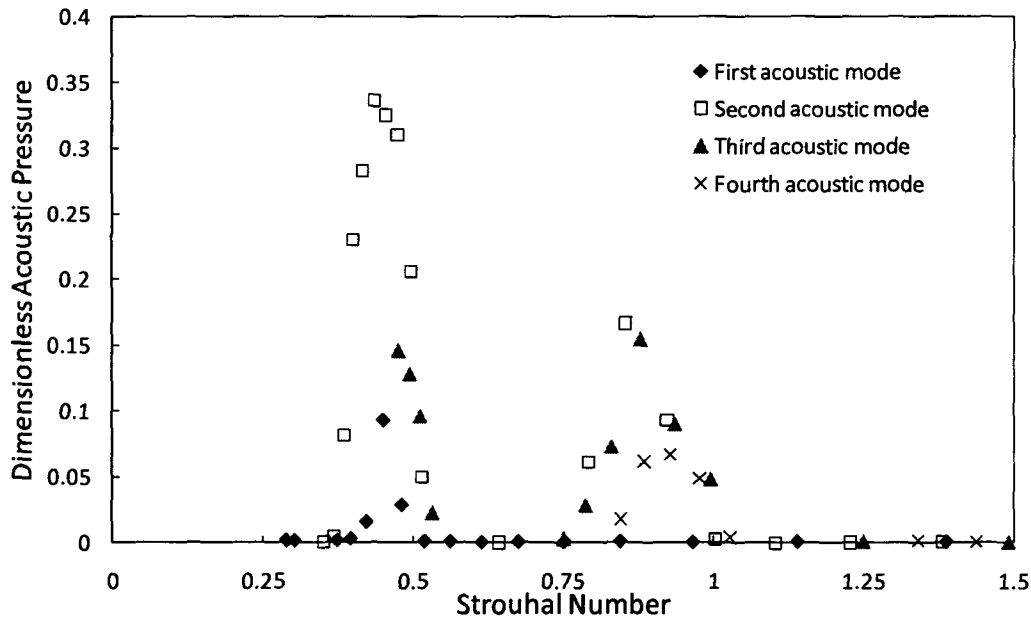


Figure 4-25 Dimensionless pressure as a function of the Strouhal number for $L/d=2$, $d/D=1/12$.

excitation level of longitudinal modes increases slightly with the cavity length, however, it does not dominate the system behaviour as in the case of $d/D=2/12$, as shown in figs. A-8, A-9 & A-10.

For the third studied depth ($d/D=4/12$), all the cases exhibit very high level of acoustic pressure. Figure 4-23 shows the waterfall and the 2-D contour plots for the cavity with $L/d=1/2$, $d/D=4/12$. This case has length to depth ratio of 0.5, which makes it a deep cavity. Though, the system behaviour is very similar to that of the other cavities because, as mentioned earlier, the acoustic response depends on the length to the pipe diameter ratio (L/D). In this case, it can be seen that the first three diametral modes are strongly excited. Also, some of the longitudinal modes are excited. The RMS amplitude of the second diametral resonance mode reaches 25 kPa at a mean flow velocity of 107 m/s. This amplitude is about 40% of the mean static pressure of the system. During the strong excitation of the first and second diametral modes, the system resistance increases substantially such that the rate of increase of the mean flow rate with the blower rotational speed dropped by 35% to 40% of the average rate. A similar reduction is observed for the case of cavity with $L/d=1$, $d/D=4/12$ during the excitation of the first diametral mode near 110m/s, see fig. A-11. These results indicate the significant effect of acoustic resonance on altering the operating conditions of the system.

Figure 4-26 shows the dimensionless amplitude of the acoustic pressure as a function of Strouhal number. The Maximum dimensionless amplitude is about 4.3 and it occurs at a Strouhal number of 0.35, where the first free shear layer mode excites the first diametral mode. The second and third diametral modes reach dimensionless amplitudes of 3.6 and 1, respectively. The Strouhal number of the second free shear layer is about 0.8 with a maximum dimensionless amplitude of 1.25.

Regarding the diametral modes frequencies, they are all lower than those of the case $L/d=1$, $d/D=2/12$, which is a result of the increase in the average diameter of the system. More importantly, the frequencies of the diametral modes do not seem to experience a reduction with the increase of the mean flow velocity, which was observed for shallower cavities, $L/d=2$, $d/D=1/12$ and

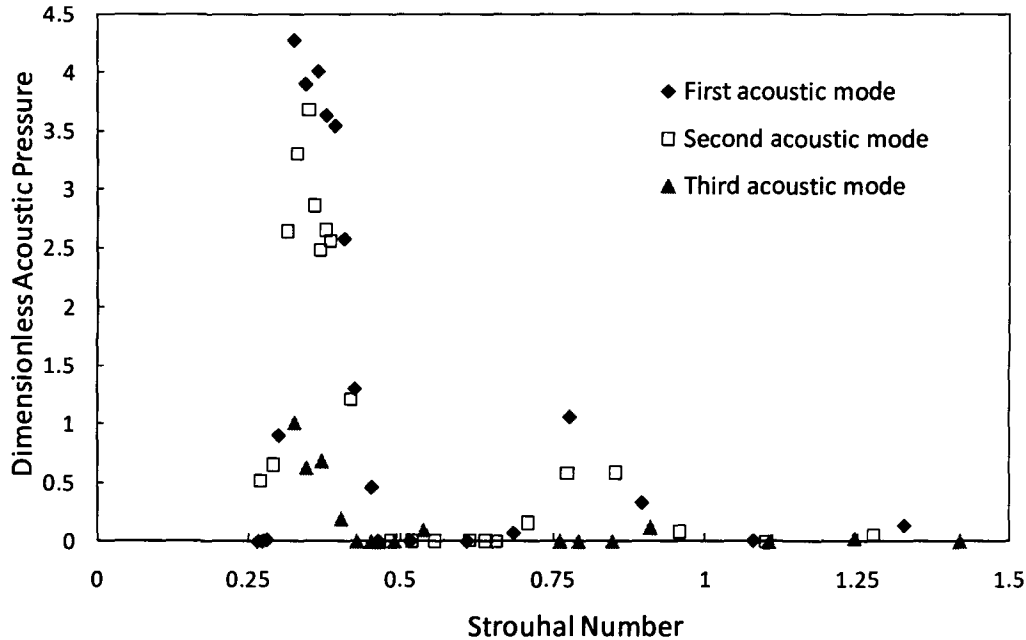


Figure 4-26 Dimensionless pressure as a function of the Strouhal number for $L/d=1/2$, $d/D=4/12$.

$L/d=1$, $d/D=2/12$. Considering all the previous observations, it is evident that the frequencies of the diametral acoustic resonance modes decrease with the mean flow velocity when the cavity size is small. If either the depth or the length of the cavity increases, the rate of the drop in the frequencies is reduced. This phenomenon will be investigated in chapter 7 by means of numerical simulation of the diametral acoustic modes.

All the other five cases with cavity depth equal to 50 mm ($d/D=4/12$) exhibit higher level of excitation compared to similar cases with depth equal to 25 mm ($d/D=2/12$), which is consistent with the discussion in the previous paragraph. Figure 4-24 shows the waterfall and the 2-D contour plots for the cavity with $L/d=3/2$, $d/D=4/12$. Comparing fig. 4-24 and fig. 4-11 shows that the overall behaviour of the 50 mm depth cases is very much similar to the 25 mm depth cases. It is worth mentioning that the high order diametral modes ($m=3$, 4) experience a lower level of amplification compared to the lower order ones ($m=1$, 2). This trend is discussed in detail in section 4.4.4. Regarding the

excitation process of the longitudinal modes, it starts at $L/d=1\frac{1}{2}$ ($L=75\text{mm}$). The amplitude then increases with the increase of the cavity length, as shown in figs. A-12, A-13 & A-14.

To summarize the main points of this discussion, it is evident that the three tested cavity depths are capable of exciting the diametral modes. The amplitude of the acoustic pressure increases with the increase of the cavity depth. Moreover, the increase of the cavity depth decreases the frequency of the diametral modes due to the increase of the cavity-duct system mean diameter. In the next subsections, the effects of cavity length to depth ratio on the Strouhal number, pressure amplitude, mode shape and mode selectively are discussed.

4.4.1. Strouhal number of cavity resonance

Figure 4-27 shows the Strouhal numbers of cavity free shear layer modes for all the studied cases. The general trend is similar to that reported by Rockwell & Naudascher (1978). Generally, the Strouhal number seems to change with the cavity length to depth ratio (L/d), which controls the flow field inside

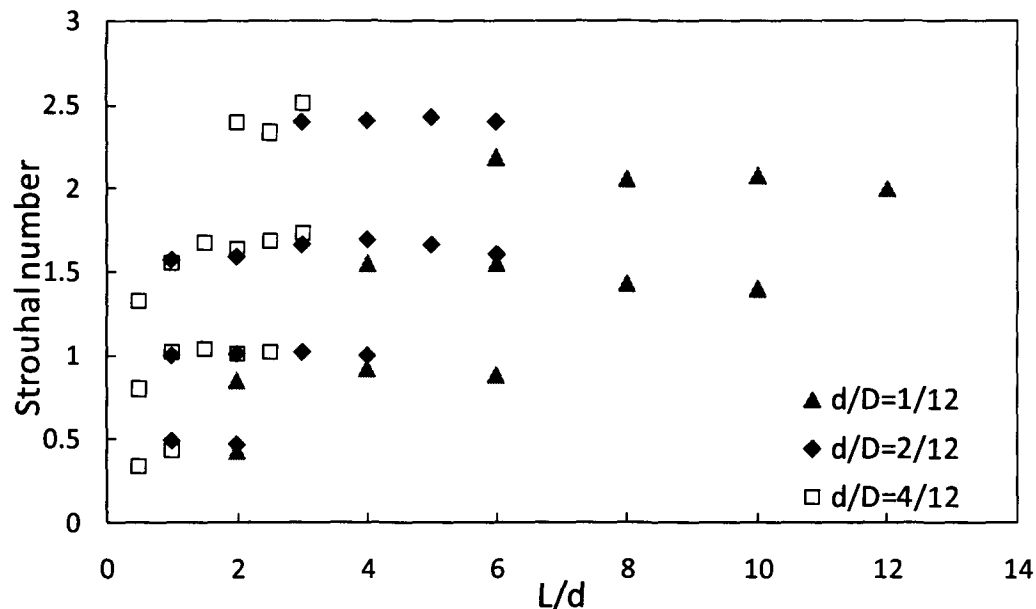


Figure 4-27 Strouhal numbers of cavity free shear layer modes for all tested cases

the cavity. For small L/d , less than two, the Strouhal number increases with the cavity length. However, for L/d greater than four, the Strouhal number seems to slightly decrease with the cavity length.

On the other hand, the cavity depth to pipe diameter ratio does not seem to have a significant effect on the Strouhal number. The data for the three different depths match relatively well. However, the data of $d/D=1/12$ is slightly lower, which could be attributed to the effect of the ratio of the depth to the momentum thickness, which is about 15 at a flow velocity of 70m/s.

4.4.2. Effect of cavity depth on the pressure amplitude

As mentioned earlier, the amplitude of the acoustic pressure is found to be strongly dependent on the cavity depth, or in other words, on the cavity depth to the pipe diameter ratio (d/D). Figure 4-28 shows the maximum dimensionless acoustic pressure of the lowest diametral mode ($m = 1$) when excited by the first shear layer mode (fig. 4-28a) and by the second shear layer mode (fig. 4-28b). The results are given for the three tested cavity depths (d/D), and the cavity length is taken as a parameter. It is evident that the ratio d/D has a strong effect on the excitation level of the diametral acoustic modes.

The maximum dimensionless acoustic pressure achieved for $d/D=4/12$ is an order of magnitude higher than that observed for $d/D=1/12$. The trend shown in fig. 4-28 indicates that a further decrease in the cavity depth may suppress the diametral mode resonance altogether. Based on the available results, this suppression is likely to occur for a cavity depth as small as $d/D<5\%$. This indicates how small the cavity depth should be to alleviate the resonance of the diametral acoustic modes. The trend discussed above seems to be independent of the cavity length or the cavity free shear layer mode. To determine the physical reason behind this trend, the change of mode shape with the cavity depth is investigated in the next subsection.

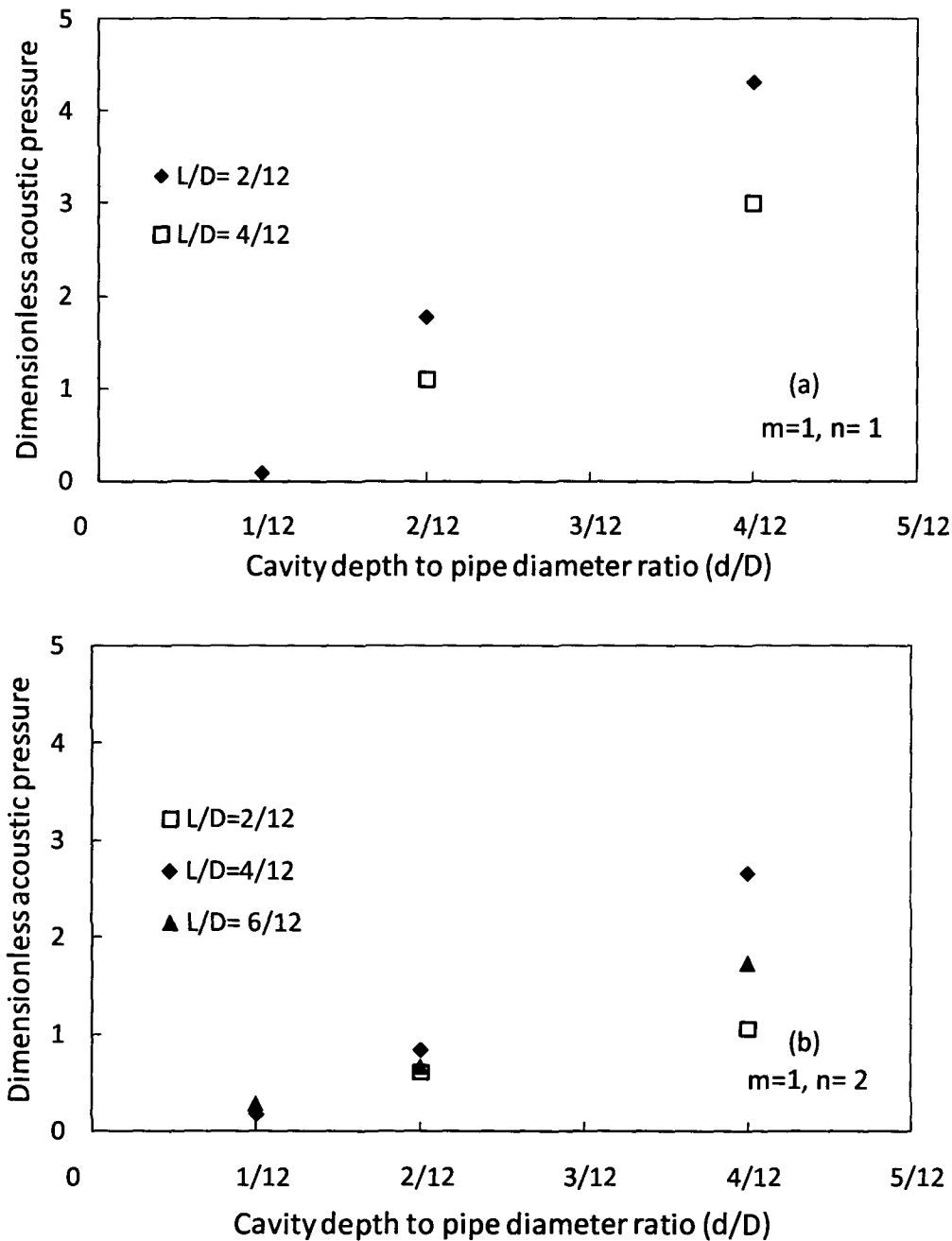


Figure 4-28 Maximum dimensionless acoustic pressure of the first diametral mode for different cavity depths to pipe diameter ratio, (a) excitation by cavity first free shear layer mode ($n=1$); (b) excitation by cavity second free shear layer mode ($n=2$).

4.4.3. Effect of cavity depth on the mode shape

a) Acoustic particle velocity

As mentioned earlier, the radial component of the acoustic particle velocity at the cavity free shear layer is the acoustic parameter that affects the level of acoustic power production. The amplitude of the radial component for different cavity depths is shown in fig. 4-29 for the first three diametral modes. These data were extracted from the simulation of the acoustic modes, as discussed in section 4.3.3 (see fig. 4-19 for example). The presented amplitudes correspond to a maximum acoustic pressure of one Pascal at the centre of the cavity floor.

For all three diametral acoustic modes, it is evident from fig. 4-29 that the amplitude of the radial particle velocity along the cavity mouth increases with the cavity depth. For example, the particle velocity of the first mode for

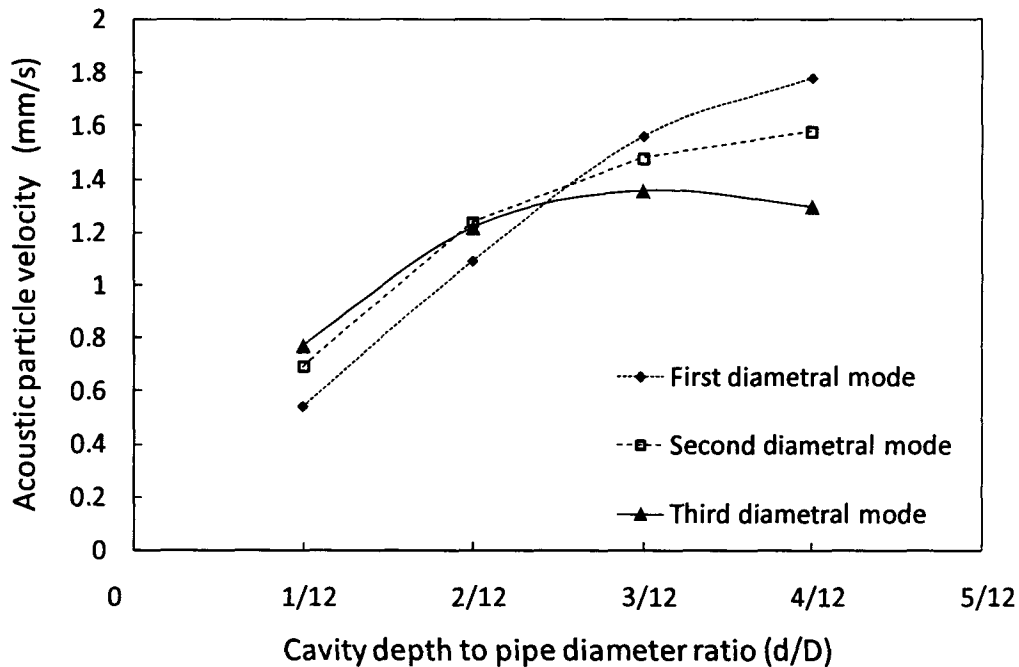


Figure 4-29 Maximum radial acoustic particle velocity for different d/D ratios. The data corresponds to acoustic pressure of one Pascal at the center of the cavity floor ($L/D=2/12$)

$d/D=4/12$ is almost three times higher than that corresponding to $d/D=1/12$. However, this ratio is much smaller than the measured increase in the acoustic pressure level, which is shown in fig. 4-28. This is partially because of the mutual enhancement mechanism between the vorticity-based excitation power and the acoustic particle velocity. Any increase in the vorticity-based sound power enhances the resonant sound field and therefore increases the particle velocity amplitude which, in turn, enhances the vorticity-based sound power. This cycle of events continues until the system reaches a saturation limit due to increased acoustic attenuation.

Referring again to fig. 4-29, the change in the acoustic particle velocity amplitude is not linear with the cavity depth and the rate of change is not the same for different acoustic modes. To clarify these features, the contour plots of the radial component of the particle velocity for the first three diametral modes are depicted in fig. 4-30. The contours are at cross section B-B of fig. 4-19, which is midway along the cavity length. The darkest and brightest areas represent the maximum amplitudes and are out of phase. The plots show that the areas with maximum radial particle velocity become closer to the cavity floor as the diametral mode number increases. Therefore, the order of the diametral mode *which has the highest radial particle velocity* changes with the cavity depth. For example, as can be seen in fig. 4-29, the third diametral mode has the largest value of the radial particle velocity for $d/D=1/12$, while it has the lowest value for $d/D=4/12$. It seems that the maximum value of the radial particle velocity component for the third mode occurs close to $d/D=3/12$.

b) Radiation losses

The level of the acoustic power radiation from the pipe ends depends on the shape of the resonance mode and the pressure amplitude at the pipe terminations. As mentioned earlier, the pressure amplitude of the diametral modes decays exponentially along the main pipe further away from the cavity. The rate of this decay depends on the ratio of the frequency of the diametral mode to the cut off frequency of the main duct. Therefore, since the frequency of the diametral mode is controlled by the cavity dimensions, the cavity dimensions control the rate of the pressure decay and consequently the relative

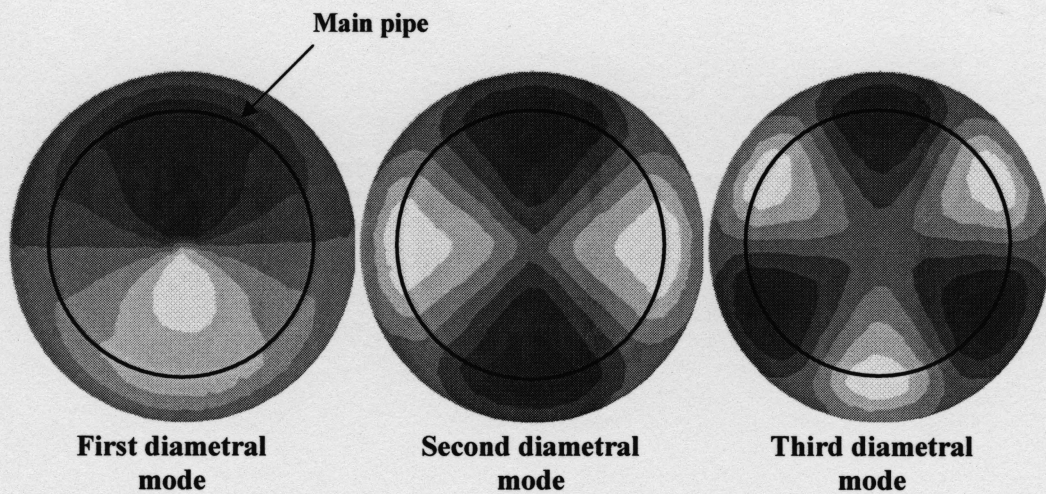


Figure 4-30 Contour plots of the radial particle velocity ($d/D=2/12$, $L/d=1$)

pressure amplitude at the pipe ends in comparison to the pressure amplitude at the cavity floor.

Figure 4-31 shows the pressure decay with axial distance from the cavity center. The decay distributions are obtained from the results of the finite element simulations of the acoustic modes for different cavity dimensions. The acoustic pressure seems to decay faster with the increase of either the cavity depth or length. For the cavity with $L/d=2$, $d/D=1/12$, the pressure amplitude of the first diametral mode at the pipe end is about 20% of the amplitude at the cavity floor, but for the cavity with $L/d=1$, $d/D=2/12$, it is about 2.5% and for the cavity with $L/d=4$, $d/D=1/12$, it is about 7%. This indicates the relative increase in the acoustic radiation losses from the pipe ends as the cavity gets shorter or shallower (i.e. as its size becomes smaller). The figure shows also that the amplitude of the second diametral mode decays much faster than the amplitude of the first diametral mode. Moreover, the rate of decay of the third diametral mode seems to be even higher. These results illustrate the fact that the rate of acoustic power radiation decreases with the increase of the order of the diametral mode.

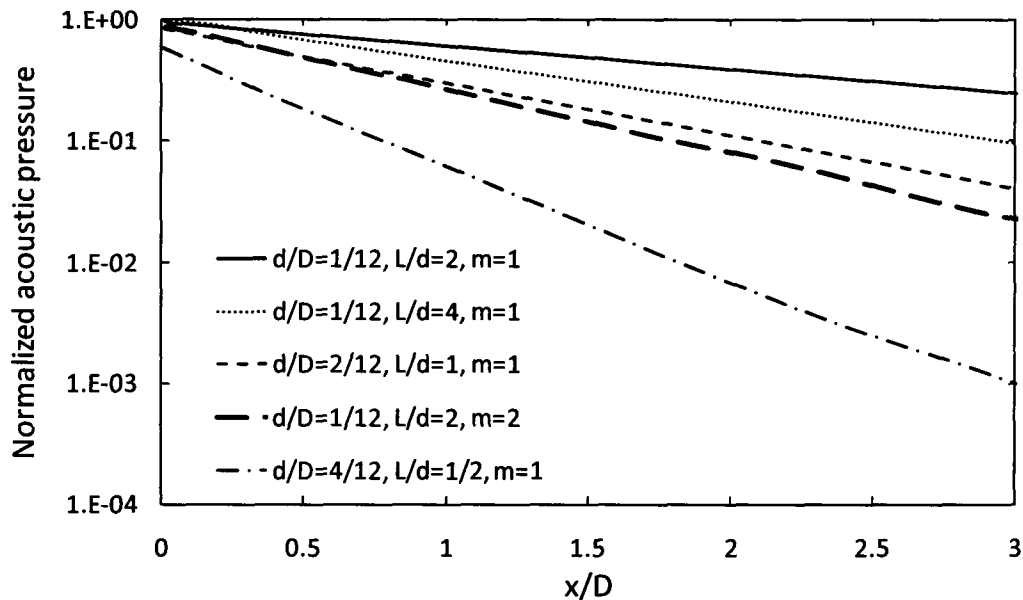


Figure 4-31 Axial distribution of acoustic pressure decay for various cavity dimensions. m is the acoustic mode order. x is measured from the cavity center.

In the next subsection, the above described effects of the cavity depth on the acoustics particle velocity and mode shape and the radiation losses are used to elucidate the phenomenon of mode selectivity for acoustic resonance as the cavity depth is changed.

4.4.4. Mode selectivity

Figures 4-32(a), (b) & (c) show the dominant acoustic modes over the tested flow velocity range for three cavities of equal length ($L/D = 2/12$), but with different depths ($d/D=1/12$, $d/D=2/12$ & $d/D=4/12$), respectively. Figure 4-32(b) shows the same data in fig. 4-7, it is included here to facilitate visual comparison. These figures illustrate the phenomenon of susceptibility of different acoustic modes to excitation by various shear layer modes. They also exemplify the dependence of this phenomenon on the cavity depth ratio. It is noteworthy that all three cavities have the same length to ensure that the coincidence between the frequency of each shear layer mode and a particular acoustic mode occurs at approximately the same velocity. For $d/D=1/12$, the first diametral acoustic mode is not excited except over a very narrow velocity range near 70 m/s. In this case, the higher order acoustic modes seem to be

more liable to excitation. On the other hand, for $d/D=4/12$, the lower order acoustic modes are more liable to excitation. The cavity with $d/D=2/12$ is an intermediate case where all modes are excited. This indicates that for the deeper cavity ($d/D=4/12$), the lower order acoustic modes are more susceptible to acoustic resonance than the higher order modes; and this trend is reversed for the shallower cavity ($d/D=1/12$).

Recalling fig. 4-29, the results of the simulation of the acoustic modes show that in the case of the deepest cavity ($d/D=4/12$), the acoustic particle velocity amplitude at the cavity mouth decreases with the increase of the acoustic mode order. However, for the shallowest cavity ($d/D=1/12$) the trend is reversed such that the particle velocity increases with the increase of the acoustic mode order. It should be recalled here that more acoustic power is produced by the mode with the higher radial particle velocity. Thus, the effect of cavity depth on the acoustic particle velocity partially clarifies the phenomenon of mode selectivity of acoustic resonance and its dependence on the cavity depth. The results also provide new insight into the effect of changes in the diametral mode shapes on the aerodynamic excitation mechanism.

The sharp drop in the resonance amplitude of the first diametral mode for the cavity with $L/D=2/12$, $d/D=1/12$ (fig. 4-28) can also be attributed to the high level of acoustic radiation losses of this mode in comparison with the other modes. The effect of high radiation losses and small acoustic particle velocity add-up to reduce the susceptibility of this mode for self-excitation.

This subsection concludes the investigation of the effect of the ratio of the cavity depth to pipe diameter on the aeroacoustic response. The cavity depth alters the acoustic mode shape strongly, especially at the free shear layer region. The changes in the mode shape lead to variations in the acoustic particle velocity field which affect the process of mode selectivity and the amplitude of acoustic pulsation at resonance. Next section examine the effect of the shear layer hydrodynamic instability on the excitation process.

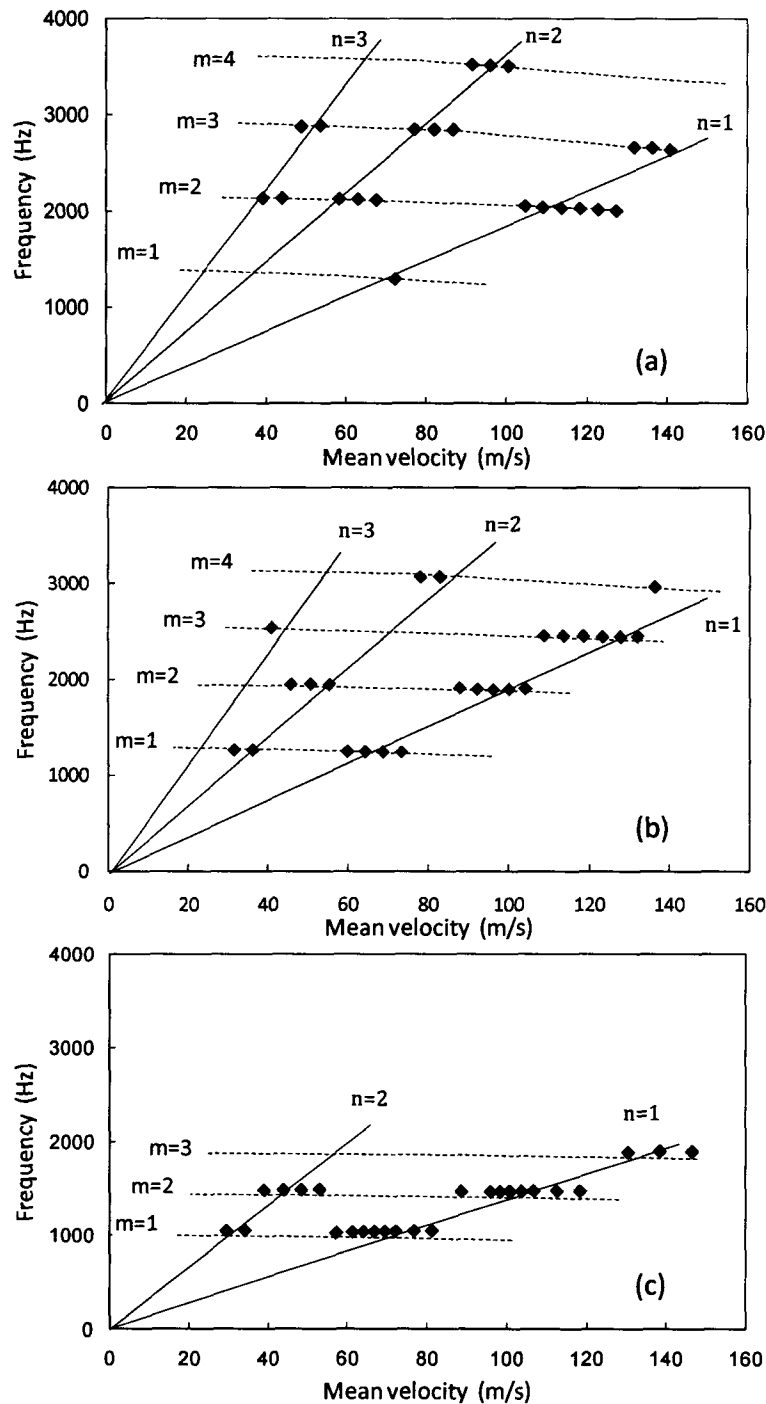


Figure 4-32 Frequency of the dominant diametral acoustic modes a) $d/D=1/12, L/D=2/12$; b) $d/D=2/12, L/D=2/12$; c) $d/D=4/12, L/D=2/12$. (m: the acoustic mode order, n: the free shear layer mode number)

4.5. Effect of the shear layer hydrodynamic instability

The maximum dimensionless amplitudes of the first diametral mode response to the excitation by different free shear layer modes are plotted in fig. 4-33 against the Strouhal number, which is based on the momentum thickness of the boundary layer at the separation edge of the cavity. The momentum thickness at different mean flow velocities is calculated by curve fitting the measured values listed in table 4-1. The data in fig. 4-33 correspond to cavities with $d/D=2/12$ and $L/d=1$ to 6. Similar trends are found for the other tested cavities. The data show that the amplitude of the dimensionless acoustic pressure increases as the Strouhal number approaches 0.02. From the literature, the maximum amplification rate of disturbance in the shear layer occurs at a Strouhal number of 0.017 for laminar flow. For the turbulent flows, this value, as reported by Hussain & Zaman (1981), is slightly higher (0.022 to 0.024). The two data points with Strouhal number above this range show that the amplitude is decreasing with further increases in the Strouhal number. Although the available data are not sufficient to determine the Strouhal number at the

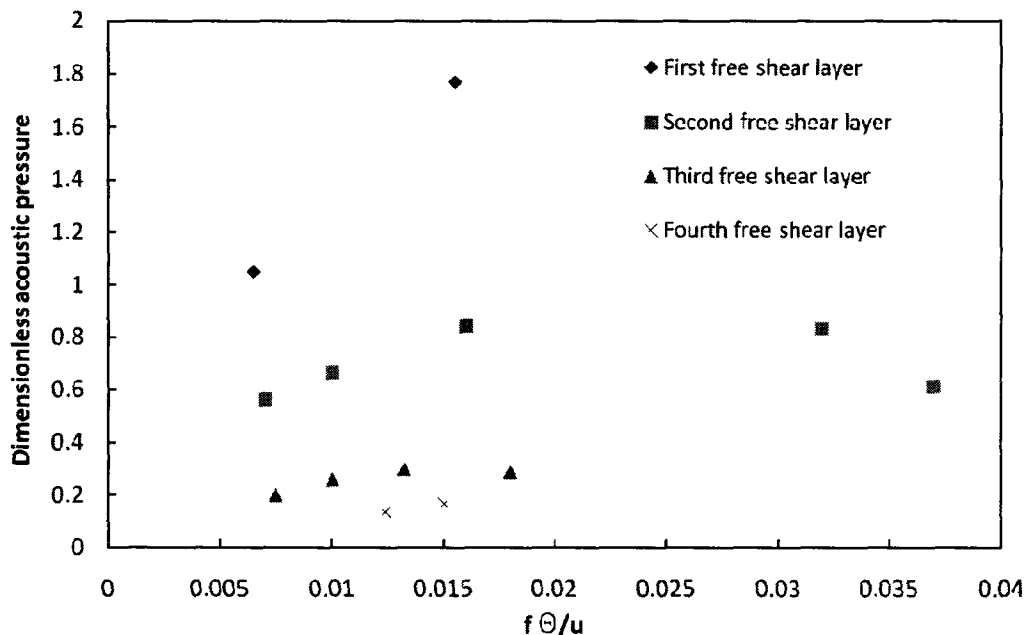


Figure 4-33 Dimensionless acoustic pressure with the Strouhal number based on the separation momentum thickness. The data are for cavities with $d/D=2/12$, $L/d=1$ to 6. All the data points correspond to the first reonance mode.

maximum dimensionless acoustic pressure, the measured values suggest strongly that the shear layer instability, and not the jet column instability, is the source exciting the diametral modes.

4.6. Summary

The self-excitation of acoustic diametral modes of a cavity-duct system by flow oscillation over the cavity mouth has been investigated experimentally. The test results have revealed, for the first time, the details of the aeroacoustic response of the diametral modes to flow excitation up to a Mach number of 0.4. The investigation has also clarified the effects of the cavity length to depth ratio (L/d), the cavity length to pipe diameter ratio (L/D) and the cavity depth to pipe diameter ratio (d/D) on the aeroacoustic response. The main findings are summarized in the following:

1. The axisymmetric cavity can excite strongly the acoustic diametral modes although these acoustic modes do not have a preferred orientation. In addition, the excitation is self-sustainable for Mach numbers higher than 0.09.
2. The general aeroacoustic response depends on the dimensions of the cavity (L and d) relative to the main pipe diameter (D).
3. The dimensionless pressure amplitude decreases with the cavity length to pipe diameter ratio (L/D). This decrease seems to be related to the increase in the Mach number at resonance when the cavity is made longer.
4. The Strouhal number of the fluid-resonance mechanism depends on the cavity length to depth ratio. On the other hand, the Mach number and the acoustic mode order have no effect on the Strouhal number.
5. The cavity depth to pipe diameter ratio (d/D) alters the acoustic mode shape strongly, especially at the free shear layer region. The changes in the mode shape and acoustic radiation losses lead to an increase in the acoustic pressure as the ratio d/D is increased. Also, the cavity depth to pipe diameter ratio determines the most susceptible acoustic mode for aerodynamic excitation.

6. As the cavity becomes shallower, the acoustic resonance of the diametral modes becomes weaker. The test results suggest that the diametral modes will not be excited for cavity depth smaller than 5% of the pipe diameter (i.e. $d/D \leq 5\%$).
7. The longitudinal modes are excited for relatively long cavity ($L/D > 1/2$). The excitation level of these modes increases with the increase of the cavity length.
8. The frequencies of the diametral modes decrease with the increase of the Mach number. This decrease is more noticeable when the cavity size is small. For cavity with $d/D \geq 4/12$, this phenomenon has not been observed.

CHAPTER 5

DIAMETRAL MODES

AZIMUTHAL BEHAVIOUR

The purpose of this chapter is to characterize the azimuthal behaviour of the diametral modes. The excitation of the diametral acoustic modes, which are asymmetric modes, by the cavity axisymmetric free shear layer produces a peculiar condition in which the diametral mode has no preferable orientation. Therefore, the acoustic mode can have a stationary orientation or it can be spinning. The interaction between the shear layer and acoustic mode depends on which of those two scenarios is dominant. Thus, to devise suppression techniques, it is important to determine the characteristics of the azimuthal behaviour and the dependency of the excitation process on this behaviour.

The results of the first test section design, described in chapter 3, show that the excited diametral mode were neither stationary nor spinning. This appeared to be caused by slight deviations from perfect axisymmetry. To verify this explanation, the second test section was designed and manufactured to have much more precise dimensions and far more robust structure. The results of both designs are compared to indicate the differences in the azimuthal behaviour.

As described earlier in chapter 3, the test section was instrumented with multiple pressure transducers to measure simultaneously the pressure oscillation at different orientations at the cavity floor. The measurements were performed for all cavity dimensions listed in table 3.1. The time signals of the pressure transducers are investigated considering different approaches. In section 5.1, the time average pressure amplitudes and phase differences are analysed. In section 5.2, the instantaneous relative phase between the pressure signals is presented to clarify how the orientation of the acoustic modes changes with time. Based on this analysis, an analytical model is proposed in section 5.3 to characterize the different azimuthal behaviours observed in the experiments. The interaction between the shear layer and acoustic mode is investigated using the pressure transducers and a set of two hotwire probes inserted in the free shear layer, as presented in section 5.4. The effect of introducing geometrical preference of orientation on the interaction between the shear layer and the acoustic modes is also presented in section 5.4.

5.1. Analysis of the time average phase data

In this section, the time average phase data of selected cases is presented. The selected cases represent the different behaviour observed during the experiment. The phase is actually the relative phase between the pressure signals of different pressure transducers. For this purpose, one of the pressure signals was assigned to be the reference signal, and the phase of the other pressure signals were determined relative to it. Fast Fourier transformation is used to extract the phase data of the time signal. The sampling parameters and procedure are described in section 4.2.

Ideally, for the stationary mode, the relative phase between any two pressure transducers should be either zero or 180° . This depends, respectively, on whether they are on the same side of the diametral nodal line or not. Also, because the mode amplitude is modulated over the circumference following sine-function distribution, the amplitude ratios between different pressure transducer should represent their relative location with respect to the principal orientation of the acoustic mode. On the other hand, for spinning modes, the phase should be equal to the physical enclosed angle between the transducers

multiplied by the order of the diametral acoustic mode; and all the transducers should measure the same pressure amplitude. These scenarios are compared to the measured data of the first and second test section designs in the following two subsections.

5.1.1. Results of the first test section design

Table 5-1 shows selected examples of the amplitude ratio and the phase difference between the pressure transducers. The data corresponds to different cavity lengths. The presented relative phase and amplitude ratio are between two pressure transducers with physical enclosed-angle of 45° between them. Also, the data points were chosen to correspond to the mean flow velocity where the pressure amplitude peaks over each of the selected lock-on ranges (see fig. 4-7).

The data show that the ideal stationary or spinning scenarios were not observed. But, further scrutinizing the data suggests that the modes transform from a state like stationary to almost a spinning state as the flow velocity increases. However, it is notable that inconsistency always exists between the simultaneously measured phase differences. For example, in the case with $L/d = 1$ & $U = 65$ m/s, the listed value in the table for the phase difference is 27.3° ; however, the phase difference between the two other pressure transducers, with 45° angle between them, is only 14° . With such inconsistency, it is rather difficult not only to determine the spinning behaviour of the acoustic diametral mode but also to identify the resonant mode shape.

The level of discrepancy in the data is observed to decrease with the increase of the flow velocity. Part of this can be attributed to the averaging process, during which, even if the mode is stationary, the mode principal orientation can change. This will change the relative positions of the pressure transducers with respect to the diametral nodal line. The phase data show also progressively increasing level of discrepancy as the cavity length increases. This is accompanied with a drop in the coherence level between different pressure signals. In summary, the amplitude and phase distributions obtained from the first test section design highlighted the complexity of the investigated

phenomenon and indicated the need to test a more robust and accurate axisymmetric cavity.

Table 5-1 Phase difference and pressure amplitude ratios for different experimental cases of the first test section design ($d/D=2/12$)

L/d	Diametral mode	Shear layer mode	Velocity (m/s)	Δ Phase ($^{\circ}$)	Amplitude ratio
1	1	1	65	27.3	0.58
1	2	1	96	93	0.71
1	3	1	122	134.5	0.97
2	1	2	58	15	0.2
2	2	2	89	75.5	0.65
2	1	1	123	42.6	0.78
3	1	3	80	28	0.71
3	2	3	123	87	0.53
4	1	3	114	24	0.62

5.1.2. Results of the second test section design

The effect of stiffening the cavity structure and improving the accuracy of the test section dimension can be observed from comparing the data in table 5-1 and table 5-2. The latter shows selected examples of the data obtained with the second test section design. The amplitude ratios and the phase differences between the pressure transducers are for the same cases listed in table 5-1 to facilitate the comparison. The cavity depth for all the cases is 25mm ($d/D=2/12$). The comparison between the two tables shows that the amplitude ratios for all the cases of the second test section design are closer to unity than the first test section design cases. However, the phase-data do not indicate perfect spinning behaviour for all cases. This observation is not just for the data listed in the table but for the whole tested velocity range. Even for very weak excitation cases, when the coherence between different pressure transducers is low, the amplitude ratio is close to one. This indicates that, even when the acoustic diametral mode is not spinning, the mode changes its orientation

randomly which results in constant amplitude over the cavity circumference when a long time average is considered.

Table 5-2 Phase difference and pressure amplitude ratios for different experimental cases of the second test section design ($d/D=2/12$)

L/d	Diametral Acoustic mode	Shear layer mode	Velocity (m/s)	Δ Phase ($^{\circ}$)	Amplitude ratio
1	1	1	64	30	0.85
1	2	1	100	90	1
1	3	1	128	133	1
2	1	2	59	22	.87
2	2	2	90	90	1
2	1	1	123	37	0.97
3	1	3	85	44	1
3	2	3	125	91	0.9
4	1	3	111	37	1
5	1	4	82	19	1
6	1	4	103	34	1

To conclude, the data of table 5-2 show that improving the design of the test section leads to increased dominance of the spinning behaviour. This seems to be the case although the precision of the dimensions of the first test section is of the order of 0.2 mm. This indicates that a small deviation from axisymmetry can provide preference to the mode orientation, especially for the low velocity range. The data provide solid evidence that the diametral mode azimuthal behaviour does not follow perfectly the ideally stationary or spinning scenarios. Further analysis is needed to better understand the observed azimuthal behaviour of the diametral modes.

5.2. Analysis of the time signal

Scrutiny of the time signals of pressure transducers (PT) and analyzing the instantaneous phase difference between them provided new insights into the nature of the diametral modes. Figure 5-1 shows the time signals of the three

pressure transducers for two cases correspond to the first row (fig. 5-1(a)) and the six row (fig. 5-1(b)) of table 5-1. In the first case, the three acoustic pressure signals have different amplitudes. This seems to support the aforementioned conclusion that this acoustic mode is, to an extent, stationary. However, it is not clear why the strong amplitude modulation observed at PT2 is much weaker in the other pressure signals measured at PT0 & PT1. This case was analyzed further by extracting the instantaneous phase differences between the various pressure transducers, as shown in fig. 5-2. The results illustrate that the phase difference is changing with time. Moreover, the phase difference between PT1 and PT2 is systematically larger than that between PT0 and PT1. This indicates that: first, the distribution of acoustic pressure phase over the cavity perimeter is not uniform; and secondly the diametral mode is not totally stationary.

Similar analysis has been performed for the second case. As can be seen in fig. 5-1(b), the acoustic pressure amplitudes of the three pressure transducers are virtually constant and equal. In addition, the instantaneous phase difference between neighbouring transducers is found to be constant over time and equal to 45° . Thus, this case represents a spinning acoustic mode, which agrees with the conclusion drawn from the time average phase data. Based on the above results, it can be concluded that the diametral modes always involve a spinning portion. This spinning portion is rather weak at low flow velocities, but gains strength with increasing flow velocity until the diametral mode transforms into a pure spinning mode.

5.2.1. Visual representation

To better understand the instantaneous azimuthal behaviour, a visualization technique of the time data is considered. The visualization is used to clarify how the diametral mode orientation changes over one cycle. The technique takes advantage of the fact that the acoustic pressure has sinusoidal azimuthal distribution at any instant. Therefore, a cosine function can be used to represent the azimuthal pressure distribution as follow:

$$p_a(\theta, t) = A(t) * \cos(\theta - \varphi(t)) \quad 5-1$$

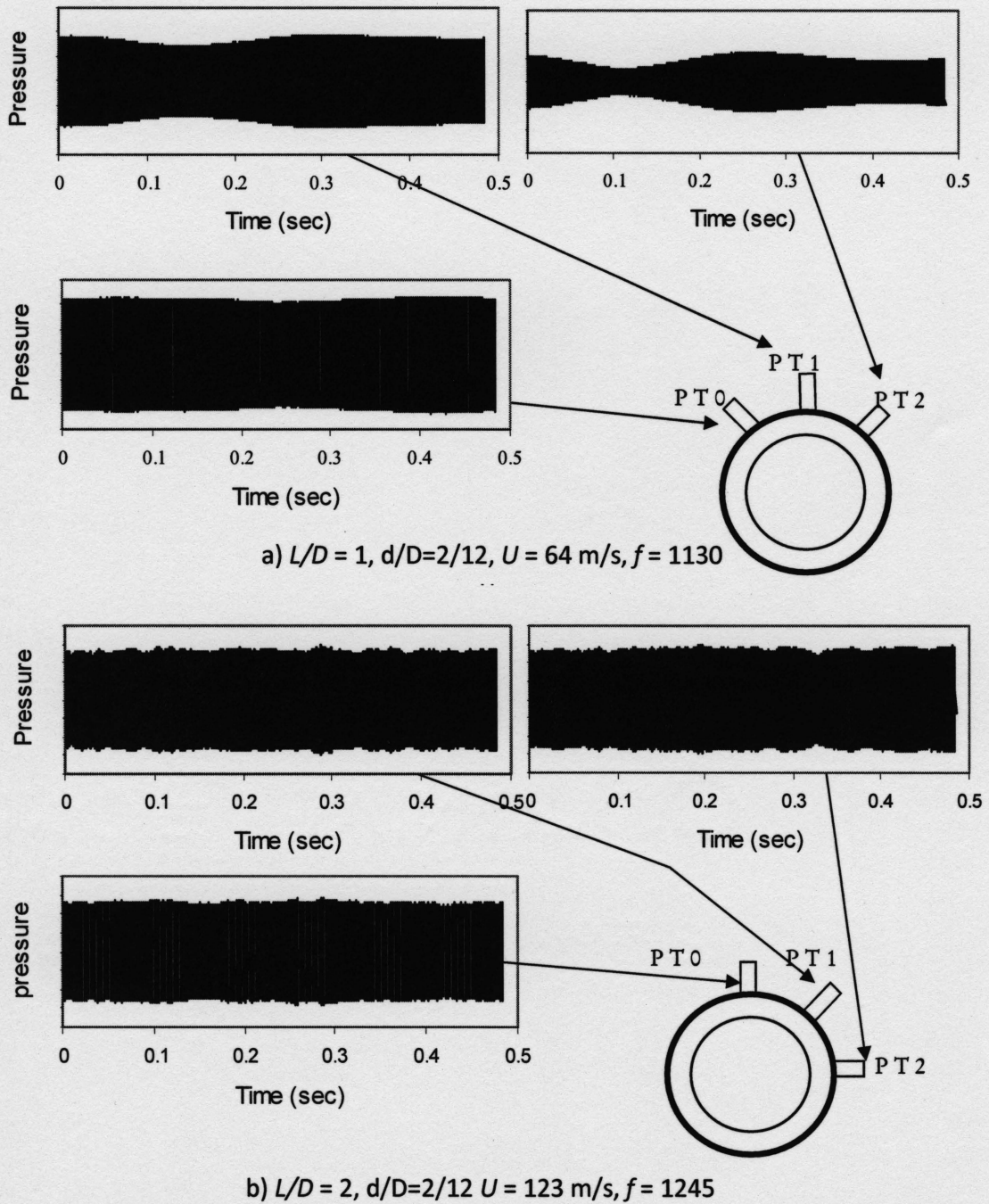


Figure 5-1 Typical time signals of different pressure transducers during the resonance of the first diametral acoustic mode. First test section set-up.

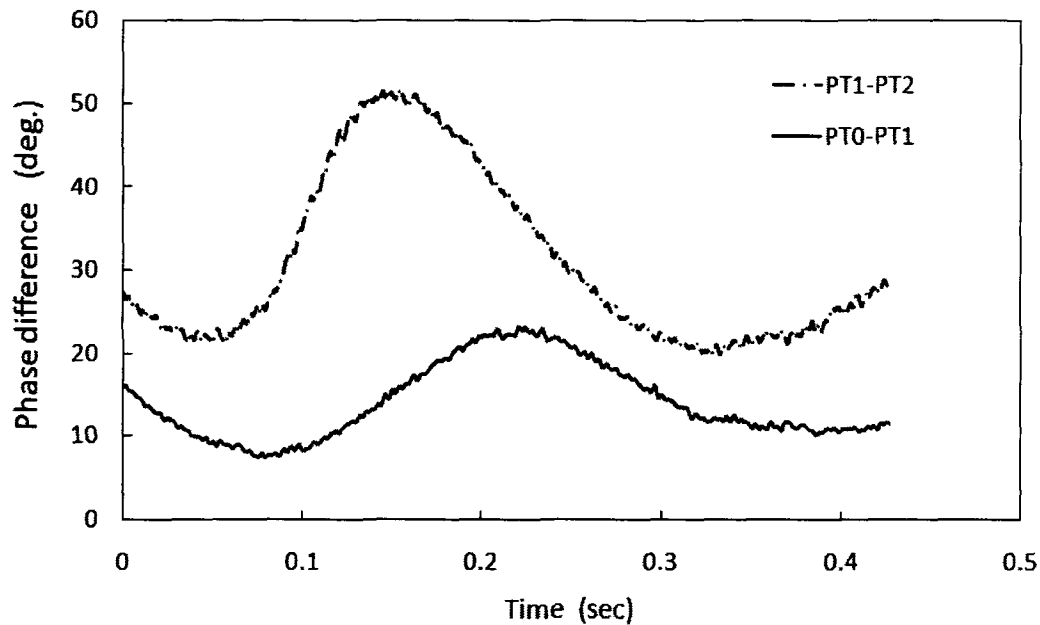


Figure 5-2 The time change of the phase difference between pressure transducers. For $L/d = 1$, $d/D=2/12$ & $U= 64$ m/s

where $p_a(\theta, t)$ is the acoustic pressure as a function of the time and orientation, $A(t)$ the maximum pressure over the cavity perimeter, θ the angle relative to PT0 and $\varphi(t)$ the orientation of pressure maximum amplitude relative to PT0. Figure 5-3 shows a schematic illustrating the different parameters. Two equations are obtained by substituting $p(\theta, t)$ with the time signal of two pressure transducers and θ with the corresponding physical angle. The two equations are then solved simultaneously to obtain $A(t)$ and $\varphi(t)$ as function of time. To examine the reliability of the approach, different combinations of the pressure transducers were considered. Comparisons between the results of different combinations showed good agreement. The average difference in $A(t)$ amplitude from different combinations is about 10% of the mean, and the average difference in $\varphi(t)$ is 12° .

Figure 5-4 shows 8 snapshots of the azimuthal pressure distribution taken along half acoustic cycle for the case $L/d=1$, $d/D=2/12$ & $U=64$ m/s (first test section design). The 8 snapshots are equally spaced equal time. The snapshots show that the maximum amplitude over the cycle occurs around a

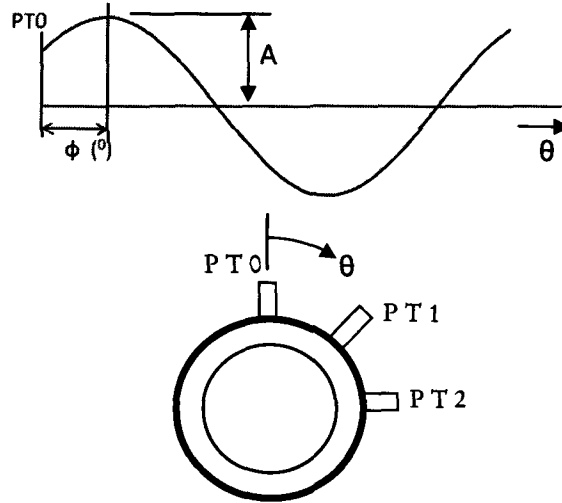


Figure 5-3 Schematic illustration of the parameters of the visual representation technique

fixed orientation. *For the rest of the discussion, the orientation of the maximum amplitude is designated as the principal orientation.* On the other hand, the instantaneous orientation, $\varphi(t)$, is changing over the cycle resembling spinning behaviour. As the mode turns away from the principal orientation, the amplitude fades out to reach a minimum at 90° away from the principle orientation. Also, the spinning speed (rate of orientation change) depends on $\varphi(t)$. It has a minimum at the principle orientation and increases to reach a maximum at 90° from the principle orientation. This behaviour is found to be persistent with the time. However, the principal orientation and the ratio of the minimum amplitude to maximum amplitude change with the time. Referring back to fig. 5-1(a), a change in the orientation is detected in the time period during which the pressure transducer (PT2) experienced neck like decrease in the amplitude.

The same analysis were conducted for the case $L/d=2$, $d/D=2/12$, & $U=123$ m/s. The results show that the mode in this case is spinning with relatively constant amplitude in all directions. However, the amplitude is still lower at one direction than the other. The visualization technique was applied to other cases as well. In all the cases that can be described as stationary, a similar

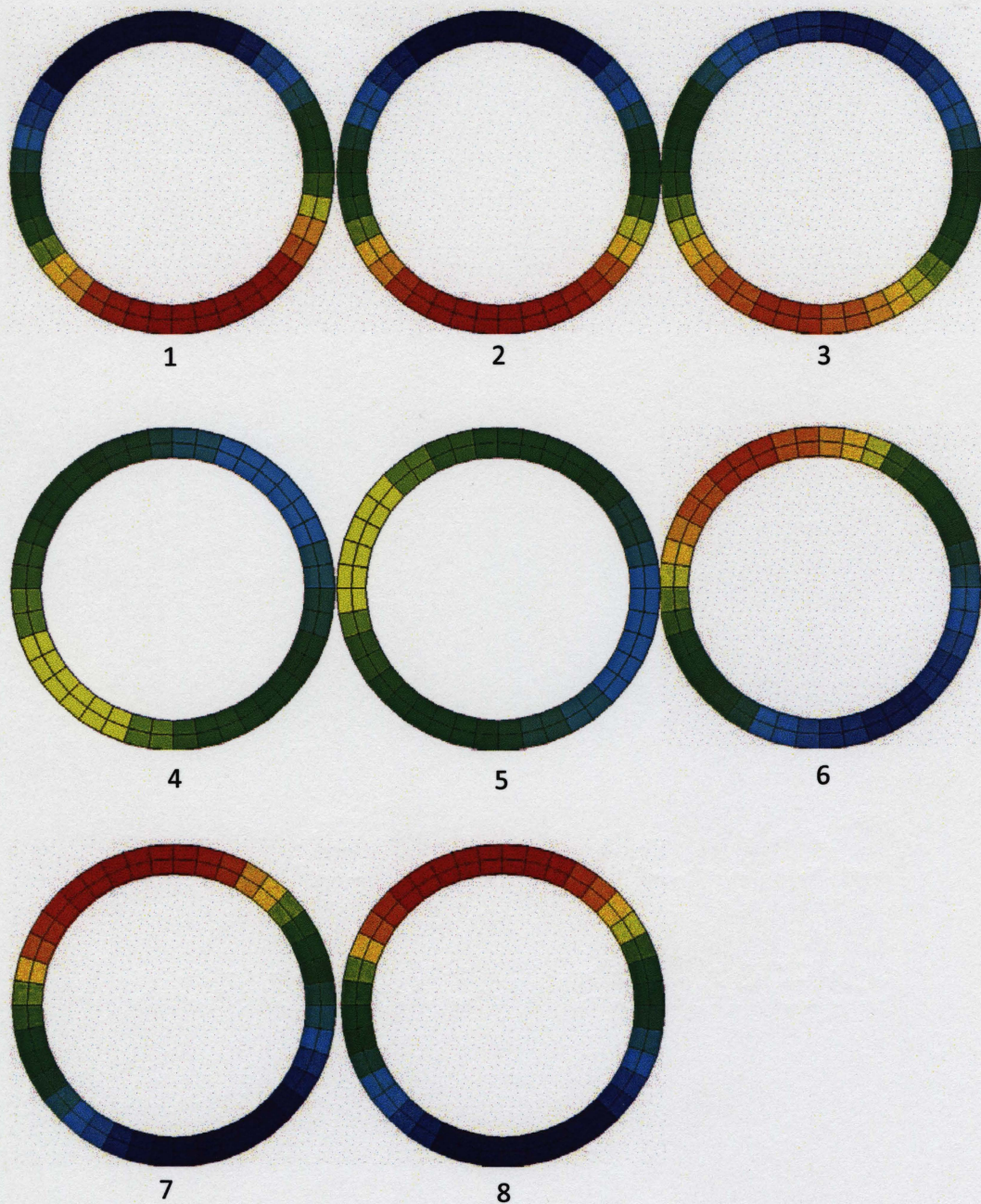


Figure 5-4 Snap shots of the instantaneous pressure distribution at the cavity floor. The snap shots are equally spaced over half a cycle. The red and blue contours are out of phase ($L/d=1$, $d/D=2/12$ & $U=64\text{m/s}$)

behaviour to the one described in the previous paragraph was always noticed. This indicates that, in most cases, the diametral mode is neither stationary nor spinning but rather experiences what can be described as partially spinning. In the next section, a model is developed to describe analytically and quantify this phenomenon.

5.3. Two orthogonal modes model

In the previous section, different analyses were performed to explore azimuthal behaviour. However, none of the presented analyses could provide an adequate clarification of the nature of the excited acoustics modes. In this section, an analytical model is developed to explain the main azimuthal features observed during the experiments.

Generally, a stationary mode at certain orientation can be presented by the superposition of two spatially orthogonal modes. This resembles the conversion of cylindrical coordinates (amplitude and orientation) to Cartesian coordinates (two amplitudes at pre-specified orientations). This concept is extended to present spinning and partially spinning modes by altering the temporal phase shift between the two modes. The following subsection details the mathematical formulation of the model. A parametric study to determine the best method to quantify the azimuthal behaviour is discussed in subsection 5.3.2. Subsections 5.3.3 & 5.3.4 present the characteristics of the partially spinning modes and the application of the model to quantify the experimental data, respectively.

5.3.1. Mathematical formulation

The analytical model consists of superimposing the velocity potential functions of two perpendicular diametral modes. For simplicity, the study is conducted in 2-D circular plane representing the center plane of the cavity. Also, the analysis is limited to the first diameter mode, but it can be easily extended to higher order modes. A general formula for the velocity potential function of an ideal mode at zero flow velocity is given by (Blevins, 1979):

$$\Phi_v = A \frac{c^2}{\omega} \tilde{\varphi} \sin(\omega t + \psi) \quad 5-2$$

where, A is a dimensionless constant which specifies the pressure amplitude, c is speed of Sound, t is time, $\tilde{\varphi} = \tilde{\varphi}(x,y,z)$ is mode shape of the potential function, ω is angular frequency of the acoustic mode, and ψ is the time phase angle. For the first diametral mode, $\tilde{\varphi}$ is given by the following formula (Blevins, 1979):

$$\tilde{\varphi} = J_1(1.841 \frac{r}{R}) \sin(\theta) \quad 5-3$$

where, J_1 is Bessel function of first kind and first order, r is radius coordinate, θ is physical angle, and R is the outer radius.

5.3.2. Parametric study

The first parameter that was tested is the effect of two modes relative amplitude. The temporal phase shift between the two modes is set to zero. Figure 5-5 shows the contour plot of the amplitude of the resultant mode for three different amplitude ratios. The amplitude B was kept constant in all cases. The resultant modes are stationary. The orientation of the modes from the vertical axis, θ , as shown in fig. 5-5, depends on the amplitude ratio, A/B , where $\theta = \tan^{-1}(B/A)$. The amplitude of the resultant mode is $\sqrt{A^2 + B^2}$. The results of the model illustrate that the combination of a number of diametral modes *with no temporal phase shift* is a stationary mode with an equivalent amplitude and orientation. Moreover, it illustrates that two orthogonal diametral modes can be used to represent modes at any orientations.

A second set of runs were performed to explore the effect of changing the temporal phase shift. In these runs, the amplitude ratio is set to one whilst the time phase between them is changed. Figure 5-6 shows snap shots of the pressure contours, over one cycle, for the case with amplitude ratio of one and time phase difference of 90° . The resultant mode is spinning with constant amplitude at all the orientations. This indicates that a spinning diametral mode

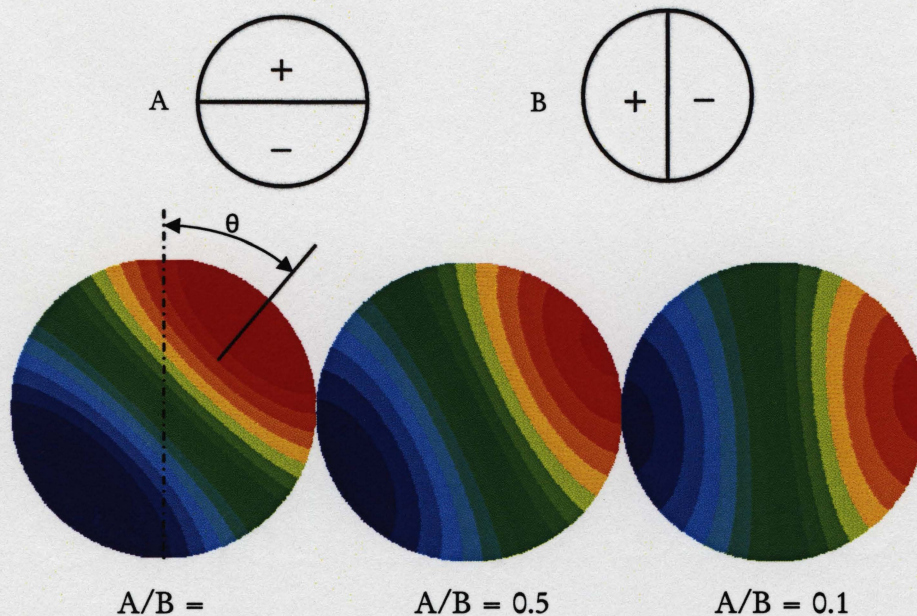


Figure 5-5 Pressure amplitude contour plots of the resultant modes of the superposition of two orthogonal modes with zero temporal phase difference

can be presented by the combination of two orthogonal modes with 90° phase shift. On the other hand, the resultant mode for phase shifts other than 90° is a partially spinning mode. For this partially spinning mode, the principal orientation is always at an angle midway between the two orthogonal modes, while the maximum amplitude and the ratio of the minimum amplitude to maximum amplitude depend on the phase shift.

The last set of runs was designed to explore the effect of changing the amplitude ratio while keeping the phase shift at 90° . The results show that as the amplitude ratio decreases from one, the resultant mode starts to be partially spinning instead of spinning. The principal orientation is always in the direction of the orthogonal mode with the higher amplitude. The ratio of the minimum amplitude to the maximum amplitude equals the amplitude ratio. This ratio reflects the degree of spinning. A stationary mode has a ratio of zero and a spinning mode has a ratio of one. Figure 5-7 shows snap shots of the pressure contours, over half a cycle, for the case with amplitude ratio of 0.4 and time phase difference of 90° . This case resembles the visualization of case $L/d=1$,

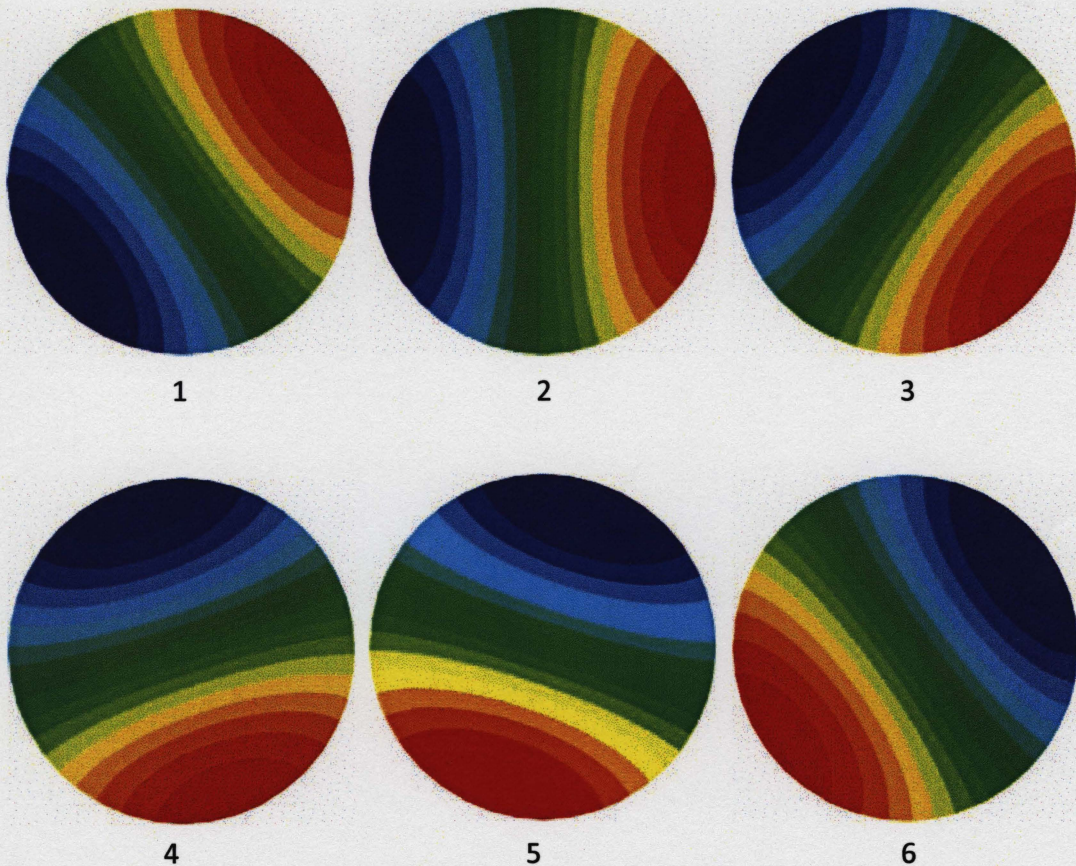


Figure 5-6 Snap shots of the pressure contour of spinning mode. The snap shots are equally spaced over half a cycle. The mode is the result of the superposition of two orthogonal modes with 90° temporal phase shift, and amplitude ratio of 1.

$d/D=2/12$ & $U=70\text{m/s}$, shown in fig. 5-4. In general, both cases show a wagging behaviour. However, it is noteworthy that both cases show an increase in the spinning speed when the amplitude fads out.

To conclude, the performed parametric study demonstrates the ability of using different combinations of orthogonal modes to reproduce cases similar to those observed in the experimental study. The superposition of two orthogonal modes with temporal phase shift of 90° is the most straight forward way to represent different states of azimuthal distributions. One of the two orthogonal modes must be oriented in the direction of the experimentally determined

principal orientation. Note that the amplitude ratio between the two orthogonal modes represents the degree of spinning of the experimental mode shape.

5.3.3. Characteristics of partially spinning modes

Before applying the two orthogonal modes model to analyze the experimental data, it is important to understand the characteristics of partially spinning modes. In particular, this reproduces the most common scenarios and

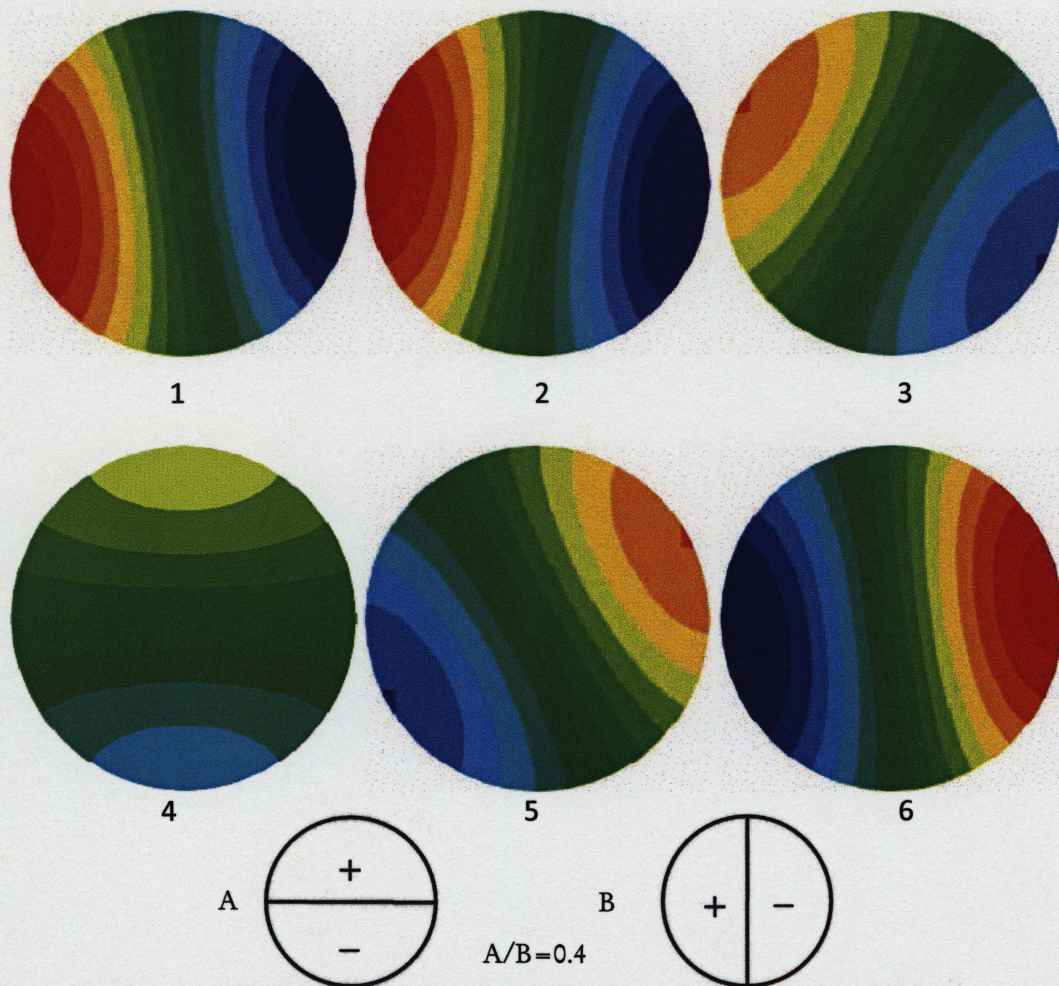


Figure 5-7 Snap shots of the pressure contour of a partially spinning mode. The snap shots are equally spaced over half a cycle. The mode is the result of the superposition of two orthogonal modes with 90° temporal phase shift, and amplitude ratio of 0.4.

shows high level of discrepancy when the average phase and amplitude ratio are considered in the analysis. In this section, description of the modulation of the pressure amplitude and phase over the outer perimeter for the partially spinning mode is provided.

Figures 5-8 shows the distribution of the pressure amplitude over the outer perimeter. These data are for amplitude ratio of 0.4 and time phase difference of 90° . The pressure amplitude changes between 1 and 0.4. The distribution is not sinusoidal. However, it approaches the sinusoidal distribution as the amplitude ratio becomes closer to zero (Stationary mode) and approaches a constant value as the amplitude ratio approaches one (spinning mode).

On the other hand, the phase shows a very interesting behaviour, as depicted in fig. 5-9. The rate of change in phase increases around the position of the minimum amplitude. *This demonstrates how different values of relative phase can be measured at different locations over the perimeter, even if the physical enclosed angle between the pressure transducers is kept constant.* This explains

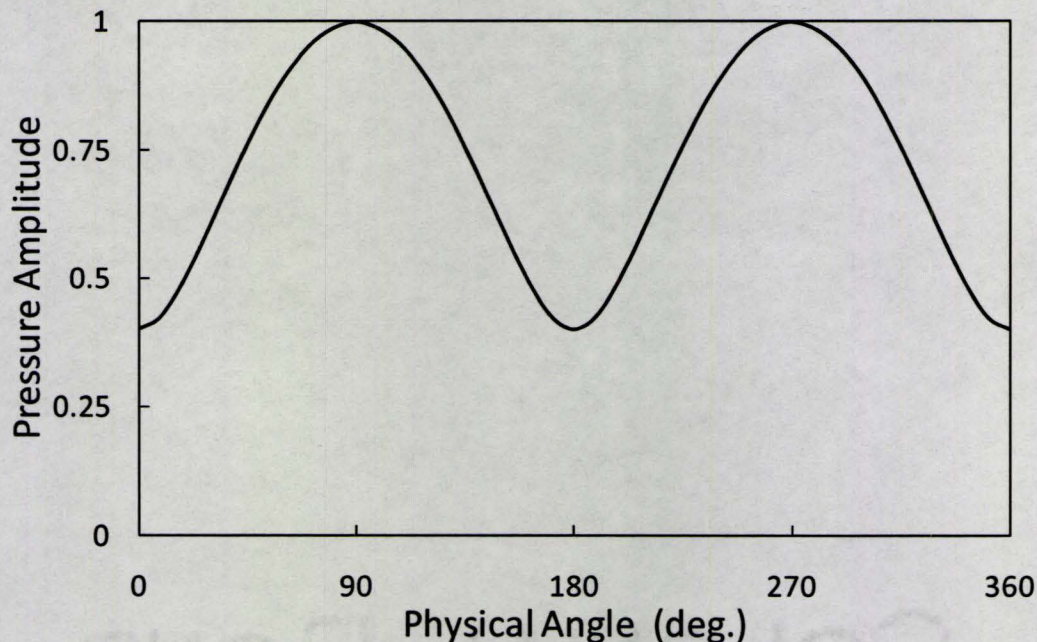


Figure 5-8 Pressure amplitude over the outer perimeter for a partially spinning mode with amplitude ratio of 0.4

what has been described earlier as inconsistency in the experimental data (sections 5.1.1 & 5.2). This finding also agrees with the observed increase in the spinning speed as the amplitude approaches its minimum. Moreover, it should be noted that the slope of the phase near the minimum amplitude increases with the decrease of the amplitude ratio.

5.3.4. Analysis of the experimental data

An example of how the experimental data can be interpreted with the aid of the two orthogonal modes model is discussed in this section. The diametral mode will be defined in term of the mode principal orientation, the principal mode amplitude (*maximum amplitude*) and the ratio of the amplitude of the secondary mode to that of the principal mode. The secondary mode is the mode perpendicular to the principal one. A FORTRAN code was developed to calculate the aforementioned quantities from the time signals. The calculations require the simultaneous time signals of two pressure transducers. The time signals are first filtered with a narrowband filter to remove all the low frequency

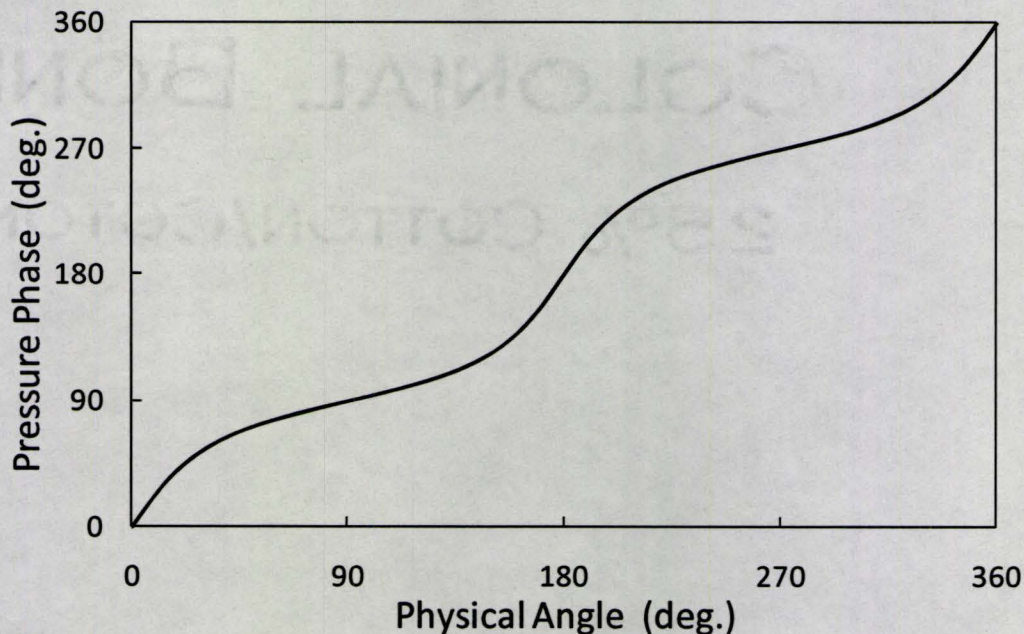


Figure 5-9 Pressure phase over the outer perimeter for a partially spinning mode with amplitude ratio of 0.4

fluctuations and any other acoustic mode co-excited with the mode under consideration. The instantaneous pressure distribution over the perimeter is then calculated according to the methodology introduced in section 5.2.1. In this way, the time dependent pressure amplitude ($A(t)$) is obtained. The maximum amplitude occurring within a time cycle of pressure oscillation (see fig. 5-8) is taken as the principal amplitude of this cycle and the orientation at which it occurs is taken as the principal orientation. The pressure amplitude after $\frac{1}{4}$ of the cycle (i.e. after 90° in time) from the occurrence of the principal amplitude (see fig. 5-8) is taken as the secondary amplitude. The spatial orientation and absolute amplitude of the secondary mode are checked to make sure that the mode is perpendicular to the principal one and it has the lowest absolute amplitude. A second order interpolation was used to minimize the error in determining the exact amplitudes and orientations of the principal and secondary modes. This error arises due to the time signal digital resolution.

Figure 5-10 shows the time dependent change of the orientation of the principal mode relative to pressure transducers (PT0). These data are for the first test section design ($L/d = 2$, $d/D=2/12$ & $U = 123$ m/s). The orientation is almost constant. It is changing with time by about $\pm 7^\circ$. Figure 5-11 shows the amplitude ratio of the secondary to the principal mode. The ratio is changing in the range from 0.6 to 0.8 with a mean value equal to 0.7. The results of this representation are consistent with the observation of the visualization analysis. However, it provides a physical explanation of the azimuthal behaviour of the acoustic modes. Several other cases were also analysed successfully with the developed code. This proves that the two-orthogonal model is able to capture the behaviour of the diametral modes for different conditions.

5.4. Free shear layer azimuthal behaviour

In this section, the azimuthal behaviour of the cavity free shear layer is investigated. The essential aspect that is under investigation here is the level of azimuthal coherence and the dependency of the aerodynamic excitation on it. Two separate experiments were devised for this investigation. In the first experiment, a geometrical preference for the diametral acoustic mode orientation is introduced to investigate the excitation under this condition. In

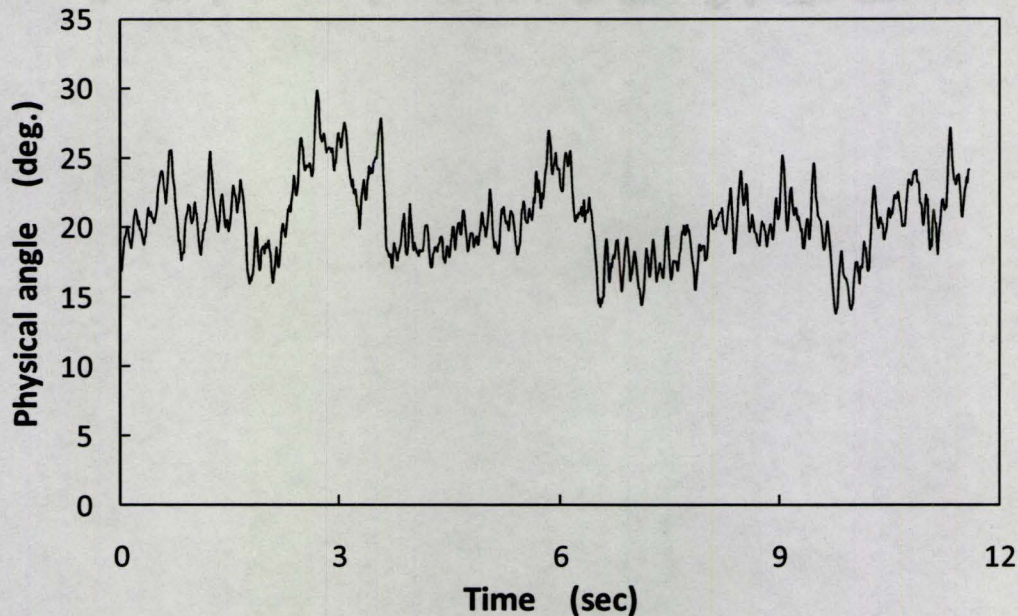


Figure 5-10 The time dependent change of the principal orientation of the first acoustic mode ($L/d = 2$, $d/D = 2/12$ & $U = 123$ m/s), first test section design.

the second experiment, two hot wire probes were used to measure the relative phase in the free shear layer at different azimuthal orientations. In the next subsections, the results of the two experiments are discussed.

5.4.1. Cavity with splitter plate

To introduce a geometrical preference for the acoustic mode orientation, acrylic plate, 5 mm thick, was inserted inside the cavity with $L/d = 1$, $d/D = 2/12$ as shown in fig. 3-6. The new geometry with the plate was simulated using the finite element package “ABAQUS” to determine the resonance frequency and mode shape of the first diametral mode. The simulation showed that this geometry has two diametral modes perpendicular to each other and with locked orientations relative to the plate as shown in Fig. 5-12. The frequency of the mode with the nodal diametral plane oriented in line with the plate is 5 Hz lower than that of the other mode. This frequency difference facilitates the differentiation between the contribution of each mode to the pressure transducer signal. As previously discussed in chapter 3, three pressure transducers were used. The pressure transducers were located so that one

pressure transducer is set at the pressure anti-node of each one of the two modes. The third pressure transducer was located between the first two. This arrangement allows studying the importance of the azimuthal coherence of the shear layer.

The discussion in this section focuses on the excitation of the first diametral mode by the first shear layer mode which reaches a peak amplitude at 64 m/s. The time signals of the pressure transducers show that both modes were simultaneously excited. Figure 5-13 shows the time signal of the middle pressure transducer. The overlap of the two frequencies causes the beating modulation of the pressure amplitude. Figure 5-14 shows the close-up at the resonance peak in the pressure amplitude spectra of the three pressure transducers. The power spectra are for mean flow velocity of 64m/s. The maximum peak of pressure transducer PT0 is at the low frequency diametral mode (1244 Hz). Logically, the pressure transducer PT2 has its maximum peak at the high frequency mode. Moreover, the amplitude spectrum of each pressure transducer shows a lower value peak for the other mode. This shows clearly the

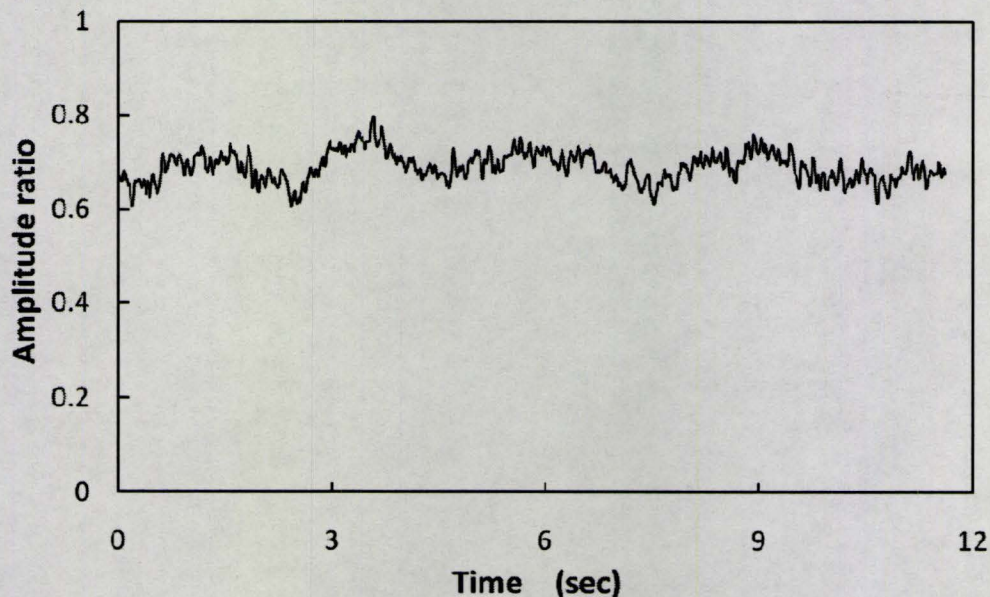


Figure 5-11 The time change of the amplitude ratio of the first acoustic mode ($L/d=2$, $d/D=2/12$ & $U = 123$ m/s) , first test section design.

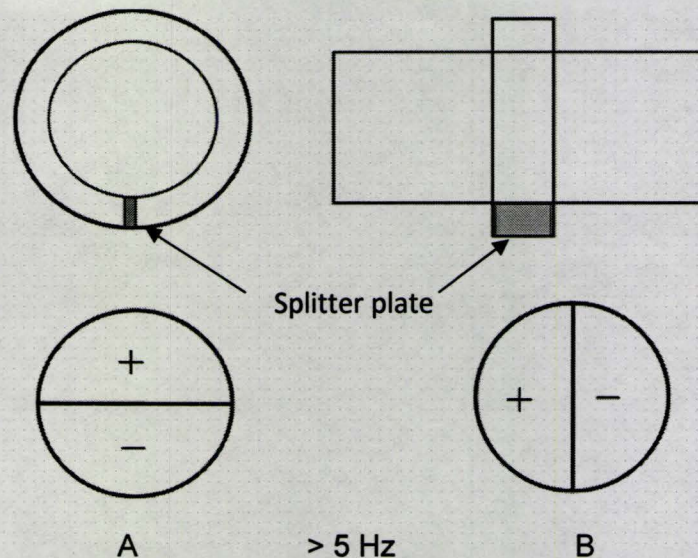


Figure 5-12 Configuration of cavity with one splitter plate and the diametral modes associated with it ($L/d=1$, $d/D=2/12$), first test section design.

directionality of the resonance modes relative to the splitter plate, which is in a good agreement with the numerical predictions. This leads to the conclusion that the cavity free shear layer can excite simultaneously more than one diametral mode. Regarding the amplitude level, the pressure amplitude is lower by a factor of two to three compared to the similar case without the splitter plate. This supports the notion that a spinning mode can produce more energy than a stationary one. However it is noteworthy that comparisons based on the pressure amplitude alone are not conclusive.

Driven by the idea that two independent perpendicular modes can co-exist, another experiment was conducted with four splitter plates inserted inside the cavity at ninety degree angle to each other as shown in fig. 3-6. This configuration has two diametral first mode perpendicular to each other and have the same resonance frequency. Three pressure transducers were used to measure the sound pressure level; two of them were located directly beside two neighbouring splitter plates. The third pressure transducer was located between the other two. The aim from this experiment was to examine the possibility of two perpendicular modes, having the same frequency, to be excited independently from each other. The results showed that the three pressure

transducers measure almost the same sound pressure level. This is because the combination of the two modes produces pressure amplitude at the middle transducer similar to that at the other transducers. To judge the dependency of the two perpendicular modes on each other, the coherence between each two of the pressure transducers was calculated. The calculations showed, gratifyingly, very low coherence between different pressure transducers at the resonance frequency. The coherence value between the two pressure transducers, with 90° separation angle, was almost zero at the frequency of maximum amplitude. This indicates that the diametral mode can be excited by only a part of the free shear layer and formation of coherent structure over the entire axisymmetric free shear layer is not a necessity for the excitation process.

5.4.2. Hot wire measurements

The objective of this set of measurements is to compare the phase characteristics of the free shear layer fluctuations to the phase distribution of the acoustic pressure. The phase difference of the shear layer fluctuation in the

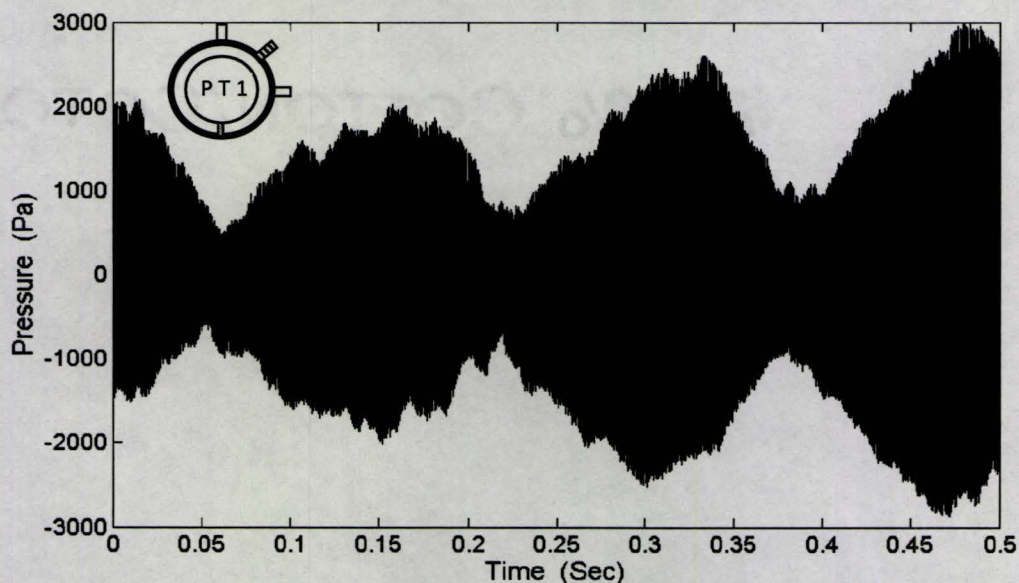


Figure 5-13 Time signal of pressure transducer (PT1) for cavity with single splitter plate. ($U=64\text{m/s}$), first test section design.

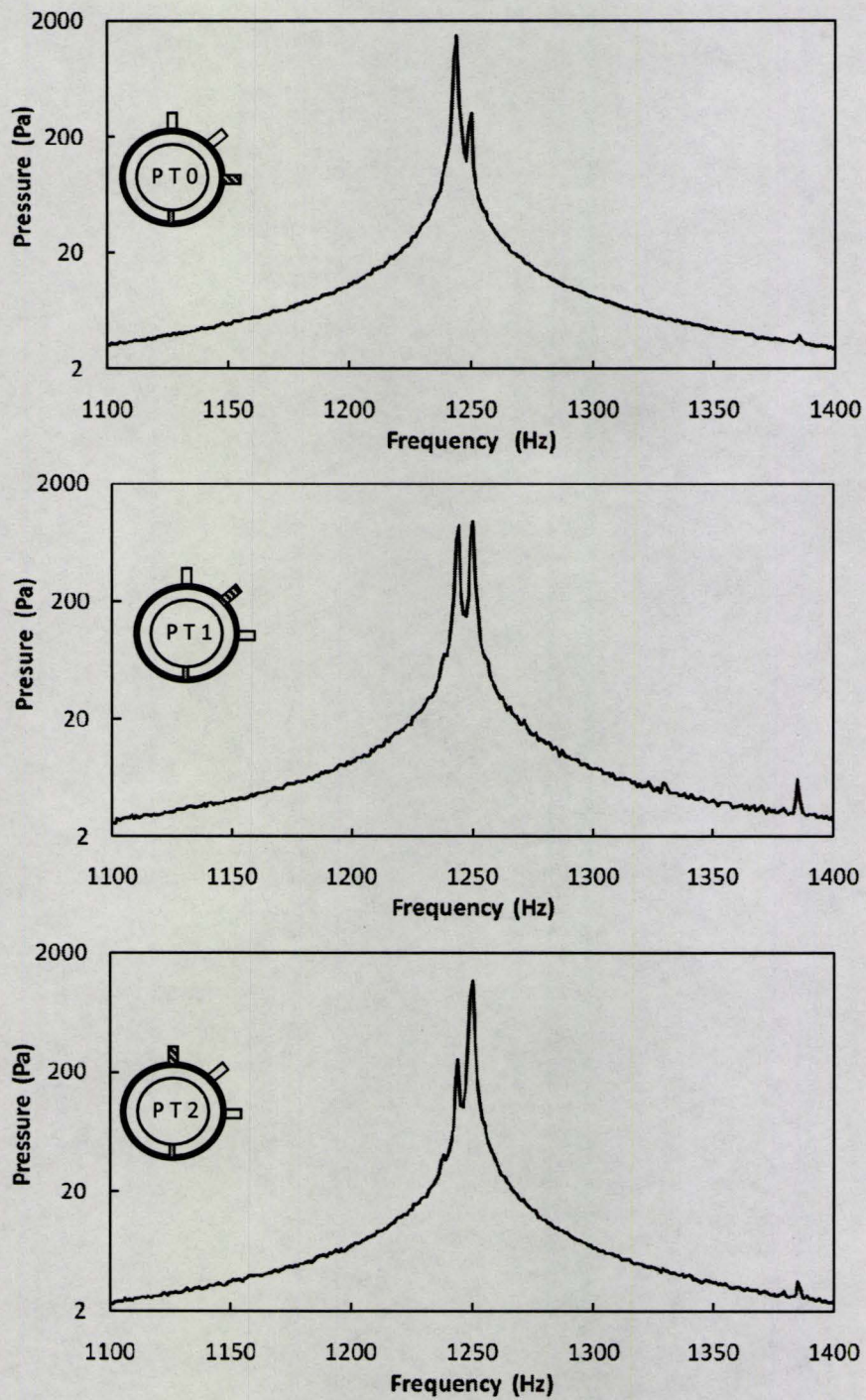


Figure 5-14 Close-up details of the sound pressure RMS amplitude spectra for cavity with single splitter plate, first test section design.

azimuthal direction was measured with two hot wire probes, while the acoustic pressure phase is measured by pressure transducers as discussed earlier in this chapter. The second test section design was used to perform this measurement. The hotwire probes were located at the mid-length of 1 inch cavity as described in chapter 3. Figure 5-15 shows a schematic of the locations of the hotwire probes and the pressure transducers used in this measurement. It should be noted that the following discussion considers the phase only at the acoustic resonance frequency.

Before measuring the phase difference of the free shear layer velocity fluctuation, an effort was made to determine the suitable radial position for the measurement. The main reason is to avoid the radial location where the phase of the velocity fluctuation changes sharply along the radial direction within the shear layer. Therefore, the radial distribution of the shear layer fluctuation was measured first. The measurements were performed for the excitation of the first acoustic mode by the first and second cavity shear layer modes for the cavity with $L/d=1$ & $d/D=2/12$.

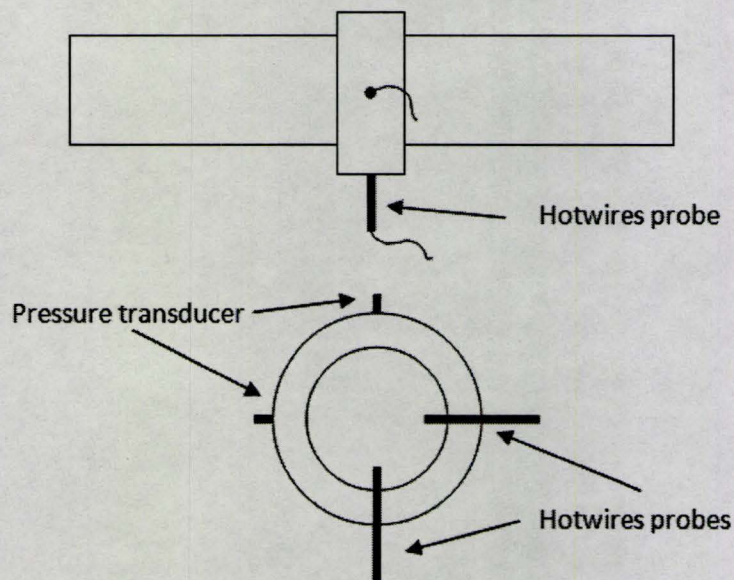


Figure 5-15 Schematic of the locations of the pressure transducers and the hot wire probes used in measuring the azimuthal phase of the velocity fluctuation, second test section design.

a) *Radial distribution of velocity fluctuation*

Figure 5-16 shows the radial distribution of the streamwise velocity fluctuation that corresponds to the acoustic resonance frequency. The mean flow velocity was 67m/s, at which the first diametral resonance mode is excited by the first free shear layer mode. The cavity mouth was taken as the datum of the radial direction. The presented values in the graph are the time average and the error bars are the standard deviation over the time. The maximum amplitude of the velocity fluctuation is about 20% of the mean flow velocity.

Figure 5-17 shows the phase distribution of the velocity fluctuation. The phase was measured relative to the signal of a pressure transducer mounted at 180° from the hotwire. The slope of the phase is very steep near the cavity mouth. The slope decreases substantially 2-3 mm away from the cavity mouth. The standard deviation is also very high inside the cavity and decreases with the distance from the cavity mouth.

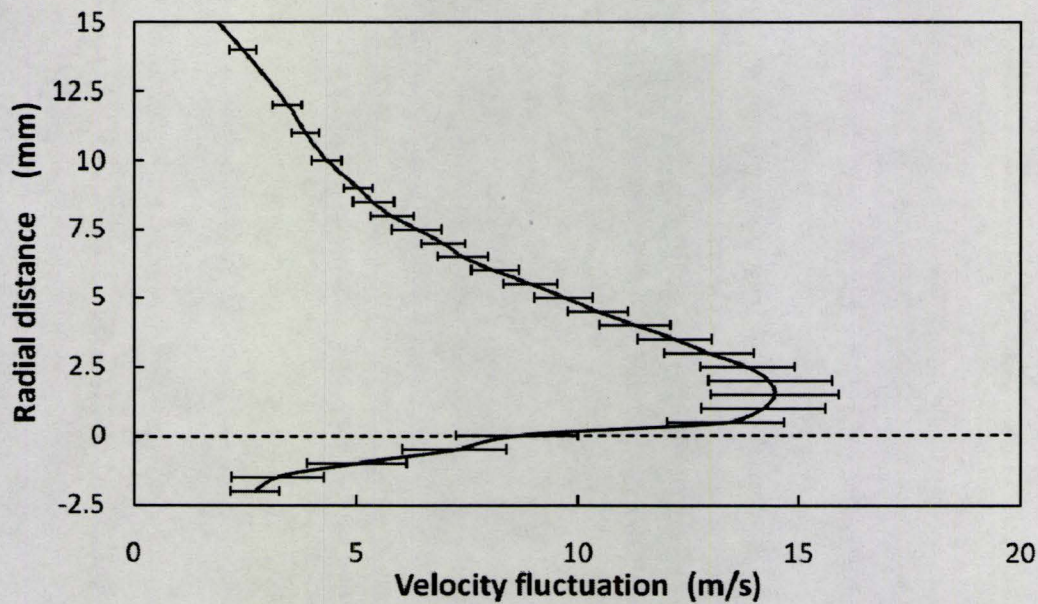


Figure 5-16 Radial distribution of the amplitude of the velocity fluctuation during the resonance of the first diametral mode excited by the first shear layer mode; $m=1$, $n=1$, $U=67$ m/s, $x/L=0.5$.

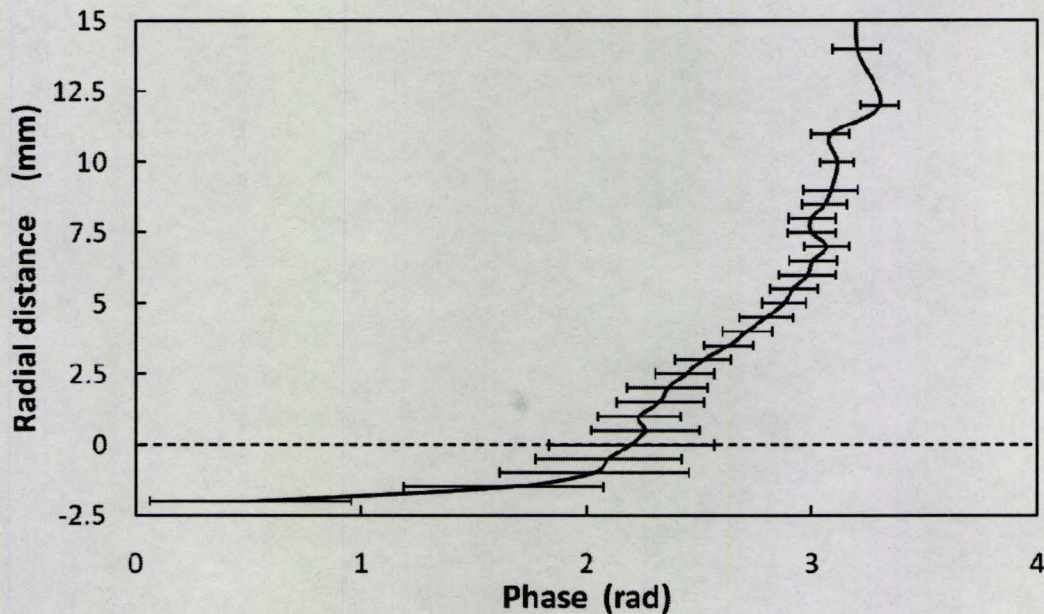


Figure 5-17 Radial distribution of the phase of the velocity fluctuation during the resonance of the first diametral mode excited by the first shear layer mode; $m=1$, $n=1$, $U=67$ m/s, $x/L=0.5$.

Figure 5-18 shows the radial distribution of the velocity fluctuation for the second free shear layer mode. The mean flow velocity is 33m/s and the first diametral resonance mode was excited. The maximum amplitude of the velocity fluctuation is about 8% of the mean flow velocity, which is about the level of the turbulence fluctuation in the boundary layer at the cavity upstream edge (see fig. 4-2). The standard deviation is also higher as a percentage value compared to that of the first free shear layer mode. Although this measurement is not intended to characterize the level of the vortical structure coherence, the increase of the standard deviation is a good indication that the first free shear layer mode is more coherent in time compared to the second free shear layer. This is in full agreement with the conclusion drawn from the acoustic pressure measurements in the previous chapter. Regarding the radial distribution of the phase, it behaves very similar to the case of the first shear layer mode. However, the radial distance over which the phase changes rapidly is shorter than that of the first shear layer mode.

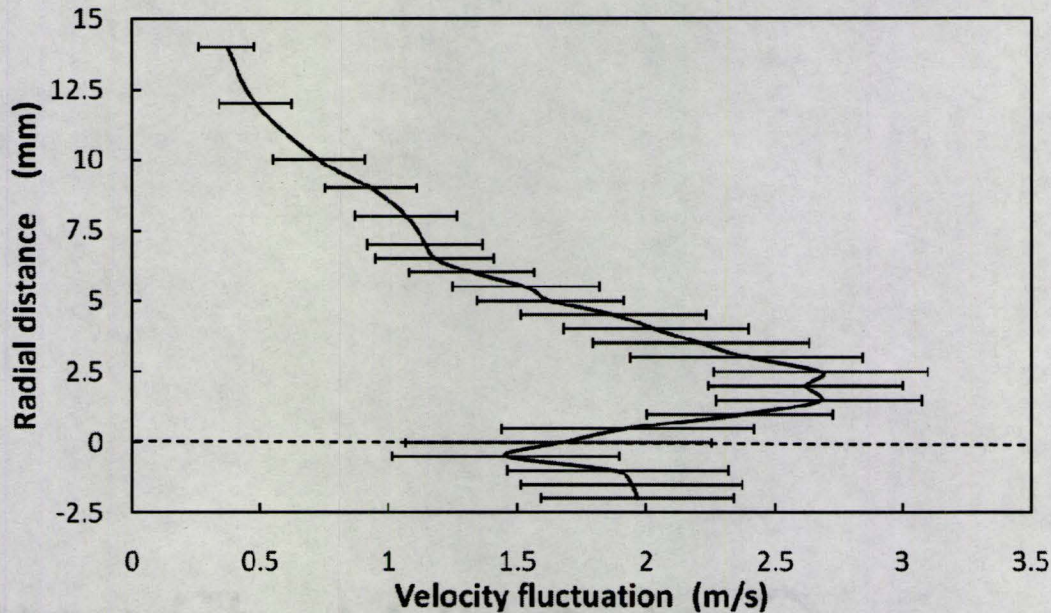


Figure 5-18 Radial distribution of the amplitude of the velocity fluctuation during the resonance of the first diametral mode excited by the first shear layer mode; $m=1$, $n=2$, $U=33$ m/s, $x/L=0.5$.

b) Azimuthal phase

Based on the amplitude and phase distributions, the hotwire probes were located 5 mm inside the main flow from the cavity mouth. This ensures that the probes are away from the region of steep phase gradient (near the center of vertical structure) and are not in a region of relatively low level of fluctuation (the outer skirt of the vortical structure) especially for the second shear layer mode.

Figure 5-19 shows the time dependent change of the azimuthal phase difference of the velocity fluctuation and the corresponding change in the phase of acoustic pressure for the first shear layer mode. The phase data is calculated using *short term Fourier transform* with a window of one second and time shift of half a second. The phase differences of the velocity fluctuation and the acoustic pressure are coherent. This is clear at the instances where the phase changes abruptly. At about 2.5sec and 11sec, the change in the phase sign indicates a reversal in the direction of the azimuthal spinning. Also, the data

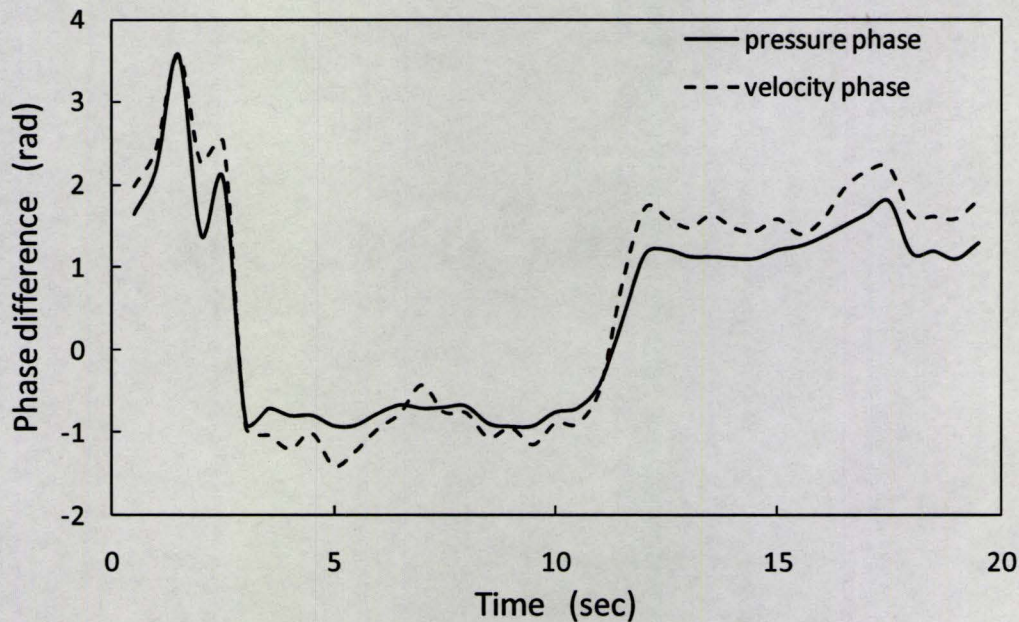


Figure 5-19 The time dependent change of the azimuthal phase difference of the velocity fluctuation and the acoustic pressure for the first acoustic mode excited by the first free shear layer modes, test conditions correspond to those of fig. 5-16.

show that the level of fluctuations in the velocity phase difference is higher which can be attributed to the flow turbulence. Figure 5-20 shows the time dependent change of the azimuthal phase difference of the velocity fluctuation and the acoustic pressure for the second shear layer mode. The coherence between the velocity and pressure is also evident in this case, despite the high level of fluctuations in the phase difference.

To conclude the discussion of sections 5.4.1 & 5.4.2, it is evident that the shear layer is not coherent in the azimuthal direction due to any hydrodynamic mechanism. Moreover, it is the acoustic field that dictates the azimuthal phase of the shear layer fluctuation. Therefore, the azimuthal phase distributions of the shear layer and the acoustic pressure phase distributions are similar.

5.5. Summary

The azimuthal behaviour of the diametral modes has been investigated experimentally. The analysis of the experimental data has determined that the

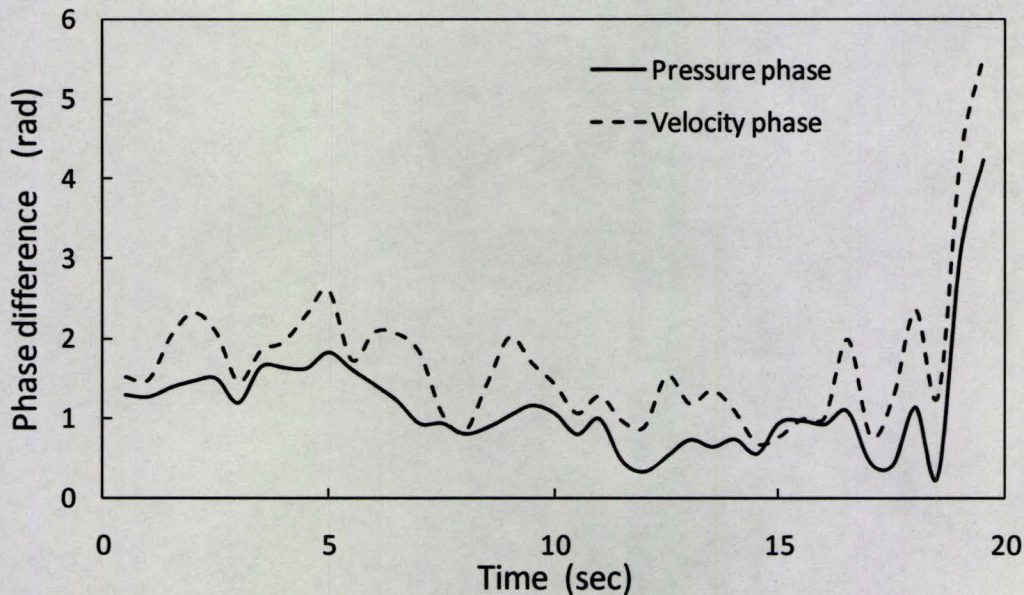


Figure 5-20 The time dependent change of the azimuthal phase difference of the velocity fluctuation and the acoustic pressure for the first acoustic mode excited by the first free shear layer modes, test conditions correspond to those of fig. 5-18.

aerodynamically excited diametral modes are likely to be spinning when the cavity-duct system is perfectly axisymmetric. Small geometrical deviations from axisymmetry or localized damping introduce orientation preference that results in partially spinning behaviour. The spinning modes also dominate at high flow Mach number ($M > 0.2$). For long cavities ($L/D > 0.5$), the orientation becomes rather random with time, which can be attributed to increased randomness in the free shear layer oscillation (turbulent flow) and consequently the acoustic power source.

An analytical model has been developed to understand and produce the observed azimuthal phase distributions. The acoustic mode is decomposed into two spatially orthogonal stationary modes with a 90° temporal phase shift between them. The ratio of the amplitudes of the two modes determines the degree of the mode spinning. The model is used to determine the characteristics of the partially spinning behaviour and to explain the different experimental observations.

The azimuthal behaviour of the cavity shear layer has been characterized experimentally. The results showed that hydrodynamic azimuthal coherence of the shear layer is not a necessity for the excitation of the diametral modes and that the diametral mode can be excited by only a portion of the shear layer with the rest of the shear layer not necessary contributing to this mode or even exciting a different mode. Also, the results show that the azimuthal phase in the shear layer is controlled by the acoustic perturbation and consequently the azimuthal phase of the shear layer fluctuation is identical to the azimuthal phase of the acoustic field.

CHAPTER 6

NUMERICAL APPROACH AND CODE DEVELOPMENT

This chapter details the numerical approach developed to simulate the trapped acoustic modes of the cavity-duct system. A two-step approach is adopted to allow consideration of the effect of the mean flow on the acoustic mode shape and frequency. In the first step, the mean flow is simulated by solving steady state Reynolds Average Navier-Stokes equations. The unsteady acoustic field is simulated in the second step, which involves solving a system of linearized acoustic perturbation equations. This allows the use of a relatively large grid size for the unsteady simulation. In this approach, the acoustic effect on the mean flow and the aeroacoustic sources were not considered. A commercial finite volume package, FLUENT, was used to perform the mean flow simulations. A FORTRAN finite difference code was developed to solve the linearized acoustic perturbation equations. Two-dimensional and three-dimensional versions of the code were developed. The system of governing equations used in each step is presented in this chapter. The schemes used in the FORTRAN code to calculate the spatial and temporal derivatives are also discussed in this chapter with a focus on the accuracy and the limitation of each scheme.

6.1. Unsteady acoustic calculations

6.1.1. System of governing equations

A linearized system of “Acoustic Perturbation equations”, developed by Ewert & Schröder (2003), was used to describe the acoustic propagation. The linearized Euler equations (LEE) were first used in the code. However, vorticity waves were developed at the cavity free shear layer, as shown in fig. 6.1, which shows the contour plots of the axial velocity fluctuation for a 5cmX5cm two-dimensional cavity. The simulation predicts the first transverse mode at 100m/s mean flow velocity. The light and dark contours represent the positive and negative velocity, respectively, and ψ represents the phase angle within the oscillation cycle. At $\psi = 0^\circ$ the pressure is at its maximum at the bottom floor. It is clear from the positive and negative axial velocities on both sides of the free

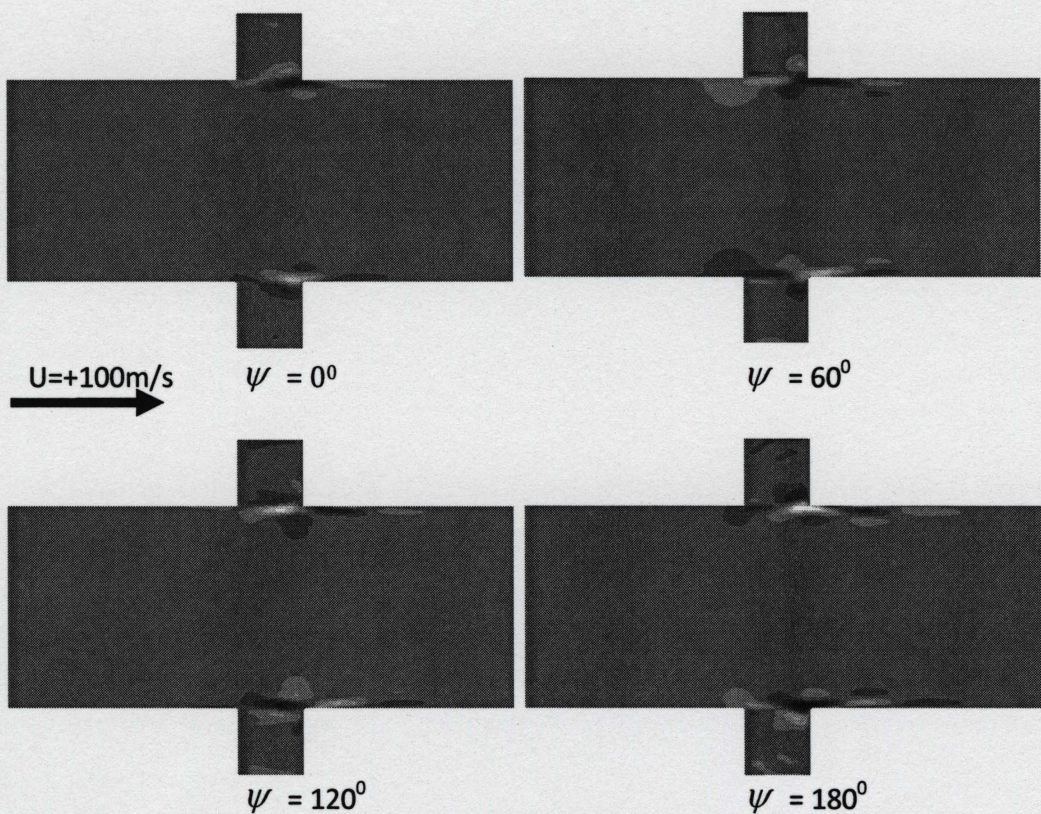


Figure 6-1 The axial velocity fluctuation contours at different times

shear layer that vortical structures are generated near the upstream edge of the cavity and grow as they travel downstream.

The generation of the vortical structures results from the excitation of the hydrodynamic instability of the free shear layer. The shear layer oscillation contaminates the velocity field and in some cases leads to unstable solutions. This problem arises from the fact that the Linearized Euler equations have different eigenmodes that govern the vorticity, entropy and acoustic waves. Ewert & Schröder (2003) were able to develop a system of equations that can reasonably describe the propagation of the acoustic wave without suffering from the excitation of the hydrodynamic instability. The different eigenmodes of the linearized Euler equations were separated in the frequency wave number domain. The eigenmodes governing the vorticity and entropy wave were then removed and the system of equations was transferred back to the spatial-time domain. The resulting acoustic perturbation equations (APE) for multidimensional domain without source terms can be written as follows:

$$\frac{\partial p_a}{\partial t} + c^2 \nabla \cdot (\rho_0 \vec{U}_a + \vec{U} \frac{p_a}{c^2}) = 0 \quad 6-1$$

$$\frac{\partial U_a}{\partial t} + \nabla \cdot (\vec{U} \cdot \vec{U}_a) + \nabla \cdot \left(\frac{p_a}{\rho_0} \right) = 0 \quad 6-2$$

where, p_a is the acoustic pressure perturbation, \vec{U}_a is the acoustic particle velocity vector, \vec{U} is the mean velocity obtained from the simulation of the RANS equations, ρ_0 is the mean density and c is the mean acoustic speed, which is set 340 m/s. The source terms are ignored as they describe mainly the effect of the turbulence or the entropy fluctuations on the acoustic field. At steep velocity gradients, these equations may become inaccurate due to the absence of one of the source terms. However, Ewert & Schröder (2003) showed that the error is small. Moreover, in the current case, the steep velocity gradient occupies only a small area of the computational domain.

6.1.2. Calculation of the spatial derivatives

The spatial derivatives were calculated using the *three points stencil optimized prefactored compact* finite difference scheme developed by Ashcroft & Zhang (2003). This scheme is a fourth order accurate with low dissipation and low dispersion characteristics. The numerical dissipation produces an artificial reduction in the perturbation amplitude with time, while, the numerical dispersion produces an artificial scatter of waves with different frequencies as it travels in space. Therefore, this scheme is very suitable for accurate simulation of acoustic wave propagation. Also, this scheme requires a relatively small stencil, as well as fewer boundary stencils that allow a simple formulation of the boundary conditions.

The developed scheme is based on six order accurate non-dissipative central difference stencil. The central difference scheme is split into two lower order backward and forward difference stencils. The coefficients of the new stencils were chosen such that the original central difference stencil is restored when the two derivatives are added together. The coefficients were optimized to improve the prediction of the wave number and to lower the dispersion level of the scheme. The optimization process lowers the order of accuracy of the scheme to four. Figure 6-2 shows the relation between the predicted wave number and the actual wave number based on the number of points per wavelength as reported by Ashcroft & Zhang (2003). The number of points per wavelength is computed as $2\pi/\kappa \Delta x$, where κ is the wave number. It is clear that the wave number of a certain wave can be predicted if $\kappa \Delta x$ for this wave is lower than 2.1 ($\kappa'_{max}\Delta x$). For $\kappa \Delta x$ equal to 1.4 ($\kappa'_c\Delta x$), the error is below 10^{-3} . This means that a minimum of 4.5 points per wavelength is needed to achieve this level of accuracy in the propagation of a certain wave. Ashcroft & Zhang (2003) reported also the error in the calculation of the phase speed to give a better indication of the dispersion characteristic of the scheme. For $\kappa \Delta x$ equal to 1.4 and lower, the error in the phase speed is less than 10^{-3} which is considered a reasonable level of error.

The derivative D_i can be written in terms of forward and backward operators D_i^F and D_i^B , respectively, as follows:

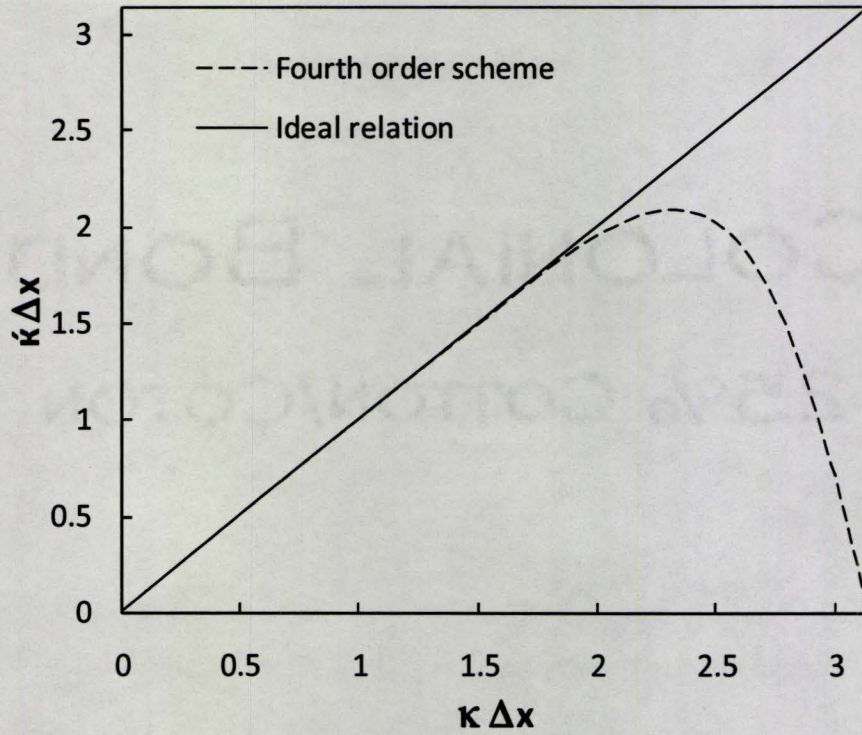


Figure 6-2 Dispersive characteristics of the fourth order optimized scheme (Ashcroft & Zhang, 2003)

$$D_i = \frac{1}{2}(D_i^F + D_i^B) \quad 6-3$$

$$\frac{1}{2}D_i^F = \frac{1}{2\beta\Delta x} [b(\mathcal{F}_{i+1} - \mathcal{F}_i) + g(\mathcal{F}_{i-1} - \mathcal{F}_i)] - \frac{\alpha}{2\beta} D_{i+1}^F \quad 6-4$$

$$\frac{1}{2}D_i^B = \frac{1}{2\beta\Delta x} [b(\mathcal{F}_i - \mathcal{F}_{i-1}) + g(\mathcal{F}_i - \mathcal{F}_{i+1})] - \frac{\alpha}{2\beta} D_{i-1}^B \quad 6-5$$

For the first and last points of the grid, $i=1$ & N , respectively, one sided explicit third order accurate formulas are provided to calculate the forward and backward operators as follow:

$$D_1^B = \frac{1}{\Delta x} \sum_{j=1}^4 s_j \mathcal{F}_j, \quad D_N^B = \frac{1}{\Delta x} \sum_{j=N-3}^N e_j \mathcal{F}_j \quad 6-6$$

and

$$D_1^F = \frac{1}{\Delta x} \sum_{j=1}^4 -ee_{N+1-j} \mathcal{F}_j, \quad D_N^F = \frac{1}{\Delta x} \sum_{j=N-3}^N -s_{N+1-j} \mathcal{F}_j \quad 6-7$$

For internal boundaries a fourth order accurate central explicit formula is provided:

$$D_i^F = \frac{1}{\Delta x} \sum_{j=-5}^5 bb_j \mathcal{F}_{i+j}, \quad D_i^B = \frac{1}{\Delta x} \sum_{j=-5}^5 -bb_{-j} \mathcal{F}_{i+j} \quad 6-8$$

All the coefficients in equations 6-4 to 6-8 are listed in table 6-1. It is noteworthy that the optimized prefactored compact finite difference scheme is an implicit scheme. A bidiagonal matrix needs to be solved to determine the derivatives. This small additional computational cost results from the prefactorization process.

6.1.3. Time marching scheme

A two-step 6/5 stages low-dissipation and low dispersion Runge-Kutta scheme (LDDRK) was used to perform the numerical integration with time (Hu et al, 1996). This scheme is a fourth order accurate. Hu et al. (1996) optimized the scheme coefficients to minimize the numerical dissipation and dispersion. This optimization increases the time step limit that is based on the level of numerical dissipation. The use of a two-step scheme allows the optimization without significant reduction in the order of accuracy. The time step limitation is given as follows:

$$c \frac{\Delta t}{\Delta x} = \min \left(\frac{2}{\kappa'_c \Delta x}, \frac{2.85}{\kappa'_{max} \Delta x} \right) \quad 6-9$$

where, c is the speed of sound, Δt is the time step, Δx is the smallest grid size, $\kappa'_c \Delta x$ and $\kappa'_{max} \Delta x$ correspond to the finite difference scheme. The term $\frac{2}{\kappa'_c \Delta x}$ represents the stability limit which corresponds to a dissipation error of 0.001. For this condition, the error in the phase is less than 0.001. The term $\frac{2.85}{\kappa'_{max} \Delta x}$ represents the stability limit where the numerical dissipation turns positive.

Table 6-1 coefficients of the Optimized prefactored scheme

Coefficient	Numerical Value
b	0.71518963303413346
g	-0.14065396116337958
α	0.29749586350149729
β	0.71518963303413346
s_1	-1.968010730879214299
s_2	3.336693493864702415
s_3	-1.769354795091761932
s_4	0.400672032106273816
ee_N	1.69865593578745236
ee_{N-1}	-2.66330650613529758
ee_{N-2}	1.23064520490823806
ee_{N-3}	-0.26599463456039285
bb_{-5}	-0.00083442741566041
bb_{-4}	0.01022630353651893
bb_{-3}	-0.05956199104811759
bb_{-2}	0.22724621139300842
bb_{-1}	-0.72224477117316119
bb_0	-0.21013712054967647
bb_{+1}	0.96979343766394390
bb_{+2}	-0.27390976718640895
bb_{+3}	0.07031776392683924
bb_{+4}	-0.01184575620106222
bb_{+5}	0.00095011705377633

Stanescu & Habashi (1998) developed a 2N-storage implementation of this scheme. N is the number of degrees of freedom of the system which is the number of gird points multiplied by the number of variables. The low storage scheme is written as follow for $du/dt = F(t,u(t))$:

$$g_i = \epsilon_i g_{i-1} + \Delta t \mathcal{F}(t_{i-1}, \mathcal{F}_{i-1}) \quad 6-10$$

$$\mathcal{F}_i = \mathcal{F}_{i-1} + \epsilon_i g_i \quad 6-11$$

where $i=1,\dots,s$, and s is the number of stages. This yields 2N-storage algorithm, as w and u are the only values being stored for each degree of freedom. The list of coefficients for the two-step schemes is provided in tables 6-2 and 6-3.

Table 6-2 Coefficients of the five stages step of LDDR

i	ϵ_i	ϵ_i	ct
1	0.0	0.2687454	0.0
2	-0.6051226	0.8014706	0.2687454
3	-2.0437564	0.5051570	0.5852280
4	-0.7406999	0.5623568	0.6827066
5	-4.4231765	0.0590065	1.1646854

Table 6-3 Coefficients of the six stages step of LDDR

i	ϵ_i	ϵ_i	ct
1	0.0	0.1158488	0.0
2	-0.4412737	0.3728769	0.1158485
3	-1.0739820	0.7379536	0.3241850
4	-1.7063570	0.5798110	0.6193208
5	-2.7979293	1.0312849	0.8034472
6	-4.0913537	0.15	0.9184166

6.1.5. Treatment of the boundary conditions

a) Wall boundary condition

At the grid nodes of the wall, the velocity is set to zero and the velocity derivative in the perpendicular direction on the wall is calculated using the explicit formulas given by equations 6-6 and 6-7. The use of a compact discretization scheme allows this simple implementation.

b) Zero pressure boundary condition

The pressure is set to zero at the inlet and outlet of the cavity-duct system. This boundary condition reflects all pressure waves back inside the domain. The rationale behind this implementation is discussed in chapter 7. The pressure derivative perpendicular to the boundary is calculated using the explicit formulas given by equations 6-6 and 6-7. The velocity derivative perpendicular to the boundary is set to zero.

c) Centerline treatment

To avoid the geometrical singularity in the cylindrical coordinates in the case of the 3-D simulation, the finite difference grid was designed in a way to avoid having a grid point at the center. Figure 6-3 shows an example of such a

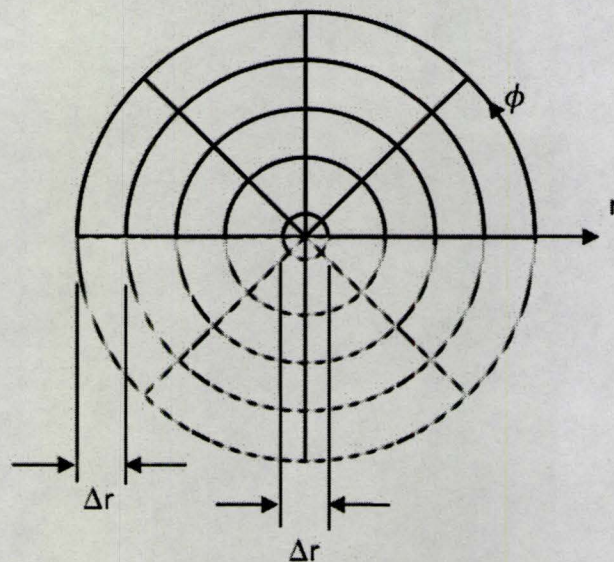


Figure 6-3 schematic of a computational grid used to avoid a grid point at the centerline

grid. The calculation was performed for only half of the domain where $0 \leq \phi \leq \pi$. The radial distribution of the nodes is given as follow:

$$r_n = \frac{(2n+1)\Delta r}{2} \quad n=0,1,2 \dots\dots \quad 6-12$$

The radial derivatives at $n=0$ are calculated using the internal boundary formula given by equation 6-8 using the information on both sides of the centerline as will be described in next subsection.

d) Azimuthal boundary condition

The azimuthal boundary condition is needed for the axisymmetric simulations. Given that the interest of the current investigation is to simulate the first acoustic mode only, we take advantage of the asymmetric nature of this mode and performed the simulation considering only half of the circular cross-section of the domain as shown in fig. 6-3. This reduced domain has azimuthal boundaries at $\theta = 0$ and $\theta = \pi$. The derivatives at these boundaries were calculated using the internal boundary formula given by equation 6-8, which requires the value for variables in the unsolved half of the domain. The values of the unsolved half are expressed in term of the solved half values in a way to preserve the asymmetric nature of the problem. The relation between the values of the two halves is formulated as follows:

$$\left. \begin{aligned} u_a(x, r, \phi + \pi) &= u_a(x, r, \phi) \\ v_a(x, r, \phi + \pi) &= -v_a(x, r, \phi) \\ \omega_a(x, r, \phi + \pi) &= -\omega_a(x, r, \phi) \\ p_a(x, r, \phi + \pi) &= -p_a(x, r, \phi) \end{aligned} \right\} 0 \leq \theta \leq \pi \quad 6-13$$

6.1.6. Program algorithm

The flow chart of the FORTRAN program that was developed to solve the acoustic perturbation equations (APE) is shown in fig. 6-4. The program starts with reading the input data that specify the geometry and simulation conditions. The computational mesh is then created by defining the coordinates of the mesh points. The mean flow derivatives are calculated at all the mesh points. Note that the input mean flow velocities and pressure are interpolated to the numerical

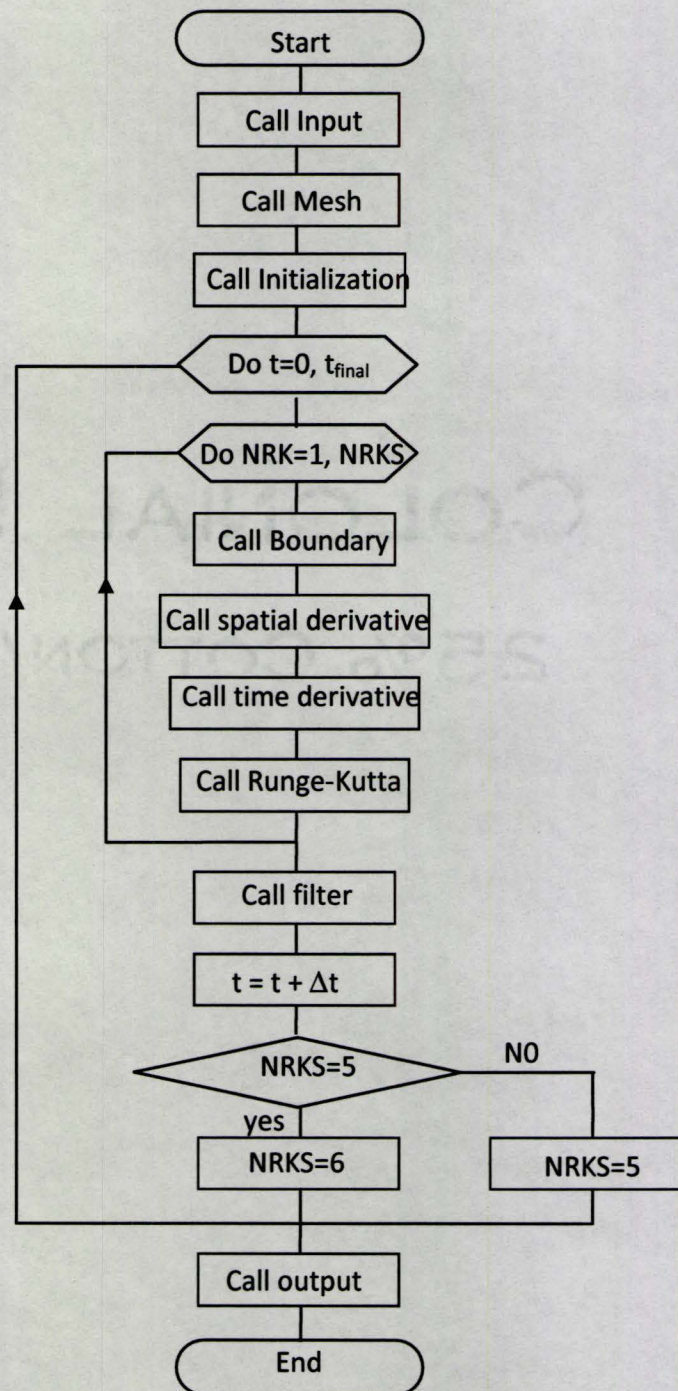


Figure 6-4 The algorithm of the FORTRAN code developed to solve the acoustic perturbation equations

mesh beforehand, using the commercial package TECPLOT. The time marching starts at time zero and continues until the target time. In each time step, five and six stages Runge-Kutta are used alternately.

In each stage, boundary conditions are first calculated then followed by the spatial derivatives calculations. The time derivatives of all the variables are calculated using the governing equations and the spatial derivatives. The values of the variables are updated applying equations 6-10 and 6-11. The numerical filter is applied at the end of each time step to eliminate the noise generated in the calculations.

6.2. Mean flow calculations

The mean flow was simulated using the finite volume code FLUENT. The code solves the incompressible Reynolds Averaged Navier-Stokes equations. The Reynolds stress model was used to model the turbulent characteristics of the flow. This model calculates the individual Reynolds stresses, using the appropriate transport equations. The modeling of the unknown terms of the Reynolds stresses transport equations is provided in Fluent 6.2 documentation (2003). The isothermal condition was considered in the simulation, which eliminates the need to solve the energy equations.

The governing equations are discretized using a finite volume scheme. The discrete values of the different variables are assigned to the center of the control volumes. The face values required for the convection terms are interpolated from the values of the control volumes. An upwind scheme is used to perform the interpolation. This means that the face value is obtained from values of the control volume upstream. FLUENT 6.2 provides different upwind schemes (Fluent 6.2 documentation, 2003).

An iterative solver is considered in the simulation. In each iteration, the discretized equations are solved sequentially (i.e., segregated from one another). The momentum equations are solved first based on the current values of the different variables. Because the new values of the velocities may not satisfy the continuity equation, the pressure correction equation is then solved to correct

both the velocity and pressure field to satisfy the continuity equation. The turbulent model is solved after that, based on the new values. The iteration continues until convergence is achieved.

CHAPTER 7

RESULTS OF THE NUMERICAL SIMULATION

This chapter details the results of the numerical simulation performed using the developed two-step approach described in the previous chapter. As mentioned earlier, the objective is to determine the effect of the mean flow field on the acoustic resonance mode. Several aspects of the resonance mode characteristics were considered in the investigation, such as the acoustic resonance frequency, distribution of the pressure amplitude and phase and the distribution of the acoustic particle velocity amplitude and phase. To obtain the mode shape of the acoustic resonance, the computational domain is excited at the resonance frequency that is obtained from a random excitation analysis. The simulations were performed for a 2-D planar geometry and a 3-D axisymmetric geometry.

In section 7.1, the simulation procedure adopted to determine the resonance frequencies for different cases is described. Section 7.2 presents the results of the 2-D geometry simulations focusing on the change in various parameters with the flow Mach number. The simulation of the 3-D axisymmetric cavity-duct system is presented in section 7.3.

7.1. Determination of the resonance frequency

The first step to simulate the acoustic resonance is to determine the frequency of the resonance mode of interest. Experimentally, the resonance frequency can be determined by exciting the physical domain using a loudspeaker driven by a random signal. Using a technique analogous to this experimental method, the numerical domain is excited by a broad band excitation by vibrating the cavity floor.

To produce a broad band excitation, the cavity floor was forced to oscillate according to the following function:

$$v_e(t) = 0.5 \frac{\sin(2\pi f_e(t-aa))}{2\pi f_e(t-aa)} \quad 7-1$$

where $v_e(t)$ is the instantaneous vertical velocity of the cavity floor, f_e is the maximum frequency of excitation, aa is a shift in the time to ensure that the vibration at the beginning of the simulation has low amplitude, as shown in fig. 7-1. This prevents the generation of high frequencies in the solution due to the discontinuity of the initial condition, which cannot be handled by the numerical grid.

The Fourier analysis of the cavity floor oscillation function shows that the cavity floor oscillation can be described by a rectangular function in the frequency domain = $\frac{1}{f_e} \text{rect}\left(\frac{f}{2f_e}\right)$. The rectangular function is described as follow:

$$\text{rect}\left(\frac{f}{2f_e}\right) = \begin{cases} 0 & \left|\frac{f}{2f_e}\right| > \frac{1}{2} \\ \frac{1}{2} & \left|\frac{f}{2f_e}\right| = \frac{1}{2} \\ 1 & \left|\frac{f}{2f_e}\right| < \frac{1}{2} \end{cases} \quad 7-2$$

Figure 7-2 shows the amplitude spectrum of the cavity floor vibration velocity as implemented in the program. The amplitude and the shape of the perturbation agree perfectly with the analytical formula given by equation 7-2.

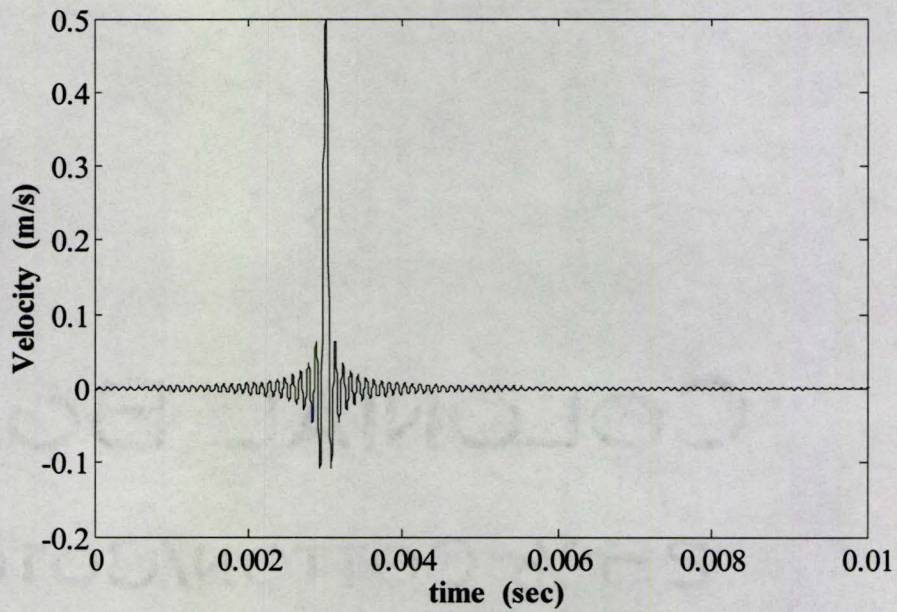


Figure 7-1 Time signal of the cavity floor forced oscillation

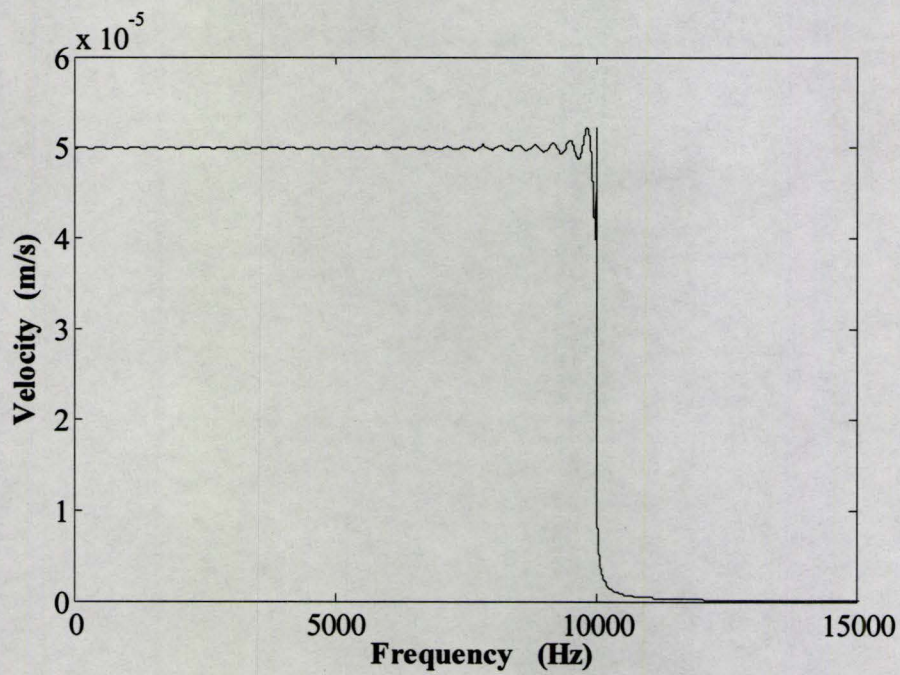


Figure 7-2 Amplitude spectra of the cavity floor forced oscillation

Figure 7-3 shows the amplitude spectrum of the pressure fluctuation corresponding to the 2-D cavity duct system excited by the forced oscillation described by equation 7-1. The 2-D duct has 2 cavities attached to the middle of the duct on the top and bottom walls. The cavities are 25 mm in length and 25 mm in depth and the duct height is 150 mm. The amplitude spectrum is for pressure time trace at the middle of the cavity floor. The maximum frequency, f_e , of the random excitation is set to 10000 Hz. The floor of both cavities were forced to oscillate out of phase to excite the first transverse mode and to avoid exciting the longitudinal and the second transverse modes. The power spectrum shows a strong peak at 1110 Hz which corresponds to the first transverse mode. The finite element analysis solving the mass stiffness matrix for the same geometry results in a frequency of 1112 Hz. This demonstrates the good agreement between the current methodology, in the case of zero flow velocity, and the solution of the mass stiffness matrix. Numerous other peaks with smaller amplitudes appear in the spectrum. These peaks represent the combined transverse-longitudinal modes.

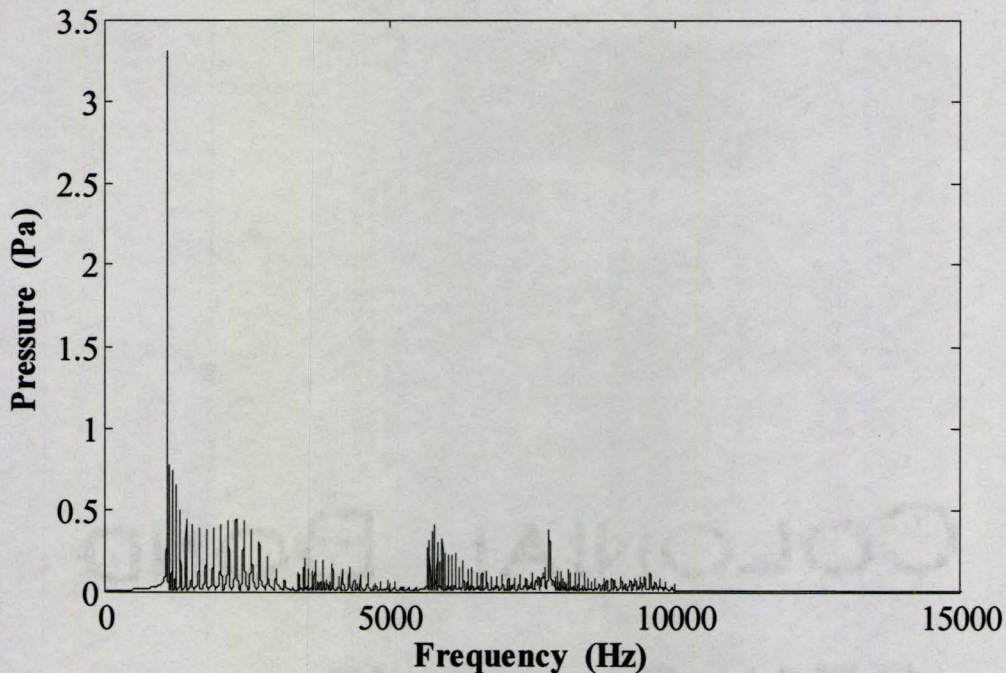


Figure 7-3 Spectrum of the pressure fluctuation resulting from the broad band excitation of the numerical domain

7.2. The effect of mean flow field on acoustic resonance

The investigation of the effect of the mean flow field on the acoustic resonance is presented in this section. The investigation provides explanation of some of the experimental observations discussed in chapter 4. It also details the changes in the first mode shape with the increase in the mean flow velocity. For the sake of simplicity, the investigation is based on the simulation of the 2-D planar cavity-duct system geometry to avoid any complexity arising due to the three dimensionality of axisymmetric geometry. Figure 7-4 shows a schematic of the geometry of the 2-D cavity-duct system. The duct has 2 cavities attached at the center on the top and bottom walls. The cavities have 25 mm length and 25 mm depth which is similar to the experimental base case discussed in section 4.2. The duct height is chosen to be 150 mm. A relatively long duct, 2 m, is considered to ensure that the artificial boundary conditions of zero pressure at the duct ends would not influence the general behaviour. Three different mean flow Mach numbers (0.1, 0.2, and 0.3) were simulated in addition to the case of zero flow.

A brief presentation of the results of the mean flow velocity is first presented to give an overview of mean flow field characteristics. This is followed by a description of the simulation of the acoustic field. The presentation of the output of the numerical simulation starts with the results of the random excitation of the different flow Mach numbers to show the effect of the mean flow field on the acoustic mode frequency. This is followed by the effect of the mean flow field on the acoustic mode shape. Finally, some physical

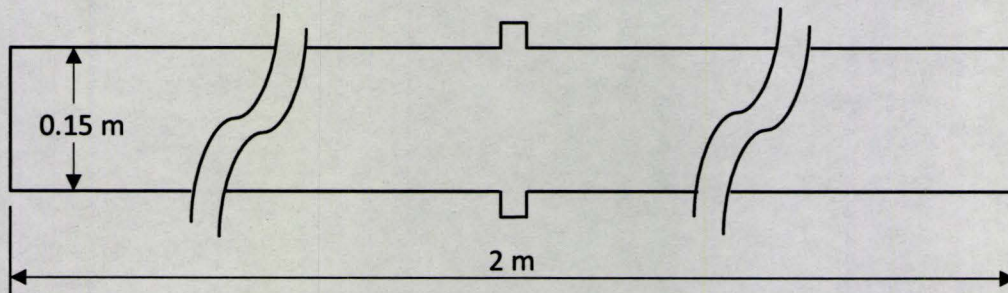


Figure 7-4 Schematic of the 2-D computational domain. Cavity length is 25 mm and cavity depth is 25 mm

interpretations of the observed effects are provided based on analytical analysis of simplified conditions.

7.2.1. Mean flow simulation

Figure 7-5 shows the profile of the normalized axial velocity over the cross section of the main pipe. This profile is calculated at the middle of the cavity length. For this case, the average mean flow velocity is 34m/s, which corresponds to Mach number of 0.1. For $M=0.2$ & 0.3 , the dimensionless velocity profiles are identical to the one shown in fig. 7-5. The dimensionless velocity profiles show uniform velocity over most of the duct width. The velocity decreases sharply as the cavity mouth is approached. The dotted lines in fig. 7-5 mark the location of the cavity mouth at both sides of the main duct. Inside the cavity itself, the rate of the velocity decrease is lower because of the circulation zone inside the cavity. The maximum axial velocity inside the cavity is about 20% of the average flow velocity.

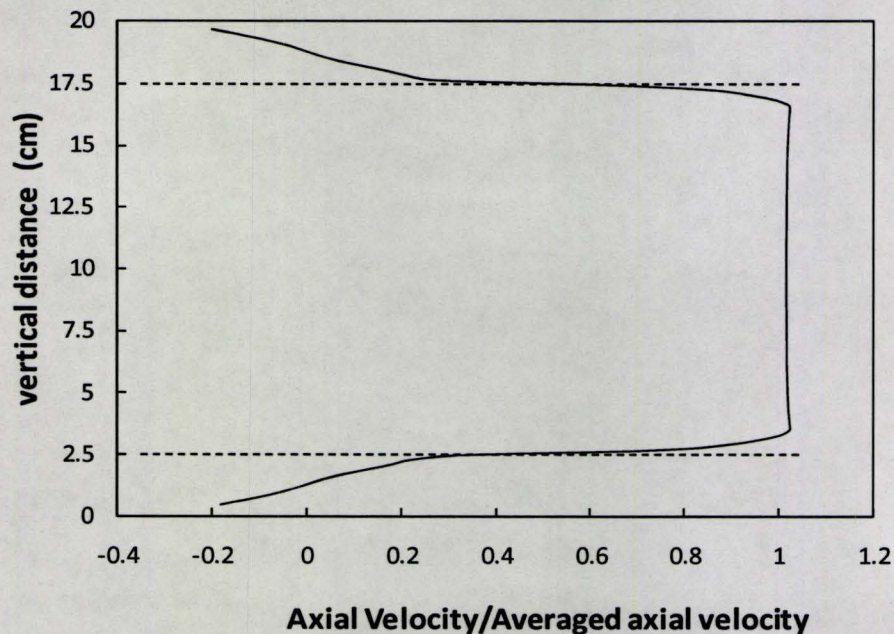


Figure 7-5 Dimensionless velocity profile of the mean flow at the middle of the 2-D computational domain for $M=0.1$. The dotted lines mark the cavity mouth

7.2.2. Effect of mean flow on the resonance frequency

The cavity-duct geometry was simulated considering different average mean flow Mach number. A uniform mesh with grid spacing of 1.5625 mm was used in the simulation of the different flow rates. With this grid spacing, about eight grid points existed within the free shear layer thickness. This is to ensure adequate representation of the effect of the velocity gradient of the free shear layer on the pressure wave propagation. Reducing the grid spacing to 1.25 mm changed the resonance frequency by about 0.5% at low Mach number. Moreover, with grid spacing of 1.25mm, the solution became unstable near the wall at Mach number of 0.3. Therefore, the 1.5625 mm grid spacing was used in the simulation of all the cases to ensure no effect from changing the grid spacing on the comparison between the resonance frequencies of the different flow Mach number cases.

Figure 7-6 shows the resonance frequency of the first transverse mode (f_1) for different mean flow Mach numbers as a ratio to the resonance frequency

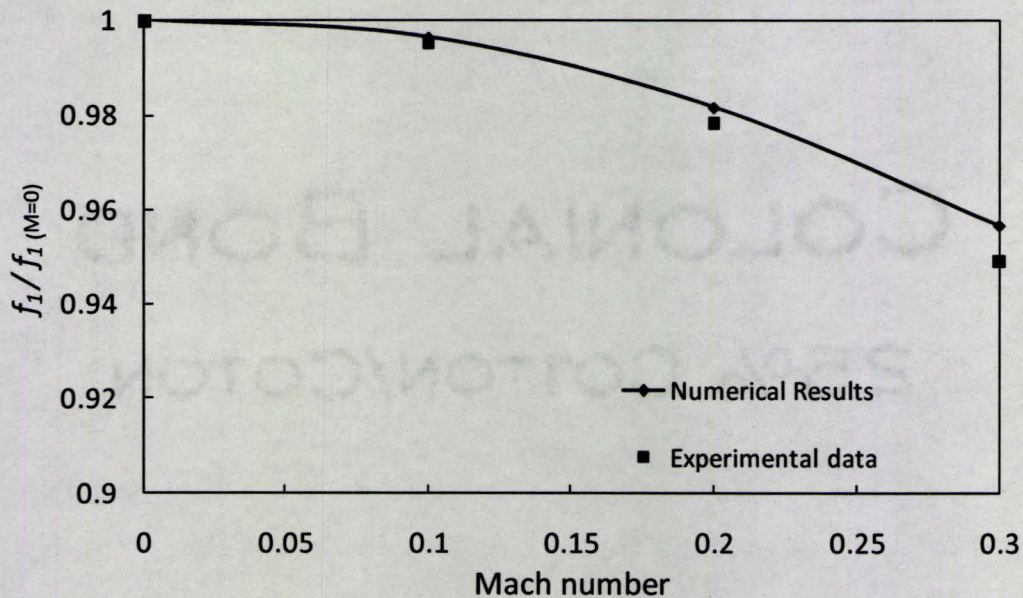


Figure 7-6 Dimensionless frequency of the first transverse mode as a function of the mean flow Mach number

at zero flow ($f_{1(M=0)}$). At zero flow velocity, the resonance frequency is 1109 Hz, which is about 0.975 of the cut-off frequency of the main duct. Referring to fig. 7-6, the numerical results show that the resonance frequency decreases with the flow Mach number. The rate of the frequency drop increases with the Mach number. Similar behaviour was observed in the experimental results as shown in fig. 7-6. The experimental data shown in fig. 7-6 corresponds to a cavity with 12.5 mm depth and 50 mm length. This experimental case has a resonance frequency at a very low flow velocity of about 0.975 of the main duct cut-off frequency. This ratio proved to be a good dimensionless parameter that can be used to characterize the impact of the mean flow on the resonance frequency. At a Mach number of 0.3, the difference between the experimental and numerical dimensionless frequencies is about 0.008 which is considered good given all the simplifications implemented in the numerical model.

7.2.3. Effect of mean flow on the mode shape

In this section, the effect of the mean flow on the mode shape of the first transverse acoustic mode is discussed. This includes the characterization of the effect of the mean flow on; (a) pressure amplitude; (b) the pressure phase; (c) the particle velocity amplitude and (d) the particle velocity phase.

To obtain the pressure and particle velocity fields, the numerical domain, which is shown in fig. 7-4, is excited at the resonance frequency by vibrating the cavity floor. The grid spacing used is the same as described in the previous section for the random excitation to ensure the same resonance frequency in both cases. The solution for the pressure field amplitude and phase was considered adequate when the change of the pressure amplitude at the cavity floor became less than 0.5% of the amplitude of the previous cycle. This requirement ensured that the effect of transient response on the results is negligible.

a) Amplitude of the acoustic pressure

Figure 7-7 shows the contour plot of the pressure amplitude of the first transverse acoustic mode. The plot corresponds to zero mean flow velocity. The plot shows that the maximum pressure amplitude is located at the center of

cavity floor. The amplitude decreases with the distance from the cavity center. This agrees with the general description of the transverse modes. For the cases with mean flow Mach numbers of 0.1, 0.2 and 0.3, the distribution of the pressure amplitude is similar to the distribution shown in fig. 7-7.

Figure 7-8 shows the ratio of the pressure amplitude along the duct wall and the cavity mouth to the pressure amplitude at the middle of the cavity floor for the four simulated mean flow Mach numbers. The x-axis is the distance measured from the center of the cavity. Also, it is important to mention that the flow direction is from the left to the right. For the four cases, the pressure amplitude decays exponentially with distance from the cavity. According to Kinsler et al. (2000), the exponential decay of a transverse wave with a frequency below the cut-off frequency of constant cross section infinite wave guide is given as follows:

$$P_a(x) = Ae^{-kkx} \quad 7-3$$

$$kk = \frac{\sqrt{\omega_k^2 - \omega^2}}{c} \quad 7-4$$

where, $P_a(x)$ is the pressure amplitude in the x-direction, ω_k is the cut-off frequency of the wave guide (rad/s), ω is the frequency of the decaying wave (rad/s) and c is the speed of sound.

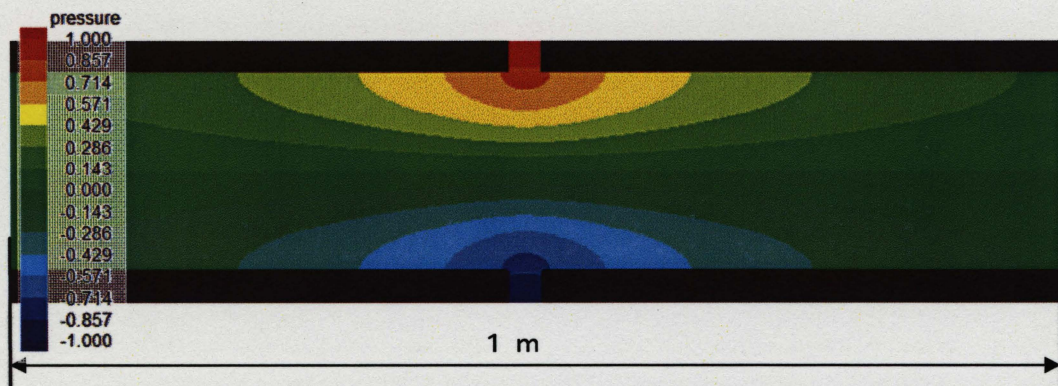


Figure 7-7 Contours of the pressure amplitude of the first transverse acoustic mode of planar cavity-duct system. $M=0$, $L=25\text{mm}$, $d=25\text{mm}$ and the duct height = 150mm .

For the case of zero flow, the cut-off frequency is 1136 Hz and the resonance frequency is 1109 Hz. Using equation 7-4, the exponential decay exponent, k , for the case of zero flow velocity is 4.475. From the numerical results, the exponential decay exponent is 4.47. This indicates the high level of accuracy in predicting the acoustic wave propagation using the current numerical method. For the other flow velocities, the exponential decay exponent decreases with the increase of the flow Mach number. For Mach number of 0.3, the decay exponent is 4.15 upstream of the cavity and 4.0 downstream of the cavity. The difference in the rate of decay between the upstream and downstream sides of the duct is evident in all the cases.

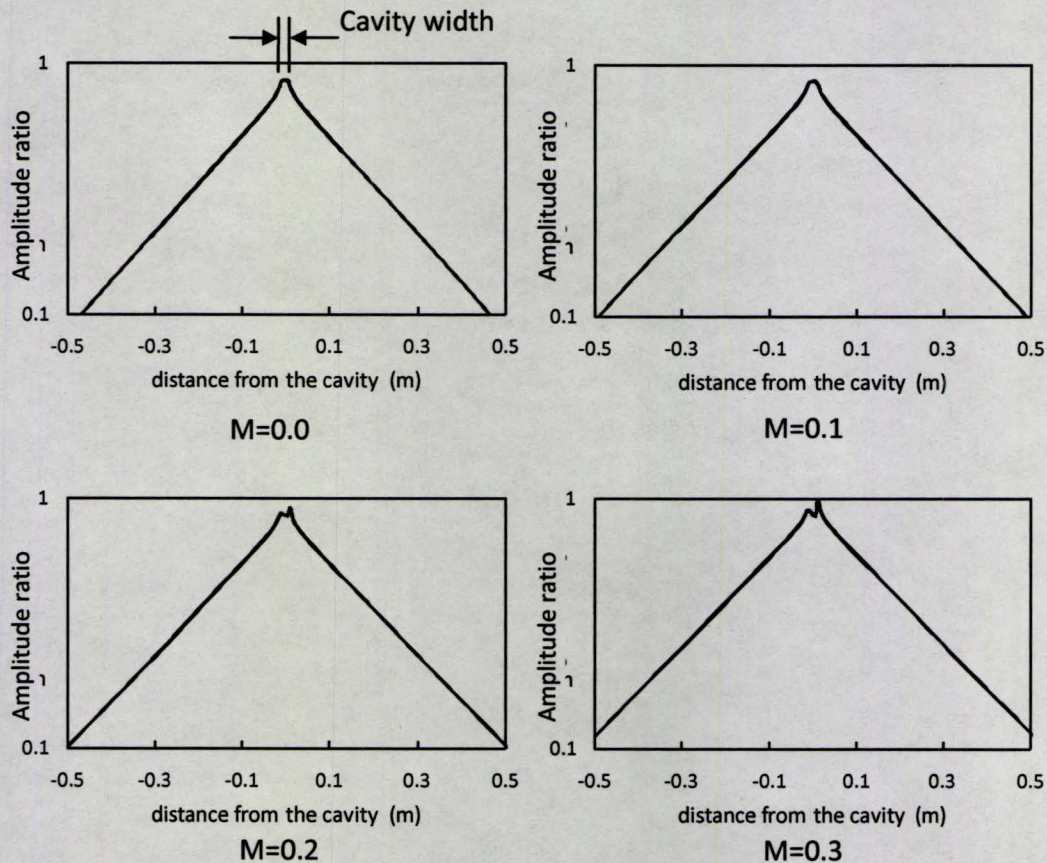


Figure 7-8 Pressure amplitude along the duct wall as a ratio to the amplitude of the pressure at the cavity floor. $L=25\text{mm}$, $d=25\text{mm}$ and the duct height = 150mm.

Referring back to fig. 7-8, the pressure amplitude at the cavity mouth is around 84% of the pressure amplitude at the cavity floor in the case of zero flow. As the Mach number increases, the pressure amplitude increases near the downstream edge of the cavity. At a Mach number of 0.3, the pressure amplitude at the downstream edge is almost equal to the amplitude at the center of the cavity floor.

b) Phase of the acoustic pressure

It is well known that, at zero flow, the change in the phase of the acoustic pressure of the first transverse acoustic mode along the axial direction of the duct is zero. In the transverse direction, the phase change is zero everywhere except across the duct centerline where the pressure switches polarity and a phase jump of 180° occurs. The current numerical results follow exactly this description at zero flow velocity. However, the numerical results show an axial change in the pressure phase when the mean flow velocity is greater than zero. Figure 7-9 shows several snap shots of the pressure contours over almost half a cycle. The snap shots are equally spaced in time. The mean Mach number is 0.2 and the flow direction is from the left to the right. As shown in these contour plots, the transverse mode travels upstream in the opposite direction to the flow. The traveling speed (group speed) and consequently the axial phase distribution are found to depend on the Mach number.

Figure 7-10 shows the distribution of the phase of the acoustic pressure in the axial direction for Mach numbers of 0.1, 0.2 and 0.3. These results correspond to the pressure distributions shown in fig. 7-8. The phase of the pressure at the mid-length of the floor of the top cavity is taken as a reference during the phase calculation. To determine the phase at a selected point, the time period between the occurrence of maximum pressure amplitude at this point and the occurrence of maximum amplitude at the middle of the cavity is calculated. Thereafter, this time difference is multiplied by the angular frequency to determine the phase difference between the selected point and the middle of the cavity floor. This procedure is repeated for all the grid point to obtain a comprehensive picture of the phase change within the computational domain.

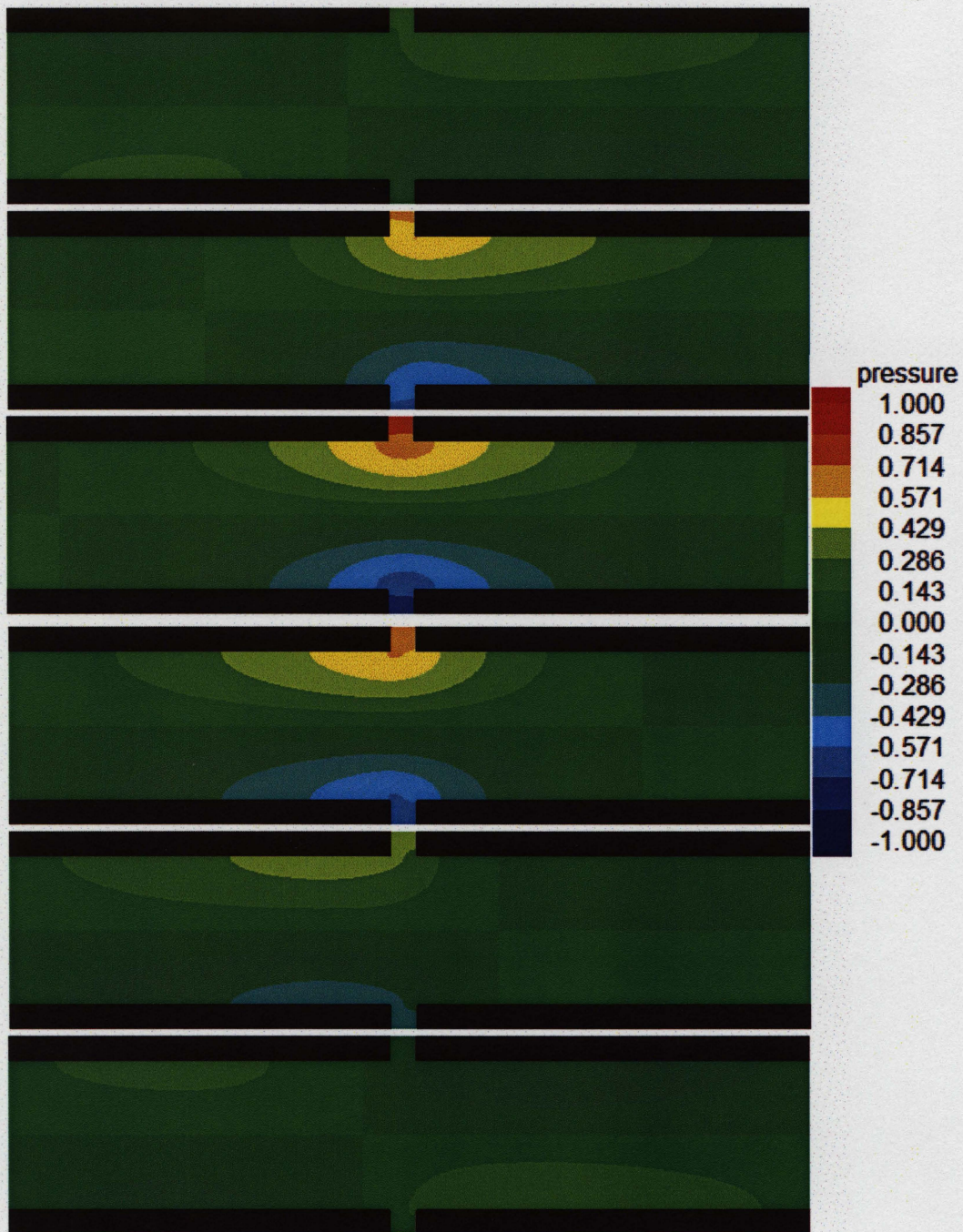


Figure 7-9 Snap shots of the contours of the acoustic pressure over half a cycle. The contours legend is just to demonstrate the relative amplitude of the contours. $M=0$, $L=25\text{mm}$, $d=25\text{mm}$ and the duct height = 150mm .

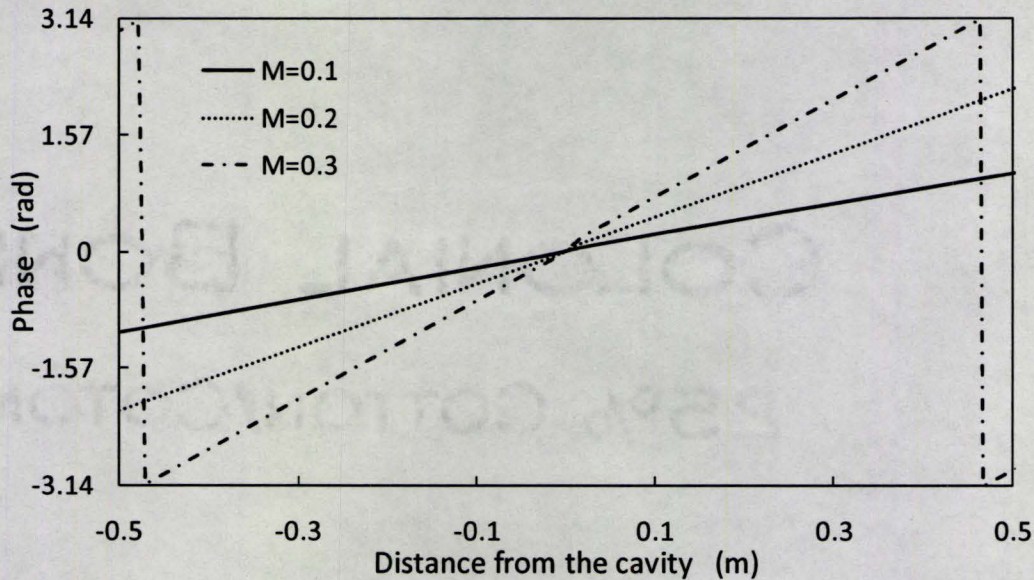


Figure 7-10 Variation of the pressure phase in the axial direction along the duct wall. $L=25\text{mm}$, $d=25\text{mm}$ and the duct height = 150mm .

As can be seen in fig. 7-10, the rate of the axial phase change appears to be constant along the axial direction. This rate increases with the increase of the Mach number. It is noteworthy that there is no phase change in the transverse direction except the change of pressure polarity at the center line, see fig. 7-9. To quantify the rate of the phase change, the axial phase speed was calculated. The phase speed is the speed at which the phase is propagating in a certain direction. The local phase speed was calculated as follow:

$$c_p = -\omega \frac{\Delta x}{\Delta \text{phase}} \quad 7-5$$

where, ω , is the angular frequency. The negative sign indicates that when $\frac{\Delta x}{\Delta \text{phase}}$ is positive the wave propagates in the negative x -direction. Figure 7-11 shows the distribution of the absolute value of the phase speed along the axial direction for $M=0.2$. The average phase speed away from the middle of the duct, where the cavity is located is about 1595 m/s . In the vicinity of the cavity location, the phase speed decreases. This phenomenon is observed also in the results of $M=0.1$ and 0.3 . The average phase speed for $M=0.3$ is about 1010 m/s and 3290

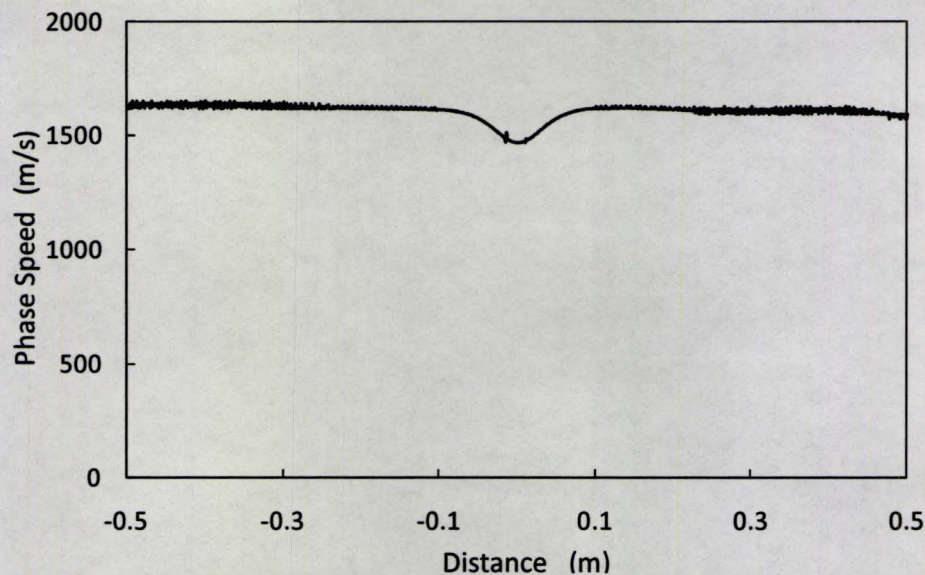


Figure 7-11 Axial Phase speed of the pressure for $M=0.2$. $L=25\text{mm}$, $d=25\text{mm}$ and the duct height = 150mm .

m/s for $M=0.1$. In a study of the aerodynamic excitation of the transverse mode of 2-D duct by the flow over two tandem cylinders, Mohany (2006) reported phase change in the axial direction of the same order as that observed in the numerical results.

c) Amplitude of the acoustic particle velocity

It has already been mentioned that the acoustic power production during the aerodynamic excitation of the acoustic resonance depends on the acoustic particle velocity distribution. More specifically, for the two-dimensional geometry under investigation, fig. 7-4, the power production depends on the vertical component of the acoustic particle velocity. Figure 7-12 shows the contour plot of the vertical particle velocity for zero flow condition. The results for Mach numbers of 0.1, 0.2 and 0.3 are found to be similar to the zero flow condition near the centerline of the duct, except that the location of the maximum particle velocity at the centerline shifts slightly downstream as the Mach number increases. As an example, for Mach number of 0.3, the location of the maximum particle velocity shifts by 7 mm downstream. However, the main changes in the amplitude of the vertical particle velocity occur at the cavity mouth where the acoustic power is produced.

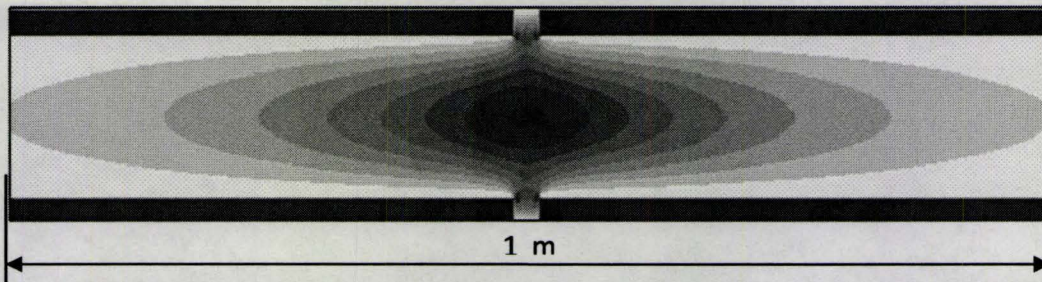


Figure 7-12 Contour plot of the amplitude of the vertical particle velocity at zero flow. $L=25\text{mm}$, $d=25\text{mm}$ and the duct height = 150mm .

Figure 7-13 shows the contour plots of the vertical particle velocity near the cavity mouth for the four studied flow Mach numbers. All figures correspond to the same acoustic pressure at the center of the cavity floor. At zero flow, the distribution of the particle velocity amplitude is symmetric with the amplitude increasing near the cavity edges. For a Mach number of 0.1, the amplitude is higher near the upstream edge of the cavity. For Mach numbers of 0.2 and 0.3, the maximum amplitude starts to move toward the downstream edge. These results demonstrate the significant change in the distribution of the vertical particle velocity with the mean flow Mach number. However, it is important to point out that smaller grid spacing would produce more accurate distributions of the particle velocity amplitude in the area of steep mean velocity gradient. This can be achieved without significant computational penalty by considering local refinement of the mesh.

d) Phase of the acoustic particle velocity

The phase distribution of the acoustic particle velocity is important in determining the Strouhal number at which the aerodynamic excitation of the transverse mode reaches its maximum strength. In this section, the change of the phase distribution of the vertical particle velocity with the mean flow Mach number is discussed. Figure 7-14 shows four snap shots of the vertical particle velocity contours over half a cycle. The snap shots are equally spaced in time. The Mach number for these snap shots is 0.2 and the flow direction is from the left to the right side. As shown in the contour plots, the vertical particle velocity follows the pressure in the main duct, fig. 7-9, by traveling upstream in the opposite direction to the flow. However, in the area surrounding the cavity free

shear layer and inside the cavity, the contours of the vertical particle velocity progress downstream with the mean flow. Similar behaviour is observed in the other two cases with $M=0.1$ & 0.3 .

Figure 7-15 shows the distribution of the phase of the vertical particle velocity along the cavity mouth of the top cavity for Mach numbers of 0.1, 0.2 and 0.3. The pressure at the mid-length of the floor of the top cavity is taken as a reference during the phase calculation. The phase is calculated following the same procedure used to calculate the phase distribution of the pressure. For zero flow, the numerical results show that the phase between the pressure and particle velocity is nearly constant with an average of $\pi/2$, which agrees with the analytical results of constant phase of $\pi/2$. The small error in the numerical solution arises from the physical singularity at the cavity corners. For Mach numbers of 0.2 and 0.3, the phase distribution over the mouth is almost linear.

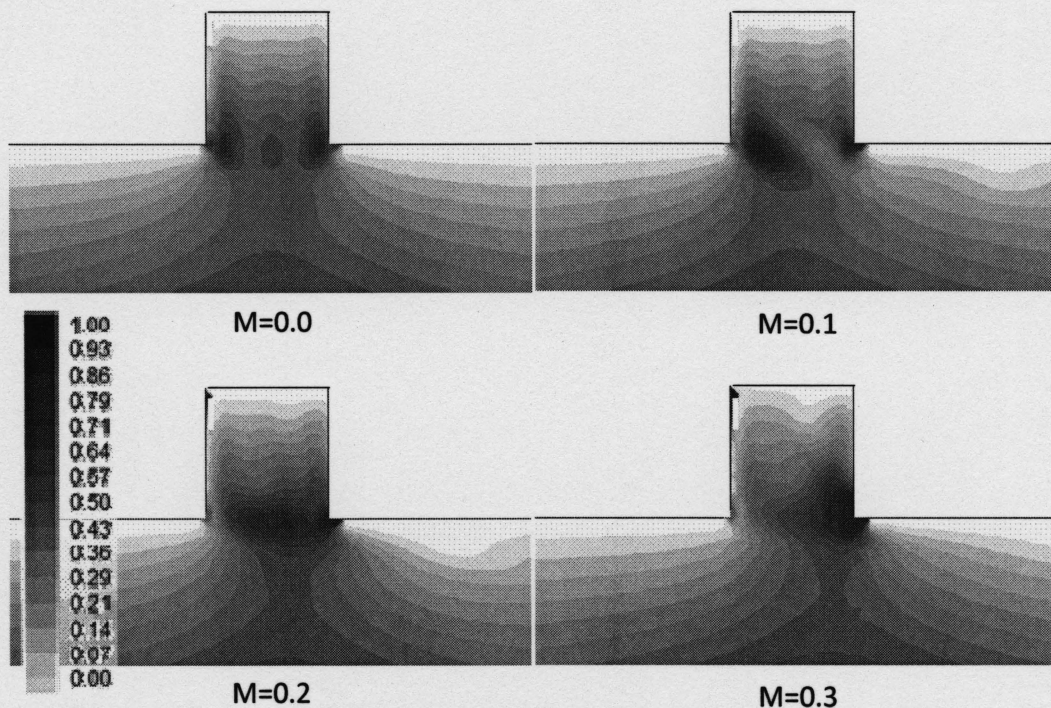


Figure 7-13 Contour plots of the amplitude of the vertical particle velocity. The contours legend is just to demonstrate the relative amplitude of the contours. $L=25\text{mm}$, $d=25\text{mm}$ and the duct height = 150mm .

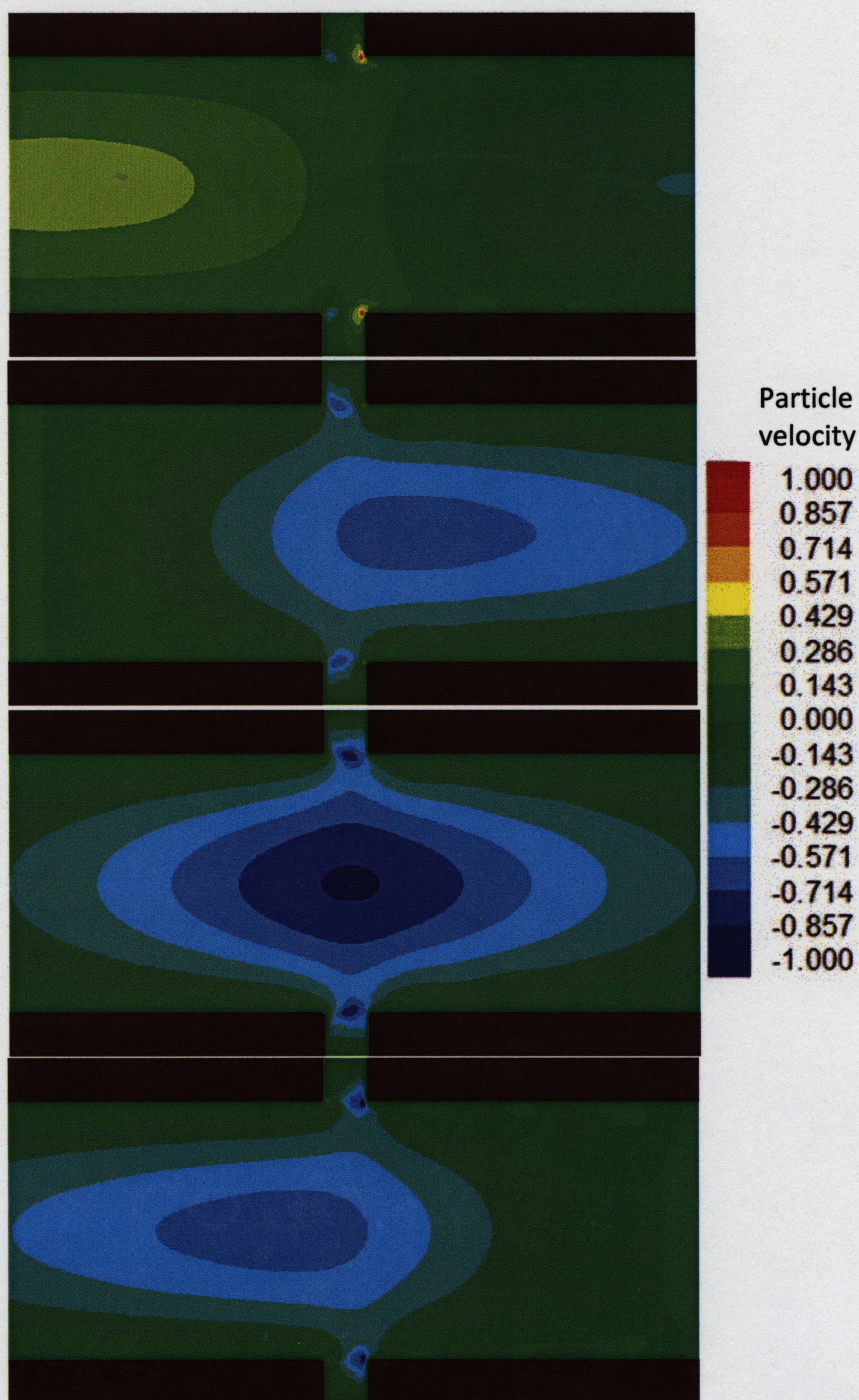
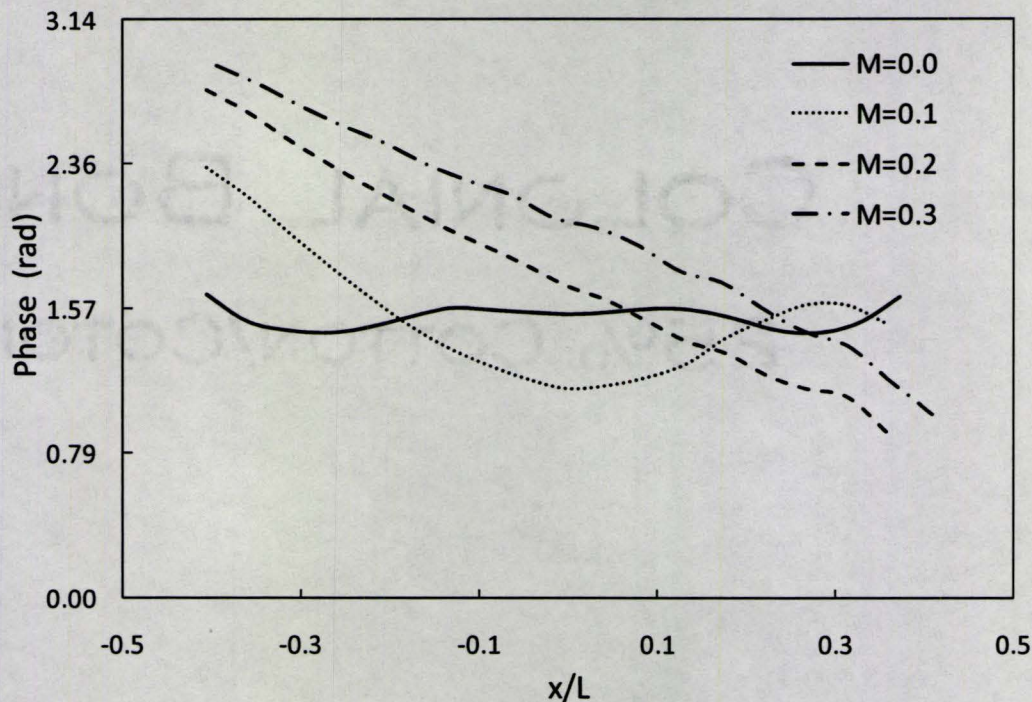


Figure 7-14 Snap shots of the vertical particle velocity contours for $M=0.2$. The contours legend is just to demonstrate the relative amplitude of the contours.



**Figure 7-15 Phase of the vertical particle velocity along the cavity mouth.
L=25mm, d=25mm and the duct height = 150mm.**

For Mach number of 0.1, the phase decreases steadily over the upstream half of the cavity mouth and fluctuates around $\pi/2$ over the downstream half. The rate of the phase change decreases slightly with the increase in the Mach number and, on average, the phase difference increases with the increase of the Mach number.

7.2.4. Analytical consideration and comparison with numerical simulation

a) Analytical study of axial modes of straight duct

The effect of the mean flow with uniform velocity profile on the axial modes of a straight duct is studied analytically in this section. The objective is to provide a validation of the numerical results via comparing it to the analytical results. Also, the analytical study yields simplified formulas that can be used to evaluate the phase speed obtained from the numerical simulation.

The axial acoustic mode can be represented by two waves of equal amplitude and frequency traveling in opposite directions. The superposition of the two waves describes the waveform of a standing wave with the same frequency. The wave traveling downstream with the flow is propagating with speed equal to $(c+U)$, where c is the speed of sound in quiescent medium and U is the mean flow velocity. On the other hand, the wave traveling upstream opposite to the flow is propagating with a speed equal to $(c-U)$. Assuming that the flow is in the positive direction of the axis and A is the wave amplitude, the problem can be formulated as follow:

$$p_a = A \left(e^{i\omega(t - \frac{1}{(c+U)}x)} + e^{i\omega(t + \frac{1}{(c-U)}x)} \right) \quad 7-6$$

$$p_a = Ae^{i\omega t} \left(e^{-\frac{i\omega}{(c+U)}x} + e^{\frac{i\omega}{(c-U)}x} \right) \quad 7-7$$

$$p_a = Ae^{i\omega t} \left(e^{\frac{i\omega(U-c)}{(c^2-U^2)}x} + e^{\frac{i\omega(c+U)}{(c^2-U^2)}x} \right) \quad 7-8$$

$$p_a = 2A \cos\left(\frac{\omega c}{(c^2-U^2)}x\right) e^{i\omega(t + \frac{U}{(c^2-U^2)}x)} \quad 7-9$$

From equation 7-9, the result of the superposition of the two waves is a standing wave with wavelength of $\frac{2\pi(c^2-U^2)}{\omega c}$. The standing wave form is multiplied by a propagating waveform with phase speed of $\frac{(c^2-U^2)}{v}$. These formulas agree with the literature on the effect of mean flow on sound wave propagation in ducts (Eversman, 1991). The phase can be rewritten in terms of the Mach number as follow:

$$c_p = c \left(\frac{1}{M} - M \right) \quad 7-10$$

Table 7-1 lists the phase speed at different Mach numbers as calculated using equation 7-10 and as estimated from the numerical simulation of the transverse mode. The difference between the results of the two methods is 2-3% of the mean value. This provides a physical explanation of the numerical results as well as a fundamental understanding of the effect of the mean flow on the

transverse acoustic mode Also, equation 7-10 provides a simple way to estimate the phase speed.

Table 7-1 The phase speed at different Mach numbers

Mach Number	Theoretical axial mode	Numerical simulation of transverse mode
0.1	3366 m/s	≈3160-3400 m/s
0.2	1632 m/s	≈1595 m/s
0.3	1031 m/s	≈1010 m/s

b) Analytical study of transverse modes of straight duct

In this section, an investigation of the transverse mode of infinite straight duct with uniform flow is performed to provide an explanation of the drop of the resonance frequency with the increase in the Mach number. The resonance frequency of the first transverse mode is given by:

$$f = \frac{c_t}{2h} \quad 7-11$$

where, c_t is the speed of wave propagation in the transverse direction and h is the height of the duct. For the wave to travel straight in the transverse direction without being convected in the flow direction, the wave has to have a propagation component in the opposite direction of the flow. This component is needed to overcome the convection effect of the mean flow. Therefore, the propagation speed in the axial direction, c_a , is equal to the convection speed of the mean flow, v , and in the opposite direction. The propagation speeds in the axial and transverse directions can be related to the sound speed as follow:

$$c^2 = c_t^2 + c_a^2 \quad 7-12$$

$$c_t = \sqrt{c^2 - c_a^2} \quad 7-13$$

$$c_t = c\sqrt{1 - M^2} \quad 7-14$$

where, M is the Mach number of the mean flow. The frequency calculated using equations 7-11 and 7-14 is compared to the results of the 2-D numerical simulation of a cavity with a depth of 1.25 cm and a length of 2.5 cm. The small cavity was chosen to ensure that the transverse mode of the cavity-duct system is very close to the transverse mode of the straight duct. The first transverse mode frequency of this cavity-duct system is 0.994 of the cut-off frequency of the duct at zero flow velocity. The results of the two methods are in good agreement with differences less than 1-2%.

Figure 7-16 shows the frequency of the transverse mode calculated using equations 7-11 and 7-14 for different Mach numbers as a ratio to the frequency of the same mode at zero flow. The same quantity is plotted for the experimental data of the axisymmetric cavity with $L/d=2$, $d/D=1/12$. This experimental case has a diametral resonance frequency of 0.99 of the cut-off frequency of the main pipe at zero flow velocity. The trend of the experimental data and the analytical prediction is the same. However, the experimental data is slightly lower than the analytical prediction.

As already mentioned in chapter 4, the drop in the resonance frequency decreases with the increase of the size of the cavity. The increase of the cavity dimensions, especially the cavity depth, transforms the transverse mode of the cavity-duct system from being similar to the transverse mode of straight duct to being similar to the acoustic mode inside the cavity. The experimental data indicates that such a transition is achieved when the ratio of the diametral resonance frequency at zero flow velocity to the cut-off frequency of the main pipe is about 0.8 or less. This value can change slightly depending on the cavity length to depth ratio.

7.3. Axisymmetric cavity-duct system

In this section, the results of the 3-D simulation of an axisymmetric cavity-duct system are presented. This aims to determine the differences, if any, in the effect of the mean flow on the acoustic mode between the 3-D and 2-D cases. Simulations were performed for four different mean flow Mach numbers ($M=0.0, 0.1, 0.2$ & 0.3). The numerical mesh that was used in the simulations is

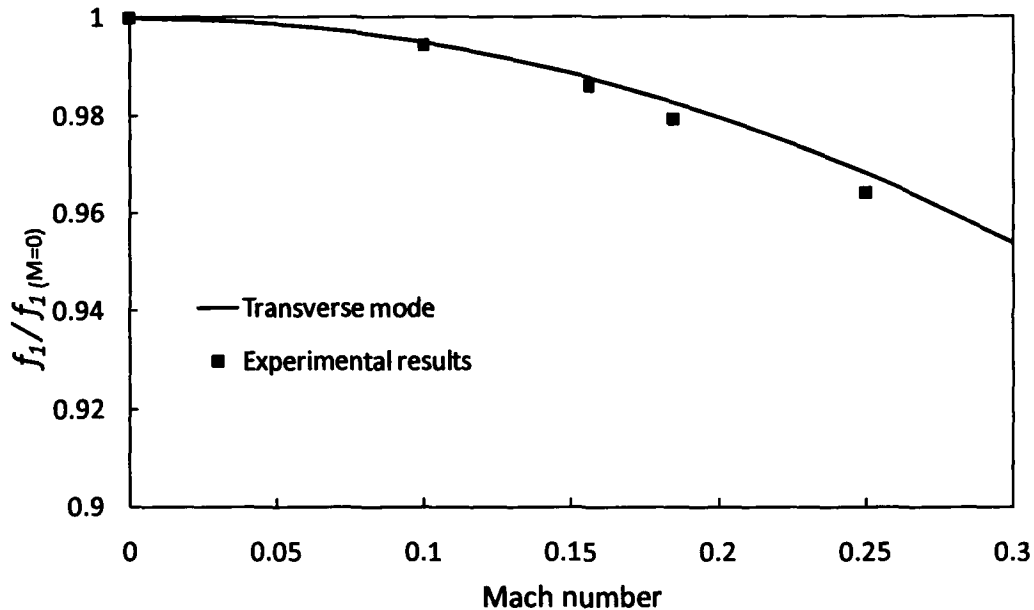


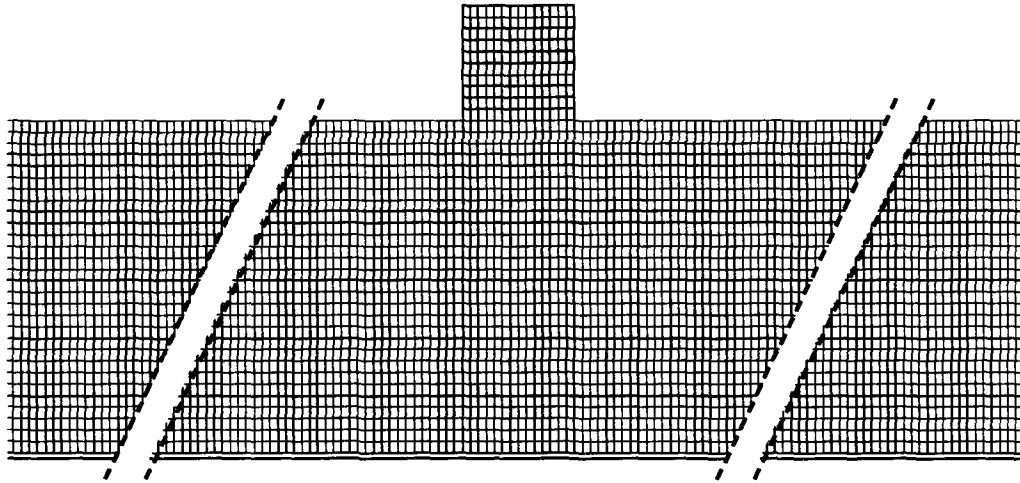
Figure 7-16 Dimensionless frequency of the first transverse mode as a function of the mean flow Mach number. Experimental data is for $L/d=2$, $d/D=1/12$.

presented in subsection 7.3.1. In subsection 7.3.2, the effects of the mean flow on the resonance frequencies and the mode shape are discussed with focus on comparing the results with those of planar 2-D results.

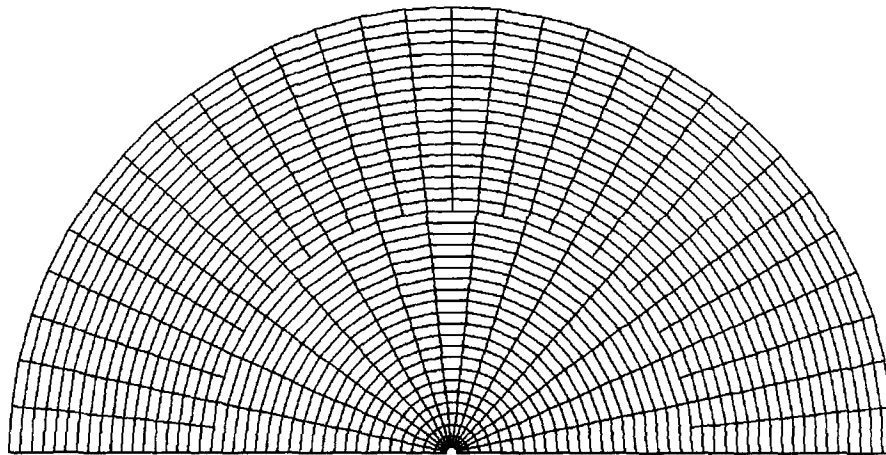
7.3.1. Numerical mesh

Figure 7-17 shows the longitudinal and circular cross sections of the mesh used in the simulations. Taking advantage of the properties of the first diametral mode, only half of the duct cross section is simulated, with imposing asymmetric boundary conditions at azimuthal angles of zero and π . This configuration limits the simulation to the first diametral mode. The dimensions of the experimental test section were used for the numerical simulation with the cavity length and depth taken to be 25 mm.

The grid spacing in the longitudinal direction was set to 1.785714 mm, which results in 14 grid points along the cavity length. The grid spacing in the radial direction was set to 2.5 mm. Thirty one grid points were used in the



Longitudinal Cross section



Circular Cross section

Figure 7-17 longitudinal and circular cross section of the mesh used in the simulation of the axisymmetric geometry. $L/d=1$ and $d/D=2/12$.

azimuthal direction. However, the grid azimuthal spacing is proportional to the radial location on the grid. Therefore, it decreases dramatically as the radius approach zero. The decrease of the grid spacing limits the maximum time step that can be used for the marching scheme. In order to increase the maximum time step that can be used, the number of the grid points in the azimuthal direction was reduced to half for the region within a radius of 5.5 cm. This ensured that the change in the azimuthal spacing is away from the free shear layer region.

The reduction of the number of grid points in the azimuthal direction generated an internal boundary in the radial direction at the truncated radial grid lines, as can be seen from the circular cross section in fig. 7-17. The internal boundary was resolved by interpolating the backward derivatives for end points of these grid lines based on the continuous grid lines values.

7.3.2. Effect of mean flow on the resonance frequency

Figure 7-18 shows the decrease in the dimensionless frequency of the first diametral mode with the mean flow Mach number. Both the numerical results and the experimental data are presented. The difference between the experimental and numerical values is about 0.01 at a Mach number of 0.27. This agreement is good given the simplifying assumptions which were made in the numerical simulation. Moreover, this is also consistent with the comparison between the 2-D simulations and the experimental data. This indicates that the numerical model captures the main physical mechanism responsible for the reduction in the resonance frequency.

7.3.3. Effect of mean flow on the mode shape

The mode shape of the diametral mode is perfectly predicted with the 3-D axisymmetric numerical code. Figure 7-19 shows the mode shape of the diametral mode in terms of the pressure amplitude contours as predicted by the numerical code for zero flow velocity. The maximum pressure is located at the orientation where the cavity floor is forced to oscillate. The comparison with the finite element results, fig. 3-8, shows a good agreement between the two methods.

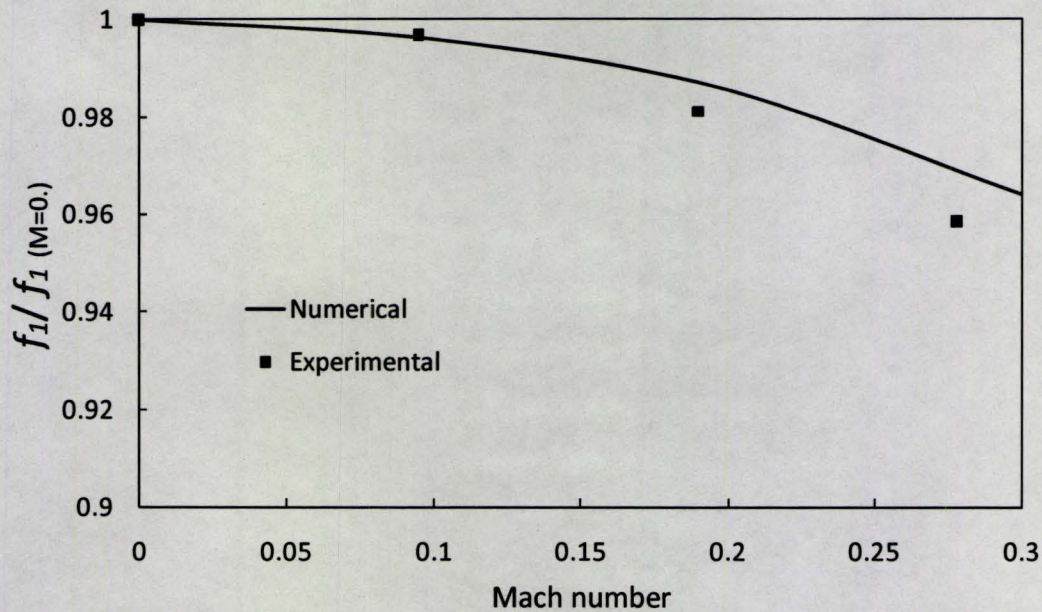


Figure 7-18 Dimensionless frequency of the first diametral mode as a function of the mean flow Mach number. $L/d=1$ and $d/D=2/12$.

The change in the mode shape of the diametral acoustic resonance with the Mach number is consistent with the change observed in the 2-D simulation with very minor differences. The change in the pressure amplitude with the mean flow Mach number follows perfectly fig. 7-8, with a slight change in the decay rate because of the difference in the ratio of the resonance mode frequency to the cut-off frequency between the two cases. The pressure axial phase distribution, shown in fig. 7-20, is also similar to the 2-D axial phase distribution, fig. 7-10. The phase speed for the 3-D simulation is on average 3% lower than the phase speed of the 2-D simulation.

Another example of the similarity is the change in the radial particle velocity with the mean flow Mach number. Figure 7-21 shows the contour plots of the radial particle velocity amplitude near the cavity mouth for the four Mach numbers that were simulated. Comparing these plots with the plots for the transverse component of the particle velocity for the 2-D case in fig. 7-13 shows that the effect of the Mach number on the location of the high velocity region is similar in both cases. However, the slight differences between the two sets of

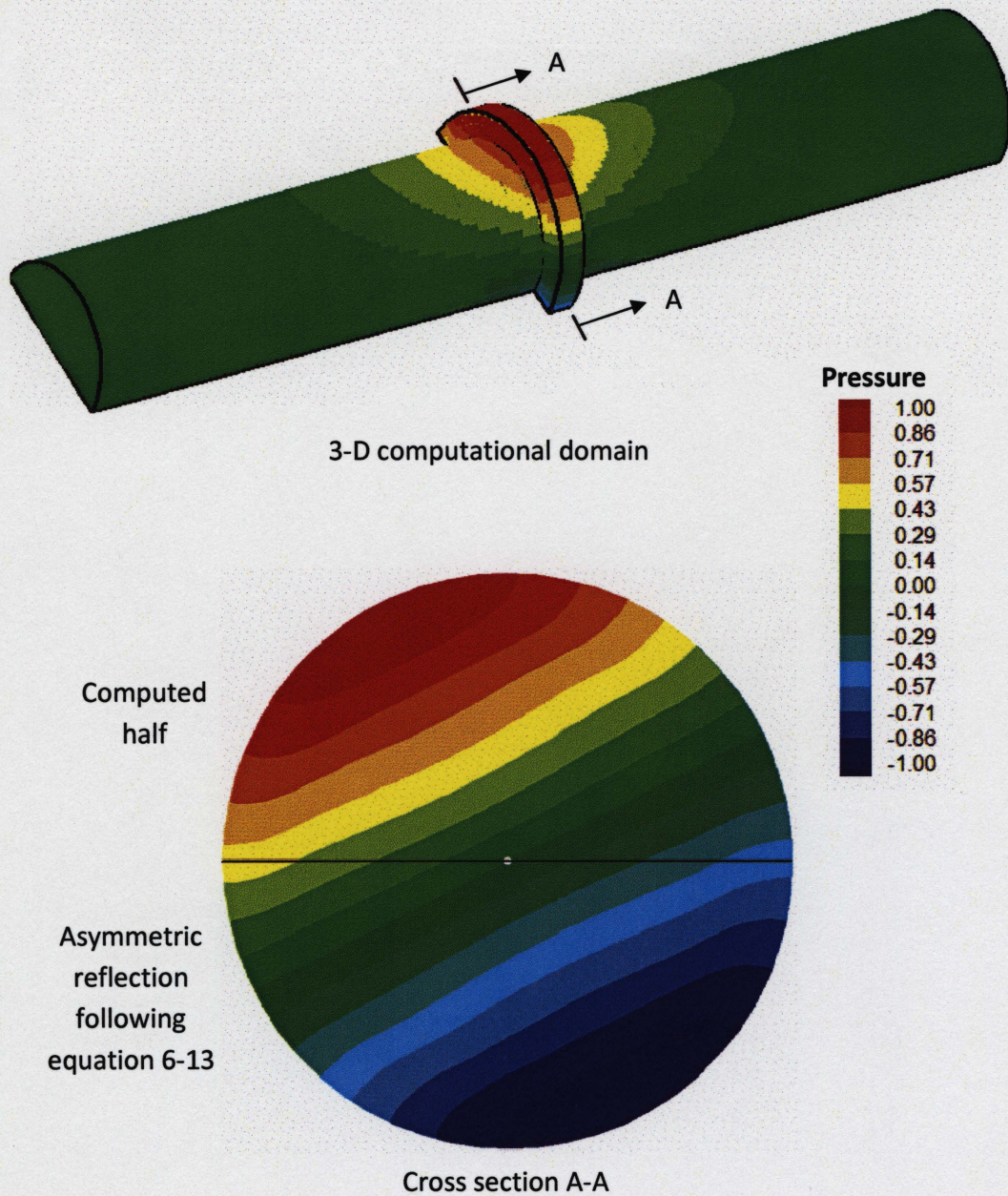


Figure 7-19 Mode shape of the first diametral mode in terms of the contours of the pressure amplitudes. The contours legend is just to demonstrate the relative amplitude of the contours. $M=0.0$, $L/d=1$ and $d/D=2/12$.

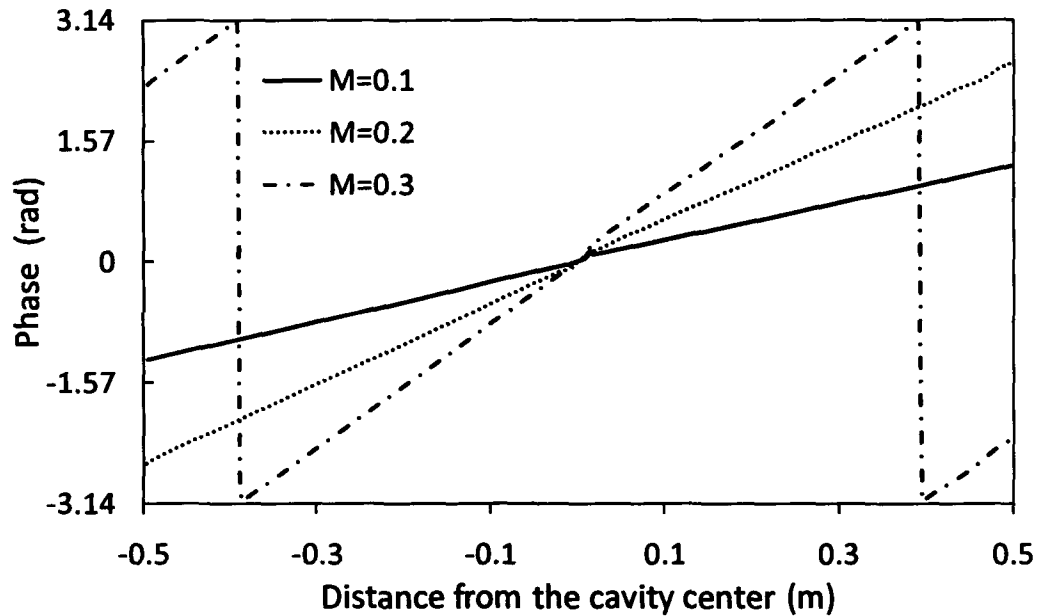


Figure 7-20 Variation of the first diametral mode pressure phase in the axial direction along the duct wall. $L/d=1$ and $d/D=2/12$.

plots can be attributed to the difference in the physical geometry. Also, the axial phase of the radial velocity over the cavity mouth, shown in fig. 7-22, is very similar to the data of the 2-D simulation plotted in fig. 7-15. The slight differences between the two cases can be attributed to the difference in the shear layer velocity profile and the physical geometry. It is important to note that the trends, with which the pressure and radial particle velocity change with the Mach number, were found to be independent of the azimuthal angle.

To conclude, the comparison between the 3-D and 2-D simulations demonstrates that there is no significant difference between the two cases. The differences in the physical geometry explain the slight variation between the two cases. Therefore, all the analysis conducted on the 2-D geometry can be extended to the 3-D case.

7.4. Summary

A numerical simulation study has been performed to determine the effect of the mean flow on the acoustic mode of 2-D planar and 3-D axisymmetric

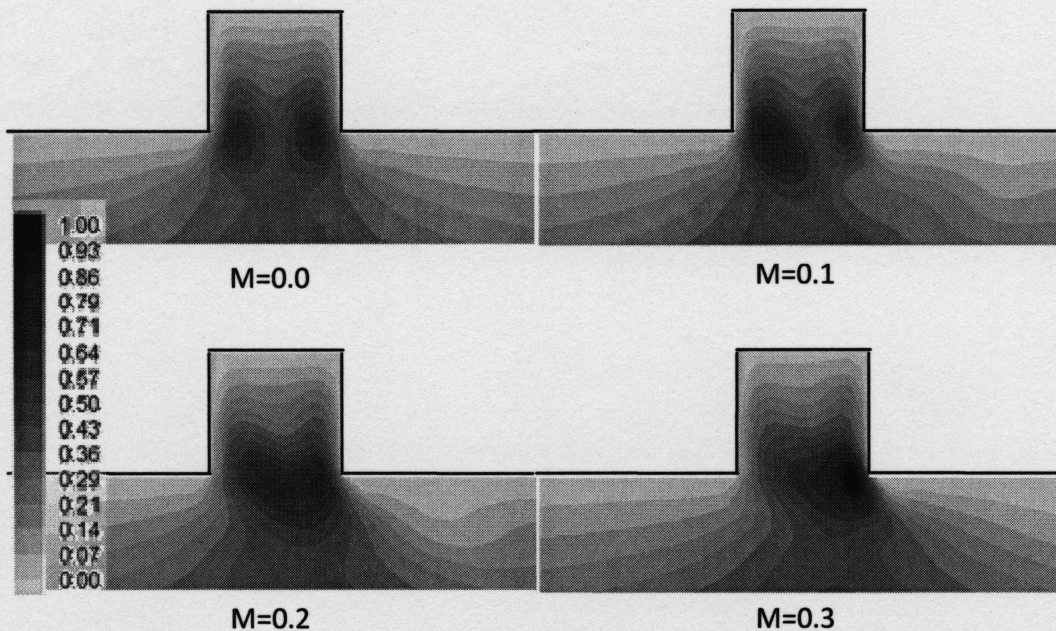


Figure 7-21 Contour plots of the amplitude of the radial particle velocity of the first diametral mode. The contours legend is just to demonstrate the relative amplitude of the contours. $L/d=1$ and $d/D=2/12$.

cavity-duct systems. Four different mean flow Mach numbers ($M=0.0, 0.1, 0.2$ & 0.3) have been considered in the investigation. Also, an analytical study of the longitudinal and transverse modes of straight duct has been performed. The numerical results show that the effect of the mean flow on the 2-D and the 3-D acoustic modes is the same. The two geometries have been found to behave similarly with the increase of the mean flow Mach number.

The numerical simulation shows that the frequency of the acoustic mode decreases with the increase of the mean flow Mach number. This is in full agreement with the experimental results discussed in chapter 4. The results of the analytical study of the transverse mode of a straight duct show that the decrease in the frequency is caused by the increase in the effective wavelength due to the mean flow convection effect. The axial phase gradient of the pressure and particle velocity is developed also due to the convection effect of the mean flow. The phase speed corresponding to this gradient is in the opposite direction of the mean flow, except near the cavity mouth where the particle velocity phase

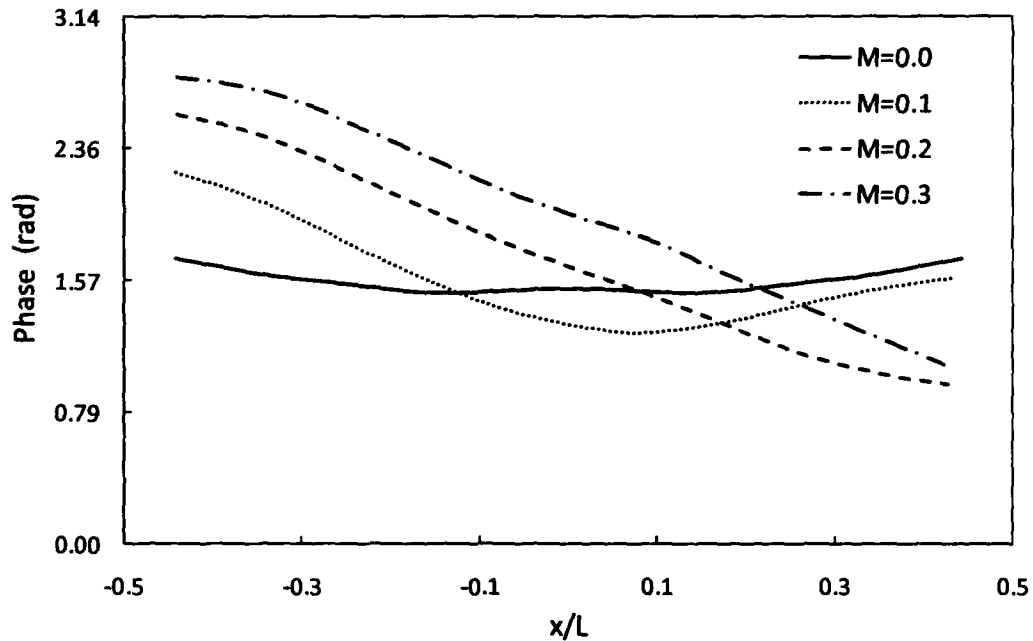


Figure 7-22 Phase of the first diametral mode radial particle velocity along the cavity mouth. $L/d=1$ and $d/D=2/12$.

speed is in the same direction as the mean flow. The phase speed away from the cavity mouth can be calculated using an analytical relation derived from the effect of mean flow on longitudinal mode. The amplitude of the pressure field does not change noticeably due to the mean flow. However, the particle velocity amplitude near the cavity mouth changes significantly with the mean flow. The particle velocity amplitude near the downstream corner increases with the Mach number.

CHAPTER 8

SUMMARY AND CONCLUSIONS

The aerodynamic excitation of the diametral modes of an axisymmetric cavity-duct system has been investigated. The diametral modes are classified as trapped modes for which the associated acoustic pressure level decays exponentially with axial distance away from the cavity. An experimental setup of a cavity-duct system has been devised to facilitate the study of the excitation process up to Mach number of 0.4. Different cavity dimensions have been investigated, focusing on the shallow cavity aspect ratio (cavity length to depth ratio ≥ 1). Three different cavity depths have been investigated with cavity depth, d , to pipe diameter, D , ratios of $1/12$, $2/12$ & $4/12$. For each depth, the cavity length, L , was changed from $L/D=2/12$ to 1. The characteristics of the upstream boundary layer have been determined using a hotwire anemometer. The acoustic response has been measured by a series of pressure transducers flush mounted on the cavity floor at different azimuthal angles.

The experimental results demonstrate the strong susceptibility of the diametral modes to the aerodynamic excitation when the Mach number is higher than 0.1. The diametral modes are excited systematically by the lowest 4 shear

layer modes. The strongest resonances are those excited by the first shear layer mode.

The pressure amplitude at resonance decreases with the increase in the ratio between the cavity length and the pipe diameter, L/D , as a result of the change in different aerodynamic factors. Most important is the increase of the three dimensionality of the shear layer oscillation which alters the azimuthal phase distribution of the velocity fluctuations and consequently reduces the integral acoustic power generation. The hydrodynamic instability and the increase of the shear layer mode number also contribute to the decrease in the pressure amplitude. The excitation of the longitudinal modes has been observed for $L/D > 1/2$. The excitation level increases with the increase of L/D . This trend is the opposite of that of the diametral modes, which are more liable to excitation by short cavity length. The excitation of the longitudinal modes dominates the aeroacoustic response for $L/D \geq 5/6$.

The cavity depth to pipe diameter ratio, d/D , is found to alter the diametral mode shapes strongly, especially at the free shear layer region. Generally, the increase of this ratio leads to the increase of the radial acoustic particle velocity at the shear layer zone and consequently the acoustic power generation. The level of this increase depends on the diametral mode order, as a low order mode experiences a higher level of increase compared to a relatively higher order mode. The Strouhal number of the excitation is found to be a function only of the cavity length to cavity depth ratio, L/d , with no significant change with the Mach number or any other tested parameter.

The azimuthal behaviour of the diametral modes has been investigated with multiple pressure transducers measuring simultaneously the pressure oscillations at different orientations at the cavity floor. The analysis of the data has shown that the aerodynamically excited diametral modes are very likely to be spinning modes when the cavity-duct system is perfectly axisymmetric. Small geometrical deviations from axisymmetry or localized damping introduce orientation preferences that result in partially spinning behaviour. However, the increase of the Mach number restores the spinning behaviour ($M > 0.2$). The partially spinning mode is a spinning mode with modulating amplitude over the

circumference similar to the stationary mode. For long cavities ($L/D > 1/2$), the orientation changes randomly with time, which can be attributed to the three dimensionality and the randomness in the free shear layer (oscillation) and consequently the randomness of the acoustic power source.

An analytical model has been developed which adequately describes the different azimuthal behaviours observed during the experiments. The model consists of the superposition of two spatially orthogonal stationary modes with 90° temporal phase shift between them. The ratio of the amplitudes of the two modes determines the degree of the mode spinning. The model is used to explain the nature of the partially spinning behaviour, which includes, time dependent, azimuthal phase and amplitude distributions. Also, the model has been successful in predicting the degree of spinning and the orientations of the maximum and minimum amplitudes.

A geometrical preference was introduced into the cavity by inserting multiple acrylic plates inside the cavity. For this configuration, two orthogonal modes with slightly different frequency were excited simultaneously. These results demonstrated that the azimuthal coherence of the shear layer is not a necessity for the excitation of the diametral modes and that the diametral mode can be excited by only a portion of the shear layer.

The azimuthal behaviour of the cavity shear layer was characterized using two hotwire anemometers. The radial distribution of the free shear layer fluctuation has been measured first to determine a suitable radial position for the anemometers. The results showed that the azimuthal phase of the shear layer is identical to that of the acoustic pressure. Therefore, it can be concluded that the azimuthal phase in the shear layer is controlled by the acoustic perturbation.

The effect of the mean flow on the diametral modes was investigated numerically. A numerical code was developed based on the two-step computational aeroacoustics approach. In the first step, the mean flow was simulated by solving steady state Reynolds Average Navier-Stokes equations. In the second step, the unsteady acoustic field was simulated considering the mean

flow field to be constant. This involved solving a system of linearized acoustic perturbation equations. In this approach, the acoustic effect on the mean flow and the aeroacoustics sources were not considered. A FORTRAN finite difference code was developed to solve the linearized acoustic perturbation equations. Two-dimensional planar and three-dimensional axisymmetric versions of the code were developed. The simulations were performed for a 2-D planar cavity geometry and also a 3-D axisymmetric cavity geometry for four different mean flow Mach numbers ($M = 0.0, 0.1, 0.2$ & 0.3).

The numerical simulation shows that the frequency of the acoustic mode decreases with the increase of the mean flow Mach number, which is in full agreement with the experimental results. The analytical study of the transverse mode of a straight duct shows that the decrease in the frequency is due to the increase in the effective wavelength due to the mean flow convection effect. Also, the mean flow convection effect results in an axial pressure phase gradient. The amplitude of the phase speed depends on the mean flow Mach number and its direction is always opposite to the mean flow direction. The analytical analysis of longitudinal modes has provided a relationship that estimates the value of the phase speed based on the Mach number. The phase and amplitude of the particle velocity change significantly near the cavity shear layer with the Mach number. The amplitude of the particle velocity increases near the downstream corner with the increase in the Mach number. The phase speed of the particle velocity at the cavity shear layer is in the direction of the mean flow and its value changes with the Mach number.

8.1. Research contributions

The present research has provided a fundamental understanding to the interaction mechanism between the diametral modes and the axisymmetric cavity shear layer. It also has demonstrated the important effect of the mean flow on the acoustic mode shape. The main contributions of this research are:

- 1) The test results have clarified the range of the cavity length to pipe diameter ratio over which the self-excitation of the diametral modes dominates the aeroacoustic response of cavity-duct systems.

- 2) The effect of cavity depth on the susceptibility of various diametral modes to the aerodynamic excitation has been clarified.
- 3) The azimuthal characteristics of the aeroacoustic response have been revealed, understood and documented. This includes the characteristics of the acoustic mode, the free shear layer oscillations and the interaction between them.
- 4) An analytical model has been developed to describe and quantify the different azimuthal feature. The model provides detailed characteristics of the excited modes which could not be determined experimentally.
- 5) A numerical code has been developed to predict the effect of the mean flow on the acoustic mode shape. The code is used to predict for the first time the transverse and diametral mode shapes at different Mach numbers.
- 6) The mean flow was found to have a strong effect on the transverse mode frequency and shape. The phase and amplitude distributions of both the acoustic pressure and the particle velocity changed substantially with the mean flow Mach number, especially near the cavity mouth.

8.2. Recommendations for future work

The findings of the current research provide fundamental understanding of several physical phenomena associated with the self-excitation mechanism of the diametral modes. However, they also demonstrate that further research is needed to improve the current state of knowledge. Three recommendations for future work are presented in this section. They address the effect of the approaching flow, the effect of the change of the mode shape with the Mach number on power production and suppression techniques.

The dependency of the fluid-dynamic oscillation on the approaching boundary layer momentum thickness is well demonstrated in the literature. The current research and some work in the literature suggest similar dependency for the case of fluid-resonance oscillation. However, there was no thorough investigation dedicated to determine the different characteristics of this

dependency. For example, the effect of the approach boundary layer thickness on the most unstable Strouhal number and on the overall characteristics of diametral mode acoustic resonances should be considered, especially for the case of fully developed turbulent flow. Moreover, different studies showed that, for fluid-dynamic oscillation, an increase of the thickness of the approaching boundary layer beyond a certain limit can suppress the oscillation entirely. The existence of similar condition for the case of the fluid-resonance oscillation should be investigated with emphasis on the case with small cavity depth, $d/D \sim 1/12$.

The current research showed that the mode shape of the acoustic resonance is altered with the increase of the Mach number. Hitherto, this change in the mode shape was never considered when models to predict the acoustic power production were developed. The change of the mode shape is expected to have direct effect on the location and size of the region of power production and on the Strouhal number of the excitation process, as a function of the Mach number. This goal can be achieved by performing numerical simulation using highly efficient discretization and integration schemes.

The third recommendation is to investigate the different possible suppression techniques that can be applied to the excitation of the diametral modes. The behaviour of any suppression technique is highly dependent on the nature of the excitation source and the characteristics of the acoustic resonance. Therefore, there is a need to investigate the effect of the different suppression techniques for the case of diametral mode acoustic resonances. Suppression techniques can be categorized into passive control and active control techniques. Passive techniques usually involve geometrical modifications. Examples of this are rounding or chamfering the cavity edges, adding a lip at, or upstream of the cavity edge and changing the slope of the cavity floor to alter the shear layer flow at the impinging edge. Examples of active control techniques are steady injection at the cavity floor, oscillating mechanical fence upstream of the cavity, and synthetic jet through the leading edge.

BIBLIOGRAPHY

- Ahuja k. k. and Mendoza j. Effect of cavity dimensions, boundary layer and temperature on cavity noise on emphasis on benchmark data to validate computational aeroacoustic codes [Report]. NASA contractor, 1995. - 4653.
- Ahuja K.K. and Chambers F.W. Prediction and measurement of flows over cavities - a survey [Conference] // AIAA. - 1987. - 87-022.
- Alpert P. Implicit filtering in conjunction with explicit filtering [Journal] // journal of computational physics. - 1981. - Vol. 44. - pp. 212-219.
- Ashcroft G. and Zhang X. Optimized prefactored compact scheme [Journal] // journal of computational physics. - 2003. - Vol. 190. - pp. 459-477.
- Astley R. J. and Eversman W. Acoustic transmission in non=uniform ducts with mean flow, part II: the finite element method [Journal] // journal of sound and vibration. - 1981. - Vol. 74. - pp. 103-121.
- Blevins R. D. Formula for natural frequency and mode shape [Book]. - [s.l.] : Litton Educational Publishing, Inc, 1979.
- Block P. J. W. Noise response of cavities of varying dimensions at subsonic speeds [Report] : NASA-TN-D-8351. - 1976.
- Bogey C., Bailly C. and Juve D. Computation of flow noise using source terms in linearized Euler's equations [Journal] // AIAA J.. - 2002. - Vol. 40. - pp. 235-243.
- Brown R. S. [et al.] Vortex shedding as a source of acoustic energy in segmented solid rockets [Journal] // Journal of Spacecraft and Rockets. - 1981. - Vol. 18. - pp. 312-319.
- Bruggeman J. C. [et al.] Self-sustained aero-acoustic pulsations in gas transport systems: Experimental study of the influence of closed side branches [Journal] // Journal of sound and vibration. - 1991. - Vol. 150. - pp. 371-393.

Bruggeman J.C. [et al.] Flow induced pulsations in gas transport systems: analysis of the influence of closed side branches [Journal] // Journal of Fluids Engineering. - 1989. - Vol. 111. - pp. 484-491.

Chatellier L., Laumonier J. and Gervais Y. Theoretical and experimental investigations of low Mach number turbulent cavity flow [Journal] // Experiments in Fluids. - 2004. - pp. 728-740.

Chevray R. Entrainment in turbulent flows: mechanisms and implications [Book]. - North-Holland : Elsevier Science Publishers B.V., 1984. - pp. 365-369.

Colonus T. and Lele S. Computatuonal aeroacoustics: progress on nonlinear problems of sound generation [Journal] // progress in aerospace sciences. - 2004. - Vol. 40. - pp. 345-416.

Cooper A. J. and Peake N. Trapped acoustic modes in aeroengine intakes with swirling flow [Journal] // journal of fluid mechanics. - 2000. - Vol. 419. - pp. 151-175.

Davies P. Flow-acoustic coupling in ducts [Journal] // Journal of sound and vibration. - 1981. - Vol. 77. - pp. 191–209.

Disimilea P. J. and Toy N. Acoustical properties of a long rectangular cavity of constant cross-section immersed in a thick boundary layer [Journal] // International Journal of Mechanical Sciences. - 2004. - Vol. 46. - pp. 1827–1844.

East L. F. Aerodynamically induced resonance in rectangular cavities [Journal] // journal of sound and vibration. - 1966. - pp. 277–287.

Elder S. A. Self-Excited Depth-Mode Resonance for a Wall-Mounted Cavity in Turbulent Flow [Journal] // journal of Acoustic Society of America. - 1978. - Vol. 64. - pp. 877-890.

Ethembaoglu S. Some characteristics of unstable flow past slots [Journal] // Journal of Hydraulic Division. - 1978. - Vol. 104. - pp. 649-666.

Eversman W. Energy Flow Criteria for Acoustic Propagation in Ducts With Flow [Journal] // Journal of Acoustic Society of America. - 1971. - Vol. 49. - pp. 1717-1721.

Eversman W. Theoretical model for duct acoustic propagation and radiation. In *Aeroacoustics of Flight Vehicles: Theory and Practice. Volume 2: Noise Control [Report]*. - [s.l.] : NASA, 1991. - pp. 101-164. - RP-1258.

Ewert R. and Schröder W. Acoustic perturbation equations based on flow decomposition via source filtering [Journal] // *journal of computational physics*. - 2003. - Vol. 188. - pp. 365-398.

Flandro G. A. Vortex Driving Mechanism in Oscillatory Rocket Flows [Journal] // *Journal of Propulsion*. - 1986. - Vols. ,2. - pp. 206-214.

Freymuth P. On transition in a separated laminar boundary layer. *J. Fluid Mech [Journal]* // *journal of fluid mechanics*. - 1966. - Vol. 25. - pp. 683-704.

Geveci M. [et al.] Imaging of the self-excited oscillation of flow past a cavity during generation of a flow tone [Journal] // *Journal of fluids and structures*. - 2003. - Vol. 18. - pp. 665-694.

Gharib M. and Roshko A. The effect of flow oscillations on cavity drag [Journal] // *Journal of fluid mechanics*. - 1987. - Vol. 177. - pp. 501-530.

Hixon R. Prefactored small stencil compact schemes [Journal] // *journal of computational physics*. - 2000. - Vol. 165. - pp. 522-541.

Ho C. and Huerre P. Perturbed free shear layers [Journal] // *Annual review of fluid mechanics*. - 1984. - Vol. 16. - pp. 365-422.

Ho C. M. and Huang L. S. Subharmonics and vortex merging in mixing layers [Journal] // *journal of fluid mechanics*. - 1982. - Vol. 119. - pp. 443-473.

Hourigan K. [et al.] Aerodynamic sources of Acoustic Resonance in a duct with Baffles [Journal] // *Journal of fluid and structures*. - 1990. - Vol. 4. - pp. 345-370.

Howe M. S. Contributions to the Theory of Aerodynamic Sound, with Application to Excess Jet Noise and the Theory of the Flute [Journal] // *Journal of Fluid Mechanics*. - 1975. - Vol. 71. - pp. 625-673..

Hu F., Hussaini M. and Manthey J. Low-dissipation and low-dispersion Runge–Kutta schemes for computational acoustics [Journal] // journal of computational physics. - 1996. - Vol. 124. - pp. 177-191.

Huang X.Y. and Weaver D.S. Control of flow-induced fin vibration by anti-sound [Journal] // Journal of sound and vibration. - 1994. - Vol. 169. - pp. 428-432.

Hussain A. F. and Zaman K. Q. The "preferred mode" of the axisymmetric jet. d. Fluid Mech [Journal] // journal of fluid mechanics. - 1981. - Vol. 110. - pp. 39-71.

Karamcheti K. Acoustic Radiation from Two-Dimensional Rectangular Cutouts in Aerodynamic Surfaces [Report]. - [s.l.] : NACA TN 3487, 1955.

Keller J. J. and Escudier M. P. Flow-excited resonances in covered cavities [Journal] // Journal of Sound and Vibration. - 1983. - Vol. 86. - pp. 199-226.

Kennedy C. A. and Carpenter M. H. Comparison of several numerical methods for simulation of compressible shear layer [Report] : Technical paper 3484. - [s.l.] : NASA, 1997.

Kinsler L. E. [et al.] Fundamentals of acoustics [Book]. - New York : John Wiley & Sons, Inc., 2000.

Lafon P. [et al.] Aeroacoustical Coupling in a Ducted Shallow Cavity and Fluid/Structure Effects on a Steam Line [Journal] // Journal of Fluids and Structures. - 2003. - Vol. 18. - pp. 695-713.

Larcheveque L., Sagaut P. and Labbe O. Large-eddy simulation of a subsonic cavity flow including asymmetric three-dimensional effects [Journal] // Journal of fluid mechanics. - 2007. - Vol. 577. - pp. 105-126.

Lele S. K. Compact finite difference schemes with spectral like resolution [Journal] // journal of computational physics. - 1992. - Vol. 103. - pp. 16-42.

Li X.D. [et al.] Azimuthal sound mode propagation in axisymmetric flow ducts [Journal] // AIAA Journal. - 2004. - Vol. 42. - pp. 2019-2027.

Maufl D. J. and East L. F Three-dimensional flow in cavities [Journal] // journal of fluid mechanics. - 1963. - Vol. 16. - pp. 620–632.

Michalke A. On spatially growing disturbance in an inviscid shear layer [Journal] // Journal of Fluid Mechanics. - 1965. - Vol. 23. - pp. 521-544.

Michalke A. On the inviscid instability of the hyperbolic tangent velocity profile [Journal] // journal of fluid mechanics. - 1964. - Vol. 19. - pp. 543-556.

Miksad R. W Experiments on the nonlinear stages of free shear layer transition [Journal] // journal of fluid mechanics. - 1972. - Vol. 56. - pp. 695-719.

Nayfeh A., Kaiser J. E. and Telionis D.i P. Acoustics of aircraft engine-duct systems [Journal] // AIAA J.. - 1975. - Vol. 13. - pp. 130-153.

Nelson P.A., Halliwell N.A. and Doak P.E. Fluid dynamics of a flow excited resonance. Part I: experiment [Journal] // Journal of Sound and Vibration. - 1981. - Vol. 78. - pp. 15–38.

Nelson P.A., Halliwell N.A. and Doak P.E. Fluid dynamics of a flow excited resonance. Part II: flow acoustic interaction [Journal] // Journal of Sound and Vibration. - 1983. - Vol. 91. - pp. 375–402.

Nomoto H. and Culick F.E.C. An experimental investigation of pure tone generation by vortex shedding in a duct [Journal] // journal of sound and vibration. - 1982. - Vol. 84. - pp. 247-252.

Pollack M.L. Flow-induced tones in side-branch pipe resonators [Journal] // Journal of the Acoustical Society of America. - 1980. - Vol. 7. - pp. 1153–1156.

Pulliam T. H. Artificial dissipation models for the Euler equations [Journal] // AIAA J.. - 1986. - Vol. 24. - pp. 1931-1940.

Rice E.I. Acoustic Liner Optimum Impedance for Spinning Modes With Mode Cut Off Ratio as the design criterion [Report]. - [s.l.] : NASA, 1976. - TM X-73411.

Rockwell D. and Knisely C. Observations of the three-dimensional nature of unstable flow past a cavity [Journal] // Physics of Fluids. - 1980. - Vol. 23. - pp. 425-431.

Rockwell D. and Naudascher E. Review: Self-Sustaining Oscillations of Flow Past Cavities [Journal] // *Journal of Fluids Engineering*. - 1978. - Vol. 100. - pp. 152-165.

Rockwell D. and Schachenmann A. Self-generation of organized waves in an impinging turbulent jet at low mach numbers [Journal] // *Journal of fluid mechanics*. - 1982. - Vol. 117. - pp. 425–441.

Rockwell D. and Schachenmann A. The organized shear layer due to oscillations of a turbulent jet through an axisymmetric cavity [Journal] // *Journal of Sound and Vibration*. - 1983. - Vol. 87. - pp. 371–382.

Rockwell D. Oscillations of impinging shear layers [Journal] // *AIAA journal*. - 1983. - Vol. 21. - pp. 645-664.

Rockwell D. Prediction of oscillation frequencies for unstable flow past cavities [Journal] // *journal of fluids engineering*. - 1977. - Vol. 99. - pp. 294-300.

Rossiter J. E. Wind-tunnel experiments on the flow over rectangular cavities at subsonic and transonic speeds [Report] : Aeronautical research council reports and memoranda, No. 3438. - 1964.

Rowley C. W., Colonius T. and Basu A. J. On self-sustained oscillations in two-dimensional compressible flow over rectangular cavities [Journal] // *journal of fluid mechanics*. - 2002. - Vol. 455. - pp. 315-346.

Sarohia V. Experimental investigation of oscillations in flows over shallow cavities [Journal] // *AIAA Journal*. - 1977. - Vol. 15. - pp. 984-991.

Sato H. An experimental study of non-linear interaction of velocity fluctuations in the transition region of a two-dimensional wake [Journal] // *Journal of fluid mechanics*. - 1970. - Vol. 44. - pp. 741-765.

Sato H. The transition process of the free shear layers [Conference] // *Turbulence and chaotic phenomena in fluids*. - (North-Holland) : Elsevier Science Publishers B.V., 1984. - pp. 107-109.

Schachenmann A. and Rockwell D. Self-sustained oscillations of turbulent pipe flow terminated by an axisymmetric cavity [Journal] // Journal of sound and vibration. - 1980. - Vol. 73. - pp. 61-72.

Scott M. C. and John F. Turbulent boundary layer to single-stream shear layer: The transition region [Journal] // journal of fluid mechanics. - 2003. - Vol. 494. - pp. 187-221.

Shen C. and Floryan j. M. Low Reynolds number flow over cavities [Journal] // Physics of Fluids. - 1985. - Vol. 28. - pp. 3191-3202.

Stanescu D. and Habashi W. 2N-storage Runge–Kutta schemes for acoustics [Journal] // journal of computational physics. - 1998. - Vol. 143. - pp. 674–681.

Stoubos A.K. [et al.] Aerodynamically generated acoustic resonance in a pipe with annular flow restrictors [Journal] // Journal of Fluids and Structures. - 1999. - Vol. 13. - pp. 755–778.

Stubos A.K. [et al.] Aerodynamically generated acoustic resonance in a pipe with annular flow restrictors [Journal] // Journal of Fluids and Structures. - 1999. - Vol. 13. - pp. 755-778.

Tam C. Computational Aeroacoustics: issues and methods [Journal] // AIAA J.. - 1995. - Vol. 33. - pp. 1788-1796.

Tam C. Discrete tones of isolated airfoil [Journal] // Journal of the acoustical society of America. - 1974. - Vol. 55. - pp. 1173-1177.

Tam C. Excitation of instability waves in a two-dimensional shear layer by sound [Journal] // journal of fluid mechanics. - 1978. - Vol. 89. - pp. 357-372.

Tam C. R. W. and Block P. T. W. On the tones and pressure oscillations induced by flow over rectangular cavities [Journal] // Journal of fluid mechanics. - 1978. - Vol. 89. - pp. 373-399.

Tam C., Webb J. and Dong Z. A study of short wave components in computational acoustics [Journal] // journal of computational acoustics. - 1993. - Vol. 1. - pp. 1-30.

Tracy M. and Plentovich E. Characterization of Cavity Flow Fields Using Pressure Data Obtained in the Langley 0.3-Meter Transonic Cryogenic Tunnel [Report]. - [s.l.] : NASA Technical Memorandum 4436, 1993.

Vichnevetsky R Wave propagation analysis of difference schemes for hyperbolic equations: A review [Journal] // International Journal for Numerical Methods in Fluids. - 1987. - Vol. 7. - pp. 409-452.

Wilcox Jr. F. Experimental measurements of internal store separation characteristics at supersonic speeds [Conference] // Conference of Royal Aeronautical Society. - Bath, United Kingdom : [s.n.], 1990. - pp. 5.1-5.16.

Ziada S. A Flow visualization study of flow- acoustic coupling at the mouth of a resonant side-branch [Journal] // Journal of fluids and structures. - 1994. - Vol. 8. - pp. 391-416.

Ziada S. and Bühlmann E. T Flow Impingement as an Excitation Source in Control Valves [Journal] // journal of fluids and structures. - 1989. - Vol. 3. - pp. 529-549.

Ziada S. and Rockwell D. Oscillation of an unstable mixing layer impinging upon an edge [Journal] // Journal of fluid mechanics. - 1982. - Vol. 124. - pp. 307-334.

Ziada S. and Shine S. Strouhal numbers of flow-excited acoustic resonance of closed side branches [Journal] // Journal of Fluids and Structures. - 1999. - Vol. 13. - pp. 127–142.

Ziada S., Ng H. and Blake C. E. Flow excited resonance of a confined shallow cavity in low Mach number flow and its control [Journal] // Journal of fluids and structures. - 2003. - Vol. 18. - pp. 79-92.

APPENDIX A

ADDITIONAL

EXPERIMENTAL RESULTS

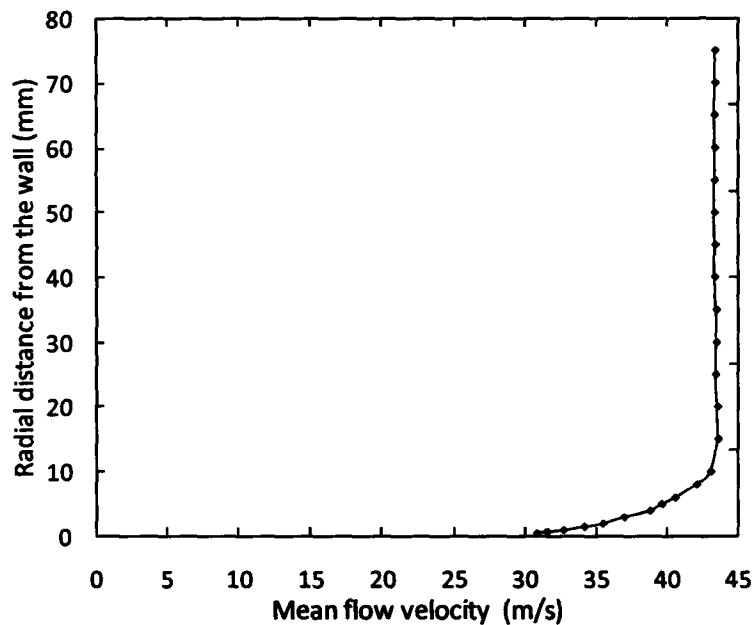


Figure A-1 Radial profile of mean velocity at the cavity upstream edge for a reference velocity of 40 m/s at the end of the bell mouth

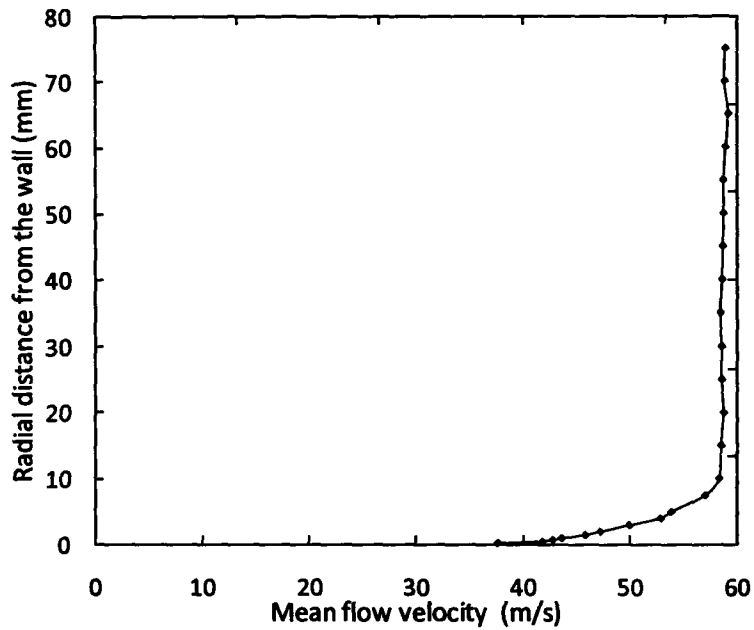


Figure A-2 Radial profile of mean velocity at the cavity upstream edge for a reference velocity of 55 m/s at the end of the bell mouth

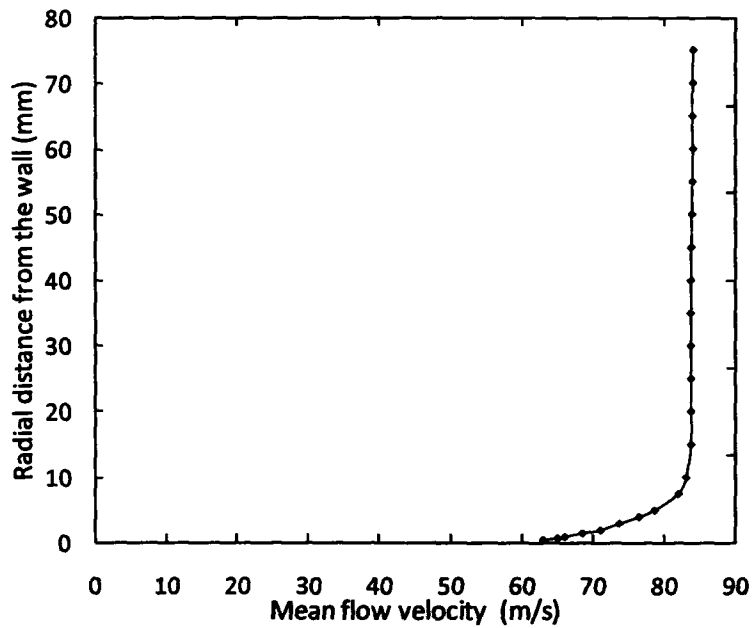


Figure A-3 Radial profile of mean velocity at the cavity upstream edge for a reference velocity of 80 m/s at the end of the bell mouth

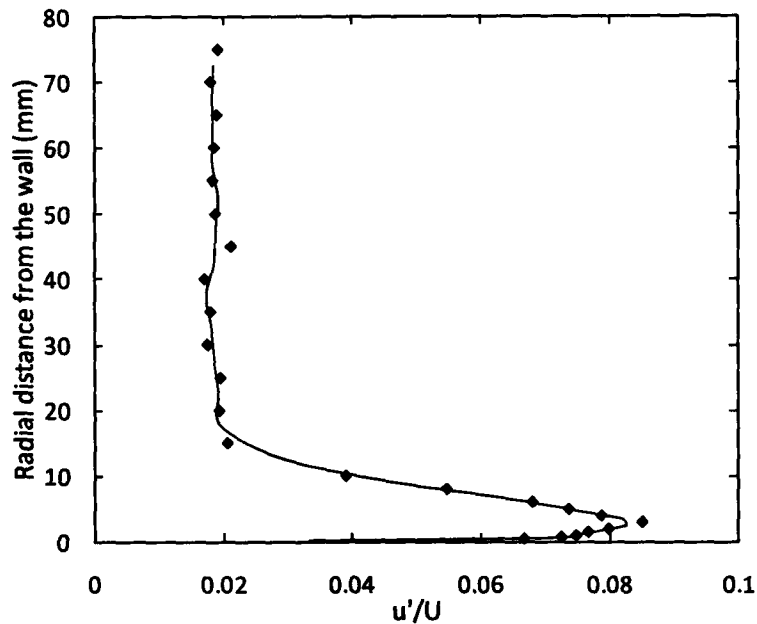


Figure A-4 Radial distribution of the dimensionless RMS amplitude of fluctuation velocity at the cavity upstream edge for a reference velocity of 40 m/s at the end of the bell mouth (the continuous line is a moving average of the measurement data)

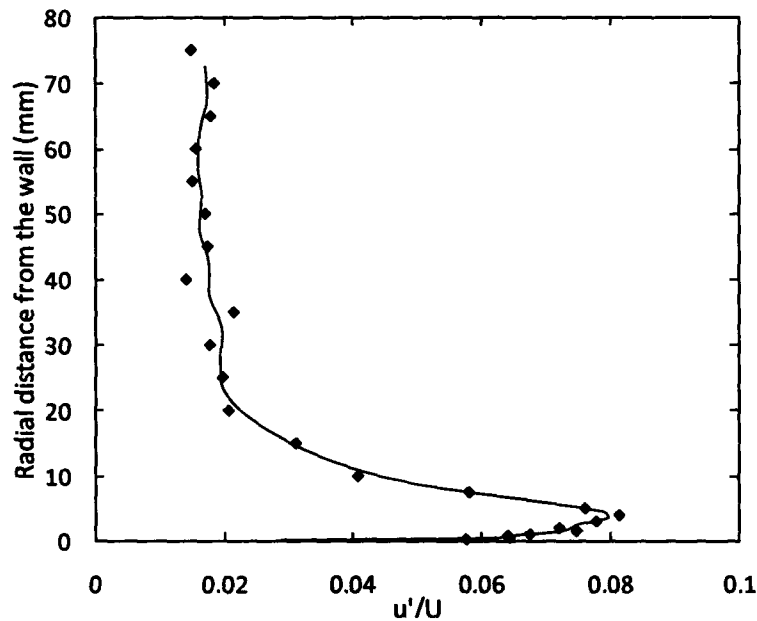


Figure A-5 Radial distribution of the dimensionless RMS amplitude of fluctuation velocity at the cavity upstream edge for a reference velocity of 55m/s at the end of the bell mouth (the continuous line is a moving average of the measurement data)

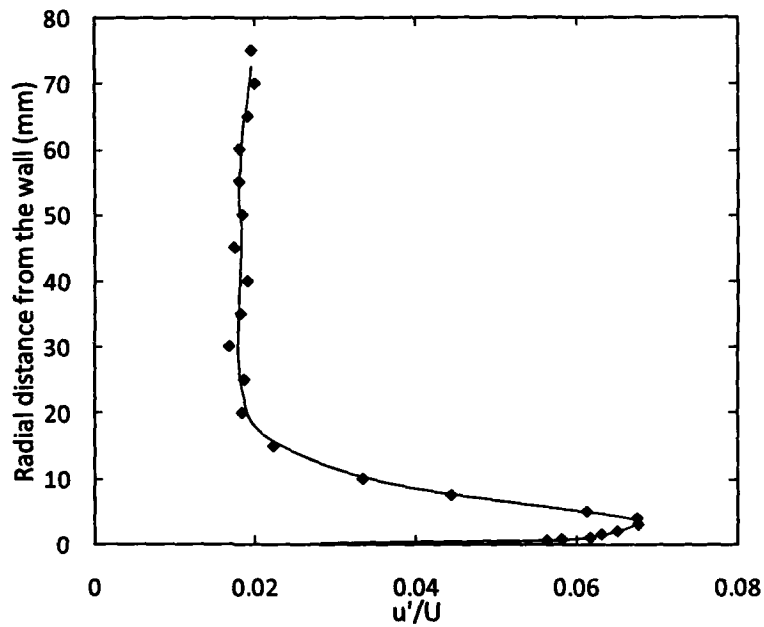


Figure A-6 Radial distribution of the dimensionless RMS amplitude of fluctuation velocity at the cavity upstream edge for a reference velocity of 80 m/s at the end of the bell mouth (the continuous line is a moving average of the measurement data)

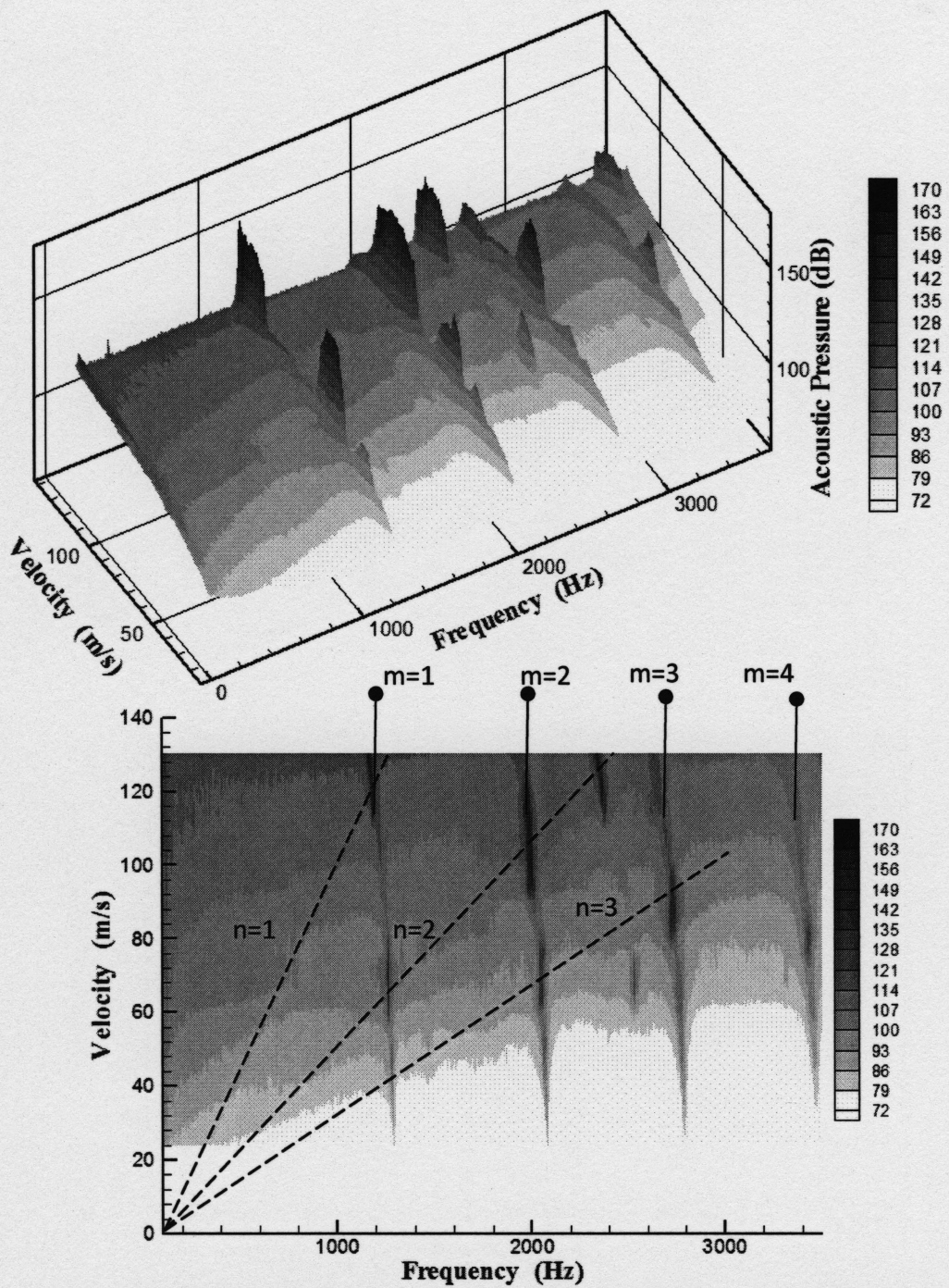


Figure A-7 Waterfall plot and 2D pressure contours for $L/d=4$, $d/D=1/12$. m is the diametral mode number, n is the free shear layer mode number

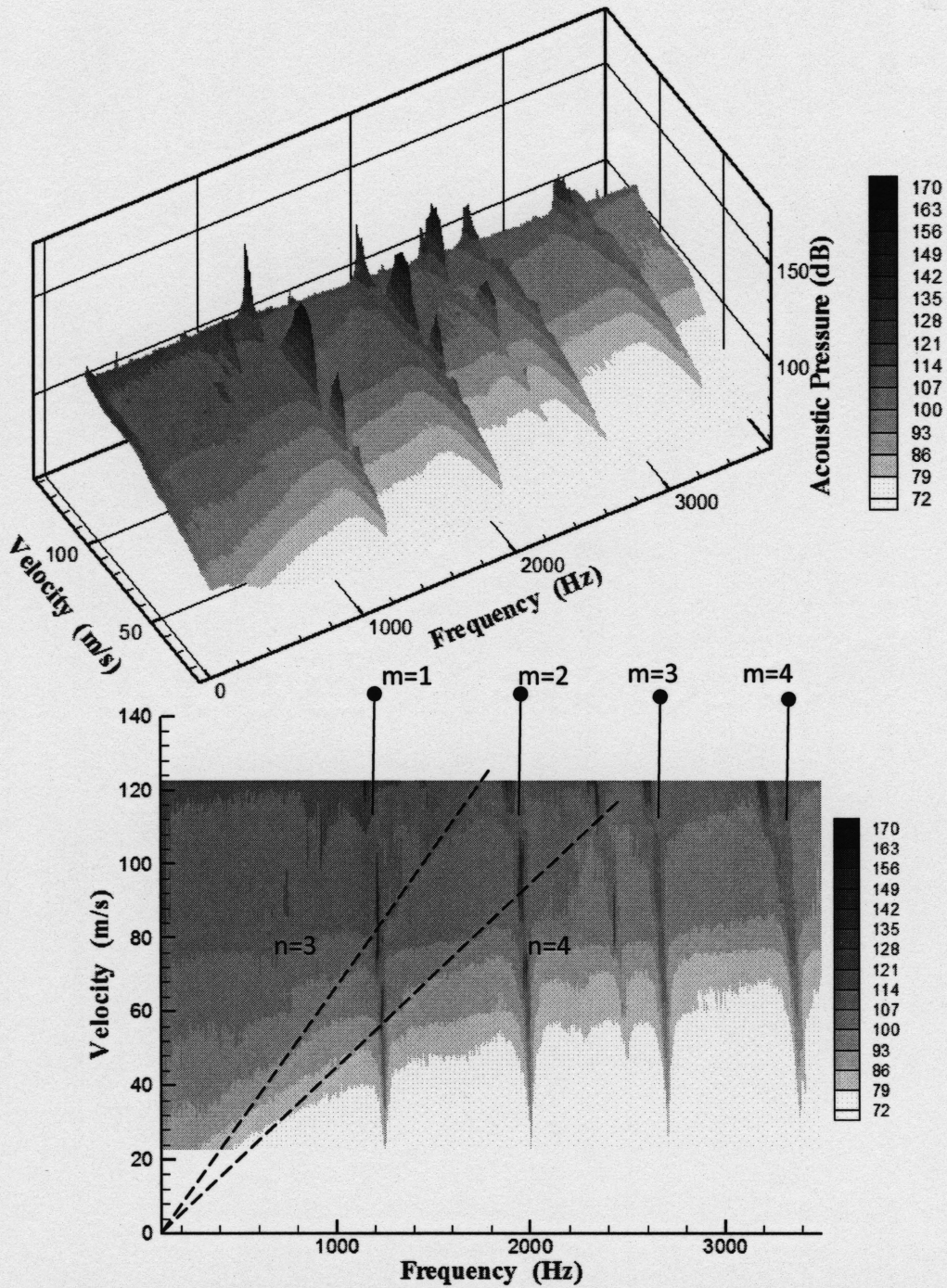


Figure A-8 Waterfall plot and 2D pressure contours for $L/d=8$, $d/D=1/12$. m is the diametral mode number, n is the free shear layer mode number

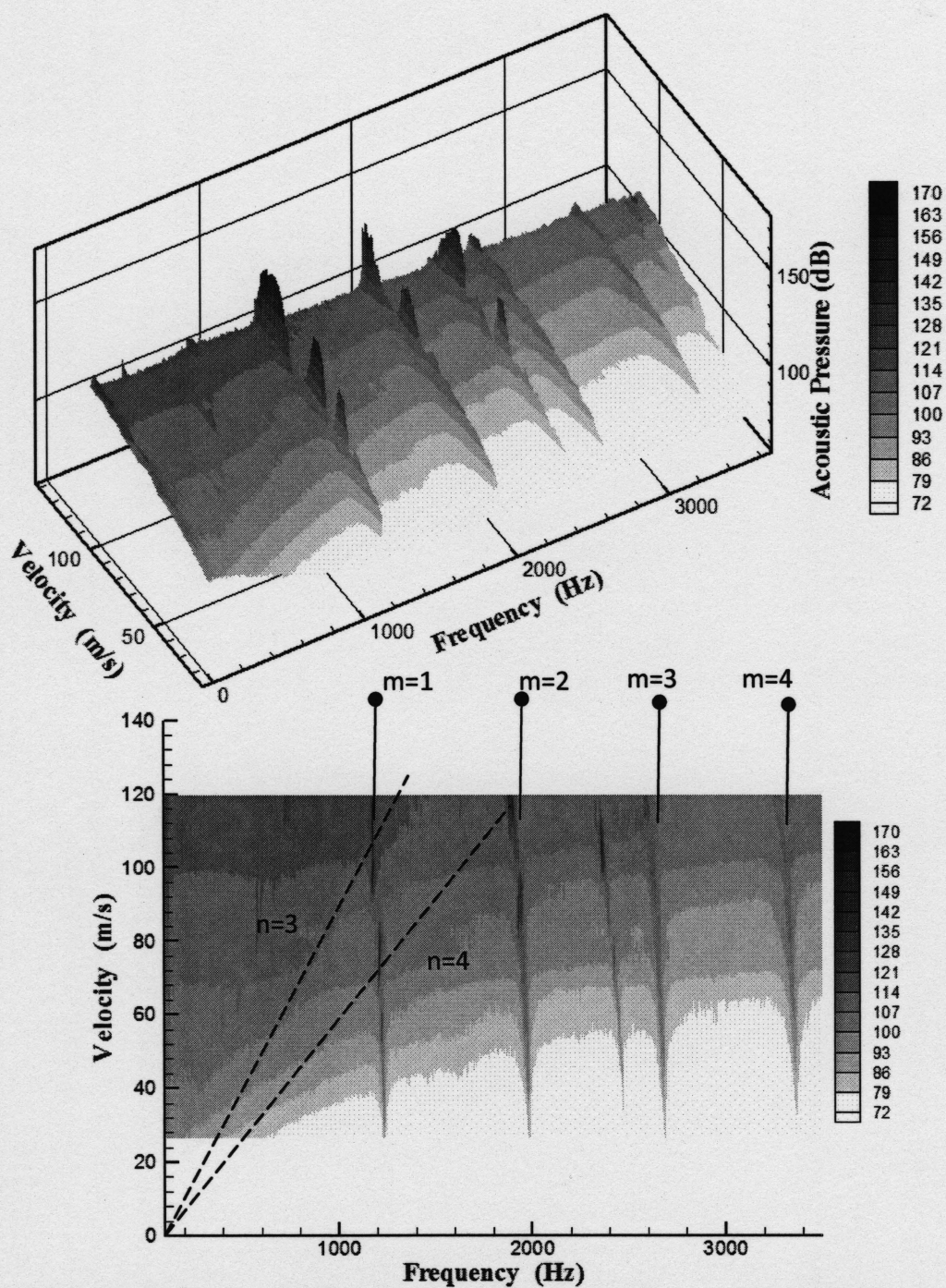


Figure A-9 Waterfall plot and 2D pressure contours for $L/d=10$, $d/D=1/12$. m is the diametral mode number, n is the free shear layer mode number

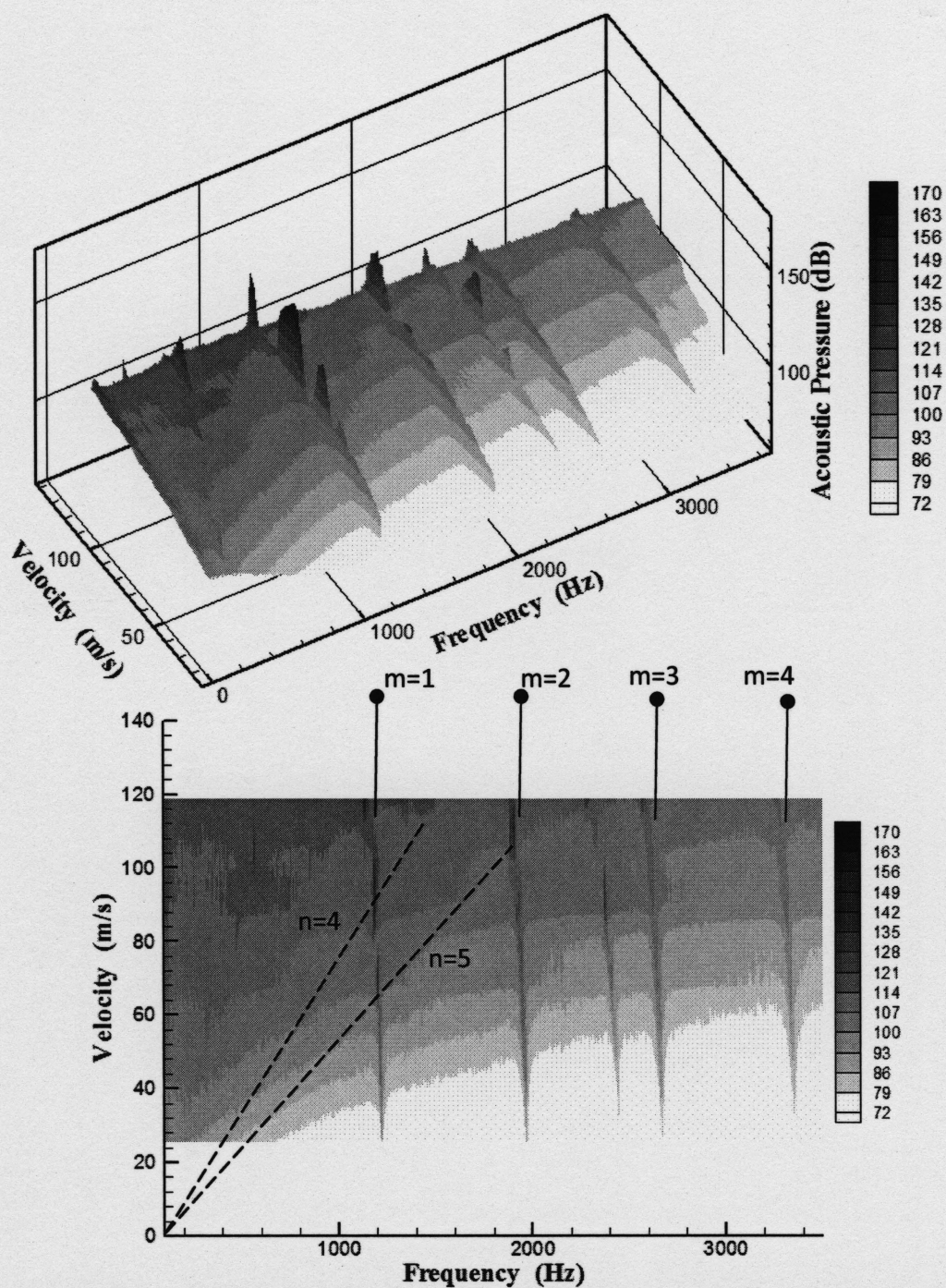


Figure A-10 Waterfall plot and 2D pressure contours for $L/d=12$, $d/D=1/12$. m is the diametral mode number, n is the free shear layer mode number

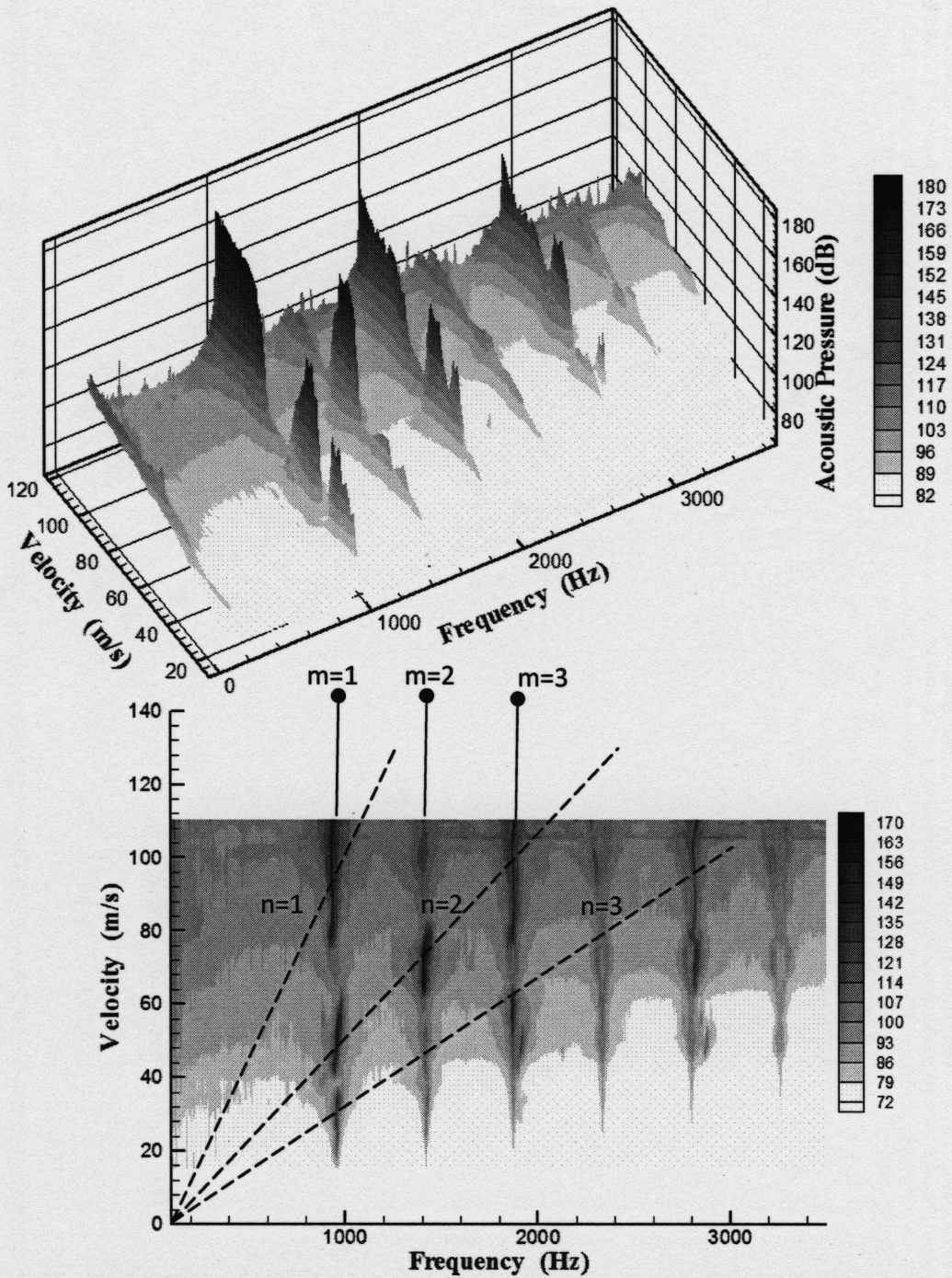


Figure A-11 Waterfall plot and 2D pressure contours for $L/d=1$, $d/D=4/12$. m is the diametral mode number, n is the free shear layer mode number

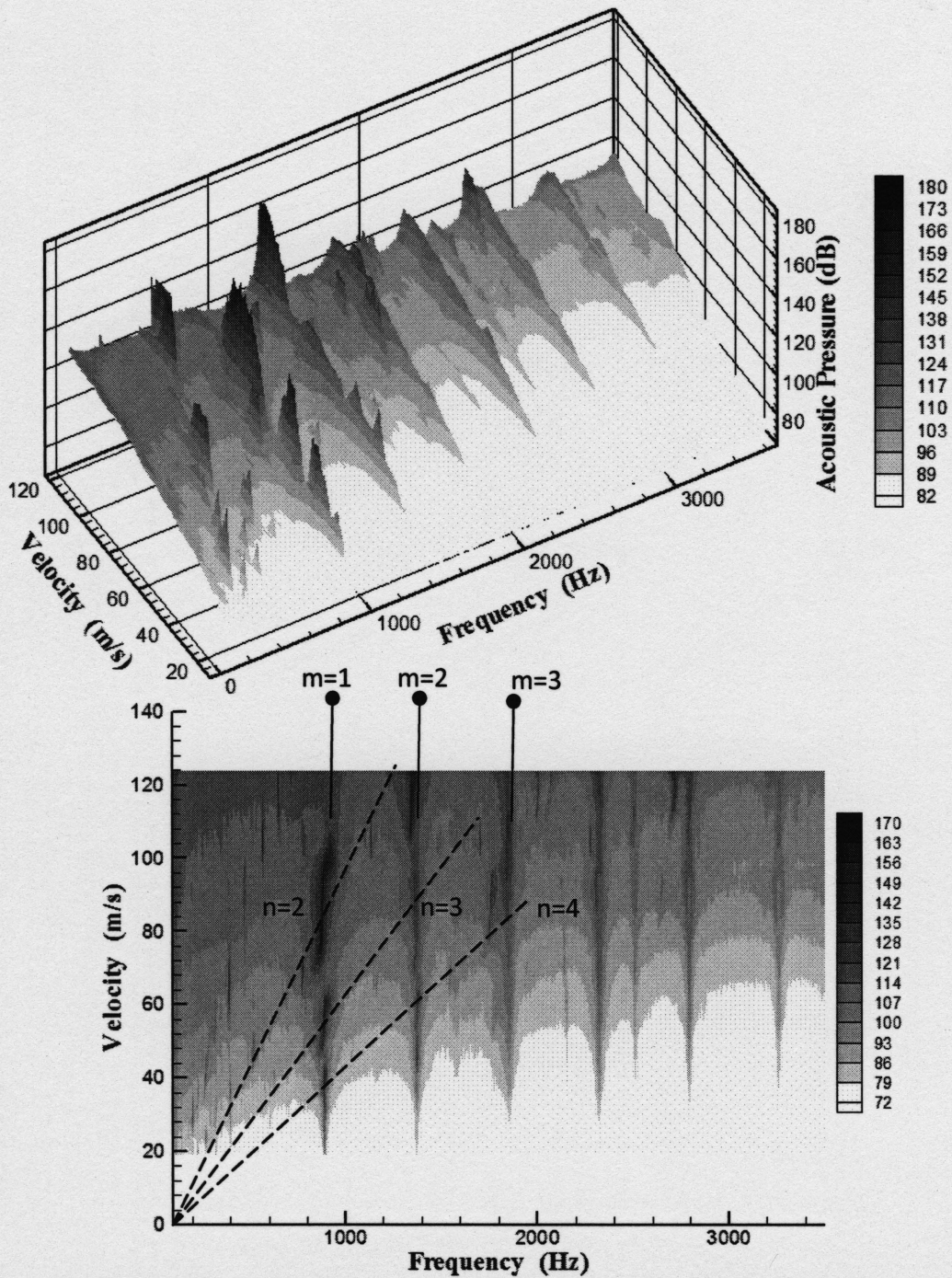


Figure A-12 Waterfall plot and 2D pressure contours for $L/d=2$, $d/D=4/12$. m is the diametral mode number, n is the free shear layer mode number

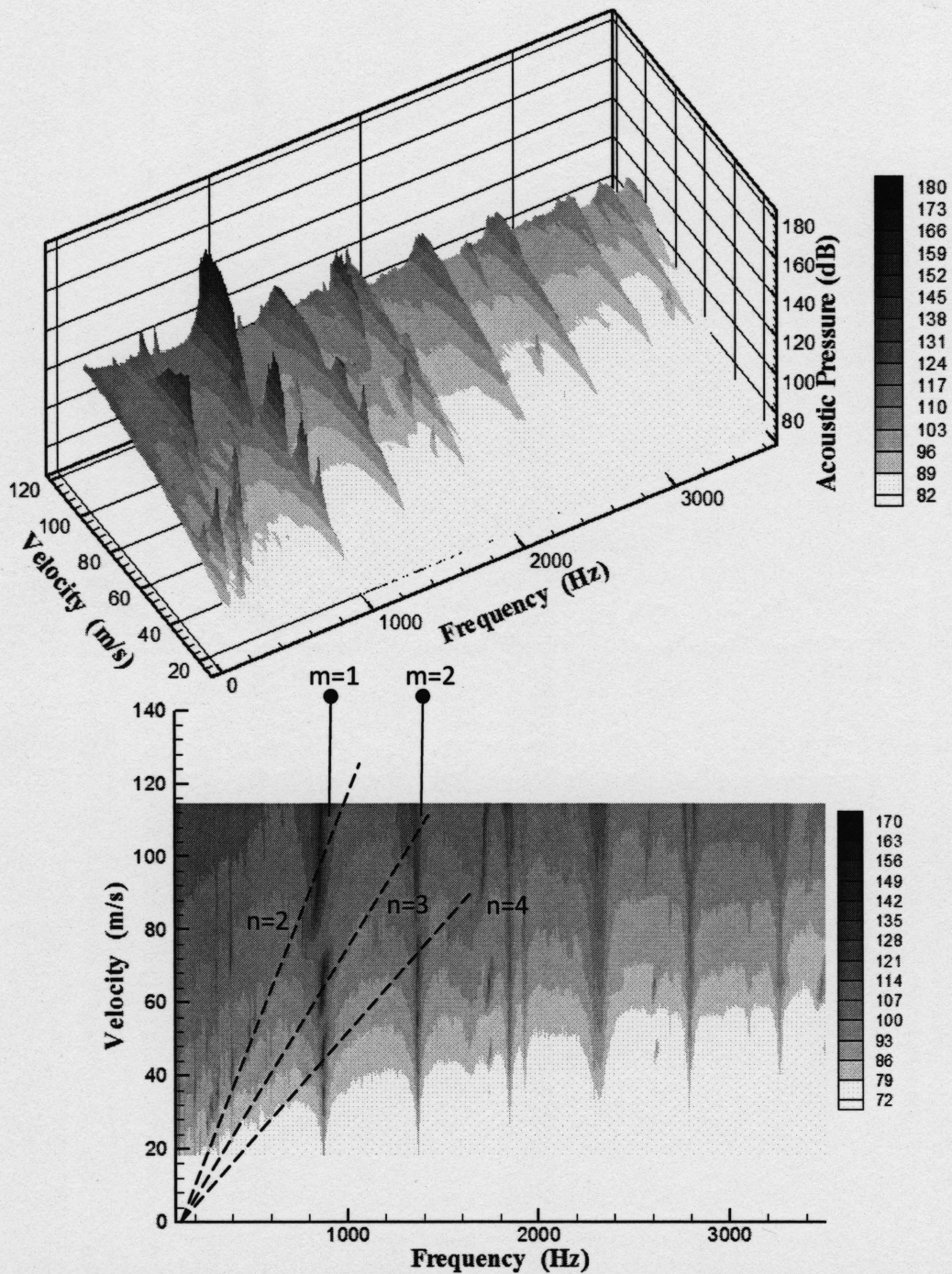


Figure A-13 Waterfall plot and 2D pressure contours for $L/d=5/2$, $d/D=4/12$. m is the diametral mode number, n is the free shear layer mode number

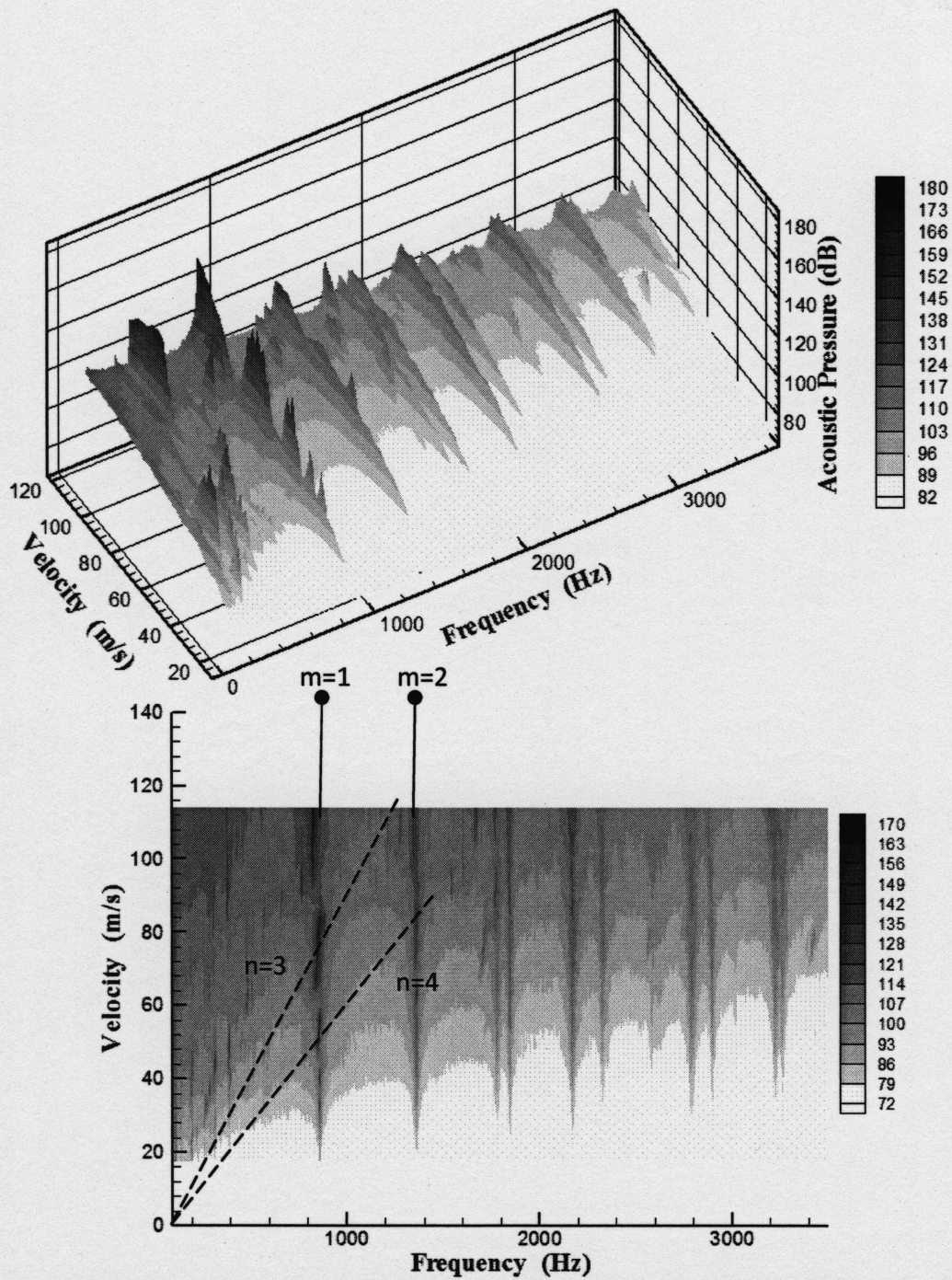


Figure A-14 Waterfall plot and 2D pressure contours for $L/d=3$, $d/D=4/12$. m is the diametral mode number, n is the free shear layer mode number

APPENDIX B

UNCERTAINTY ANALYSIS

This appendix outlines the uncertainty associated with the different measured and calculated quantities. The systematic uncertainties are considered small compared to the measurement precision. Considering only random uncertainty allows the use of Kline and McClintock method, equation B-1, to calculate the uncertainty propagation.

$$\delta Y = \sum_{i=1}^n \sqrt{\left(\frac{\partial Y}{\partial X_i}\right)^2} \delta X_i \quad B - 1$$

Where δY , is the uncertainty of the dependent variable Y and δX_i , is the uncertainty of the independent variable X_i .

The uncertainty in the acoustic pressure measurement is arising from the uncertainty in the calibration of the pressure transducers, $\approx 4\%$, the uncertainty in measurement repeatability, $\approx 5\%$, and the resolution of the pressure transducers $\approx 3\%$. These values are the maximum values observed during the measurements. Using the quadratic sum of the uncertainties, the uncertainty in the acoustic pressure is found to be $\approx 7\%$

The mean flow velocity is measured using a pitot tube connected to a differential pressure transducer. The uncertainty in the calibration of the differential pressure transducer is 2%, which results in 1% uncertainty in the velocity measurement. The standard deviation in the averaged reading of the Pitot tube is 0.5%. Based on these values, the uncertainty in the mean flow is about 1.5%.

The uncertainty of the dimensionless acoustic pressure ($P^*=P/2\rho U^2$) can be calculated as a function of the uncertainty of the acoustic pressure and the mean flow velocity:

$$\frac{\delta P^*}{P^*} = \sqrt{\left(\frac{\delta P}{P}\right)^2 + \left(2\frac{\delta U}{U}\right)^2} \quad B - 2$$

Based on this formula, the uncertainty of the dimensionless pressure is 7.5%.

The uncertainty of the Strouhal number ($St=fL/U$) depends on the uncertainty of the frequency, f ; the cavity length, L ; and the mean flow velocity, U . The Strouhal number uncertainty is calculated as follow:

$$\frac{\delta St}{St} = \sqrt{\left(\frac{\delta f}{f}\right)^2 + \left(\frac{\delta L}{L}\right)^2 + \left(\frac{\delta U}{U}\right)^2} \quad B - 3$$

The frequency is determined with resolution of 1 Hz and the minimum resonance frequency is 900 HZ which resulting in uncertainty of 0.1%. The tolerance in the cavity length is 1%. Therefore, the $\frac{\delta St}{St}$ is 1.8%.

The hotwire is calibrated using Pitot tube to measure the mean velocity. The uncertainty of the hotwire measurement can be determined following Yavuzkurt (1984):

$$\frac{\delta \bar{U}}{\bar{U}} = \sqrt{\alpha^2 + \beta^2} \quad B - 4$$

$$\frac{\delta(\overline{u'^2})^{1/2}}{(\overline{u'^2})^{1/2}} = \sqrt{\alpha^2 + \beta^2} \quad B - 5$$

Where \bar{U} is the hotwire mean flow velocity, u' is the fluctuating velocity, α is the uncertainty in the Pitot tube measurement and β is the uncertainty due to the curve fitting of the calibration data. The value of α is 1.5% and β is 1%. The uncertainty due to temperature fluctuation was kept to minimum level by using high over-heat ratio and ensuring constant surrounding temperature. Using equations B-4 and B-5, the uncertainty of the mean and fluctuation velocity is estimated to be 1.8%.

The uncertainty of the displacement and momentum thicknesses is the result of the uncertainty of the velocity measurement mainly. The resolution of the traverse mechanism used to move the hotwire is less than 0.1% of the boundary layer thickness. Therefore, the contribution of the uncertainty of the hotwire displacement is relatively small. Thus, the uncertainty of the displacement and momentum thicknesses can be calculated as follow:

$$\frac{\delta(\delta^*)}{\delta^*} = \frac{\delta\left(\frac{u(y)}{U}\right)}{\frac{u(y)}{U}} \left| \frac{\int_0^R \left(\frac{u(y)}{U}\right) \left(1 - \frac{y}{R}\right) dy}{\delta^*} \right| \quad B - 6$$

$$\frac{\delta(\theta_0)}{\theta_0} = \frac{\delta\left(\frac{u(y)}{U}\right)}{\frac{u(y)}{U}} \left| \left(1 - \frac{\int_0^R \left(\frac{u(y)}{U}\right) \left(1 - \frac{y}{R}\right) dy}{\theta_0} \right) \right| \quad B - 7$$

Where, δ^* , is the displacement thickness, θ_0 , is the momentum thickness, U , is the mean flow velocity outside the boundary layer and y , is the distance from the pipe wall.. The uncertainty of both quantities is found to reach up to 40%.